DOCTORAL THESIS

A Study on the Detection of 'Winged' Radio Sources, an Exotic Subclass

Author:
SOUMEN KUMAR BERA

Supervisor:
Dr. SOUMEN MONDAL

A thesis submitted to the Jadavpur University
for the degree of Doctor of Philosophy (Science)

in the

Department of Physics

August 2022

JADAVPUR UNIVERSITY
KOLKATA-700032, INDIA

CERTIFICATE FROM THE SUPERVISOR

This is to certify that the thesis entitled **"A Study on the Detection of 'Winged' Radio Sources, an Exotic Subclass"** submitted by **Shri Soumen Kumar Bera (Index No.: 214/18/Phys/26, Registration No.: SOPHY-1121418)** who got his name registered on **26th September 2018** for the award of Ph. D. (Science) Degree of Jadavpur University, is absolutely based upon his own work under the supervision of **Dr. Soumen Mondal**, Associate Professor, Department of Physics, Jadavpur University and that neither this thesis nor any part of it has been submitted for either any degree/diploma or any other academic award anywhere before.

Soumen Mondal
8/8/2022

.....

Dr. Soumen Mondal
Associate Professor,
Department of Physics,
Jadavpur University,
Kolkata-700032, India

Dr. Soumen Mondal
Associate Professor
Department of Physics
Jadavpur University
Kolkata - 700032

DECLARATION

I do hereby declare that the work embodied in this thesis entitled **"A Study on the Detection of 'Winged' Radio Sources, an Exotic Subclass"** which is being submitted for the degree of Doctor of Philosophy (Science) has been carried out by me in the Relativity and Cosmology Research Centre (RCRC), PG Science Building, Department of Physics, Jadavpur University, Kolkata. Neither the thesis nor any part thereof has been presented anywhere earlier for any degree/diploma or academic award whatsoever.

Date: 08/08/2022
Kolkata, India

Soumen Kumar Bera

Soumen Kumar Bera
PhD Research Scholar,
Department of Physics,
Jadavpur University,
Index No.: 214/18/Phys/26,
Registration No.: SOPHY1121418

ABSTRACT OF THESIS

submitted by

Soumen Kumar Bera, Index No.: 214/18/Phys/26

for the Degree of Doctor of Philosophy (Sc.) in the Department of Physics and entitled

"A Study on the Detection of 'Winged' Radio Sources, an Exotic Subclass"

August 2022

For many years, astronomers have been perplexed by a subclass of extra-galactic radio sources known as "winged" radio galaxies. The "winged" radio source, is a small number of exotic radio sources that exhibit a peculiar radio morphology, where an additional pair of low-surface-brightness, diffuse lobes are observed along a secondary axis of symmetry in addition to the pair of high-surface-brightness, collimated primary lobes. The pair of secondary lobes are found to be aligned at a certain angle to the primary jet axis and are known as "wings". Depending on the position of the wings with respect to the main lobe axis, the winged sources are classified into two categories, 'X'-shaped radio galaxy (XRG) and 'Z'-shaped radio galaxy (ZRG). The winged radio source is a cosmic wonder. However, the origin of such sources is still elusive. Though there are several proposed models, none of them are yet to be established. To date, no proper statistical study has been done either on the general characteristics of wings or on the global attributes of the sources as a population. The primary reason is the low number of such sources, the low sample size restricts us from exploring this field.

In this thesis, I present the identification of new winged radio sources and the study of the global properties of this class of radio sources. The identification of winged sources is done from both the high and low-frequency data surveys. In order to study the morphology of the winged radio sources and their fine details, we chose the best available high-resolution data surveys, namely the VLA Faint Images of the Radio Sky at Twenty-Centimeters (FIRST) data at 1400 MHz for the high-frequency range and the LOFAR Two-meter Sky Survey First Data Release (LoTSS DR1) at 144 MHz for the low-frequency range. Through a systematic search, a total of 458 winged sources from the VLA FIRST data and 40 winged sources from the LoTSS DR1 are identified. Out of the total 498 winged sources, 322 sources are newly discovered. This discovery significantly increased and nearly doubles the number of existing winged sources. By accumulating the newly identified source with all the previous identifications, several statistical studies on their radio and morphological properties are done. The studies give an insight into the global parameters and properties of winged radio sources. An outlook on the origin of such sources is also given.

ACKNOWLEDGMENTS

Keeping this brief, to all those who have been involved throughout my PhD, thank you for all your support. First, I would like to thank my parents and family. Without your support, it would be impossible for me to do and finish my research work. I would like to thank my supervisor, Dr. Soumen Mondal, for providing endless opportunities and a wealth of knowledge and expertise throughout the 4 years of my PhD. I would like to thank Dr. Ankan Das for his kind help on numerous points during my PhD. I would also particularly like to thank Tapan Kumar Sasmal for all the support during the PhD and beyond. I would also like to thank Sangita Chatterjee for her help during the PhD. I would also like to thank Dusmanta Patra. I would like to make a special mention of Suman Kumar Mondal. I would like to thank him for all the help he has done so far. I would also like to thank the State Government Fellowship Scheme of Jadavpur University for awarding the fellowship. I would also like to thank the Department of Physics, Jadavpur University for giving me this opportunity to do my research work. I'm lucky to have known so many people along the way. To all the students, post-docs, and staff members at the University, thank you for all your support. To those that I have met all over the world, at conferences, through collaborations, thank you for the memories and all round enlightenment that comes with exploring the Earth/Universe and the wonderful people/phenomena associated.

To my family, for everything...
...Thank you

LIST OF PUBLICATIONS

(A) In Peer-Reviewed Journals:

1. **Soumen Bera**, Sabyasachi Pal, Tapan K. Sasmal, and Soumen Mondal, *FIRST Winged Radio Galaxies with X and Z Symmetry*, 2020, **ApJS**, 251, 9
   DOI: 10.3847/1538-4365/abb367

2. Tapan K. Sasmal, **Soumen Bera**, Sabyasachi Pal, and Soumen Mondal, *A New Catalog of Head–Tail Radio Galaxies from the VLA FIRST Survey*, 2022, **ApJS**, 259, 31
   DOI: 10.3847/1538-4365/ac4473

3. **Soumen Bera**, Tapan K. Sasmal, Dusmanta Patra, and Soumen Mondal, *"Winged" Radio Sources from LOFAR Two-meter Sky Survey First Data Release (LoTSS DR1)*, 2022, **ApJS**, 260, 7
   DOI: 10.3847/1538-4365/ac5cc4

4. Tapan K. Sasmal, **Soumen Bera**, Soumen Mondal, *Miscellaneous Radio Galaxies from LOFAR survey*, 2021, **AN**, review report submitted

5. Tapan K. Sasmal, **Soumen Bera**, Soumen Mondal, *A Catalog of Bent-Tail Radio Galaxies from LoTSS DR1 and their Correlation with Associated Clusters*, 2022, **MNRAS**, review report submitted

6. **Soumen Bera**, Tapan K. Sasmal, Soumen Mondal, Dusmanta Patra, *MRG: A FIRST look at the Miscellaneous Radio Galaxies*, 2022, **JAA**, submitted

(B) In Conference Proceedings:

1. Tapan K. Sasmal, **Soumen Bera**, Sabyasachi Pal, and Soumen Mondal, *Discovery of Four Miscellaneous Radio Galaxies From LoTSS DR1*, 2020, **Journal of Physics: Conference Series**, 1579, 012021
   DOI: 10.1088/1742-6596/1579/1/012021

2. **Soumen Bera**, Sabyasachi Pal, Tapan K. Sasmal, Soumen Mondal, and Dusmanta Patra, *MRG: The Miscellaneous Radio Galaxies from the FIRST Survey*, 2020, **Journal of Physics: Conference Series**, 1579, 012023
   DOI: 10.1088/1742-6596/1579/1/012023

Contents

List of Abbreviations

2MASS	The Two Micron All-Sky Survey
2MASX	The Two Micron All Sky Survey Extended Objects–Final Release
3C	The Third (3rd) Cambridge catalogue of Radio Sources
4C	The Fourth (4th) Cambridge catalogue of Radio Sources
5C	The Fifth (5th) Cambridge catalogue of Radio Sources
6C	The Sixth (6th) Cambridge catalogue of Radio Sources
7C	The Seventh (7th) Cambridge catalogue of Radio Sources
8C	The Eighth (8th) Cambridge catalogue of Radio Sources
9C	The Ninth (9th) Cambridge catalogue of Radio Sources
ABELL	Abell Clusters of Galaxies
AGN	Active Galactic Nucleus
AIPS	The Astronomical Image Processing System
ALMA	Atacama Large Millimeter Array
APMUKS	Automated Plate Measurement United Kingdom Schmidt
ASK	Automatic Spectroscopic K-means-based Classification
ASKAP	The Australian Square Kilometre Array Pathfinder
ASTRON	The Netherlands Institute for Radio Astronomy
ATATS	The Allen Telescope Array Twenty-centimeter Survey
ATHENA	Advanced Telescope for High-ENergy Astrophysics
ATCA	The Australia Telescope Compact Array
AUI	Associated Universities, Inc.
B2	The second (2nd) radio survey catalog of the Bologna 'Northern Cross' telescope
B3	The third (3rd) radio survey catalog of the Bologna 'Northern Cross' telescope
BH	Black Hole
BLR	Broad Line Region
CMB	The Cosmic Microwave Background
Cul	The radio source catalog from all Culgoora Lists
DDRG	Double-Double Radio Galaxy
DSS	The Digital Sky Survey
DSS2	The Digital Sky Survey 2
EE	Eye Estimation
EMU	The Evolutionary Map of the Universe
ERG	Episodic Radio Galaxy
ESA	The European Space Agency

EUVE	The Extreme Ultraviolet Explorer
EVLA	Expanded Very Large Array
FAST	The Five hundred meter Aperture Spherical Telescope
FFT	The Fast Fourier Transform
FIRST	The Faint Images of the Radio Sky at Twenty-Centimeters
FR-I	Fanaroff-Riley Class I
FR-II	Fanaroff-Riley Class II
FR0	Fanaroff-Riley Class 0
FRB	Fast Radio Burst
GALEXASC	Galaxy Evolution Explorer All-sky Catalog
GALEXMSC	Galaxy Evolution Explorer Medium-deep Sky Catalog
GIN	Galaxy Identification Number
GLEAM	Galactic and Extragalactic All-sky MWA
GMBCG	Gaussian Mixture Brightest Cluster Galaxy
GMRT	The Giant Metrewave Radio Telescope
GRG	Giant Radio Galaxy
GWB	Gravitational Wave Background
HALCA	Highly Advanced Laboratory for Communications and Astronomy
HBA	High Band Antenna
HETDEX	Hobby-Eberly Telescope Dark Energy Experiment
HST	The Hubble Space Telescope
HYMORS	HYbrid MOrphology Radio Sources
ICM	Intra-Cluster Medium
IGM	InterGalactic Medium
ILT	International LOFAR Telescope
IPAC	The Infrared Processing and Analysis Center
IR	InfraRed
ISM	InterStellar Medium
IUE	The International Ultraviolet Explorer
JAXA	The Japan Aerospace Exploration Agency
JWST	The James Webb Space Telescope
LBA	Low Band Antenna
LCRS	Las Campanas Redshift Survey
LINER	Low-Ionization Nuclear Emission-line Region
LOFAR	The LOw-Frequency ARray
LoLSS	The LoFAR LBA Sky Survey
LoTSS	The LoFAR Two-metre Sky Survey
LoTSS DR1	The LoFAR Two-meter Sky Survey First Data Release
LoTSS DR2	The LoFAR Two-meter Sky Survey Second Data Release
MaxBCG	Maximum likelihood redshift Brightest Cluster Galaxy

MBH	Massive Black Hole
MGC	Millennium Galaxy Catalogue
MHD	MagnetoHydroDynamic
MRG	Miscellaneous Radio Galaxy
MSSS	The LOFAR Multifrequency Snapshot Sky Survey
MVS	Manual Visual Search
NASA	The National Aeronautics and Space Administration
NASA IRTF	The NASA Infrared Telescope Facility
NAT	Narrow Angle Tail radio source
NCRA	The National Centre for Radio Astrophysics
NED	The NASA/IPAC Extragalactic Database
NGC	New General Catalogue
NLR	Narrow Line Region
NRAO	The National Radio Astronomy Observatory
NVSS	The NRAO VLA Sky Survey
ORC	Odd Radio Circle
OSO	Orbiting Solar Observatory
OVV	Optically Violently Variable
PKS	The Parkes Catalogue of Radio Sources
PMN	Parkes–MIT–NRAO
QSO	Quasi-Stellar Object
RC	Reference Catalogue, a catalog of nearby galaxies
RG	Radio Galaxy
RGZ	Radio Galaxy Zoo
ROSAT	The RÖntgenSATellit
RRAT	Rotating RAdio Transient
RXTE	The Rossi X-ray Timing Explorer
SAGAN	Search and Analysis of Giant radio galaxies with Associated Nuclei
Sco X-1	Scorpius X-1
SDSS	The Sloan Digital Sky Survey
SFR	Star-Forming Region
SKA	The Square Kilometre Array
SMBH	SuperMassive Black Hole
SNR	SuperNova Remnant
SPRINT-A	The Spectroscopic Planet Observatory for Recognition of Interaction of Atmosphere
SSTSL2	Spitzer Space Telescope Source List version 4.2
TGSS	The TIFR GMRT Sky Survey
TGSS ADR	The TIFR GMRT Sky Survey Alternative Data Release
TGSS ADR1	The TIFR GMRT Sky Survey Alternative Data Release 1

TIFR	The Tata Institute of Fundamental Research
TONS08	Texas–Oxford NVSS Structure 08 h region
TONS08w	TONS08 wider survey
TXS	The Texas Survey of Radio Sources
uGMRT	The upgraded Giant Metrewave Radio Telescope
UHF	Ultra-High Frequency
UKIRT	The United Kingdom Infra-Red Telescope
UV	UltraViolet
VHF	Very High Frequency
VISTA	The Visible and Infrared Survey Telescope for Astronomy
VLBI	The Very Long Baseline Interferometry
VLA	The Karl G. Jansky Very Large Array
VLSS	The VLA Low-Frequency Sky Survey
VLSSr	The VLA Low-frequency Sky Survey Redux
VSA	The Very Small Array
WAT	Wide Angle Tail radio source
WB	WISE Blazar-like Radio-loud Sources
WIRO	The Wyoming Infrared Observatory
WISE	The Wide-field Infrared Survey Explorer
WRG	Winged Radio Galaxy
XMM	The X-ray Multi-Mirror Mission
XRG	X-shaped Radio Galaxy
XRISM	The X-Ray Imaging and Spectroscopy Mission
ZRG	Z-shaped Radio Galaxy

List of Figures

List of Tables

Chapter 1

Introduction

We are not simply in the
universe, we are part of it.
We are born from it.

—Neil deGrasse Tyson

The Earth, and hence the human race, is a part of the universe, which is the entire cosmic system of matter and energy. We have come a long way since civilizations considered the Earth, Sun, and Moon as the primary objects of creation, with the rest of the cosmos emerging almost as an afterthought. Today, we know that Earth is simply a little ball of rock in an unimaginably enormous space and that the creation of the solar system was most likely only one of many events that occurred against the backdrop of an already mature cosmos. This humbling lesson has revealed a remarkable fact, one that bestows a rich and noble heritage on the smallest particle in the universe: events that occurred in the first few minutes of the universe's creation 13.7 billion years ago turn out to have had a profound influence on the birth, life, and death of the galaxies, stars, and planets. Indeed, a connection can be established from the creation of the universe's matter in a fundamental "big bang" to the collection of atoms adaptable enough to serve as the foundation of life on Earth. The inherent coherence of such a worldview has strong philosophical and aesthetic appeal, and it may explain why the public interest in the cosmos has always been strong.

Since ancient times observing the sky is always a fascinating thing. From

Kopernikas' telescope to today's event horizon telescope all of them observe the sky, the events of the universe, and the celestial elements. Starting from Sun and Moon, now we are able to image a Black Hole (BH). We are interested to probe the observable universe and find the origin of all elements. Using telescopes of different wavelengths and with different bandwidths, we are now observing the universe and the elements of the universe as a whole.

Among them, the Milky Way Galaxy is a significant and intriguing element in the universe. In a moonless night sky, it appears as an indistinct strip of light sweeping across the sky. It is typically a spiral galaxy with a diameter of 150,000 to 200,000 light-years with a population of 100-400 billion stars and more than 100 billion planets. The fascinating fact about the Milky Way is that it contains our own planet Earth, the cradle of mankind. The entire solar system is around 8 kpc away from the galactic center. The Milky Way's stars form a flattened disk-like structure. The faint light from faraway stars blends into a uniform glow, giving the appearance of the Milky Way an indistinct ribbon to the human eye.

1.1 Observing the Universe: A Preview

The observation and study of the universe in all its entirety and glory, the knowledge of a night sky is not enough, we need in-depth information about what the celestial objects are made of. The universe and every object out there in the universe emit radiation at all wavelengths in the electromagnetic spectrum (Figure 1.1). Those emissions tell about its constituent parts. However, on the ground on earth, one can not receive all of that emitted light. This is because of the presence of our atmosphere around the earth. The atmosphere blocks out many kinds of radiation while letting other types through. The harmful high-energy radiations such as X-rays, gamma rays, and part of the ultraviolet (UV) rays are blocked out. A part of infrared (IR) and very low-energy radio waves are also got absorbed. The atmosphere allows only visible light, radio waves, and part of infrared light to pass through.

The knowledge about the universe and astronomical events comes from studying the electromagnetic radiation emitted in space. Hence, to study astronomical objects, we need a full spectrum observation to get a complete picture of the universe. The universe and the celestial objects show different structures and phenomena, and those different properties prevail in different wavelengths. So, a source structure and its property depend on the frequency band through which we

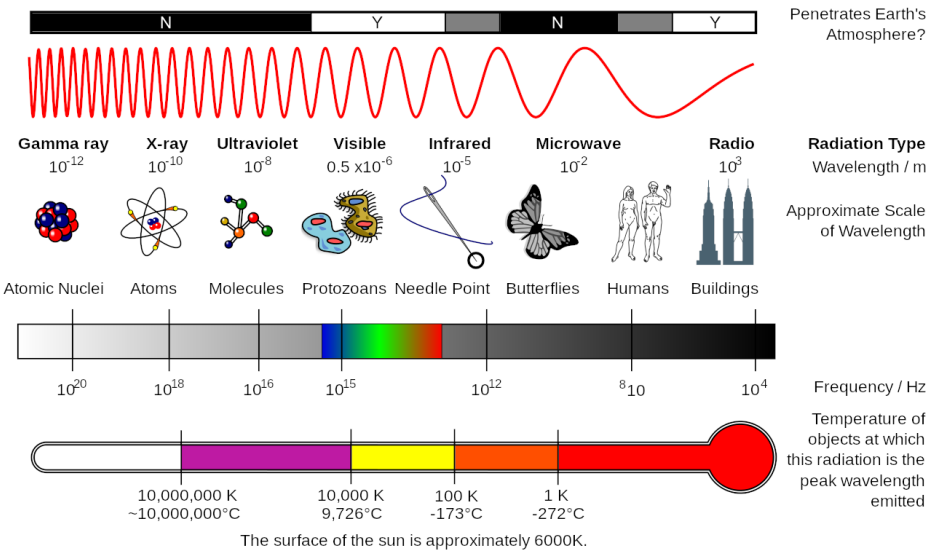

Figure 1.1: The diagram presents the full electromagnetic spectrum range. The image indicates various radiation types depending on the respective frequency ranges. The properties of the radiation types such as wavelengths, the temperature of the objects at which the particular radiation has its peak, the penetration possibility through the Earth's atmosphere, etc. (Courtesy: Wikipedia).

are observing (Figure 1.2). Thus to conclude the whole picture of a celestial body, one needs to observe all the emissions at different wavelengths and then sum up those findings to explain that particular celestial body. There exist different kinds of observation mechanisms to observe different wavebands. A short note on the different astronomical observation methods for different frequency ranges is given in the following section.

1.1.1 Gama-ray Astronomy

Gamma-ray astronomy is the study of astronomical events of the cosmic objects that emit gamma rays. This is high-energy electromagnetic radiation with photon energies above 100 keV. Gamma rays in the range of MeV and GeV are also expected from solar flares. The gamma rays coming from space are mostly absorbed in our atmosphere. So, the gamma-ray observations are mostly done with balloons or spacecraft above the atmosphere. The first gamma-ray observation was carried out on the Explorer 11 satellite in 1961. The first significant detection of

a gamma-ray from our galaxy was done by the OSO-3 satellite. The mechanism through which gamma ray emits are electron-positron annihilation, inverse Compton effect, and decay of radioactive material. The gamma-ray observations are mainly used to observe high-energy astrophysical systems such as stellar coronas, supernova remnants, neutron stars, white dwarf stars, black holes, and clusters of galaxies. In our Milky Way galaxy, there is also a "gamma-ray background" radiation observed.

1.1.2 X-ray Astronomy

The branch of astronomy where the study of astronomical events and astronomical bodies are studied with X-ray observations. The astronomical objects that emit X-ray emissions have a range of temperatures from about a million kelvin (K) to hundreds of millions of kelvin (MK). The atmosphere absorbs the X-ray and hence the detectors and telescopes are placed at high altitudes or in space by balloons or satellites. In 1949, the first X-ray radiation from the Sun was noticed, though the detectors could not detect the radiation clearly. The first clear and successful cosmic X-ray radiation was from Scorpius X-1 (Sco X-1), which was detected in 1962 by a sounding rocket. Some important X-ray satellite telescope systems are the Chandra X-Ray Observatory, XMM-Newton X-ray satellite, RXTE (Rossi X-ray Timing Explorer), and XRISM (X-Ray Imaging and Spectroscopy Mission). The upcoming ATHENA (Advanced Telescope for High-ENergy Astrophysics) is a futuristic X-ray observatory by European Space Agency (ESA). The operation energy range of ATHENA will is 0.2–12 keV. This will offer spectroscopic and imaging capabilities of one order better in magnitude on several parameters than today's telescopes e.g., Chandra X-ray Observatory and XMM-Newton. The X-ray emission is useful in studying the celestial X-ray sources, stellar coronae, young and low-mass stars, coolest M dwarfs, stellar magnetic fields, coronal mass ejection, etc.

1.1.3 Ultraviolet Astronomy

It is a study of cosmic objects which emits the ultraviolet (UV) portion of the electromagnetic spectrum. The range of UV is roughly within 90 to 350 nanometers. As ultraviolet radiation is absorbed by the atmosphere, ground-based observation in the UV range is not possible. The ultraviolet observations are made in the upper atmosphere or in space. Although the detection of ultraviolet radiation started in

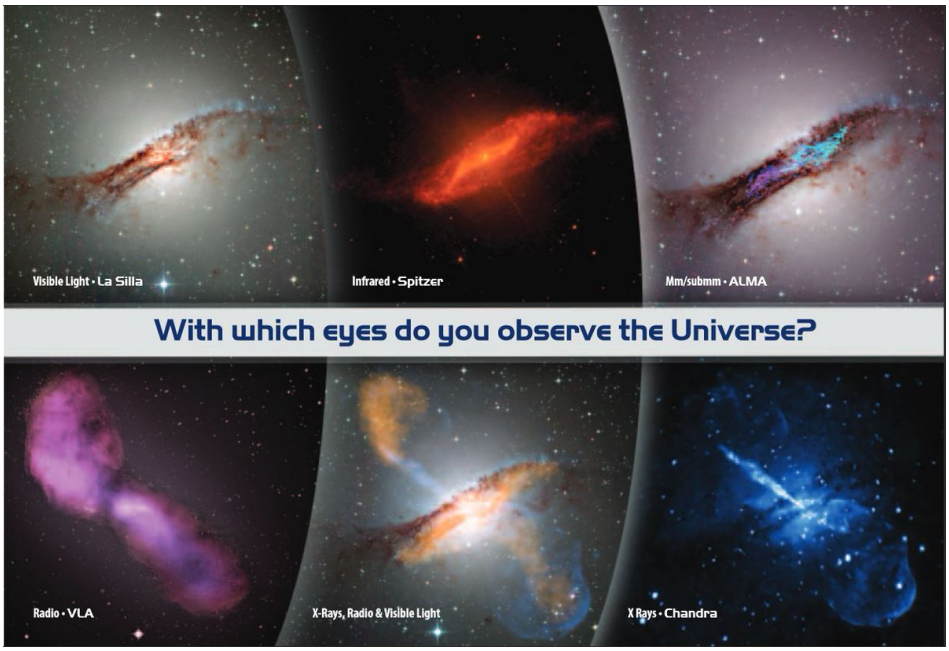

Figure 1.2: This image shows a relative picture of a galaxy Centaurus A, also known as NGC 5128 or Caldwell 77. The image indicates that the galaxy reveals different structure in different wavelength windows (Courtesy: ALMA).

the 1920s, the first successful detection is done in 1946 by a rocket-borne camera. The first UV radiation detection satellite Orbiting Solar Observatory (OSO) was launched by the National Aeronautics and Space Administration (NASA). To date, numerous satellites are used to detect astronomical UV radiation. Some of the ultraviolet space telescopes are the International Ultraviolet Explorer (IUE)-a joint project of the United States, the European Space Agency, and Great Britain, the Extreme Ultraviolet Explorer (EUVE), ROSAT (Röntgensatellit), Hisaki, also known as the Spectroscopic Planet Observatory for Recognition of Interaction of Atmosphere (SPRINT-A), operated by the Japan Aerospace Exploration Agency (JAXA), Astrosat. The Astrosat is India's first dedicated multi-wavelength space telescope. The line spectrum of UV observation is used to study the chemical composition, densities, and temperatures of interstellar gas and dust. The evolution of galaxies and the temperature and composition of hot young stars are also studied from such observations.

1.1.4 Optical Astronomy

Optical or visible-light astronomy is the branch of observational astronomy that deals with the visible range of electromagnetic radiation. Optical astronomy started in ancient times when people began to look into the night sky. The first optical telescope was made by Galileo Galilei in 1609. Later in 1789, Sir William Herschel, assisted by his sister, Caroline Herschel built up a telescope with a small diameter of 122 cm. Since then optical telescopes have evolved with time and as of now the largest grouping array of optical telescopes is on the top of Mauna Kea on the island of Hawaii. The largest optical telescope is the Gran Telescopio Canarias (10.4-meter). Some other notable optical telescopes are Keck telescopes (10-meter), Subaru Telescope (8.2-meter), and two Gemini telescopes (both 8.1-meter each). Along with these the most sought telescopes are the Hubble Space Telescope (HST) and the James Webb Space Telescope (JWST). The James Webb Space Telescope is a successor of HST. The study of the universe started with optical astronomy; the optical observations include the study of stars, galaxies, and black holes.

1.1.5 Infrared Astronomy

It is the study of celestial objects in the infrared (IR) radiation that they emit. The infrared range is approximately from nearly one micrometer to one millimeter. Infrared astronomy started in the 1800s after the detection of the infrared wave by the British astronomer Sir William Herschel. Though the infrared study started in the 1800s the first proper infrared study of a stellar object was done in the 1920s by the American astronomers W.W. Coblentz, Edison Pettit, and Seth B. Nicholson. Many optical telescopes such as Keck Observatory can detect near-infrared radiation. In the submillimeter range; far-infrared wavelengths are detected through telescopes such as the James Clerk Maxwell Telescope at Mauna Kea Observatory. The notable ground-based infrared telescopes are the Visible and Infrared Survey Telescope for Astronomy (VISTA), United Kingdom Infra-Red Telescope(UKIRT), NASA Infrared Telescope Facility (NASA IRTF), Wyoming Infrared Observatory (WIRO). The main issue in this range is that the radiation is mostly absorbed by water vapor and carbon dioxide in the atmosphere. There is another issue that the atmosphere itself radiates in the infrared region. Along with the ground-based telescope, there are several space telescopes e.g., the Herschel Space Observatory, the Spitzer Space Telescope, and in recent times the James Webb Space Tele-

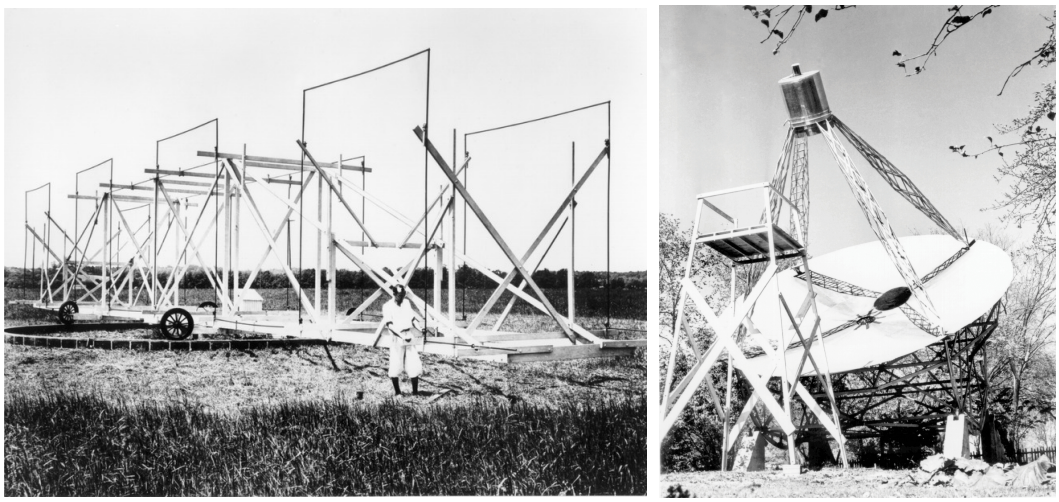

Figure 1.3: The two images show the first two radio antennas, made by Karl Jansky and Grote Reber. (a) The left panel: Karl Jansky and his "merry-go-round" antenna in Holmdel, New Jersey. In the 1930s he built the world's first radio telescope. The rotating antenna array was used to discover radio emissions from our Milky Way (Courtesy: NRAO/AUI). (b) The second panel on the right side: Grote Reber's Antenna at Wheaton, Illinois, in his backyard (in 1937). This is the world's first parabolic radio telescope (Courtesy: NRAO).

scope. The Two Micron All-Sky Survey (2MASS) and Wide-field Infrared Survey Explorer (WISE) are the two most ambitious sky surveys to map the whole sky in the infrared range. The IR observation is mostly useful in the study of proto-planetary disks of dust and gas clouds around young stars, atmospheric structure, composition, and dynamics of several extrasolar planets.

1.1.6 Radio Astronomy

Radio astronomy is a discipline of astronomy that deals with celestial objects and astronomical events in the radio frequency range. The present work falls in this frequency range and we discuss it in detail, given in the following section, Section 1.2.

1.2 Radio Astronomy

Radio astronomy is a subfield of astronomy where celestial objects are studied in the radio frequency range that those objects either emit or reflect. It helps to reveal the unknown attributes of those astronomical bodies and their inherent cosmic makeup.

The detection of the first cosmic radio wave from an astronomical object was done by the American physicist Karl Guthe Jansky. In 1932, Karl Jansky at Bell Telephone Laboratories built a rotating directional antenna array (Figure 1.3 (a)), operable at a frequency of 14.6 meters to investigate radio disturbances that interfered with transoceanic telephone service. The detected radio noise was coming from the center of our own galaxy, the Milky Way galaxy. The central radio source of the Milky Way is now known as Sagittarius A. Later in 1940, the American radio operator Grote Reber built the first radio telescope to detect the "cosmic noise" at frequencies of 3300 MHz and 900 MHz. He built a parabolic radio telescope with a diameter of 9.4 meters (Figure 1.3 (b)) but failed to detect any radiation at those frequencies. However, he found emissions along the galactic equator at a frequency of 162 MHz. This is the first time when astronomers could observe astronomical objects in a new region of the electromagnetic spectrum outside of the visible range. In February 1942, the first detection of radio waves emitted from the Sun was made by James Stanley Hey, a British Army research officer. George Clark Southworth also detected radio emissions from the Sun in the same year 1942 at the Bell Laboratories. In the time period 1940 to 1950s, several other scientists were also able to identify a number of radio emissions from discrete celestial sources.

After the initial development and detection of cosmic radio emission from discrete sources in 1951, Harold Ewen and E.M. Purcell first detected 21-cm radiation which is emitted by the cold clouds of interstellar hydrogen atoms. This discovery was helpful to study the spiral arms of the Milky Way Galaxy and its rotation. In the 1950s, a radiophysics group was created at Cambridge University. The team of astronomers published three catalogs of astronomical radio sources to map the radio sky. The three catalogs are quite useful and notable radio source catalogs. Among the three catalogs, the third catalog (3C) is the most popular and most used one. The third catalog first contained some notable sources like 3C 273. In the time of late 1950s, different phenomena of planets like radio storms in Jupiter's atmosphere, Van Allen radiation belts surrounding Jupiter, the existence of the greenhouse effect on Venus, and internal heating sources within the interiors of

Saturn and Jupiter are revealed through radio studies. The studies of interstellar molecular gas clouds are also done using the radio telescope. In 1963, a hydroxyl (OH) molecule was detected, which was the first molecule to be identified using radio telescopes. To date, nearly 150 molecular species have been detected. Out of those, only a few can be observed at optical wavelengths. The detected molecules are carbon monoxide, water, ammonia, methyl and ethyl alcohol, formaldehyde, hydrogen cyanide, etc. A few heavy organic molecules like the amino acid glycine are also found. Robert Wilson and Arno Penzias, two scientists from the Bell Telephone Laboratories detected the faint cosmic microwave background (CMB) signal, a residual effect of the big bang.

1.2.1 Why Radio Astronomy?

In modern-day astrophysics, radio astronomy plays an essential role. Radio astronomy is primarily used to study the "cold" universe when the optical observations are for the "hot" universe. The study of optical astronomy gives the measurement of the parameters such as distance, size, temperature, motion through space, and chemical compositions. On the contrary in radio astronomy, actually, the electric and magnetic fields of objects are observed. This means we can study the motion of charged particles around these objects, which gives information about the mass, motion, and energy of the astronomical object. The primary advantages of radio astronomy over other wavelengths are mentioned in the following:

(i) **No absorption** – Radio waves did not get absorbed by the gas and dust in space, as well as by the planetary clouds or atmospheres. The radio waves easily penetrate through the Earth's atmosphere. Thus a much clear picture of the astronomical sources and events is possible to observe compared to the other wavelength observations. The no absorption also helps to study the most distant objects in the universe.

(ii) **Weather Condition** – The radio wave is not much affected by the weather condition. As a result, radio astronomy can be done from the earth (observing from the ground) without much interference from the weather and its condition.

(iii) **Day and night** – One can easily choose any time irrespective of day and night to 'see' the radio universe. There is no preference for day or night to observe the radio signals. As the radio wavelengths are far longer than air dust grains and the Sun is not a particularly bright radio source, the radio sky is always dark and numerous radio observations may be done at any time of day or night.

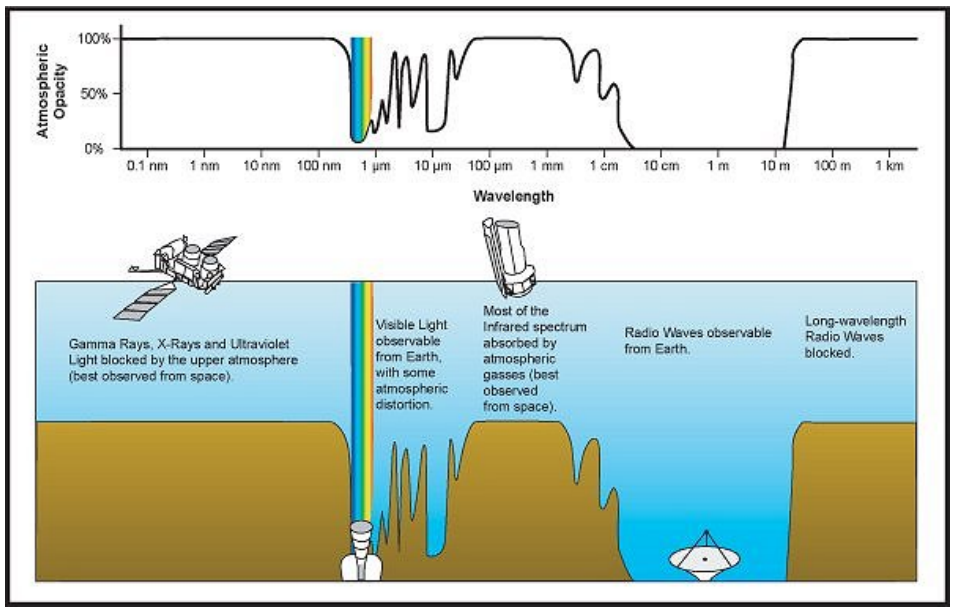

Figure 1.4: A comparative plot of frequency windows to show the radio band with the other wavelengths of electromagnetic radiation as observed from Earth. The plot shows that the Earth's atmospheric absorption and scattering (or opacity) primarily blocks out other frequency bands except for radio frequency. Though optical and a part of infrared radiation is visible from the Earth's surface, the observable radio frequency window is much greater. (Courtesy: NASA/IPAC).

(iv) **Hydrogen, the most abundant element** – Nearly 90% of the visible matter in our universe is Hydrogen. The corresponding wavelength is 21.106114 cm. That means the atomic hydrogen signal lies in the radio wavelengths and hence a radio telescope can study the most abundant element in the universe.

Since the time of Karl Jansky, radio astronomy has advanced a lot. In today's new generation of high-resolution radio telescopes with cutting-edge technology, we are able to study the faint to faint radio sources and radio emissions. The imaging of black hole (BH) is now possible with such instruments. With the upcoming radio observation systems like the Square Kilometre Array (SKA), it is possible to detect even fainter radio signals like the reflected radio waves from nearby astronomical bodies such as the Moon, the nearby planets, some comets, and asteroids.

1.3 Techniques to Carry Out Radio Astronomy

In radio astronomy, different techniques are used to observe radio emissions. To map a particular source or particular region of the sky multiple observations are made and then they are superposed to form a mosaic image. The type of instrument used depends on the strength of the source and the details we need to extract. Radio observations from the ground are possible as the Earth's atmosphere does not absorb much of radio wavelengths. However, in the low-frequency range, there is some limitation as the ionosphere reflects the waves in such range. This kind of constraint is also applied for the higher frequency range, where the water vapor interferes. Due to this reason the millimeter radio astronomy is done at a very dry and high location. There is another factor, the transmitting devices which may also cause radio-frequency interference. Because of this radio observatories are located in remote places.

Depending on the power of the object and the distance from the earth we use either a single radio telescope that points out toward the object or we put a complex multiple telescope system, radio interferometry.

1.3.1 Radio Telescope

A radio telescope is the simplest device to detect radio signals in the range of 10 meters (30 MHz) to 1 millimeter (300 GHz). A radio telescope is consist of two main components (i) a radio antenna and (ii) a receiver or radiometer. The radio antenna catches the extraterrestrial radio emission when the receiver or radiometer is used to amplify and detect the signals. There is also a computing device to process and analyze the received radio data. To ensure a clear radio map for faint to faint sources the radio telescope has to be more and more sensitive. A better radio image needs a better sensitivity of the instrument. The sensitivity of a radio telescope depends on the area and efficiency of the antenna and the responsiveness of the radio receiver. The sensitivity also depends on the bandwidth of the receiver for broadband continuum emission. As the radio emission is weak in nature we have to ensure a greater sensitivity for our radio telescope to get a resolved structure. Now, the angular resolution depends on the diameter of the "objective". If D is the objective diameter then angular resolution (θ) is

$$\theta = 1.22\lambda/D \tag{1-1}$$

when λ is the wavelength. So, a radio telescope needs to be large to give a better resolution. The need for a huge radio telescope is also for receiving signals with a low signal-to-noise ratio. Generally, radio telescopes are very large up to hundreds of meters. For better sensitivity, we also use the most sensitive radio receivers available. Moreover, we need to filter the radio signals and protect the radio telescopes from man-made radio emissions and terrestrial radio interference.

The common and most familiar shape of a radio antenna consists of a parabolic dish. This type of telescope is also known as the dish or filled-aperture telescope. The operation of such a telescope is quite similar to the television satellite dish, it collects the incoming signals onto a small antenna called the feed. The feed is a typical waveguide horn, it transfers the incoming radiation to the receiver. The receiver accumulates the signals using the solid-state amplifiers with a possible minimum internal noise. Thereafter the signal is recorded, stored, and computed in a computer. A model telescope system is given in Figure 1.5. In some cases, the parabolic surface is equatorially mounted. Here one axis is parallel to the Earth's rotation axis. This equatorial mount is very engaging as it is easy to trace a particular source or region in the sky by moving the antenna along the parallel axis. However, such equatorially mounted telescopic systems are quite difficult and expensive to build. Nowadays, in a modern radio telescope, a digital computer is used to rotate the telescope along the azimuth and elevation axes with the motion of a source across the sky. In a general case, the receiver is placed at the focal point of the parabolic reflector. Then the received signal is carried through a cable to the recorder or analyzer. The primary issues with such arrangement are maintenance, repair, and weight restrictions. As there is a certain weight limit we can not increase the number of individual receivers on the telescope. However, we may place multiple feeds and receivers where the weight restriction is not a major constraint. In some cases, a secondary reflector is used. The secondary reflector is placed in front of or behind the focal point of the paraboloid. The placement of the second reflector is such that it focuses the signals to a point near the center or vertex of the main reflector. In the secondary focus systems, it is possible to shape the primary and secondary reflecting surfaces to increase the gain. In past, a symmetric tripod or quadruped structure is used to hold the feed or secondary reflector. Such arrangements block part of the incoming radiation and distorted the response. Nowadays in the new structure, the feed or secondary reflector is placed off the central axis and thus it does not block the incoming signal. Due to this off-axis radio telescopes are relatively more sensitive. It is also less affected by interference reflected from the support structure into the feed.

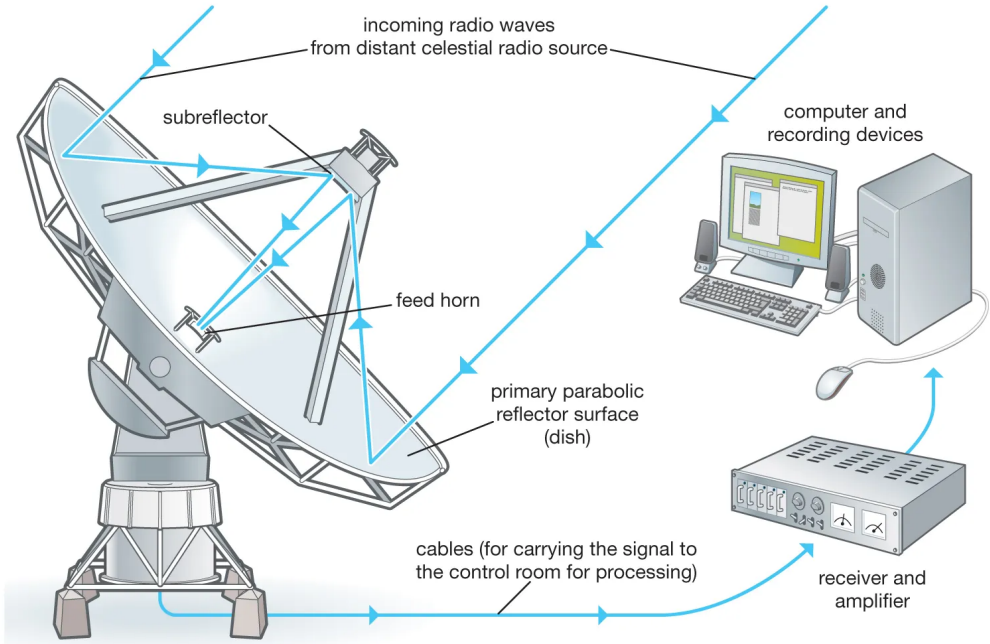

Figure 1.5: This is a schematic diagram of a radio telescope system (Courtesy: Encyclopaedia Britannica, Inc.).

The performance of a radio telescope is restricted by a list of reasons, such as deviations or irregularities from the ideal shape of the reflecting surface. The irregularity may arise due to manufacturing defects. As the telescope is very large in size wind load is also a factor. The change in weather temperature and any thermal change results in either expansion or contraction and hence creates deformations. To counter the wind and temperature effect protective enclosures called radomes are used. By using the radomes we can nearly eliminate both the effect of wind and temperature gradients. However, this is a quite costly method. The gravitational force also creates deflections as the antenna is happened to be pointed at different parts of the sky. The effect of gravity is minimized using a movable structure as sturdy as possible. To minimize the gravity effect, there is another effective technique based on the principle of homology. In this method, the reflecting structure of the telescope is allowed to deform under gravity force, in such a way to form a new paraboloid reflecting structure with a slightly different focal point. Here, we just need to move the feed or secondary reflector to maintain the optimum performance. The deformation of the shape of the parabolic surface affects the study maximum when the deformation is equal or in the order of the operational wavelength.

Figure 1.6: The images are examples of some single-dish radio telescopes (in the left to right direction): (a) Lovell (Jodrell Bank Observatory, England, 1957), (b) DSS 14 "Mars" antenna (Goldstone Deep Space Communications Complex, Mojave Desert, California, US, 1958), (c) Parkes 64m Radio Telescope (Parkes, New South Wales, Australia, 1969), (d) Green Bank Telescope (Green Bank, West Virginia, US, 2002), (e) Arecibo Telescope (Arecibo, Puerto Rico, Collapsed on 1 December 2020), (f) Five hundred meter Aperture Spherical Telescope (FAST; China, 2016, under construction). (Courtesy: Wikipedia)

The atomic and molecular lines from the astronomical objects are found in the spectroscopic feature of the radio spectrum. To study the full radio spectrum a radio telescope is used to measure both broad-bandwidth continuum radiation and narrow-bandwidth. In the early days, spectroscopic observations were done by tuning the receiver to a large frequency range to cover the particular required frequencies. This process is time-consuming as the spectrometer had a narrow frequency range. Now, in present times the full frequency range is divided into thousand separate frequency channels and thus it can cover a larger bandwidth, up to hundreds of megahertz. A radio spectrometer uses a large number of filters, each of which is tuned to a separate frequency and followed by a separate detector. The detector combines the signal from the filters to produce a multichannel, or multifrequency, receiver. In an alternate method, a single broad-bandwidth signal is converted into digital form and then analyzed by the mathematical process of autocorrelation and Fourier transforms. To detect faint signals, it is necessary to

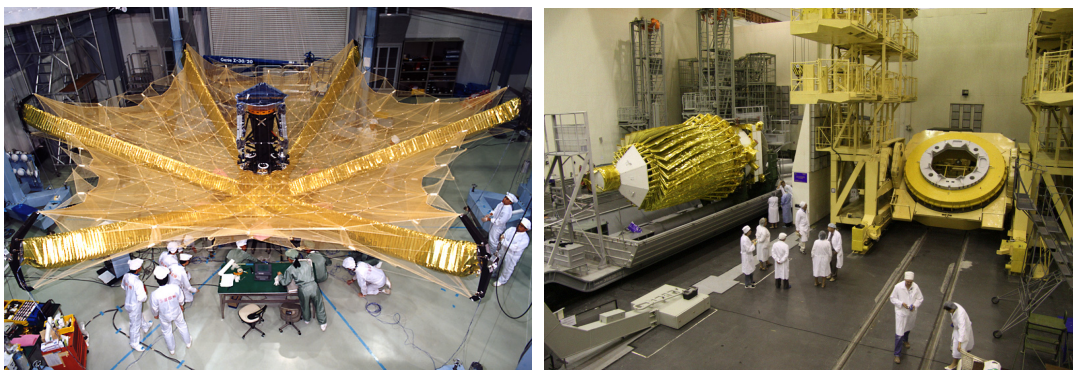

Figure 1.7: These are the images of two space radio telescopes. The left panel: (a) Japanese HALCA dish, the right panel: (b) Assembled Spektr-R (Courtesy: Wikipedia).

minimize the effect of noise generated by the thermal radiation in the receiver. This is done by averaging the receiver output over a period of time, up to several hours.

The first radio observation started in 1932 by Karl Guthe Jansky at Bell Telephone Laboratories in Holmdel, New Jersey by an antenna. The first parabolic dish radio telescope by Grote Reber had a diameter of 9.4 meters. The single-dish radio telescope system has evolved a lot with time from 9.4 meters to today's big dish telescope of 500-meter diameter. The size of the telescope changes with the target operational wavelength. For millimeter wavelength, the radio telescope will have the size of a few tens of meters across, while the diameter size goes up to 300 meters for centimeter wavelengths. The Five-hundred-meter Aperture Spherical Telescope (FAST in China) is the world's largest filled-aperture radio telescope with a diameter 500-meter. The Arecibo radio telescope located in Arecibo, Puerto Rico was the world's second-largest filled-aperture telescope. However, the telescope collapsed on 1 December 2020. Some notable big dish telescopes are the 100-meter Green Bank Telescope (Green Bank, West Virginia, US, 2002, the largest fully steerable radio telescope dish), the 100-meter Effelsberg (Bad Münstereifel, Germany, 1971), the 76-meter Lovell (Jodrell Bank Observatory, England, 1957), the 70-meter DSS 14 "Mars" antenna (Goldstone Deep Space Communications Complex, Mojave Desert, California, US, 1958), the 70-meter Yevpatoria RT-70 (Crimea, first of three RT-70, former the Soviet Union, 1978), the 70-meter Galenki RT-70 (Galenki, Russia, second of three RT-70 in the former Soviet Union, 1984). Some ground-based single-dish radio telescope images are given in Figure 1.6. Apart

from the ground-based telescopes, there are a few space radio telescopes 1.7 like KRT-10 (the first one and this was attached to Salyut 6 orbital space station in 1979), HALCA (Highly Advanced Laboratory for Communications and Astronomy, Japan, 1997). The last space radio telescope is Spektr-R and it was sent by Russia in 2011.

1.3.2 Radio Interferometry

With the passing days, we expect to observe fainter sources that need instruments with higher resolution. Now, the higher resolution needs a greater "objective" size (see equation 1-1) i.e.; a larger instrument size. However, there is a certain limit up to which one can increase the size of a single instrument. To achieve a particular resolution, one just can not increase the size of a single instrument infinitely. For comparison, the angular resolution of a radio telescope using the largest antennas to operate at their shortest wavelength is only a few arc seconds, which is about 10 times poorer than a ground-based optical telescope's resolution. The problem of achieving higher resolution is solved by the principle of interferometry. In this method, we synthesize a very large "effective aperture" from a number of antennas. To understand the basic working principle, let us consider a simple two-antenna radio interferometry system. The signals from an unresolved source arrive in the two interferometers in phase (constructive interference) and out of phase (destructive interference); there is a difference in path length between the two signals due to the Earth's rotation. Thus interference fringe is created, similar to the interference of light. For a radio source with finite angular size, the path difference to the elements of the interferometer varies along the source. Thus the produced interference fringes from each interferometer pair depend on the radio "brightness" distribution. A single Fourier component of the brightness distribution of a radio source is measured by each of the interferometer pairs.

In 1946, the British radio astronomer Martin Ryle and two Australian radio astronomers Joseph Lade Pawsey and Ruby Payne-Scott first developed this interferometry technique. Using a single converted radar antenna, on 26 January 1946, Payne-Scott, Pawsey, and Lindsay McCready first made a radio astronomical observation at 200 MHz. By the end of the 1950s, the astronomer group of Martin Ryle was able to demonstrate that the movable antenna elements combined with Earth's rotation can sample a sufficient number of Fourier components to synthesize the effect of a large aperture and thus reconstruct high-resolution images of the radio sky. The Fourier transforms to obtain images from interferometer data are

done using high-speed computers and the fast Fourier transform (FFT), a mathematical technique designed specifically for computing discrete Fourier transforms. In 1974, Ryle received a Nobel prize for his contributions to the development of this Fourier synthesis technique, also known as aperture synthesis or earth-rotation synthesis. A diagram is presented in Figure 1.8 that shows the basic principle of aperture synthesis interferometry. Swedish physicist Jan Hogbom in the 1960s invented a new technique called CLEAN. The CLEAN technique is used to remove spurious responses from a celestial radio image caused by the use of discrete, rather than continuous, spacings in calculating the radio image. A new concept of self-calibration was developed by two British scientists, Roger Jennison and Francis Graham Smith. Through this technique, the observed source was calibrated using itself as a calibrator. This self-calibration helps to remove errors in a radio image caused by uncertainties in the response of individual antennas and the small errors introduced by radio signal propagation through the terrestrial atmosphere. Through these processes, a radio telescope can achieve a better angular resolution and a better image quality. A large number of different separations between different telescopes are required in order to produce a high-quality image. The projected separation between any two telescopes as seen from the radio source is known as "baseline". So, different possible baselines are required to produce a good quality image. For example, the Karl G. Jansky Very Large Array (VLA) (Figure 1.9 (a)), a centimeter-wavelength radio astronomy observatory has 27 telescopes giving 351 independent baselines at once. In the low-frequency range, the Giant Metrewave Radio Telescope (GMRT) (Figure 1.9 (b)) and the Low-Frequency Array (LOFAR) are two popular array radio telescopes. The GMRT has thirty fully steerable parabolic radio telescopes, each of which has a 45-meter diameter. This is located at Khodad, Pune, India, and operated by National Centre for Radio Astrophysics (NCRA), as a part of the Tata Institute of Fundamental Research (TIFR), Mumbai, India. It has baselines of up to 25 kilometers and it observes at meter wavelength. This has recently been upgraded with new receivers and is known as the Upgraded Giant Metrewave Radio Telescope (uGMRT). The LOFAR is a large radio telescope system in the Netherlands, which is built and operated by ASTRON, the Netherlands Institute for Radio Astronomy. A detailed description of LOFAR and the data survey is given in Chapter 4 (Section 4.1). The upcoming Square Kilometre Array (SKA) is an intergovernmental radio telescope that will be built in Australia and South Africa. This will operate over a wide range of frequencies. It will be operational after 2027. This will give a sensitivity fifty times better than today's telescope and it will map the sky ten thousand times

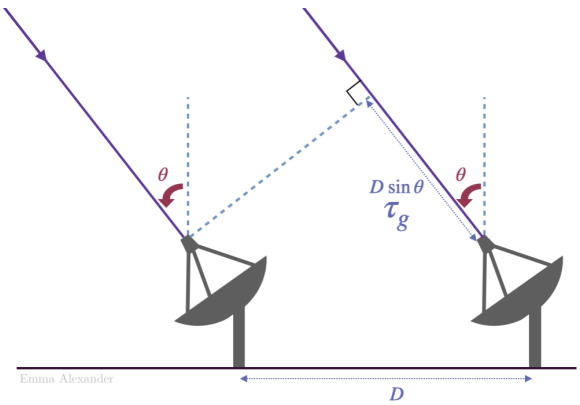

Figure 1.8: The diagram exhibits a sketch to represent the basic principles of aperture synthesis interferometry. Here, D is the distance between two telescopes and θ is the angle of the source position in the sky with the zenith. Here, τ_g is the time difference corresponding to the distance difference $Dsin\theta$. (Courtesy: Emma L. Alexander)

faster than before.

1.3.3 Very-Long-Baseline Interferometry

The greater the distance between our radio antennas, the larger the telescope they imitate. The phase shifts they observe are even greater, implying that their narrower overlap provides a more detailed view of the sky. With this level of precision, radio telescopes located thousands of miles apart can pinpoint the exact location of radio objects in space, including distances from Earth. This system is known as Very Long Baseline Interferometry, or VLBI in short. Coaxial cable, waveguide, or even fiber-optic links are used in conventional interferometers and arrays to distribute a common local-oscillator reference signal to each antenna and to return the received signal from an individual antenna to a central laboratory where it is correlated with the signals from other antennas. However, when the antenna separations are more than a few tens of kilometers, it becomes too expensive to use real physical links to distribute the signals. Very high frequency (VHF) or ultrahigh-frequency (UHF) radio links have been used, but the requirement for a large number of repeater stations makes this impractical for spacings greater than a few hundred kilometers. The technique of very long baseline interferometry (VLBI) can be used to create interferometer systems with essentially

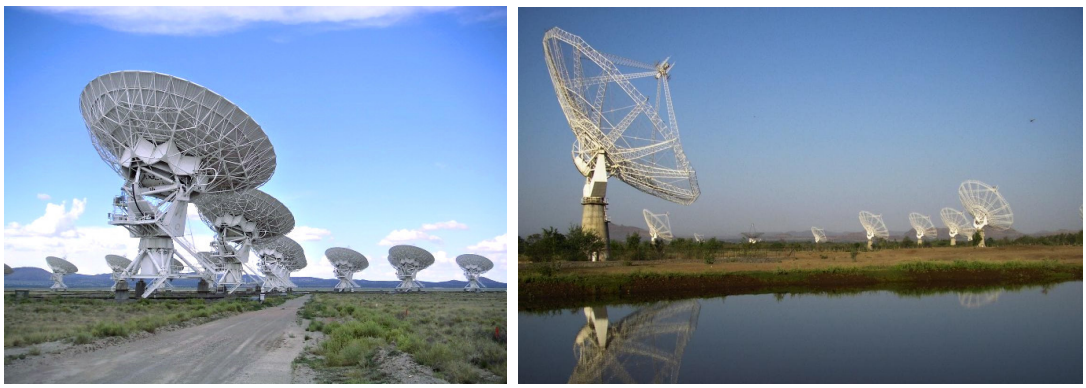

Figure 1.9: These are images of two array radio telescope systems. The first one, in the left panel is (a) the Karl G. Jansky Very Large Array (VLA, located at Socorro County, New Mexico) (Courtesy: Wikipedia). The second one in the right panel is (b) the Giant Metrewave Radio Telescope (GMRT, located at Khodad, Pune, India) (Courtesy: National Centre for Radio Astrophysics/TIFR).

infinite element separation. Early VLBI systems used broad-bandwidth videotape recorders at each antenna to record the signals received at each element. Data are now stored on discs, thanks to the development of low-cost, dependable computer disc drives. The discs are then transported to a central location where the signals are combined to form interference fringes. To operate a VLBI system successfully, the tape recordings must be synchronized within a few millionths of a second, and the local oscillator reference signal must be stable to better than one part in a trillion. Data from a few hours of observation typically contains one trillion bits of information, which is roughly equivalent to storing the entire contents of a small library. The use of hydrogen maser frequency standards allows for timing accuracy of a few billionths of a second and frequency stability of one part in a million billion.

The Very Long Baseline Array (telescopes located across North America, which is the world's largest VLBI system dedicated to full-time research) and the European VLBI Network (telescopes in Europe, China, South Africa, and Puerto Rico) are the two most important VLBI arrays operating today.

1.3.4 Radar Techniques

Radar techniques in radio telescopes utilize the similar technology that is used in the military and civilian radar. These kinds of techniques are mainly used to

study the surface of planets and asteroids in our solar system. By measuring the spectrum and time of flight of signals reflected from planetary surfaces, it is possible to examine topographical features with a linear resolution of 1 km, deduce rotation rates, and determine the distance to the planets with high accuracy. High-power radar transmitters are needed to detect measurable signals as the radio signals reflected from the planets are weak. Even at the planet's closest approach to Earth, a radar signal takes about five minutes to travel to Venus and come back. It takes more than two hours for Saturn.

1.4 Radio Source

In astronomy, a radio source is an object that emits large amounts of radio waves. All types of sources radiate in radio wavelength, but all are not in the detectable range. We receive radio signals from sources of our solar system, some galactic sources, and extra-galactic sources. Some strong radio sources in our universe are pulsars, certain nebulas, quasars, and radio galaxies.

1.4.1 Radio Emissions from our Solar System

The Sun and Jupiter are the prominent radio source in our solar system. As the Sun is the nearest star, we receive radio signals from it. However, the galactic background noise dominates at longer wavelengths when the Sun is quiet. In low frequencies, the Sun shows dominating radiation during the geomagnetic storms. The radio emission from the Sun was first detected by a group of British army radar operators, in 1942. Jupiter emits radio waves in the decimeter range. The magnetosphere of Jupiter produces this strong radiation. The radio waves are generated through a cyclotron maser mechanism due to the injection of gas by Io (Jupiter's moon) in the polar region of Jupiter.

1.4.2 Galactic Radio Sources

The strongest radio sources in our Milky Way galaxy are the Galactic Center, Pulsars, Rotating Radio Transients, and Star-forming regions. A short note on these sources is given below:

• *Radio emission from the Galactic Center*

The radio emission from the center of our galaxy is the first detected radio emission by Karl Jansky, in 1932. The major radio sources in the galactic center are Sagittarius A, a black hole. The compact region around the supermassive black hole is Sagittarius A*.

• *Supernova Remnants*

A Supernova remnant (SNR) is the left behind structure, after a supernova explosion. A Supernova remnant gives diffuse radio emission. Cassiopeia A and the Crab Nebula are two well-known examples of Supernova remnant that shows strong radio emission. Cassiopeia A is the brightest extrasolar radio source in the sky.

• *Pulsars*

The collapsed core of a massive supergiant star is known as a Neutron star. This has a mass of between 10 to 25 solar mass ($M_\odot$). A highly magnetized rotating neutron star that emits beams of electromagnetic radiation from its magnetic poles, is known as Pulsar. The pulsars emit radio waves mainly through synchrotron radiation. The first identified pulsar is the Crab Pulsar. The Parkes radio telescope discovered the first known system of two pulsars orbiting each other in 2003.

• *Rotating Radio Transients*

Rotating radio transients (RRATs) are kinds of pulsars, with short, moderately bright, radio pulses. Rotating radio transients are first discovered in 2006 by Maura McLaughlin at Jodrell Bank Observatory. The Rotating radio transients emit radio signals. However, the signal is quite difficult to trace due to its transient nature (David Biello 2006).

• *Star Forming Regions*

The molecules of the star-forming regions (SFR) produce short radio waves. Some well-known star-forming regions are RCW 36, Westerhout 40 (W40), Vela Molecular Ridge, etc.

1.4.3 Extra-Galactic Radio Sources

Most of the known strong radio sources are extragalactic. The primary radio-loud extra-galactic source is Radio Galaxy. Apart from radio galaxies radio emissions were also detected from the Cosmic Microwave Background (CMB), Extragalactic pulses - Fast Radio Burst.

- *Radio Galaxies*

The galaxies that produce large amounts of radio waves are known as radio galaxies. More details are given in Section 1.7.

- *Cosmic Microwave Background*

According to the Big Bang theory, the cosmic microwave background (CMB) is the remnant radiation from the early era of the universe. It is a blackbody background radiation and we measure and make a distribution map in the radio wavelengths.

- *Fast Radio Burst*

The transient radio pulse on a time scale of a fraction of a millisecond to a few milliseconds is known as a Fast Radio Burst (FRB). The first burst was detected by D. R. Lorimer by analyzing some archival data. The time duration of the burst was less than 5 milliseconds. In 2010, 16 such kinds of pulses were detected by the Parkes Telescope (Burke-Spolaor et al. 2011).

1.5 Types and Mechanisms of Radio Emission

The radio emission from the sources is basically two types - (i) Continuum radio emission and (ii) Line radio emission.

(i) **Continuum radio emission:** A continuum radio emission is the summation of a large wavelength range. There are two mechanisms through which astronomical radio sources generate a continuum radio emissions and those are thermal radiation and synchrotron radiation. This type of radiation is made up of photons of various wavelengths that are emitted by electrons as they are accelerated by adjacent protons and change in orbits. This is the case for hot, ionized interstellar gases of an emission nebula; an H II region. The synchrotron radiation

is a nonthermal radiation. The synchrotron radiation happens when electrons with speed nearby the light are spiraled in a magnetic field. Radio emissions from radio galaxies, supernova remnants, and pulsars are all through this mechanism. The continuum radiation is identified and studied using radio telescopes by tunning the telescope to the preferred wavelength.

(ii) **Line radio emission:** Line emissions occur at particular wavelengths like an optical spectral line. The most important radio line emission is the 21-centimeter line or the H I line. This is emitted by the neutral hydrogen atoms. H I line was first detected in 1953, however, this was predicted in 1944 by Dutch astronomer Hendrik C. van de Hulst. Different molecules in the interstellar medium emit and absorb radiation at radio frequencies. For example, the hydroxyl (OH) radical's 18-centimeter line was discovered in 1963. More such lines e.g., water (H_2O), ammonia (NH_3), formaldehyde (CH_2O), and carbon monoxide (CO) lines were discovered during the time period 1968 to 1970. To date, there are about 200 such molecules and radicals are identified. As line emission occurs at only one particular wavelength the radio telescopes are set exactly at that wavelength.

1.6 Active Galactic Nucleus

Before going to the details of the radio galaxy, let's take a look at the Active Galactic Nucleus or AGN. The active Galactic Nucleus (AGN) is a small compact region at the central core of a galaxy that produces a remarkably large amount of energy in the full electromagnetic spectrum. The AGN phenomenon is believed to occur as a result of matter accretion by a supermassive black hole at the center of the host galaxy (Krolik 1999). The nature of the AGN activity is found to be episodic (Saikia et al. 2010).

The canonical structure of an AGN shows a supermassive black hole (SMBH) (with a mass range $\sim 10^6 M_\odot to 10^9 M_\odot$) at the center. The central SMBH accrete the surrounding matters. A disc, revolving around the central black hole and transport matters, is known as an accretion disc. The disc is made of normal gas, dust, or ionized gas. A narrow line region (NLR) and a broad line region (BLR) surround the black hole. Both NLR and BLR are made of heavy ionized clouds. In the case of a radio-loud AGN, there is a jet emerging from the central black hole. This radio jet has the ability to extend over a few pc to several hundred kpc distances in the two opposite directions (Urry & Padovani 1995). A model diagram of an AGN indicating different regions and types is presented in Figure

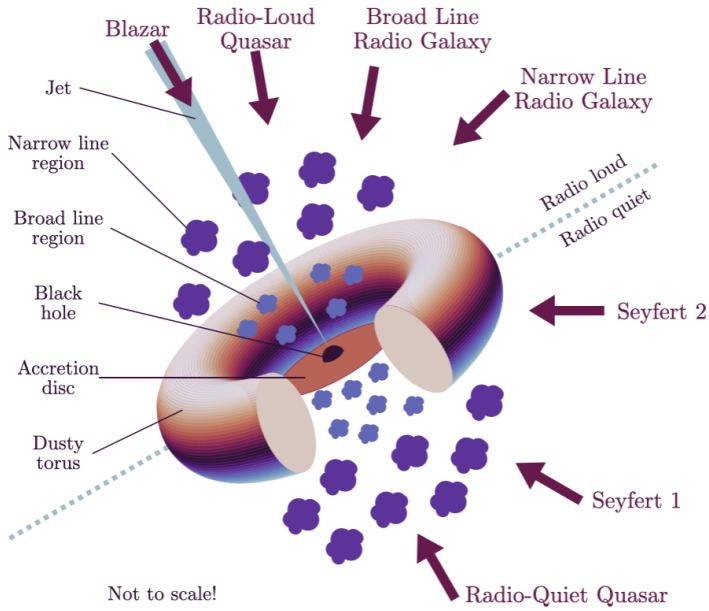

Figure 1.10: The image presents a unified model of AGN, mentioning different areas and classes of AGN (Courtesy: Emma L. Alexander; the image is adapted from Urry & Padovani (1995)).

1.10.

Though AGNs emit radiation at all wavelengths, maximum AGNs are strong in the X-ray range. The X-ray emission is due to a scattering process from the jets and the hot corona of the accretion disc and it follows a power-law spectrum (Haardt & Maraschi 1991; Krolik 1999). However, a small amount of AGNs ($\sim 10\%$) shows strong emission in the radio wavelength range. These are called Radio loud AGN. The luminosity range in radio wavelength is $\sim 10^{30} - 10^{38} W$. The sources with weak radio emissions are called radio-quiet AGN. These are two types of AGNs. Some radio-loud AGNs are Radio galaxy, Blazar, BL Lac object, and some Quasar. A quasar (quasi-stellar object or QSO) is an extraordinarily high luminous AGN, powered by a supermassive black hole. Quasars are one of the brightest objects in the universe. There are different types of quasars, e.g.; radio-loud quasars, optically violently variable (OVV) quasars are radio-loud AGN when radio-quiet quasar is a weak emitter of the radio waves. A blazar is an AGN having relativistic jets, composed of ionized matter. A BL Lac object (BL Lacertae object) is another type of AGN that is featured by strong optical polarisation and rapid and large-amplitude flux variability. Some radio-quiet AGNs are LINERs, Seyfert galaxies

(I and II), and some radio-quite quasars. The LINER (low-ionization nuclear emission-line region) is a type of AGN characterized by its spectral line emission. Seyfert galaxies are the type of AGNs that have quasar-like nuclei and have very high surface brightness.

1.7 Radio Galaxy

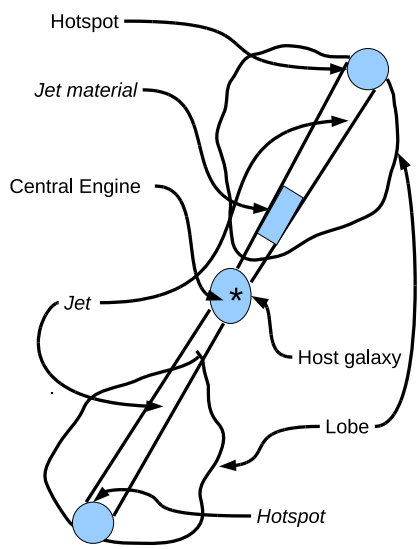

Figure 1.11: The image is a schematic diagram of a typical radio galaxy. The different portion of a radio galaxy is mentioned in the figure. Note that, in this picture, the presented figure is an FR-II type of radio galaxy. (Courtesy: Konar & Hardcastle, 2013)

A galaxy that is a strong emitter of radio waves is called a radio galaxy. Radio galaxies are one of the most luminous sources in the sky with luminosity 10^{41} to $10^{46} ergs^{-1}$ in the frequency range of 10 MHz to 100 GHz. Radio galaxies were first discovered during the 1950s. A typical radio galaxy has a linear structure with two diffuse emission regions known as lobes. The two lobes are located on the opposite side of the host galaxy. There is a tiny and bright spot lying at the adjacent point of the two lobes that coincide with the host galaxy. There is a collimated structure that connects the lobes to the central core known as jets. The radio jets are the signature of the energy outflows from the galactic nucleus

to the extended regions of emission. Sometimes, there is a small and strong region is found at the outer edge of the lobe. This is known as a hotspot. The hotspot is created due to the interaction of the endpoint of the jet with the surrounding medium. A schematic diagram for a classical double-lobed radio galaxy is given in Figure 1.11. The radio image of Cygnus-A, a well-known radio galaxy, is given and the components are labeled in Figure 1.12.

As mentioned before (in Subsection 1.5), the radio emission from a radio galaxy is mainly due to a synchrotron process. As we referred, there is a synchrotron process, hence there is the electron in spiral motion with a relativistic speed along with a magnetic field. Now, the plasma is supposed to be a neutral entity, so there is also either positron or proton. However, we can not estimate the particle compositions and the magnetic field through observations. There is also another process called the inverse-Compton process. In the inverse-Compton process, the electron with a near speed of light interacts with the surrounding photons. This interaction emits high radiation through the Thomson scattering process. However, this radiation is mostly contributed to the X-ray emission. There is also another probable process that happened in the radio galaxy and the process is known as Fermi acceleration or diffusive shock acceleration. In this process, the charged particle is repeatedly reflected by a magnetic trap or magnetic mirror.

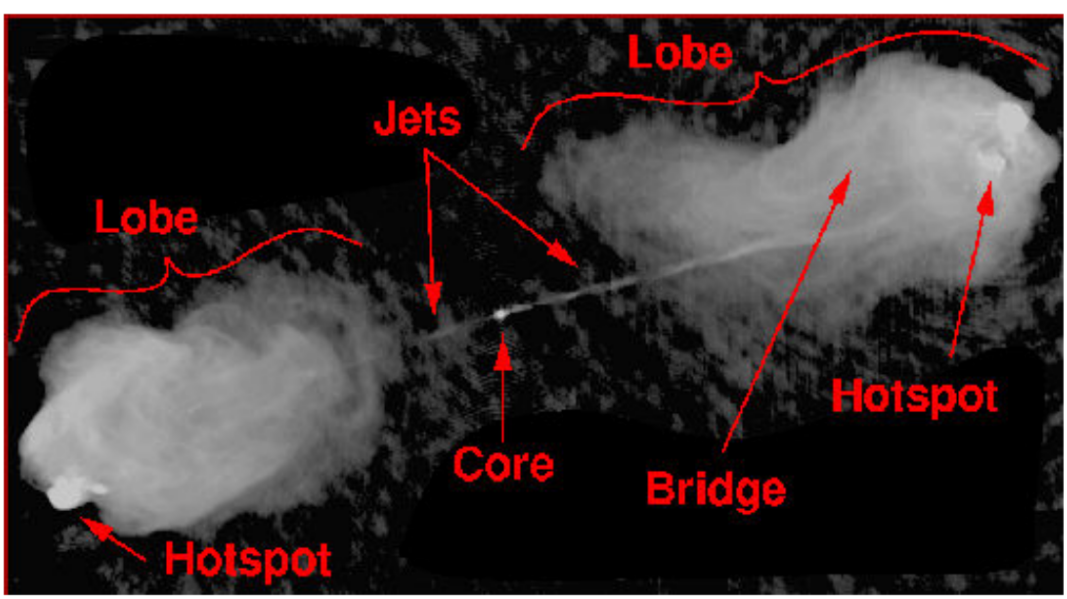

Figure 1.12: The image shows the radio image of a well-known radio galaxy, Cygnus-A, (Courtesy: Leah et. al. 1999).

1.8 Fanaroff-Riley Classification

In 1974, B.L. Fanaroff and J.M. Riley classified the double-lobed radio galaxies into two categories; Fanaroff-Riley Class I (FR-I) and Fanaroff-Riley Class II (FR-II) (Fanaroff & Riley 1974). The classification was done on the basis of the distribution of their luminosity or brightness. Radio sources with relatively dark edges are classified as FR-I. On the other hand, radio sources of the FR-II type have brighter edges than their central areas (see Figure 1.13). The significance of this classification is that it gives an idea about the luminosity of the radio galaxy and also introspects the flow of energy from the central core to the outer lobe. To distinguish the FR-I and FR-II sources there is no sharp boundary of luminosity value. There are some overlap regions and approximate values in different frequency ranges. For low frequency, the boundary is quite sharp, at 178 MHz, and the reliable luminosity (L_{178}) is $2 \times 10^{25} W Hz^{-1}$. The FR-I sources have luminosity below the value and the FR-II sources have luminosity above this (Fanaroff & Riley 1974). For high frequency, at 2.7 GHz the luminosity ($L_{2.7}$) for FR-I sources goes up to $6 \times 10^{26} W Hz^{-1}$. The $L_{2.7}$ for FR-II sources is observed down to $2 \times 10^{25} W Hz^{-1}$ (Laing et al. 1983) or even to $3 \times 10^{24} W Hz^{-1}$ (Morganti et al. 1993).

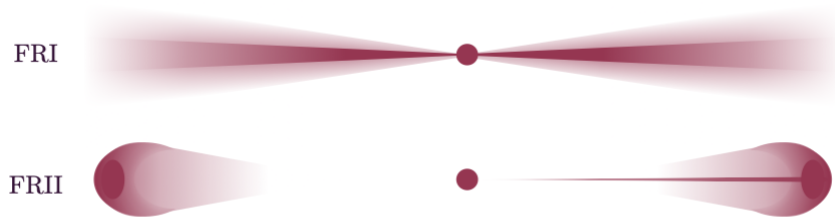

Figure 1.13: The sketch represents a simplified model of Fanaroff-Riley Class I and Fanaroff-Riley Class II radio galaxy (Courtesy: Emma L. Alexander).

1.8.1 Fanaroff-Riley Class I (FR-I)

The radio galaxy with a brighter core and fainter edges is known as the Fanaroff-Riley Class I (FR-I) source. As the FR-I sources have dark edges, these sources are also known as edge-darkened sources. The fainter edges have steep spectra, which

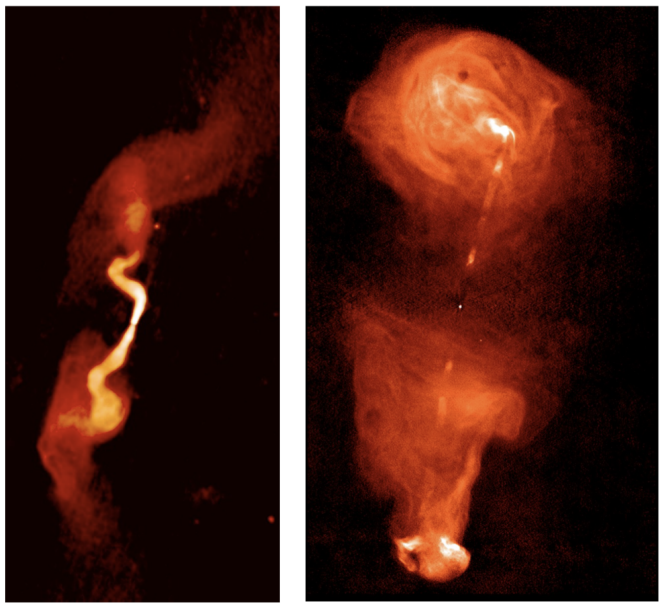

Figure 1.14: The examples of Fanaroff-Riley galaxies are presented here. The left panel (a) is a VLA map of the FR-I radio galaxy 3C 31 at 1.4 GHz (Courtesy: NRAO/AUI), The right panel (b) is a VLA map of the FR-II radio galaxy 3C 353 at 1.8 GHz (Courtesy: NRAO/AUI).

indicates that the radiating matter in the edge area is aged. The radio jets are seen for most of the FR-I sources. The jets are generally two-sided, however, a jet can begin as one-sided from the core and become two-sided after a few kiloparsecs. Initially, the component of the magnetic field in the plane of the sky along the jet is parallel to the jet axis, but soon it becomes substantially perpendicular to the axis. FR-I sources are linked with bright, massive galaxies (D or cD) that have a flatter light distribution than a typical elliptical galaxy and are frequently found in the rich clusters of extreme X-ray producing gas (Owen & Laing 1989; Prestage & Peacock 1988). The edges are seen to be distorted due to the ram pressure. A typical FR-I source, a radio galaxy 3C 31 is given in Figure 1.14 (a).

1.8.2 Fanaroff-Riley Class II (FR-II)

Radio sources with less bright core but luminous edges are classified as Fanaroff-Riley Class II (FR-II) sources. These sources are also termed edge-brightened sources. Jets are not found in most of the radio galaxies except for the quasars. Generally, the jets are one-sided due to relativistic beaming. The magnetic field

of a jet is primarily parallel to the jet axis. The FR-II galaxies are associated with normal galaxies. The galaxies are giant ellipticals, however not cluster galaxies. The FR-II galaxy environment does not exhibit galaxy clustering compared to the random elliptical galaxies (Owen & Laing 1989, Prestage & Peacock 1988). An example of an FR-II source, a radio galaxy 3C 353 is given in Figure 1.14 (b).

1.8.3 Fanaroff-Riley Class 0 (FR0)

The Fanaroff-Riley Class 0 (FR0) is a newly identified type of radio galaxy. The FR0s do not shave a large-scale structure like FR-I or FR-II sources (Baldi et al. 2015). FR0s exhibit short and weak jets up to a few to tens of kiloparsecs (Nagar et al. 2005, Baldi et al. 2019)from the central black hole. The jets are $\sim$ 10 to 1000 times weaker than typical FR-I radio galaxy jets. Despite the weak jets the FR0s are able to inject a large amount of energy into their host galaxies' interstellar medium. Two samples of FR0s are presented in Figure 1.15.

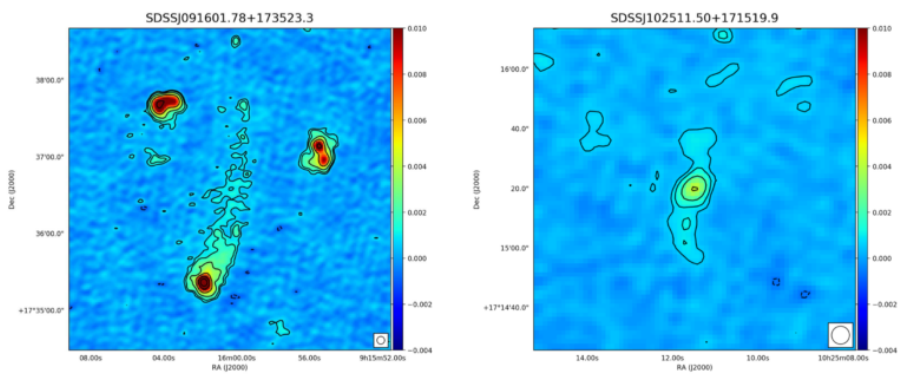

Figure 1.15: The image gives the radio map of typical FR0 sources. The images are drawn from the LOFAR survey data at 150 MHz. The left panel shows FR0 J0916+17 when the right panel shows FR0 J1025+17 (Courtesy: Capetti et al. 2020).

1.9 Types of Radio Galaxy

Apart from the regular, classical double-lobed radio galaxies, some sources show a number of finite known atypical and irregular structures. Depending on the morphology and structure, radio galaxies are classified into some classes and sub-classes.

1.9.1 'Winged' Radio Galaxy

The 'Winged' Radio Galaxy (WRG) is an exotic subclass of the radio galaxy, that discloses a pair of secondary low surface brightness radio lobes known as 'wings', oriented at a certain angle to the active, or primary high surface brightness lobes (Leahy & Parma 1992; Cheung 2007; Yang et al. 2019; Bera et al. 2020, 2022). A detailed discussion about the winged radio galaxies is presented in Chapter 2.

1.9.2 Bent-Tail Radio Galaxy

The morphology of a radio source depends on the structure and orientation of the radio jets. A typical radio galaxy shows a fairly simple and symmetric structure, with two radio jets directed in the opposite direction from the common center (see Figure 1.11). Sometimes, a deformed morphology is seen when the two radio jets are noticed to be bent in the same direction in intercluster weather. These types of galaxies are called as Bent-Tail (BT) Radio Galaxy, also known as 'C'-shaped radio sources, Head-Tail (HT) radio sources, or simply bent radio sources (Ryle & Windram 1968; Rudnick & Owen 1976; Blanton et al. 2000; Proctor 2011; Dehghan et al. 2014; Mingo et al. 2019; Sasmal et al. 2022). The BT sources are first introduced by Ryle & Windram (1968). The sources bend in such a way that the gross structure gives a 'C' or 'L' or 'V'-shape. Depending on the angle of bending, Owen & Rudnick (1976) classified BT sources into two classes, e.g.; wide-angle tail (WAT) and narrow-angle tail (NAT) radio galaxy. Morphologically, when the angle between two radio jets at the center is greater or equal to 90°, the BT sources are known as WAT sources. On the other hand, a BT source with an angle less than 90°, with both jets bending back until they are parallel is called as NAT source. The WATs are BT sources having an intermediate radio luminosity, $10^{42} \leq L_{WAT} \leq 10^{43}$ ergs^{-1} in the wavelength range of 10 MHz to 100 GHz with central, dominant galaxies in rich clusters (O'Donoghue et al. 1990, 1993). The NATs are relatively less luminous. The source 3C 465 (see Figure 1.16 a) is a good example of WAT (Eilek et al. 1984; Eilek & Owen 2002; Hardcastle et al. 2005). The radio source NGC 1265 (see Figure 1.16 b) is a prototype of NAT source (Ryle & Windram 1968; O'Dea & Owen 1986).

Typically, the objects are observed in the galaxy clusters region (Burns 1990). The bending occurs due to the strong interactions between the radio jets and their intra-cluster medium (ICM). The dynamic pressure pulls the jets back and causes the jets to bend. When these sources move at high speeds in the ICM, the

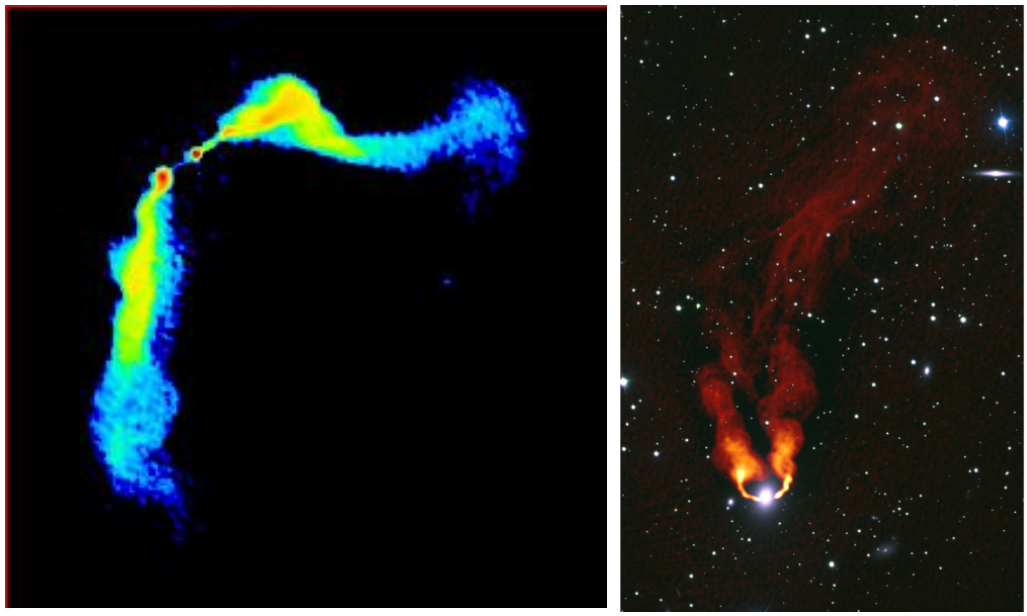

Figure 1.16: The examples of Bent-tail radio sources are presented. The left panel (a): 3C 465, a WAT source (Courtesy: 3CRR Atlas catalog). The right panel (b): NGC 1265 is a NAT source (Courtesy: NRAO).

jets bend in the same direction due to the effect of ram pressure (O'Dea 1985). Begelman et al. (1979) first proposed the "ram-pressure" model, however, this was well explained later by Baan & McKee (1985) and Vallee (1981). A buoyancy force also comes into action when the material density of the radio jets is less than the density of the surrounding medium. It causes the lobes to be pushed to regions of the ICM where the density of the jet is equivalent to that of the surrounding medium, causing jets to bend (Gull & Northover 1973; Sakelliou et al. 1996). The high velocity of the ICM caused by the cluster's merger history causes jet distortions. Studies also show that they tend to reside in galaxy clusters (Burns 1990; Roettiger et al. 1996; Blanton et al. 2000; Mao et al. 2009; Dehghan et al. 2014). This makes the BT sources a powerful tool to probe galaxy interactions on large scale and use BT sources as a tracer of galaxy clusters (Blanton et al. 2000, 2001; Smolčić et al. 2007).

Owen & Rudnick (1976) first presented the observational result of six WAT radio sources at 2695 MHz using the National Radio Astronomy Observatory (NRAO). Later, O'Donoghue et al. (1990) noted 11 WATs, seen at 20 cm from VLA. O'Donoghue et al. (1993) released pictures of 11 WATs at 6 cm and 20 cm

and investigate the dynamics of such sources. A large catalog of 384 bent-double radio sources from the VLA Faint Images of the Radio Sky at Twenty Centimeters (FIRST) survey data is detected by Blanton (2000). Using the same VLA FIRST data Proctor (2011) annotated a set of 412 bent samples by an automated pattern recognition system. Through a visual inspection of selected 5805 extended radio-loud AGN, Mingo et al. (2019) identified 264 NAT sources and 195 WAT sources. In their investigation, Mingo et al. (2019) use the data of the LOFAR Two-metre Sky Survey First Data Release (LoTSS DR1) at 144 MHz frequency from the value-added catalog (Williams et al. 2019). Missaglia et al. (2019) cataloged 47 WAT candidates using a combination of the NRAO Very Large Array Sky Survey (NVSS), FIRST, and the Sloan Digital Sky Survey (SDSS) databases. Most recently, Sasmal et al. (2022) presented the largest visually detected catalog of BT sources, which contains a total of 717 such sources. They used the VLA FIRST survey data at 1.4 GHz. Out of the 717 sources, 430 are identified as WATs and 387 as NATs. Along with the sample identification, there are also some multifrequency observations done. Recently, Patra et al. (2019) did a multifrequency study of an interacting NAT radio galaxy, J0037+18 using the GMRT and VLA data. A similar kind of work is done by Srivastava & Singal (2020) for the longest known HT radio galaxy, IC 711. The association of BT sources with nearby galaxy cluster and their interaction with the ICM is also studied. Some recent works in this field are also done by Paterno-Mahler et al. (2017), Croston et al. (2019), Mingo et al. (2019), and Vos et al. (2021).

1.9.3 Double-Double Radio Galaxy

The Double-Double Radio Galaxy (DDRG) (Schoenmakers et al. 2000; Joshi et al. 2011; Nandi & Saikia 2012; Kuźmicz et al. 2017; Mahatma et al. 2019) is the manifestation of the episodic nature of radio-loud active galactic nuclei. DDRGs exhibit a large-scale remnant radio plasma in the intergalactic medium left over from a previous episode of AGN activity, and radio jets have restarted due to a new episode. So we get a pair of double radio sources, aligned along the same axis with a coinciding radio cores. A simple and general definition state that a radio galaxy consists of a pair of double radio sources with a common center is known as a double-double radio galaxy (Schoenmakers et al. 2000). An image of a DDRG J0041+3224 is given in Figure 1.17.

The central activity of a galaxy is due to the feeding of a Super Massive Black Hole (SMBH), which have masses ranging from $\sim 10^6 - 10^{10} M_\odot$ located in the

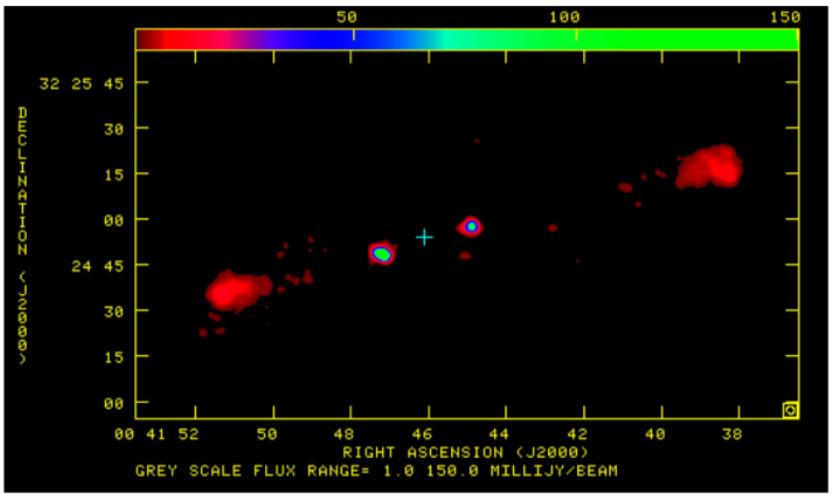

Figure 1.17: The radio image of a double-double radio galaxy, J0041+3224 is presented (Courtesy: Saikia, Konar & Kulkarni (2006)).

galaxy's centre. Generally, these SMBHs have the capacity to activate AGN. However, due to a lack of fuel, non-active SMBHs are unable to drive such AGN activity. A significant question is whether all galaxies containing an MBH experienced AGN activity. Franceschini et al. (1998) discover that many periods of activity are feasible based on SMBH observation data. The time scales of such repeating activity are extremely long, in the order of 10^9 or 10^{10} years. A duty cycle should be recognized in order to comprehend this type of recurrent action. It is possible if there is some method in place to secure nuclear activity information for a sufficient period of time before the new cycle begins. Such a method is accessible for radio lobes in the case of extended radio sources. These radio lobes are energy reservoirs created by the incredibly powerful jet-producing AGN. These lobes have the ability to store knowledge from previous activities for an extended period of time. Now, if a new AGN activity begins before the 'old' lobes fade out, a fresh, youthful pair of radio sources are discovered in the galaxy's older structure and thus a DDRG morphology may be formed. The inner radio source's two lobes have been extended and feature an edge-brightened radio morphology.

The first DDRG identifications are done by Schoenmakers et al. (2000) and Kaiser et al. (2000). Saikia, Konar & Kulkarni (2006) presented the DDRG J0041+3224, which have a projected linear size of the outer and inner doubles are 969 and 171 kpc respectively. A misalignment of 35° between the outer double

and inner double is found for the DDRG 3C 293 (Joshi et al. 2011). This finding contradicts the fact of the well alignment of the outer and inner double (Saikia, Konar & Kulkarni 2006). A similar misalignment of $\sim 30^{\circ}$ is detected for DDRG J1328+2752 (Nandi et al. 2017). For the first time, Nandi & Saikia (2012) made a catalog of 23 DDRGs from the VLA FIRST survey. Later, a larger sample of 74 sources is presented by Kuźmicz et al. (2017) using FIRST and NVSS, out of the sample 85% were DDRGs. Recently, Mahatma et al. 2019 created a sample of 33 robust DDRGs. They also found that DDRGs and conventional radio-loud AGNs are hosted by the same type of host galaxy and that the restarting event is a natural phenomenon, in particular that exists for the low-excitation radio galaxies. More studies like Brocksopp et al. (2011); Konar & Hardcastle (2013); Orrú et al. (2015) are done to find the origin and characteristics of DDRGs. These DDRGs are an interesting astrophysical source for research into galaxy morphology and emission mechanisms. DDRGs can also be used to investigate the episodic activity of the AGN.

1.9.4 Giant Radio Galaxy

As the name suggests a Giant Radio Galaxy (GRG) is featured by its gigantic size compared to normal radio galaxies. A radio galaxy with a linear size greater than 0.7 Mpc is known as a Giant radio galaxy (Willis et al. 1974; Ishwara-Chandra & Saikia 1999; Dabhade et al. 2017, 2020). The linear size is defined as the distance between the outmost edges of the galaxy. The radio image of a GRG, PKS B1545-321 is presented in Figure 1.18.

GRGs are the Universe's largest and most energetic single entities. Along with cluster radio relics, the GRGs are among the largest single structures known in the Universe (Röttgering et al. 1997; Bagchi et al. 2006; van Weeren et al. 2011). In general, it is found that GRGs have FR-II radio morphology and can be found in elliptical galaxies and quasars. The origin of such enormous size is not well understood. GRGs are by nature very old and thus have had plenty of time to spread over long distances (Subrahmanyan, Saripalli & Hunstead 1996). It is proposed that the jets may be too powerful that need the necessary thrust to reach such Mpc scales (Wiita et al. 1989). It is also considered that the GRGs stretch in low-density environments and that's why they grow comparatively fast (Mack et al. 1998; Malarecki et al. 2015; Saripalli & Malarecki 2015).

The first GRG, 3C236 was discovered by Willis, Strom & Wilson (1974). The

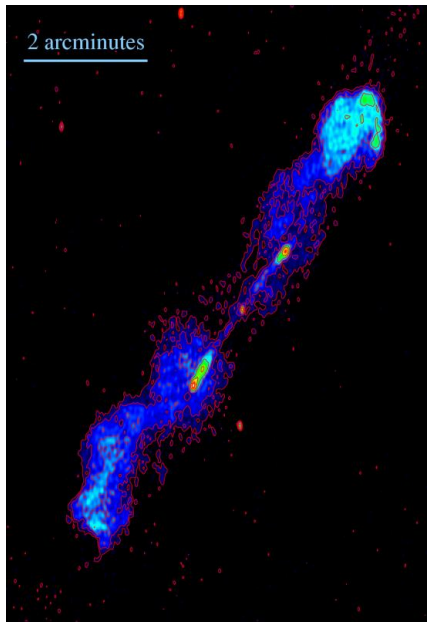

Figure 1.18: The figure depicts the radio image of a Giant radio galaxy PKS B1545-321 from the Australia Telescope Compact Array (ATCA) at 13 cm (Courtesy: Saripalli, Subrahmanyan & Shankar (2003)).

linear size of 3C236 is $\sim$ 4.62 Mpc, one of the longest GRG. The largest GRG to date is J1420-0545, which has a linear size of 4.95 Mpc (Machalski et al. 2008). Proctor (2016) gave a large list of a total of 1616 possible GRGs. Dabhade et al. (2017) discovered 25 GRGs and study their properties. Recently, through the SAGAN (Search and analysis of giant radio galaxies with associated nuclei) project the identification and study of a large sample of GRG were done (Dabhade et al. 2020). Dabhade et al. (2020) also identified 239 GRG candidates from LoTSS DR1. The study GRGs help to understand the final stages of galaxy evolution. The GRGs can serve as outstanding probes of the intergalactic medium (IGM) (Safouris et al. 2009).

1.9.5 Hybrid Morphology Radio Source

The HYbrid MOrphology Radio Sources (HYMORS) are a rare kind of double-lobed radio source which shows a different kind of FR morphology for the two lobes (Gopal-Krishna & Wiita 2000; Gawroński et al. 2006; Kapińska et al. 2017). An HYMORS exhibits FR-I morphology on one side (lobe) of the AGN and FR-II

morphology on another side (lobe). HYMORS can be associated with galaxies, quasars, and BL Lac objects. The linear size of the sources ranges from a few kiloparsecs to a few megaparsecs. A sample HYMORS NVSS J232149+484951 (de Gasperin 2017) is presented in Figure 1.19.

The origin behind such morphology is still unknown. The number of identified such sources is also very low and a small fraction of them are studied in detail. A multiwavelength study on two possible HyMoRS; J1211+743 and J1918+742 has been done by Pirya et al. (2011). Miller & Brandt (2009) also made Chandra observations of the two hybrid sources 3C 433 and 4C 65.15 in other wavelengths. A study on the orientation of the central core for the HYMORS is done by Cegłowski, Gawroński & Kunert-Bajraszewska (2013). A follow-up observation for five HYMORS are done by Cegłowski, Gawroński & Kunert-Bajraszewska (2015).

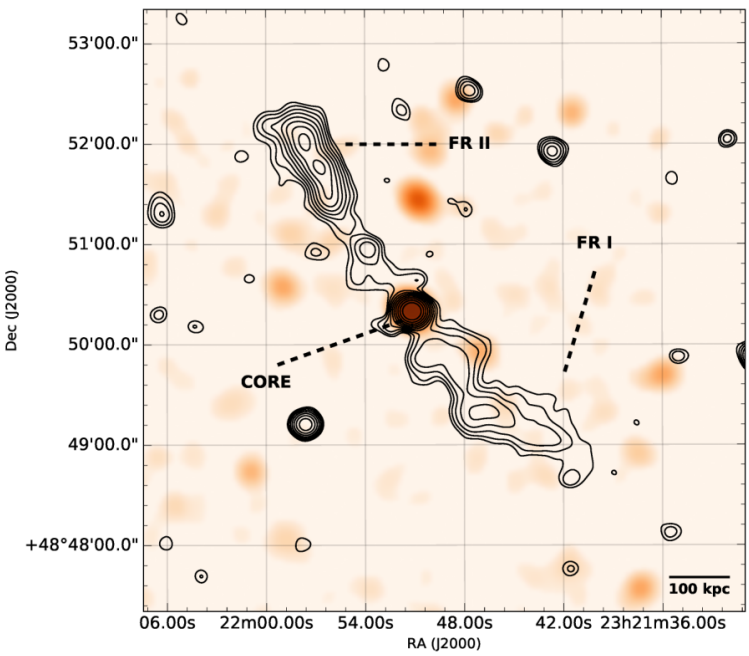

Figure 1.19: This is the radio image of a sample HYMORS NVSS J232149+484951. This is a Chandra X-ray image of the field surrounding the source when the radio contours are drawn from the VLA image at 1519 MHz (Courtesy: de Gasperin (2017)).

For the first time, Gopal-Krishna & Wiita (2000) presented six HYMORS. After that Gawroński et al. (2006) selected 21 possible HYMORS candidates by examining a sample of more than 1700 sources from the FIRST catalog. Through

a large-scale search within the international citizen science project, Radio Galaxy Zoo (RGZ), Kapińska et al. (2017) identified 25 such new sources. They also found that the sources are moderately luminous with $L_{median} = 4.7 \times 10^{24} W Hz^{-1} sr^{-1}$ at a redshift range of 0.14 to 1.0. Multi-frequency study of a new HYMORS is done by de Gasperin (2017). The origin of FR-I and FR-II sources is still unclear. The study of HYMORS may bring some important information and help to understand the mechanism of the FR dichotomy.

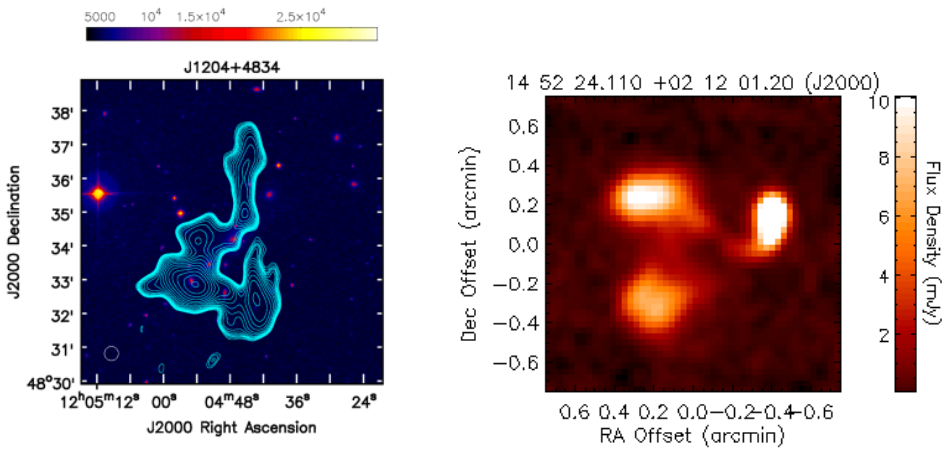

Figure 1.20: The radio image of two MRGs are presented here. The left panel (a) id the radio contour image of MRG J1204+4834 from LoTSS DR1 at 144 MHz (Courtesy: Sasmal et al. (2020)). The right panel (b) is the radio image of MRG J1452+0212 from VLA FIRST survey data at 1.4 GHz (Courtesy: Bera et al. (2020)).

1.9.6 Miscellaneous Radio Galaxy

Apart from the known morphological classes like 'Winged', Bent-Tail, and Double-double radio sources, there are some sources that exist with some peculiar morphology. As the morphology of these sources is unusual in nature, they are termed Miscellaneous Radio Galaxies (MRGs) (Sasmal et al. 2020; Bera et al. 2020). This rare kind of radio galaxies exhibits unusual and different jet alignment and orientation from a typical radio galaxy. Sasmal et al. (2020) presented four such sources from LoTSS DR1 at 144 MHz. A total of fifteen MRGs are identified by Bera et al. 2020 from FIRST survey data at 1.4 GHz. Two such miscellaneous sources are presented in Figure 1.20. The origin of such sources is still unknown.

The possible origin includes the interaction of jets and ICM, rapid spin orientations of jets, and ram pressure (Sasmal et al. 2020; Bera et al. 2020). The study of such sources may help to understand the certain phase of galaxy evolution, it may also be useful to study the morphological perturbation of a galaxy that occurred due to the surrounding medium and the presence of a nearby galaxy cluster (Sasmal et al. 2020; Bera et al. 2020).

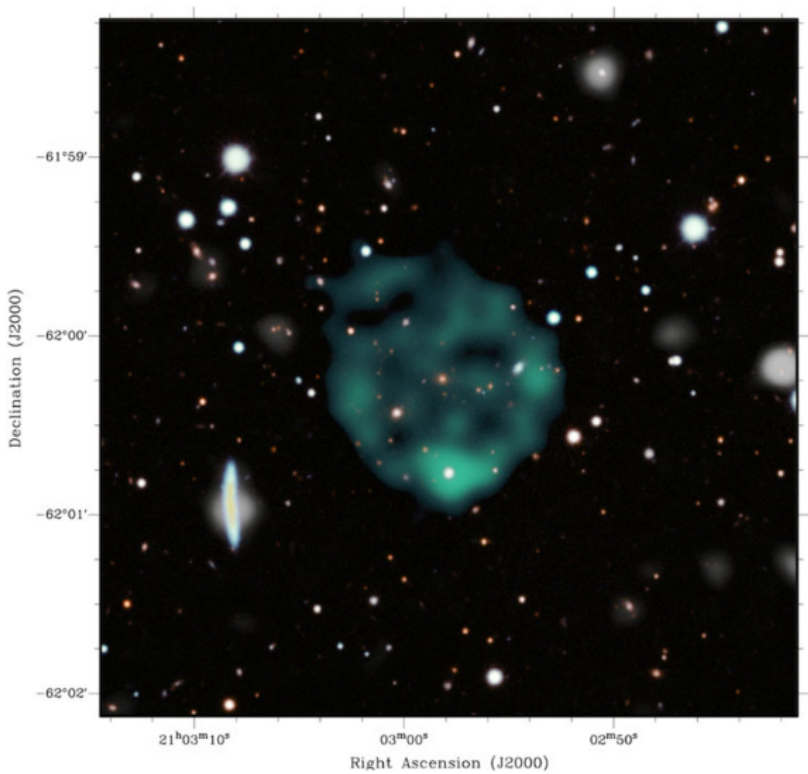

Figure 1.21: The radio image of the first Odd Radio Circle (ORC1: EMU PD J210357.9–620014) is given in the above figure. The image uses ASKAP radio continuum data at 944 MHz (Courtesy: Norris et al. (2021)).

1.9.7 Odd Radio Circle

A new class of circular radio sources is found by Norris et al. (2021) in the Evolutionary Map of the Universe (EMU) Pilot Survey, using the Australian Square Kilometre Array Pathfinder (ASKAP) telescope. The sources seem to be circular

discs with luminous edges, and the sources are called Odd Radio Circle (ORC). There are no such sources are identified before. The four ORC identified by Norris et al. (2021) have a diameter of about one arcmin. Though the circular feature is known for radio astronomical objects, like a supernova remnant, ring around Wolf-Rayet star, galactic planetary nebula, extremely bent-tail radio galaxy, einstein ring, and cluster halo. This also may be due to the imaging artifact or lobe from a double-lobed radio galaxy viewed either side-on or end-on. However, the ORC does not correspond to any of the know objects or phenomena (Norris et al. 2021). The ASKAP radio image of ORC1 (EMU PD J210357.9–620014) is given in Figure 1.21. The origin of such odd sources is unknown. Very recently, Norris et al. (2022) present a detailed study of the first ORC using the MeerKAT radio telescope at 1284 MHz. The study revealed a complex internal structure for the ORC1.

References

Baan, W. A., & McKee, M. R. 1985, A&A, 143, 136
Bagchi, J., Durret, F., Lima Neto, G.B., & Paul, S. 2006, Sci, 314, 791
Baldi, R. D., Capetti, A., & Giovannini., G. 2015, A&A, 576, 38
Baldi, R. D., Torresi, E., Migliori, G., & Balmaverde, B. 2019, Galaxies, 7, 76
Begelman, M. C., Rees, M. J., & Blandford, R. D. 1979, Natur, 279, 770
Bera, S., Pal, S., Sasmal, T. K., Mondal, S., & Patra, D. 2020, Journal of Physics: Conference Series, 1579, 012023
Bera, S., Pal, S., Sasmal, T. K., & Mondal, S. 2020, ApJS, 251, 9
Bera, S., Sasmal, T. K., Patra, D., & Mondal, S. 2022, ApJS, 260, 7
Blanton, E. L., Gregg, M. D., Helfand, D. J., Becker, R. H., & Leighly, K. M. 2001, AJ, 121, 2915
Blanton, E. L., Gregg, M. D., Helfand, D. J., Becker, R. H., & White, R. L. 2000, ApJ, 531, 118
Brocksopp, C., Kaiser, C. R., Schoenmakers, A. P., & de Bruyn, A. G. 2011, MNRAS, 410, 484
Burke-Spolaor S., Bailes M., Ekers, R., Macquart J. P., & Crawford, F. III 2011, ApJ, 727, 18
Burns, J. O. 1990, AJ, 99, 14
Capetti A., Brienza M., & Baldi, R. D. 2020, A&A, 642, A107
Cegłowski M., Gawroński M. P. & Kunert-Bajraszewska, M. 2013, A&A, 557, A75
Cegłowski M., Gawroński M. P. & Kunert-Bajraszewska, M. 2015, proceedings of science, 12th European VLBI Network Symposium and Users Meeting, 7-10 October 2014, Cagliari, Italy
Cheung, C. C. 2007, AJ, 133, 2097
Croston, J. H., Hardcastle, M. J., Mingo, B., et al. 2019, A&A, 622, A10
Dabhade, P., Gaikwad, M., Bagchi, J., Pandey-Pommier, M., Sankhyayan, S., & Raychaudhury, S. 2017, MNRAS, 469, 2886
Dabhade, P., Mahato, M., Bagchi, J., et al. 2020, A&A, 42, A153
Dabhade, P., Röttgering, H. J. A, Bagchi, J., et al. 2020, A&A 635, A5
David Biello (2006-02-16), "New Kind of Star Found", Scientific American, Archived from the original on 2007-11-19, Retrieved 2010-06-23
de Gasperin, F. 2017, MNRAS, 467, 2234
Dehghan, S., Johnston-Hollitt, M., Franzen, T. M. O., Norris, R. P., & Miller, N. A. 2014, AJ, 148, 75
Eilik, J. A., Burns, J. O., O'Dea, C. P., & Owen, F. N. 1984, ApJ, 278, 37

Eilek, J. A., & Owen, F. N. 2002, ApJ, 567, 202
Fanaroff, B. L., & Riley, J. M. 1974, MNRAS, 167, 31
Franceschini, A., Vercellone, S., & Fabian, A. C. 1998, MNRAS, 297, 817
Gawroński, M. P., Marecki, A., Kunert-Bajraszewska, M., & Kus, A. J. 2006, A&A, 447, 63
Gopal-Krishna & Wiita, P.J. 2000, A&A, 363, 507
Gull, S. F., & Northover, K. J. E. 1973, Natur, 244, 80
Haardt, F., & Maraschi, L. 1991, ApJ, 380, L51
Hardcastle, M. J., Sakelliou, I., & Worrall, D. M. 2005, MNRAS, 359, 1007
Ishwara-Chandra, C.H. & Saikia, D.J. 1999, MNRAS, 309, 100
Joshi, S. A., Nandi, S., Saikia, D. J., Ishwara-Chandra, C. H., & Konar, C. 2011, MNRAS, 414, 1397
Kapińska, A. D., Terentev, I., Wong, O. I., et al. 2017, AJ, 154, 16
Konar, C., & Hardcastle, M. J. 2013, MNRAS, 436, 1595
Kuźmicz, A., Jamrozy, M., Kozieł-Wierzbowska, D., & Wezgowiec, M. 2017, MNRAS, 471, 3806
Krolik, J.H., 1999, Active Galactic Nuclei. Princeton University Press, Princeton, New Jersey
Laing, R. A., Riley, J. M., & Longair, M. S. 1983, MNRAS, 204, 151
Leahy, J. P., Bridle, A . H., & Strom, R. G. 1999, An Atlas of DRAGNs, 3CRR Atlas: Home Page, http://www.jb.man.ac.uk/atlas/
Leahy, J. P., & Parma, P. 1992, in Extragalactic Radio Sources: From Beams to Jets, ed. J. Roland, H. Sol, & G. Pelletier (Cambridge: Cambridge Univ. Press), 307
Machalski, J., Kozieł-Wierzbowska, D., Jamrozy, M., & Saikia, D. J. 2008, ApJ, 679, 149
Mack, K.-H., Klein, U., O'Dea, C. P., Willis, A. G., & Saripalli, L. 1998, A&A, 329, 431
Malarecki, J. M., Jones, D. H., Saripalli, L., Staveley-Smith, L., & Subrahmanyan, R. 2015, MNRAS, 449, 955
Mahatma, V. H., Hardcastle, M. J., Williams, W. L., et al. 2019, A&A, 622, A13
Mao, M. Y., Johnston-Hollitt, M., Stevens, J. B., & Wotherspoon, S. J. 2009, MNRAS, 392, 1070
Miller, B. P., & Brandt, W. N. 2009, ApJ, 695, 755
Mingo, B., Croston, J. H., Hardcastle, M. J., et al. 2019, MNRAS, 488, 2701
Missaglia, V., Massaro, F., Capetti, A., et al. 2019, A&A, 626, A8
Morganti, R., Killeen, N. E. B., & Tadhunter, C. N. 1993, MNRAS, 263, 1023

Nagar, N. M., Falcke, H., & Wilson, A. S. 2005, A&A, 435, 521
Nandi, S., & Saikia, D. J. 2012, BASI, 40, 121
Nandi, S., Jamrozy, M., Roy, R., Larsson, J., Saikia, D. J., Baes, M., & Singh, M. 2017, MNRAS, 467, L56
Norris, R. P., Collier, J. D., Crocker, R. M., et al. 2022, MNRAS, 513, 1300
Norris, R. P., Intema, H. T., Kapińska, A. D., et al. 2021, pasa, 38, e003
O'Dea, C. P. 1985, ApJ, 295, 80
O'Dea, C. P., & Owen, F. N. 1986, ApJ, 301, 841
O'Donoghue, A. A., Eilek, J. A., & Owen, F. N. 1993, ApJ, 408, 428
O'Donoghue, A. A., Owen, F. N., & Eilek, J. A. 1990, ApJS, 72, 75
Orrú, E., van Velzen, S., Pizzo, R. F., et al. 2015, A&A, 584, A112
Owen, F. N., & Laing, R. A. 1989, MNRAS, 238, 357
Owen, F. N., & Rudnick, L. 1976, ApJL, 205, L1
Paterno-Mahler, R., Blanton, E. L., Brodwin, M., et al. 2017, ApJ, 844, 78
Patra, D., Pal, S., Konar, C., & Chakrabarti, S. K. 2019, Ap&SS, 364, 72
Prestage, R. M., & Peacock, J. A. 1988, MNRAS, 131, 230 Priya, A., Nandi, S., Saikia, D. J., & Singh, M. 2011, Bull. Astron. Soc. India, 39, 547
Proctor, D. D. 2011, ApJS, 194, 31
Roettiger, K., Burns, J. O., & Loken, C. 1996, ApJ, 473, 651
Röttgering, H. J. A., Wieringa, M. H., Hunstead, R. W., & Ekers, R. D. 1997, MNRAS, 290, 577
Rudnick, L., & Owen, F. N. 1976, AJ, 203, 107
Ryle, M., & Windram, M. D. 1968, MNRAS, 138, 1
Saikia, D. J., Jamrozy, M., Konar, C., & Nandi, S. 2010, Proceedings of Science, 25th Texas Symposium on Relativistic Astrophysics - TEXAS 2010, December 06-10, 2010 Heidelberg, Germany
Saikia, D.J., Konar, C., & Kulkarni, V.K. 2006, MNRAS, 366, 1391
Safouris, V., Subrahmanyan, R., Bicknell, G. V., & Saripalli, L. 2009, MNRAS, 393, 2
Sakelliou, I., Merrifield, M. R., & McHardy, I. M. 1996, MNRAS, 283, 673
Saripalli, L., & Malarecki, J. M. 2015, The Many Facets of Extragalactic Radio Surveys: Towards New Scientific Challenges, 44
Saripalli, L., Subrahmanyan, R., & Udaya Shankar, N. 2003, ApJ, 590, 181
Sasmal, T. K., Bera, S., Pal, S., & Mondal, S. 2020, Journal of Physics: Conference Series, 1579, 012021
Sasmal, T. K., Bera, S., Pal, S., & Mondal, S. 2022, ApJS, 259, 31
Schoenmakers, A.P., de Bruyn, A. G., Röttgering, H. J. A, van der Laan, H., &

Kaiser, C. R. 2000, MNRAS, 315, 371
Smolčić, Schinnerer, V. E., Finoguenov, A., et al. 2007, ApJS, 172, 295
Srivastava, S., & Singal, A. K. 2020, MNRAS, 493, 3811
Subrahmanyan, R., Saripalli, L., & Hunstead, R.W. 1996, MNRAS, 279, 257
Urry, C.M., & Padovani, P. 1995, PASP, 107, 803
Vallee, J. P. 1981, ApL, 22, 193
van Weeren, R. J., Brüggen, M., Röttgering, H. J. A.,& Hoeft, M. 2011, JApA, 32, 505
Vos, K. de., Hatch, N. A., Merrifield, M. R., & Mingo, B. 2021, MNRAS Letter, 506, L55
Wiita, P. J., Rosen, A., Gopal-Krishna, & Saripalli, L. 1989, Hot Spots in Extragalactic Radio Sources, 327, 173
Williams, W. L., Hardcastle, M. J., Best, P. N., et al. 2019, A&A, 622, A2
Willis, A. G., Strom, R. G., & Wilson, A. S. 1974, Nature, 250, 625
Yang, X., Joshi, R., Gopal-Krishna, et al. 2019, ApJS, 245, 17

Chapter 2

'Winged' Radio Source

There are more things in heaven and earth,
Horatio, Than are dreamt of in your philosophy.

— Hamlet, Act I, scene v

A small number of radio sources exhibit a peculiar radio morphology, where a pair of low-surface-brightness secondary lobes are seen to be placed at a certain angle to the high-surface-brightness primary jets. The pair of secondary lobes are known as 'wings' and this subclass of exotic sources is known as Winged Radio Galaxy (WRG) (Leahy & Parma 1992; Cheung 2007; Bera et al. 2022). The characteristic wing-lobe structure shows that the wings or secondary lobes may extend up to several hundreds of kpc (Cotton et al. 2020).

2.1 Classification

The overall morphology of a radio source depends on the relative jet-lobe structure and their orientation and propagation through the intergalactic medium (IGM). For winged radio sources, the morphology depends on the primary lobes as well as the secondary lobes or wings. Depending on the point of ejection of secondary lobes from the primary lobes, the winged sources are classified into two classes; 'X'-shaped radio galaxy and 'Z'-shaped radio galaxy.

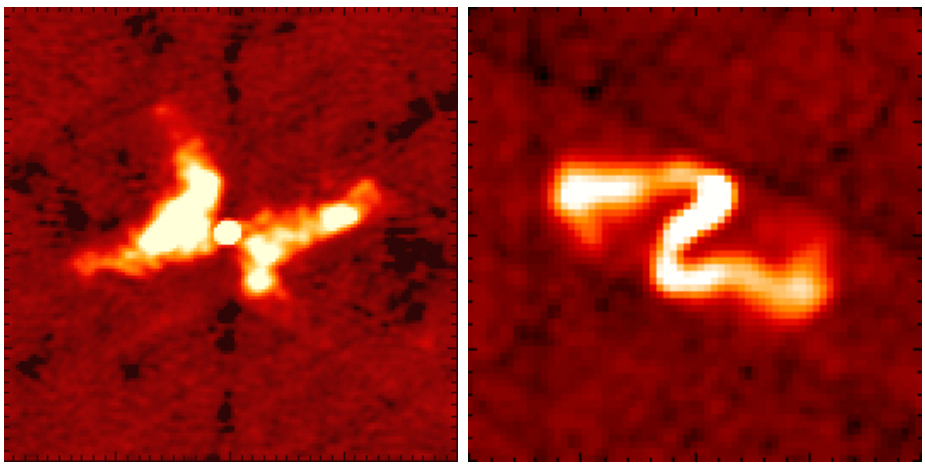

Figure 2.1: Radio images of WRG sources are presented here. The left panel (a) shows the radio image of an XRG 3C 315 (Leahy, Pooley & Riley (1986)) taken from VLA FIRST at 1.4 GHz. The right panel (b) shows the radio map of a ZRG J0902+5203 (Bera et al. 2020) in 1.4 GHz from VLA FIRST.

2.1.1 'X'-shaped Radio Galaxy

The radio maps of WRGs reveal that the secondary lobes sometimes come from the center or central region and in some other cases they are being ejected from the edges of the primary jets. Now, if the point of ejection for the secondary lobes is either the center or the near central region, the radio morphology of the radio source shows an overall 'X'-shape structure. These types of winged candidates are called 'X'-shaped Radio Galaxy (XRG) (Leahy & Parma 1992; Cheung 2007; Bera et al. 2020). Depending on the size of the source, the definition of the 'near central' region may vary in different cases. In this context; Bera et al. (2020) follow a canonical definition of the 'near central' region as the region covered by $\sim 25\%$ of the primary jet length from the central core. A radio image of a sample XRG source, 3C 315 (Leahy, Pooley & Riley 1986) is given in Figure 2.1 (a).

2.1.2 'Z'-shaped Radio Galaxy

In some cases, the secondary lobes are seen to be released from the edges or far from the central region and thus the gross structure of the radio source forms a 'Z'-shape. Radio sources with such morphology are known as 'Z'-shaped Radio Galaxy (ZRG) (Zier 2005; Bera et al. 2020). These ZRGs are also sometimes termed as 'S'-shaped Radio Galaxies. The general idea gives that the radio sources with

wings that come out either from the edges of the primary lobes or from the non-'near central region', are tagged as ZRGs. A typical example of a ZRG source ZRG J0902+5203 (Bera et al. 2020) is given in Figure 2.1 (b). The radio image shows that the secondary wings come out from the edges and the whole source morphology discloses a 'Z'-shape.

2.2 Previous Work

The first identified winged radio galaxy is 3C 272.1, which was reported by Riley (1972). It is found that the radio sources show a Z-shaped morphology. NGC 326 is identified as a prototype of an X-shape source and later revealed as a Z-like structure with probable precessing beams (Ekers et al. 1978). Recently, the X-shaped morphology was argued by Hardcastle et al. (2019). Kotanyi (1990) recognized the "S"-shaped morphology for the elliptical galaxy NGC 3309 (Dreyer 1888). A catalog of winged sources was first presented by Leahy & Parma (1992). Before Cheung (2007), a total of fourteen good examples of X-shaped sources are already been identified by Rottmann (2001), Capetti et al. (2002), and Merritt & Ekers (2002). The X-shaped characteristic of the radio source 4C +04.40 was also identified by Junor et al. (2000). Following that, Wang et al. (2003) identified 4C +01.30 as the first X-shaped source with a quasar nucleus. These types of radio galaxies have the main axis oriented near to our line of sight with broad emission lines in its spectrum. After that, one other quasar has been recognized as an X-shaped radio source (Landt et al. 2006). After such discrete identifications, Cheung (2007), for the first time did a systematic study to identify the X-shaped radio sources. Using the high-frequency FIRST (Faint Images of the Radio Sky at Twenty cm) survey (Becker et al. 1995), Cheung (2007) cataloged a total of 100 X-shaped sources. In the Cheung (2007) catalog, they included sources that have short wings, i.e.; wings with a length less than 80% of the primary lobe length. They have used 2003 April 11 survey data. They have applied some search constraints, e.g., select sources only in the high dynamic range ($\sim 40:1$ dynamic range). They also chose fields with image peaks of 5 mJy beam^{-1}. The ratio of the peak to the rms is defined as the dynamic range. A selection cut on the major axis ($> 15''$) was also applied. Finally, they investigate a total of 1648 sources, through a visual inspection. They also made corresponding optical identification and study the properties like flux in different frequencies (in 365 MHz $F_{0.365}$, in 1.4 GHz $F_{1.4}$, in 4.9 GHz $F_{4.9}$), spectral index ($\alpha_{1.4}^{0.365}$, $\alpha_{1.4}^{4.9}$), luminosity, etc. After Chenug (2007);

Proctor (2011) reports an XRG search result, in which he applied an automated morphological categorization technique. They also use the FIRST survey data of the 2003 April release. That release has a total of 811,117 entries. They divided radio sources into certain groups and their search yielded 156 possible X-shaped radio sources. In their automated method, Proctor (2011) used a separation cut of 0.96 arcmins. Out of the 156 possible X-shaped sources 21 had already been reported in Cheung (2007). Proctor (2011) also contains a well-known XRG, 3C 315. Thus the total number of new possible XRG discovered by Proctor (2011) stands as 134. Later, Yang et al. (2019) mentioned that 43 of these sources are strong candidates, while the rest of the sources are possible candidates of X-shaped sources. Except for Proctor (2011) and Cheung (2007), there is no large catalog of winged radio sources, at the time when we start our work (by the end of 2018). As the sources, cataloged by Proctor (2011) are neither checked individually nor confirmed through observational data, at that point of time when we start the number of known X-shaped radio sources were quite small (nearly 125). However, in a parallel timeline of our work Yang et al. (2019) also did a search of X-shaped radio sources from the FIRST data and identified 290 such sources. Out of these 25 sources already identified in Proctor (2011). Yang et al. (2019) used the selection criteria as a lower limit of peak flux density 5 mJy beam^{-1} at 1.4 GHz and thus set the minimum dynamic range $\sim 33:1$. They also set radio major and minor axes greater than $10''$ and $5''$. The axes' size was taken as their fitted Gaussian.

Apart from the identifications, various literature is done to study such interesting subclass of radio sources. XRGs account for around $5\% - 10\%$ of radio galaxies in the 3CRR database (Leahy & Williams 1984; Leahy & Parma 1992). Most of the sources are characterized as FR-II and the rest as either FR-I or mixed (Merritt & Ekers 2002). Hardcastle et al. (2019) recently studied the template XRG NGC 326 from the Low-Frequency Array (LOFAR) data at 144 MHz (Shimwell et al. 2017). They showed the wings are extended on large scale and the radio structure is complex. They also argued about its 'X' characteristics. They suggest that the complex structure may be due to the impacts of hydrodynamics in an ongoing group or any kind of cluster merger. After the identification of 100 sources, Cheung et al. (2009), present the optical spectroscopic observation results of the XGRs. Using the Hobby-Eberly Telescope and Multiple-Mirror Telescope they redshifts measured redshift for 27 sources, out of which 21 were new. They also placed the sources in the Owen-Ledlow diagram (Owen 1993; Ledlow & Owen 1997). The Owen-Ledlow diagram is the map of radio luminosity versus the absolute magnitude of the host galaxy. Hota et al. (2014) observed the

episodic nature of two X-shaped and one S-shaped radio galaxy. The study was done using the TIFR GMRT Sky Survey (TGSS; Intema et al. 2017) through the RAD@home project. The possible episodic nature is found for the episodic radio galaxies (ERGs): RAD-3 (08 47 23.9, –27 16 42: X-shaped Source), RAD-5 (10 46 32.4, –01 13 37: X-shaped source), and RAD-7 (11 30 41.0, –03 48 07: Z-shaped sources). Note that, the coordinates are given in the J2000.0 coordinate system.

2.3 Proposed Origins of Winged Radio Sources

From the inception of winged radio sources, we are curious about the origin of such peculiar class of sources; in particular the mechanism of the formation of the wings. There are some proposed models which explain the formation of such an exotic class of radio sources. However, they are yet to be established (Lal & Rao 2007; Hodges-Kluck et al. 2010a,b; Gopal-Krishna et al. 2012; Hardcastle et al. 2019; Cotton et al. 2020). In the following sections, we will discuss those proposed models.

2.3.1 Backflow of Plasma

The backflow of plasma model was first proposed by Leahy & Williams (1984). They suggested that the backflow is responsible for the creation of wings in the X-shaped radio sources. The backflow event occurs when the jet materials are released by the hotspots and stream back towards the host galaxy. The backflowing material is supposed to be collimated until it interacts with the backflow from the opposite hotspot. The interaction gives the lateral expansion in the form of a fat disk oriented in a perpendicular direction to the primary radio lobes axis.

However, there is a drawback in this model. They mentioned that this mechanism leads to the scenario where the disk would be axis-symmetric when the XRGs show rotational symmetry. There are two mechanisms that may lead to the bending of backflow in the opposite direction: (i) any backflowing material would be deflected preferentially in the direction parallel to the major axis of a spheroidal gas distribution that is misaligned with the radio axis and (ii) the presence of an old cavity in the ISM/IGM may provide a channel into which the backflow is favored to stream. However, in this cavity theory, the radio jet needs to be oriented in that direction. In this scenario, the mechanism is not a pure backflow model, and it requires a realignment theory in support. A schematic diagram for the

symmetry-breaking mechanism governed by Leahy & Williams (1984), is given in Figure 2.2. In the figure, we depict the above two cases, the spheroidal gas distribution case (case (i)) and the presence past cavity case (case (ii)). In the figure, we show how backflow happens and the secondary lobes are formed in both cases.

Now, there is another aspect, the length of the secondary lobes, i.e.; the linear size of the wings. For a large number of sources, the length of the wings is greater than the primary lobes (Bera et al. 2020). So, the question is if the backflow is enough to create such wings in the lifetime of the source. Though we can not observe the speed of the backflow, the sound speed gives a stiff upper limit on that. The subsonic speed of backflow is predicted by some numerical simulation by Norman (1996); Aloy et al. (1999). In addition, there is no observational evidence for the supersonic flow due to strong shock. Considering the flow speed nearly to the magnetosonic sound speed wings of a few hundred kiloparsecs need a flow-time in the order of 10^7 years for the matter to flow from the core to the edges of the secondary lobes. This is somewhat less than the lifetime of a radio source ($\sim 10^8$ years). However, this is an optimistic estimation as the consideration of the projection effect may increase the lobe size and hence backflow may reach the required speed. In the cavity scenario, the flow will be lower than the magnetosonic sound speed. Also, when the flow penetrates the surrounding medium, the rate will decrease. Thus the required time for the wings is $\sim 10^8$ years. These are the drawbacks that halt the idea of the backflow of plasma being a promising mechanism for XRGs.

Therefore, we see that the backflow is caused by jet material that is released by hotspots and then flows back toward the host galaxy. In an alternative way, the genesis of the 'wings' shape could be attributed to the lateral expansion of the surrounding medium along the minor axis (Capetti et al. 2002). Optical observations of the host galaxies of these winged sources provide a piece of observational evidence for the backflow scenario (Capetti et al. 2002; Saripalli & Subrahmanyan 2009; Gillone et al. 2016). According to these findings, the radio axis generated by the two principal lobes tends to align with the elliptical host galaxy's major axis. The pair of wings, on the other hand, exhibit a strong inclination to align along the minor axis of the host galaxy, which is consistent with the notion that the buoyancy force (discussed in Section 2.3.5) is responsible for expanding the wings along the largest pressure gradient. Capetti et al. (2002) show that the expansion would currently be driven by buoyancy and bulk flows. As described above, this expansion would be subsonic. The result of Capetti et al. (2002) was supported

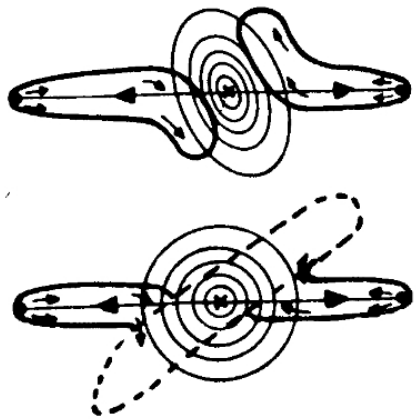

Figure 2.2: The figures show a representation of the Backflow model by Leahy & Williams (1984). The upper panel depicts the spheroidal gas distribution scenario (case (i)). The lower panel presents the presence of a past cavity scenario (case (ii)) (Courtesy: Rottmann (2001)).

by Gillone et al. (2016) through a larger sample. The hydrodynamic simulations for the creation of wings in X-shaped radio galaxies have also been performed to test the validity of this backflow model (Hodges-Kluck & Reynolds 2011). Hodges-Kluck & Reynolds (2011) showed in their simulation that the wings are significantly formed by the deflection of backflowing plasma from hotspots. They further contended that lobe interaction with the heated atmosphere could have a significant impact on the morphology of these radio galaxies. Such observational evidence was also done by Saripalli & Subrahmanyan (2009), later also confirmed by Rossi et al. (2017) through a detailed three-dimensional relativistic magnetohydrodynamic (MHD) simulation. Recently, Cotton et al. (2020) published MeerKAT 1.28 GHz observations of the X-shaped radio source PKS 2014-55 to validate the hydrodynamical backflow concept. They argued that the X-shaped morphology is created by hydrodynamical backflows from the straight motion of the jets that get deflected by the host galaxy PGC 064440's massive and oblique hot-gas halo.

2.3.2 Black Hole Merger

One of the widely discussed and popular models to explain the wings is the change of jet axis at some point in the source's lifetime. The popularity of such a model is due to the fact that the radio jets happened to be ejected along the spin axis

of the massive black hole (MBH), placed at the center. So, a mechanism that incorporates the realignment event or the theory that can explain the axis change phenomena due to the change in spin angular momentum of the central black hole, will be able to explain the origin of such sources. In this mechanism, we consider the radio emission from the low-brightness secondary lobes as the relic emission of the past active lobes in that direction. The jet direction subsequently changed quickly, probably with a sudden "flip", resulting in this currently fed active primary lobe pair. However, this model must stick to the fact that the change of axis must happen in a timescale less than the source lifetime.

The black hole merger is one such model where a radio source goes through a change in spin axis. This process involves the coalescence of two jetted SMBH (Rottmann 2001; Zier & Biermann 2001; Merritt & Ekers 2002; Dennett-Thorpe et al. 2002; Gopal-Krishna & Witta 2003). This mechanism has a special interest as the merger of two SMBH results in the creation of gravitational wave background (GWB) (discussed later in Chapter 6). Through the merger process, a second comparatively small SMBH is supposed to be deposited near the center of the primary galaxy source. Thus the two black holes create a binary system and the emission of gravitational waves occurs. During the coalescence process, the larger black hole absorbs the orbital angular momentum of the smaller black hole. This absorption results in an abrupt re-orientation of the spin axis of the larger black hole or the primary galaxy system. Gopal-Krishna & Witta (2003) proposed that the change of spin axis is the reason for the Z-symmetry of winged sources. They mentioned the Z-distortion is due to the spin-axis change as the jets propagated through the massive elliptical host's ISM. The captured galaxy had already placed the outer component of the ISM in slow rotation (approximately along its original orbital plane) as it spiraled into the radio-loud elliptical, eventually culminating in the coalescence of its BHs (Noel-Storr et al. 2003; Heinz et al. 2008; Gopal-Krishna et al. 2012). As a result, at great distances from the galactic nucleus, the two jets would be redirected in opposite directions by the revolving ISM. The deflected flows can remain for long periods of time and can emerge at great distances from the original galaxy. The study of ZRG source NGC 3801 indicates events of a recent merger and a large rapidly rotating gas disc that interacts with the jets (Hota et al. 2009).

2.3.3 Precession of Jets

Along with the black hole merger, there is another model that can cause the reorientation of the axis, known as the precession of jets. This model is also known as the jet reorientation or spin-flip model. Actually, this "spin-flip" occurs due to the previously discussed merger scheme or due to the precession or reorientation of jets. Precession or other realigning mechanisms are invoked in models proposed for jet reorientation (Ekers et al. 1978; Rees 1978; Klein et al. 1995; Dennett-Thorpe et al. 2002; Falceta-Gonçalves et al. 2010; Hodges-Kluck et al. 2010b). According to one specially detailed model, the central SMBH is realigned with the binary orbital plane during a process that involves a violent interaction between the binary and the accretion disc that twists and warps the disc, fast realigning the spin axis of the SMBH and ejecting the jets (Liu 2004).

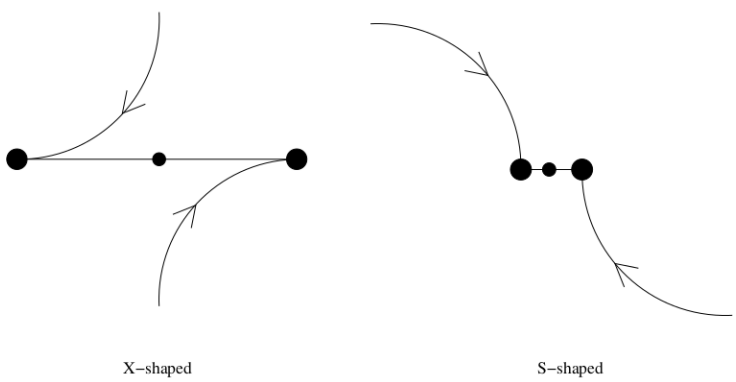

Figure 2.3: The figure gives a schematic diagram for the steady jet precessions as a mechanism for the creation of X-shaped (left panel) and Z-shaped (right panel) sources (Courtesy: Rottmann (2001)).

The precession of jets is initially considered a fundamental outcome of continuous deposition of matter carrying angular momentum. The accreting matter has angular momentum misaligned with the spin angular momentum of the central black hole and thus the matter accretion will obviously realign the spin axis of the black hole. Lense & Thirring (1918) mentioned that a rotating mass (e.g., a Kerr black hole) generates a gravitational field that is not spherically symmetric, resulting in a coupling between the black hole's spin and the angular momentum of an orbiting mass. On the basis of this; the precession event may be given as – when the in-falling matter reaches radii comparable to the radius of the outer accretion

disc, the Lense-Thirring effect causes the precession of the central black hole and consequently the jet axis. Leahy & Williams (1984) mentioned that sources with random precession may appear as X-shaped or Z-shaped (or S-shaped) sources with equal probabilities (See Figure 2.3). On the other hand, for the realignment case – Scheuer & Feiler (1996) provided an analytic computation of the timeframe on which the spin of the black hole will be realigned in the approximation of small angles between the two relevant angular momentum vectors. For the realignment event – depending on the configuration of the central engine (mass and accretion rate), the black hole will realign within 10^6 to 10^7 years (Rottmann 2001). Rottmann (2001) gives a model of the evolution of jet reorientation events. The observed age at the tips of the lobes (t_{tip}) at the start of the reorientation process is equal to 0. The jet then swings and is eventually realigned in a new path. The age at the tip of the secondary lobe is then equivalent to the time scale of reorientation. The active lobes will propagate into the ISM/IGM and become longer, whereas the secondary lobes will fade away and get shorter. The observed t_{tip} will be slightly longer than the reorientation time scale during this step. This evolution event is given in Figure 2.4.

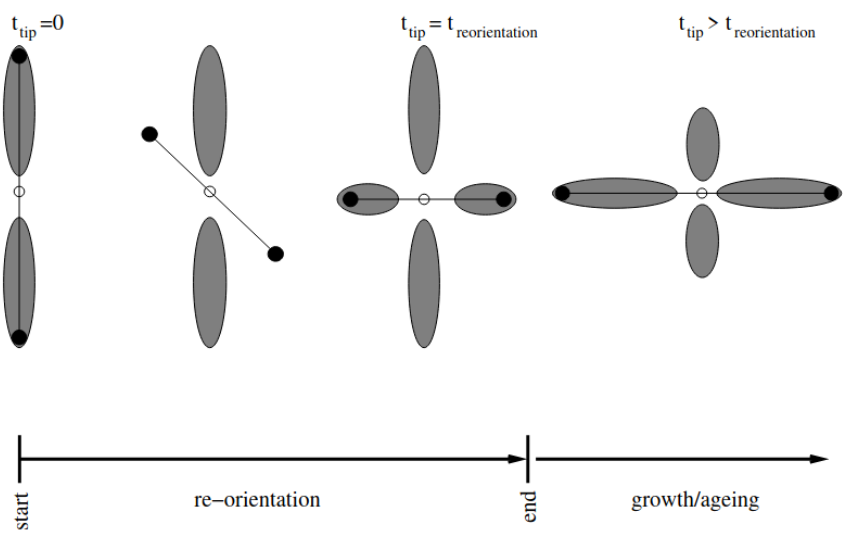

Figure 2.4: This is a schematic diagram that shows the evolution of the jet reorientation event. Here, the open circle is the radio core, the filled circle is the current hotspot, the solid line is the ejected jets, and the shaded region is the secondary lobes (Courtesy: Rottmann (2001)).

The evidence for substantial spin-flips comes from radio galaxies that appear to have restarted and have significantly mismatched inner and outer structures. The source J1448+63, for example, has a nearly 90° misalignment between its pc and kpc structures (Giovannini et al. 2005), although such disparities can be accentuated if the jet is relativistic and close to the line-of-sight. Other sources have less severe misalignments, but on far larger sizes and are thus unlikely to be impacted by such projection effects. This may be observed in the cases of sources like J0116–473 (Saripalli et al. 2002), J1453+3309 (Konar et al. 2006), and 3C 293 (Evans et al. 1999). According to Dennett-Thorpe et al. (2002), the required rapid change in the jet axis within several Myr is caused by either a delayed SMBH merger following the ingestion of a small galaxy by the radio galaxy, which left no obvious signature in the latter's stellar population or the axis flip may have occurred due to accretion disc instabilities (e.g. Natarajan & Pringle 1998).

2.3.4 Twin AGNs

The presence of an unresolved pair of AGNs in the center of the host galaxy could explain the formation of such a pair of lobes (Lal & Rao 2005). The two sets of jets are thought to be ejected in opposite directions from two unresolved AGNs. Zhang et al. (2007) identified double-peaked emission lines in the optical spectra for a few XRGs, which gives support to the twin-AGN hypothesis. Lal et al. (2019) examined spectral index maps from 26 X-shaped sources and discovered no consistent changes in spectral features across active lobes and wings. For a substantial number of sources, they reported similar spectral indices for the wings and active lobes, as well as steeper spectra in the primary lobes than in the wings. They argued that because the entire class of objects is formed by a single mechanism, it is difficult to uncover evidence for other formation models than the alternative twin-AGN model, in which the X-shaped sources consist of two pairs of jets caused by two unresolved AGNs. This model appears especially appealing when the dynamical friction is minimal, causing the two SMBHs to delay their approach. However, such stalling is not typical (Zier 2007; Gergely & Biermann 2009), as evidenced by numerous VLBI imaging studies (Burke-Spolaor 2011). Furthermore, because both central engines must be launching jets at the same time, this scenario is extremely unlikely.

This twin AGN model has the virtue of being conceptually simple, however, it fails to explain why none of the XRGs had both FR II lobe pairs. In addition, it also does not explain why the primary lobe prefers to be oriented toward the

optical host galaxy's major axis (Capetti et al. 2002; Saripalli & Subrahmanyan 2009; Hodges-Kluck et al. 2010a). Furthermore, understanding the frequently observed Z-symmetric shape of the secondary lobes is particularly difficult in this image (Gopal-Krishna et al. 2003). On the basis of these points, it is obvious that, while this twin AGN model may account for a small number of XRGs, it can not explain a vast majority of XRGs.

2.3.5 Buoyancy

Numerical simulation of Cygnus A shows that the ratio of density between the lobe and the surrounding medium is in the order of 10^4 (Williams 1991). The radio map shows that the radio lobes have a lower density than the ambient medium. So, buoyancy may have an impact on radio morphology. The buoyancy effect may bend the lobes towards the areas in the ISM/IGM which provides the density equilibrium between the lobe and its environment. The buoyancy model was first introduced by Gull & Northover (1973). Later it was explained by Cowie & McKee (1975). The buoyancy model presented the radio lobes as a non-relativistic, hydrodynamic flow that follow Euler's equation. The model was applied to the source NGC 326 (Worrall et al. 1995). Now, in this model, the density ratio largely depends on the adopted parameters related to the backflow velocity (see Section 2.3.1). For a rough estimation, if the velocity is less than $600 kms^{-1}$ the density ratio will be equal to unity. This will diminish the buoyancy effect. As we discussed earlier (see Section 2.3.1), the flow rate may have a considerable value ($\sim$ fraction of light) but as it penetrates through the ISM/IGN, there is a certain deacceleration. Observational studies are unable to detect the significant cluster gas emission. The buoyancy model also failed to explain the rotational symmetry of the X-shaped source. The buoyant bending occurs along the path of maximum pressure gradients within the cluster gas. Now, there is no reason why these gradients will be symmetric with respect to the source. However, for some sources, the secondary lobes show wider areas in the tips compared to the core. This is an expected result of an expanding buoyant bubble (Rottmann 2001). The adiabatic expansion would also cause the synchrotron spectrum to move towards lower frequencies (Carilli et al. 1991), and its fingerprint should be detectable during spectral analysis. Thus there are some issues with this model to explain X-shaped sources, however, this model is important for X-shaped radio sources (Saripalli & Subrahmanyan 2009; Hodges-Kluck & Reynolds 2011, 2012) like NGC 326. The Chandra study of NGC 326 reveals that a time scale of 40 to 70 Myr will be

needed to produce such morphology for buoyancy, depending on the distance from the core (Hodges-Kluck & Reynolds 2012). The buoyancy force will impact the large-scale structure of radio galaxies only in dense cluster environments like WAT radio sources (Burns & Balonek 1982; Sakelliou et al. 1996). The reproduction of the X-shaped morphologies only by buoyancy forces will require an improbable arrangement of the ISM/IGM (Rottmann 2001).

2.3.6 Jet-Shell Interaction

The jet-shell interaction model is based on the interaction between the jets and stellar shells (Gopal-Krishna et al. 2003). Those are found in around 10% of neighboring early-type galaxies in low-density environments (Malin & Carter 1983; Pierfederici & Rampazzo 2004; Sikkema et al. 2007). The shells are also found to be fairly gas-rich. In the kiloparsec scale, a good example of jet–shell interactions have been observed in the nearest radio galaxy, Centaurus A. It was also proposed that the S-shaped symmetry of the pattern of radio peaks around the galaxy indicates a general clockwise rotation of the shell complex. For XRGs, a similar scenario involving rotating shells is postulated, which can explain the observed oppositely oriented geometry of the wings (Gopal-Krishna & Saripalli 1984; Gopal-Krishna & Wiita 2010). The direct observation of jet-shell interactions provides important clues to understanding the XRG phenomenon (Gopal-Krishna et al. 2012). Shells were also observed in the XRGs 3C 403 and 4C +00.58 (Ramos Almeida et al. 2011; Hodges-Kluck et al. 2010b). Unfortunately, because powerful radio galaxies are uncommon in the local universe, all XRGs are so far away that the great majority of shells they may possess are undetectable with existing technology. However, given the frequency with which they have been detected in nearby elliptical galaxies that host radio galaxies (Sikkema et al. 2007), it is most reasonable to investigate the hypothesis that they are present in many such host galaxies and that accordingly oriented jets will interact with them as a matter of course.

So in this new model, if a post-merger radio galaxy (RG) has a jet orientation independent of the optical axis, as seems to be the case for powerful sources (Battye & Browne 2009), then only the random fraction of jets launched along the major axes are likely to encounter shells and thereby possibly form XRGs through this mechanism. The majority of jets would not end up being intercepted by the shells and would hence evolve as normal RGs, as is of course observed since XRGs are a small fraction of all RGs. If the preference for jets to roughly align with the

optical minor axis, as seen in weaker RGs, is at all relevant for XRGs, whose powers tend to be near the borderline between the FR-I and FR-II sources, then this preference for the minor axis would imply that the fraction of sources actually aimed toward the major axes would be less than expected from purely random jet or galaxy orientations. Still, we can speculate about a mechanism that would produce an observed correlation between the jet direction and the galaxy's optical major axis, at least as seen in projection. If the incoming, smaller galaxy has no central SMBH, as appears to be the case with M33 and other dwarf galaxies (e.g. Ferrarese et al. 2006), then during the merger, the spin of the SMBH in the primary galaxy would not be altered, nor would the jet direction be reoriented. Nonetheless, if one averages over all possible directions, the random direction of a jet is expected to be within 30° of any plane. Of course, as we can only see the entire configuration of the merged galaxies in projection, it would therefore not be surprising if the jet hits a shell.

The essence of the model is, that the jets form when a disc galaxy merges with the radio galaxy's elliptical host, resulting in a succession of shells. When the jets are disrupted by the shells, the wings appear. This concept helps explain why the wings are sometimes larger than the primary lobes, as well as the Z-shaped morphology (Gopal-Krishna et al. 2012).

Several literature offered ideas from the theoretical domain to comprehend the process behind the X-shaped structure. Multifrequency observations of two X-shaped sources 3C 223.1 and 3C 403 are done by Dennett-Thorpe et al. (2002). Based on the absence of synchrotron and inverse Compton losses, they calculated maximum ages since any re-injection of new particles of 34 and 17 Myr for the wings of 3C 223.1 and 3C 403, respectively. On morphological grounds, they support a hypothesis involving a rapid realignment of the jet axis that happened within a few Myr. There is no sign of merger activity, and the host galaxies are discovered to abide in no more than a poor cluster environment (Dennett-Thorpe et al. 2002). However, the origin of realignment and the phenomena of how the realignment happens in a short time period the time is also not clear. Later, the low-frequency study of the source 3C 223.1 was done by Lal & Rao (2005, 2007). Using the Giant Metrewave Radio Telescope (GMRT) low-frequency data at 240 and 610 MHz, they show that the secondary lobes have relatively flat spectral indices compared to the primary lobes. This result supports the previous high-frequency result of Dennett-Thorpe et al. (2002). Rossi et al. (2017)

recently performed three-dimensional relativistic magnetohydrodynamic (MHD) simulations to better understand how the X-shaped morphology forms. They demonstrated that an X-shaped morphology may be produced by a jet with a radio power of less than $10^{44} ergs^{-1}$. They also contended that a 30° misalignment of the jet axis and the primary axis of the density distribution is advantageous for the creation of such morphology. Garofalo et al. (2020) have suggested a unifying framework for XRGs. They proposed that XRGs are transition objects between cold mass-accreting retrograde and prograde black holes, and so have low spin. The spectral maps and intensity maps are studied for 28 X-shaped sources by Lal et al. (2019). They investigated the extended samples in GMRT at frequencies 610 and 240 MHz. Through their investigation, they showed that there was no systematic difference between the spectral maps of the primary lobes to the secondary lobes. Major studies on the properties of winged sources are also done by Saripalli et al. (2007), Saripalli & Subrahmanyan (2009), Roberts et al. (2018), and Saripalli & Roberts (2018). Multi-frequency investigation for a sample of 100 radio sources is done by Roberts et al. (2018) using the VLA data. In their subsequent paper, Saripalli & Roberts (2018) looked at the mechanism of such off-axis emission for the XRGs. Joshi et al. (2019) explored the parent galaxies of a large sample of 106 XRGs and evaluated the alignment of optical and radio axes, the interstellar medium, black hole mass, and large environment to uncover clues to the formation of XRGs. According to their findings, the development of XRGs appears to be difficult to reconcile with a single dominant physical explanation, and conflicting processes appear to be present.

2.4 Significance

The winged radio source is a marvel of the cosmos. The experts are still engaged to find the origin and underlying mechanism behind such exotic morphology of winged sources. The main reason for the elusive origin is the lack of study on the winged sources. The low number of study is primarily due to the low sample size. The inadequate source number also prevent a proper statistical study for the global characteristics and physical properties of such exotic class. There also no proper pilot study through multifrequency observations.

(i) The most perplexing aspect of WRG is the apparent scarcity of such sources. Although millions of radio galaxies are known to exist, only around 125 visually confirmed winged sources were identified. This proportion number has enough to

say about the rareness of such sources in literature (or maybe in the universe). The possible reason for the low number of WRGs may be due to the facts-
— The WRG sources by themselves are very rare in nature and they are formed due to some exceptional phenomena or circumstances.
— The WRGs are normal galaxies; but in either a short-lived or rare phase or both; of their evolution stage.
— The WRGs are not-identified due to either the projection effect or selection effection.
Before starting our work there are only 125 known WRG sources. The identified WRG sources are mostly discrete identification except for the first large sample of 100 sources by Cheung (2007) from VLA FIRST at 1.4 GHz. There are no findings in the low-frequency range.
(ii) There is also a lack of statistical study of its property. This is mainly due to the inadequate number of sources.
(iii) Along with this, a proper multiwavelength study for a large sample of such sources, is also missing in the literature.

So, considering the issues in chronological order the increase in the sample number of winged sources is our first priority. The increase of such sources must come from both the high-frequency and low-frequency regions. So, we need to ensure at least two sky survey data, one in high frequency and the other in low frequency that are capable of dealing with fine morphological details of a radio source. As winged radio sources deal with diffused emission, primarily for the secondary lobes we need a radio survey that has enough resolution to resolved the fine detail along with the diffuse radio emission. For high frequency, we choose VLA FIRST at 1.4 GHz (presented in Chapter 3) and low-frequency LOFAR at 144 MHz (presented in Chapter 4). Once we are able, to sum up, a certain number of such sources, we will go to the next step the study of such sources. The study includes the statistical study of the physical properties and morphological parameters of such sources. The studies will give an overall idea about the general characteristic of a winged source as a population (presented in Chapter 5). The very next step will be the multiwavelength study of the sources to study their features. This may help to give an insight into the mechanism of such peculiar morphology. The available identified source data may also be fitted to check the proposed origins if any of those are capable of explaining the wings. There is another aspect that the coalescence of supermassive black hole merger is potentially the dominant contributor to the low-frequency gravitational wave background (GWB) (Roberts et al. 2015) (see Chapter 6). Now, the black hole merger is also a widely discussed

model for the origin of X-shaped radio sources (see Section 2.2.2). So, the winged sources may be used as a tracer to probe the low-frequency gravitational wave and vice-versa.

References

Aloy, M. A., Ibáñez, J. M., Matrí, J. M., Gómez, J., & Müller, E. 1999, ApJL, 523, L125
Battye, R. A., & Browne, I. W. A. 2009, MNRAS, 399, 1888
Becker, R. H., White, R. L., & Helfand, D. J. 1995, ApJ, 450, 559
Bera, S., Pal, S., Sasmal, T. K., & Mondal, S. 2020, ApJS, 251, 9
Bera, S., Sasmal, T. K., Patra, D., & Mondal, S. 2022, ApJS, 260, 7
Burke-Spolaor, S. 2011, MNRAS, 410, 2113
Burns, J. O., & Balonek, T. J. 1982, ApJ, 263, 546
Capetti, A., Zamfir, S., Rossi, P., et al. 2002, A&A, 394, 39
Carilli, C. L., Perley, R. A., Dreher, J. W., & Leahy, J. P. 1991, ApJ, 383, 554
Cheung, C. C. 2007, AJ, 133, 2097
Cheung, C. C., Healey, S. E., Landt, H. et al., 2009, ApJS, 181, 548
Cotton, W. D., Thorat, K., Condon, J. J. et al. 2020, MNRAS, 495, 1271
Cowie, L. L., & McKee, C. F. 1975, A&A, 43, 337
Dennett-Thorpe, J., Scheuer, P. A. G., Laing, R. A., et al. 2002, MNRAS, 330, 609
Dreyer, J. L. E. 1888, MmRAS, 49, 1
Ekers, R. D., Fanti, R., Lari, C., & Parma, P. 1978, Nature, 276, 588
Evans, A. S., Sanders, D. B., Surace, J. A., & Mazzarella, J. M. 1999, ApJ, 511, 730
Falceta-Gonçalves, D., Caproni, A., Abraham, Z., Teixeira, D. M., & de Gouveia Dal Pino, E. M. 2010, ApJ, 713, L74
Ferrarese, L., Côté, P., Dalla Bontá, E., et al. 2006, ApJ, 644, L21
Garofalo, D., Joshi, R., Yang, X., et al. 2020, ApJ, 889, 91
Gergely, L. Á., & Biermann, P. L. 2009, ApJ, 697, 1621
Gillone, M., Capetti, A., & Rossi, P. 2016, A&A, 587, A25
Giovannini, G., Taylor, G. B., Feretti, L., et al. 2005, ApJ, 618, 635
Gopal-Krishna, B. P. L., Gergely, L. A., & Wiita, P. J. 2012, RAA, 12, 127
Gopal-Krishna B. P. L., & Saripalli, L. 1984, A&A, 141, 61
Gopal-Krishna, B. P. L., & Wiita, P. J. 2003, ApJL, 594, L103
Gopal-Krishna, & Wiita, P. J. 2010, New Astron., 15, 96
Gopal-Krishna, B. P. L., Gergely, L. A., & Wiita, P. J. 2012, RAA, 12, 127
Gull, S. F., & Northover, K. J. E. 1973, Nature, 244, 80
Hardcastle, M. J., Croston, J. H., & Shimwell, T. W., et al. 2019, MNRAS, 488, 3416

Heinz, S., Brüggen, M., Ruszkowski, M., Young, A., & Levesque, E. 2008, in Astronomical Society of the Pacific Conference Series 386, Extragalactic Jets: Theory and Observation from Radio to Gamma Ray, eds. T. A. Rector, & D. S. De Young (San Francisco: ASP), 327
Hodges-Kluck, E. J., & Reynolds, C. S. 2011, ApJ, 733, 58
Hodges-Kluck, E. J., & Reynolds, C. S. 2012, ApJ, 746, 167
Hodges-Kluck, E. J., Reynolds, C. S., Cheung, C. C., & Miller, M. C. 2010a, ApJ, 710, 1205
Hodges-Kluck, E. J., Reynolds, C. S., Miller, M. C., & Cheung, C. C. 2010b, ApJ, 717, L37
Hota, A., Croston, J. H., Ohyama, Y., et al. 2014, BASI, 00, 1
Hota, A., Lim, J., Ohyama, Y., et al. 2009, in Astronomical Society of the Pacific Conference Series 407, The Low-Frequency Radio Universe, eds. D. J. Saikia, D. A. Green, Y. Gupta, & T. Venturi (San Francisco: ASP), 104 (arXiv: 09124354)
Intema, H. T., Jagannathan, P., Mooley, K. P., & Frail, D. A. 2017, A&A, 598, A78
Joshi, R., Gopal, K., Yang, X., et al. 2019, ApJ, 887, 266
Junor, W., Mantovani, F., Morganti, R., & Padrielli, L. 2000, A&AS, 143, 457
Klein, U., Mack, K. -H., Gregorini, L., & Parma, P. 1995, A&A, 303, 427
Konar, C., Saikia, D. J., Jamrozy, M., & Machalski, J. 2006, MNRAS, 372, 693
Kotanyi, C. 1990, MxAA, 21, 173
Lal, D. V., & Rao, A. P. 2005, MNRAS, 356, 232
Lal, D. V., & Rao, A. P. 2007, MNRAS, 374, 1085
Lal, D. V., Sebastian, B., Cheung, C. C., & Rao, A. P. 2019, AJ, 157, 195
Landt, H., Perlman, E. S., & Padovani, P. 2006, ApJ, 637, 183
Leahy, J. P., & Parma, P. 1992, in Extragalactic Radio Sources: From Beams to Jets, ed. J. Roland, H. Sol, & G. Pelletier (Cambridge: Cambridge Univ. Press), 307
Leahy, J. P., Pooley, G. G., & Riley, J. M. 1986, MNRAS, 222, 753
Leahy, J. P., & Williams, A. G. 1984, MNRAS, 210, 929
Lense J., & Thirring, H. 1918, Phys.Z., 19, 156
Liu, F. K. 2004, MNRAS, 347, 1357
Malin, D. F., & Carter, D. 1983, ApJ, 274, 534
Merritt, D., & Ekers, R. D. 2002, Sci, 297, 1310
Natarajan, P., & Pringle, J. E. 1998, ApJ, 506, L97
Noel-Storr, J., Baum, S. A., Verdoes Kleijn, G., et al. 2003, ApJS, 148, 4
Norman, M. L. 1996, In: Energy transport in radio galaxies and quasars, p. 319,

eds Hardee P.E., Bridle A. H., & Zensus J. A., ASP, San Fransisco
Owen, F. N. 1993, in Jets in Extragalactic Radio Sources, vol. 421, ed. H.-J. Röser & K. Meisenheimer (New York: Springer), 273
Owen, F. N., & Ledlow, M. J. 1997, ApJS, 108, 41
Pierfederici, F., & Rampazzo, R. 2004, Astronomische Nachrichten, 325, 359
Proctor, D. D. 2011, ApJS, 194, 31
Ramos Almeida, C., Tadhunter, C. N., Inskip, K. J., et al. 2011, MNRAS, 410, 1550
Rees, M. J. 1978, Nature, 275, 516
Riley, J. M. 1972, MNRAS, 157, 349
Roberts, D. H., Saripalli, L., & Subrahmanyan, R. 2015, ApJL, 810, L6
Roberts, D. H., Saripalli, L., Wang, K. X., et al. 2018, ApJ, 852, 47
Rossi, P., Bodo, G., Capetti, A., & Massaglia, S. 2017, A&A, 606, A57
Rottmann, H. 2001, PhD thesis, Univ. Bonn
Sakelliou, I., Merrifield, M. R., & McHardy, I. M. 1996, MNRAS, 283, 673
Saripalli, L., Subrahmanyan, R., Laskar, T., & Koekemoer, A. 2007, Proceedings of Science, From planets to dark energy: the modern radio universe, University of Manchester, Manchester, UK, 1-5 October
Saripalli, L., & Roberts, D. H. 2018, ApJ, 852, 48
Saripalli, L., & Subrahmanyan, R. 2009, ApJ, 695, 156
Saripalli, L., Subrahmanyan, R., & Udaya Shankar, N. 2002, ApJ, 565, 256
Scheuer, P. A. G., & Feiler, R. 1996, MNRAS, 282, 291
Shimwell, T. W., Röttgering, H. J. A., Best, P. N., et al. 2017, A&A, 598, A104
Sikkema, G., Carter, D., Peletier, R. F., et al. 2007, A&A, 467, 1011
Wang, T.-G., Zhou, H.-Y., & Dong, X.-B. 2003, AJ, 126, 113
Williams, A. 1991, In: Beams and Jets in Astrophysics, p. 342, ed. Hughes P., Cambridge University Press
Worrall, D. M., Birkinshaw, M., & Cameron, R. A. 1995, ApJ, 449, 93
Yang, X., Joshi, R., Gopal-Krishna, et al. 2019, ApJS, 245, 17
Zhang, X.-G., Dultzin-Hacyan, D., & Wang, T.-G. 2007, MNRAS, 377, 1215
Zier, C. 2005, MNRAS, 364, 583
Zier, C. 2007, MNRAS, 378, 1309
Zier, C., & Biermann, P. L. 2001, A&A, 377, 23

Chapter 3

'Winged' Radio Sources from VLA FIRST Survey

Only two things are infinite,
the universe and human stupidity,
and I'm not sure about the former.

—Albert Einstein

To ensure a large sample size for winged radio sources, first, we initiate the identification process from suitable high-frequency survey data. Here, we choose the VLA FIRST survey data. The FIRST data is the better choice to study the detailed morphology of radio sources. The better resolution and the larger sky coverage make it the perfect resource for the winged sources. Due to its advantages, numerous studies are done to study the faint radio sources through this survey data. To date, the most number of winged sources are found from this survey. The details of VLA FIRST and its advantages are given in the first sections. In the next section, we discuss the search method. Thereafter, our search result and the outcomes of our search are given.

3.1 The VLA FIRST Survey

The Karl G. Jansky Very Large Array (VLA) is a centimeter-wavelength radio astronomy observatory located on the Plains of San Agustin (west of Socorro) in New Mexico. The telescope system is operated and is a part of the National

Figure 3.1: An aerial view of the Very Large Array and its 'Y-shaped' arrangement (Courtesy: NRAO).

Radio Astronomy Observatory (NRAO). The VLA is made up of twenty-eight 25-meter radio telescopes (twenty-seven are operational and one for maintenance purposes) arranged in a 'Y-shaped' array. The whole system functions as a radio interferometer array. The VLA is located at an elevation of 6,970 above sea level. Each of these large telescopes is installed on two parallel railroad tracks. The arrangement allows the array's radius and density to be altered to adjust the balance between the angular resolution and surface brightness sensitivity. Thus it achieves the highest possible resolution capability. The aerial view of the Very Large Array and its wye formation is given in Figure 3.1.

The FIRST, or Faint Images of the Radio Sky at Twenty Centimeters, is an astronomical survey of the Northern Hemisphere (mostly North and part of South Galactic Caps) conducted by the NRAO Very Large Array (Becker et al. 1994). This FIRST survey idea was proposed in 1990 and thereafter the trial observation was started in 1992. Formally, the survey began in the year 1993 in which the North Galactic Pole was observed. During that initial phase, in April to May 1993, a total of 300 square degrees were observed through 144 hours of observation. The initial survey catalog contains 28,000 sources (Becker et al. 1995). The survey observations lasted until 2004. Later, the South Galactic pole observations were also done in 2009 and 2011. After 2011, the improved Expanded Very Large

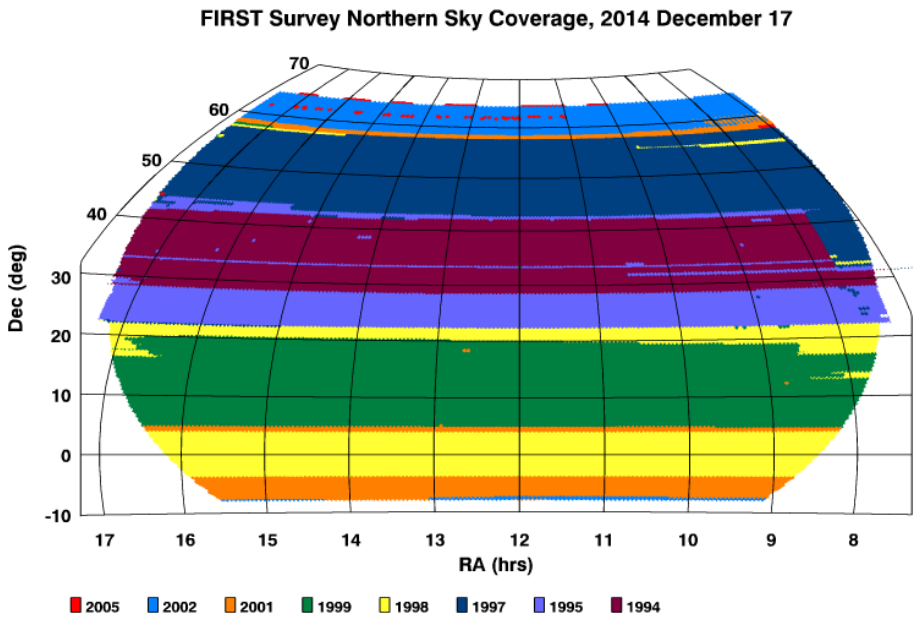

Figure 3.2: This is the sky coverage of Northen sky, for FIRST December 17, 2014 data (Courtesy: NRAO).

Array (EVLA) receiver was introduced, where some minor adjustments to survey processes were introduced. The FIRST survey (White et al. 1996) spans a radio sky of 10,575 square degrees near 1400 MHz (21 cm) in the north and south Galactic caps. The mean rms (σ) of the survey is 0.15 mJy, and the angular resolution is 5″ (Becker et al. 1995). The target flux density limit is 1 milliJansky (mJy) and these maps have 1.8″ pixels (Becker et al. 1995). At the 1 mJy threshold source detection limit, approximately 90 sources are detected per square degree. Out of these $\sim$ 35% have resolved structure in the range of scales from 25″ to 305″. The FIRST survey region includes approximately 25% of the total sky, with approximately 80% in the north Galactic cap (which is 8444 square degrees) and the remaining 20% in the south Galactic cap (2131 square degrees; Becker et al. 1995). The NRAO VLA B configuration is used in the FIRST survey. Until 2011, the FIRST sky was mapped using three-minute pictures covering a hexagonal grid with 2×7 3-MHz frequency channels centred at 1365 and 1435 MHz. After 2011, frequencies of 1335 and 1730 MHz were employed, with a one-minute iteration employing 2×64 2-MHz frequency channels. The raw data is edited, self-calibrated, mapped and CLEANed using an automated pipeline that

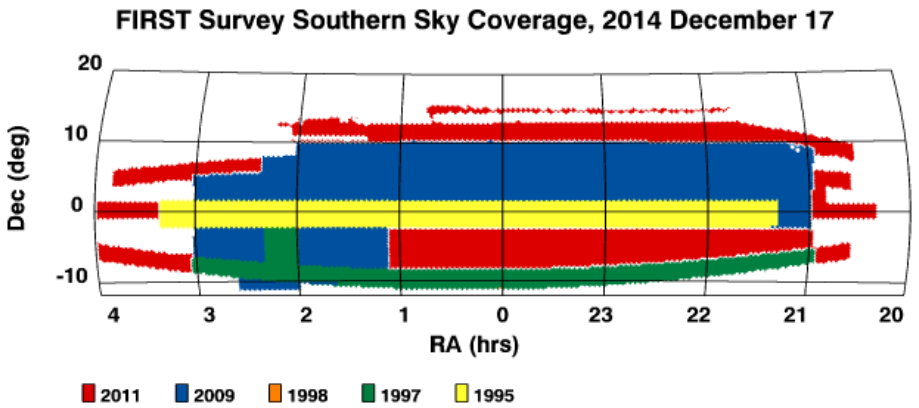

Figure 3.3: This is the sky coverage of Southern sky, for FIRST December 17, 2014 data (Courtesy: NRAO).

is based on algorithms in the Astronomical Image Processing System (AIPS)[1] (Becker et al. 1994). The most recent version of FIRST data is December 17, 2014 data, also known as 14Dec17. This 14Dec17 version includes sky regions of R.A.= 07.0 hr to 17.5 hr, Decl.= – 08.0 deg to + 57.6 deg in the northern sky and R.A.= 20.4 hr to 4.0 hr, Decl.= – 11.5 deg to +15.4 deg in the southern sky. The sky coverage areas of the FIRST 14Dec17 for the northern and southern sky are given in Figures 3.2 and 3.3, respectively.

3.1.1 Why FIRST Survey?

To observe the diffuse radio emission from a radio source and hence to study its morphology, data with the highest available resolution is needed. In the high-frequency range (1400 MHz or 1.4 GHz) there are two available radio surveys which have the largest sky coverage; one the NRAO Very Large Array Sky Survey (NVSS) and the other is VLA FIRST. The NVSS is the astronomical survey for the sky in the northern hemisphere. This is also carried out by the VLA of NRAO. The NVSS operates at 1.4 GHz and uses the VLA D configuration. The survey includes 82 percent of the sky, north of declination –40 degrees (Condon et al. 1998). The NVSS has an angular resolution of 45″ and an rms of 0.45 mJy (Condon et al. 1998). Now, the FIRST survey has a resolution of 5″ and a mean rms of 15 mJy. So, The FIRST data has approximately nine times better resolution and three times better considering the rms noise. Thus, the FIRST survey outperforms the

[1]http://info.cv.nrao.edu/aips/

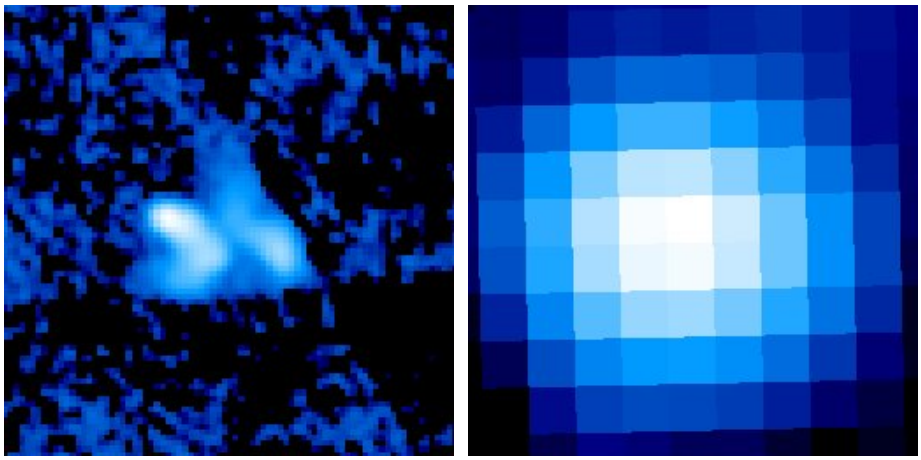

Figure 3.4: The two figures show the 256×256 pixels radio image of a radio source, J1054+5521. The left image is taken from the 1.4 GHz FIRST survey data whereas the right image is taken from the NVSS data.

earlier NVSS. Hence, with this relatively high sensitivity and resolution of the FIRST survey, it is possible to study the morphology of faint radio galaxies and their structure in detail compared to other high-frequency data. In Figure 3.4, we present a comparative image of a sample radio source J1054+5521. In this figure, we can see that the FIRST image gives a detailed morphological structure and diffuses radio emission information of the source, whereas the NVSS map shows the source just as a point source. The NVSS image can not even resolve the source structure properly.

3.2 Methodology

3.2.1 Sample Data Selection

The latest version of the FIRST survey data is known as the 14Dec17. The 14Dec17 version of the catalog is enriched with all the data of the previous versions of FIRST survey. There is a total of 946,432 sources in this catalog. Here, we first apply a selection condition where we filtered sources that have an angular size greater than $10''$. The choice of such a selection cut ($10''$) is made to keep the size of the sources greater than twice the convolution beam size (which is 5.0 arcsec FWHM circular beam). The angular size selection was chosen so as to get reasonably extended sources. We used the major axis of the fitted Gaussian to calculate the size of a

source. Our filtering process results in a total of 95,243 sources.

This kind of restricted search or selection cut was found in literature, this is not new in the field. In their search process for XRG identification from FIRST Cheung (2007) mainly used two constraints. First, they are restricted to fields with high dynamic ranges. The fields with a high dynamic range are defined as the ratio of the peak to the rms. Secondly, they chose sources with angular size greater than 15″. In this source size selection, they set the fitted major axis to $> 15''$. After applying these two condition Cheung (2007) restrict the sample size to 1648 from total $\sim$ 811,000 sources, which the 2003 April 11 version of FIRST have. In their extended catalog of winged sources, Yang et al. (2019) also implied two restrictions. Similar to Cheung (2007), the first restriction they chose sources with an acceptable dynamic range. The second restriction was on the radio major and minor axes. They selected the sources which have the size of major and minor axes larger than 10″ and 5″, respectively. They finally restrict the sample source number to 5128. Due to such restricted criteria both the study may miss several winged candidates. Apart from the source size, we did not apply any other kind of selection criteria such as conditions on the dynamic range of the source field. The single selection condition ensures the fact that we can run our search for more data samples and get the most out of the data used catalog. Thus, our search is a deep probe compared to the previous searches.

3.2.2 Identification and Classification of Winged Sources

The search for winged sources is done through a Manual Visual Search (MVS). We visually investigated all of the 95,243 sources' fields ($> 10''$) for new candidate radio galaxies with wings. First, the .fits source images are collected from the FIRST Image Cutouts[2]. The radio morphology is confirmed through their respective contour maps. The morphology of sources is determined by the number of radio contours considered, and hence by the signal-to-noise ratio. To provide consistent research, we started contours at 0.25 mJy for all sources. We reliably categorized a sufficient number of objects as having the characteristic wing lengths of greater than 80 percent of the active lobes based on the low-resolution FIRST pictures (5″). Following Cheung (2007), we also included galaxies with shorter wings (80 percent wing-to-lobe length ratios), as projection effects are likely. Secondary jets are difficult to quantify because they are frequently diffused and weak, with few

[2]https://third.ucllnl.org/cgi-bin/firstcutout

bright peaks at the end (hot spots).

The wings arise as secondary lobes in radio galaxies. We categorized the winged radio sources into two groups based on their wing position; XRGs and ZRGs. The wings (secondary lobes) of the "X"-shaped radio sources appeared to be originating from the center or near the center. The near central region is defined as the area covered by 25% of the primary jet length from the central location. When secondary lobes appear to emerge from the periphery of the primary jet or the non-near central region, the source is labeled as a Z/S-shaped radio source.

3.2.3 Identification of Optical Counterpart

It is believed that there is an AGN at the center of most radio galaxies. The AGN contains the host galaxy. The associated optical counterpart of the host is known as the optical counterpart of the radio galaxies. There are mainly two reasons why the optical identification of discrete radio sources is vital.
(i) The estimation of the distance to a radio source based solely on radio data is impossible. Only with an optical identification, followed by the redshift and then the distance is calculated using the Hubble law. The absolute radio brightness, linear dimension, and energy content can then be calculated using measurements of radio flux density and angular structure.
(ii) The optical, X-ray, and infrared studies of the radio source counterparts may provide some insight into a better understanding of the problem of the powerful radio emission's origin.
Radio sources' coordinates can be commonly estimated with an accuracy better than one second of arc, allowing for unambiguous association with optical counterparts as weak as roughly 24th magnitude, which can be achieved with huge reflectors and contemporary technology. Nonetheless, due to the vast amount of telescope time necessary for systematic colour and spectral research, optical identifications are only reasonably complete for a few hundred radio sources (Spinrad et al. 1985). However, visual identifications are frequently attainable even with very weak radio emitters.

The identification of the optical/infrared counterpart for the newly discovered winged sources is done from the Sloan Digital Sky Survey (SDSS) data catalog (Gunn et al. 2006), the Digital Sky Survey (DSS) (Lasker 1994), and the NASA/IPAC Extra-galactic Database (NED)[3]. The optical/IR counterpart iden-

[3]https://ned.ipac.caltech.edu/

tification was based on the optical/IR source position relative to the radio galaxy morphology. We overlayed radio images from the FIRST survey on the optical SDSS red images. We have used the position of the optical/IR counterpart of XRGs and ZRGs as the position coordinates of the discovered winged sources. First, the optical galaxies in the vicinity of the central region of the winged radio sources are identified. Then through visual inspection, the optical galaxy is selected as the optical counterpart based on its position on the radio map. An illustrative image of optical counter identification for a sample XRG is presented in Figure 3.5. Here, we overlay the radio image on the optical image. Note that, the field size and image size for both the images have to be exactly the same, otherwise somehow we have to make it the same. In the figure, there are three to four prominent optical galaxies found nearby the source. Now, the optical galaxy marked as 2 lies outside the image (also check the contour), so it is definitely not the optical counterpart. Now, the other two optical galaxies marked by 1 and 3 are located on the edges of the radio map hence these optical galaxies can not be the optical counterpart of the radio source. The optical galaxy that coincides at the center of the radio sources on the overlay image is the optical host galaxy and is marked in the referred figure.

3.2.4 AIPS

AIPS is the Astronomical Image Processing System, developed by National Radio Astronomy Observatory. It is a software package for the visualization, editing, flagging, calibration, and imaging of radio interferometric data.

Radio data have different axes, viz.; Baseline, Polarization (RR, LL, LR, RL), Channel, and Time. AIPS deal with radio interferometric data, from dirty unflagged data to create the final clean image. There are different AIPS tasks and each task has different inputs (Adverbs). For example: to load data: FITLD; for Visualization: UVPLT, VPLOT; for Flagging: TVFLG, UVFLG; for Calibration: CALIB, CLCAL; for Imaging: CLEAN. We have used each task accurately to get the final image. The AIPS data are saved in AIPS internal directory, when Flagging, Calibration is saved in different extension tables. We apply those tables in the original data to see the changes. In this process, the original data is always kept intact within AIPS internal directory.

Here, we use AIPS for our relevant required purposes, e.g, plotting the contour map, overlaying the radio images on the optical images, estimating the radio flux,

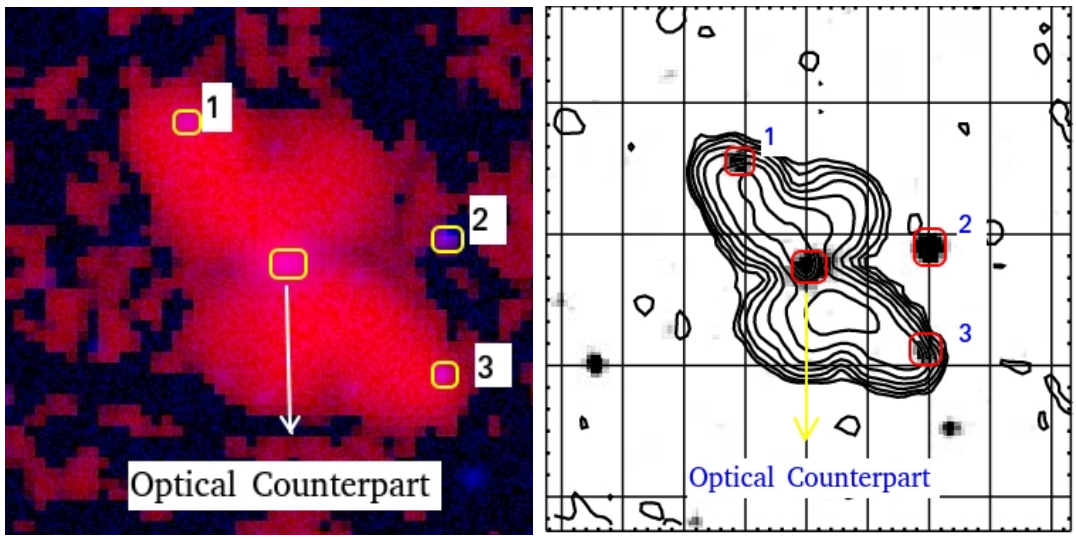

Figure 3.5: A sample image depicts the optical counterpart identification process is presented. The left panel shows the colour radio image overlaid on the optical image when the right panel shows the contour radio image for the same source overlaid on the optical image. For both the images the optical galaxies in the source field and the possible optical counterpart are indicated.

etc.

3.3 Results

Through a systematic search, we have identified a total of 458 winged sources from the VLA FIRST survey data at 1.4 GHz. However, at the same time, Yang et al. (2019) also did a search for XRGs and they report 290 sources among which 106 are strong and 184 are possible candidates for X-shaped sources. We did not include the X-shaped sources which are present in Yang et al. (2019) catalog. After, excluding the sources (also the common sources from Cheung (2007)) we find a total of 296 new winged sources. Out of the 296 winged sources, 161 sources are categorized as XRGs and the rest 135 sources are classified as ZRGs. The newly discovered XRGs and ZRGs are cataloged in Table 3.1 and Table 3.2, respectively (given at the end of this Chapter). We present sample colour stamp images of four XRGs and ZRGs in Figure 3.6 and Figure 3.7, respectively. For completeness, we did not exclude the 21 XRGs and 44 ZRGs present in Proctor (2011) in these

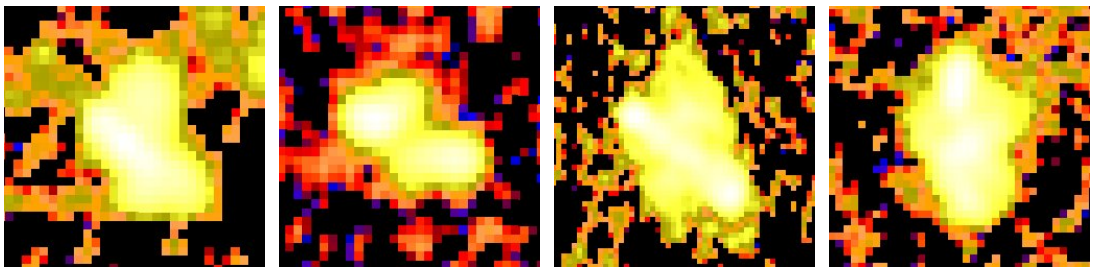

Figure 3.6: A sample colour stamp image of four identified XRGs is presented.

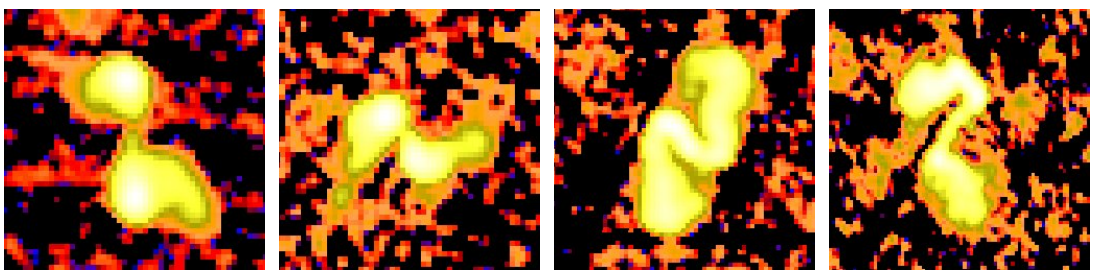

Figure 3.7: A sample colour stamp image of four identified ZRGs is shown.

tables, as we independently found those sources through our method. The sources are marked by ^{a} in the tables. We also included the sources, cataloged by Yang et al. (2019) as XRG sources, but did not identified as ZRG sources. There are 9 such sources, and they are marked by ^{b} in Table 3.2. Both of the tables have the following columns – column (1): Catalog number, column (2): Host name of the XRG or ZRG, column (3): Right ascension (R.A.) in J2000 (in hh mm ss.ss format), column (4): Declination (Decl.) in J2000 (in ±dd mm ss.s format), column (5): Position reference, column (6): Available redshifts (z) (the redshift values are approximated up to two decimal figures for the Tables, however in the calculation, we did not use the approximated values, we use the actual redshift values.), column (7): Integrated flux of the source at 1400 MHz, column (8): Integrated flux at 150 MHz, column (9): Two-point spectral index between 150 and 1400 MHz (α_{150}^{1400}) (the spectral index values are approximated up to two decimal figures for the Tables, however, the actual estimated values are used for calculation purposes), column (10): The linear size of the source in kpc, column (11): Radio luminosity (L_{rad}) at 1400 MHz (the values are presented in the order of 10^{42} in the unit $ergs^{-1}$, and the values are approximated up to two decimal figures in the Tables), column (12): Other catalogs where the sources are identified.

The XRGs and the ZRGs are presented in the ascending order of right ascension

for both Tables 3.1 and 3.2. The location of a particular radio source is identified as the position parameter of its optical or IR counterpart. We use eye estimated (EE) central core location as the position for the sources where the optical/IR counterpart is unavailable. The optical/IR counterparts are detected for 98 out of 161 XRGs and 88 out of 135 ZRGs. We found redshifts for a total of 135 sources. We also checked that 123 out of the 135 redshifts are spectroscopic, which means 91 percent of redshifts are spectroscopic. The remaining 12 redshifts are photometric. Categorically for XRGs, we found redshift for 72 sources, out of which 67 are spectroscopic and 5 are photometric. On the other hand among the 63 ZRG redshifts, 56 are spectroscopic and 7 are photometric. Unless otherwise specified, all redshifts were obtained using SDSS catalog release 12 (DR12) (Alam et al. 2015). The integrated flux at 1400 MHz is measured from NVSS data instead of FIRST. This is due to the fact that the FIRST survey is prone to flux-density loss because of its high resolution and lack of antennas with short spacing. The NVSS used the lower-resolution VLA configuration D (with a resolution of $\sim 45''$) compared to the FIRST survey's B configuration (with a resolution of $\sim 5''$), implying that NVSS is particularly suited to identifying the most extended radio structure. The flux measured from the NVSS map is significantly higher than the FIRST image for the majority of the sources. We plot the integrated flux values for XRGs and ZRGs, measured from NVSS and FIRST in Figure 3.8. We estimated the mean and median flux densities from the NVSS data are 448.5 and 155 mJy, respectively when the mean and median flux densities from the FIRST catalog are 381 and 122 mJy. We found an NVSS counterpart for each of the sources, however, due to the lower resolution, the winged morphology is not visible in any of the NVSS maps of these sources. We measured the 1400 MHz flux density from FIRST instead of NVSS for five XRGs (J0742+3339, J0932+1610, J1104+2828, J2218+0012, and J2324+1438) and two ZRGs (J0847+3147 and J1138+2039) since there were other background sources in the FIRST image inside the beam size of the NVSS image. Those flux values are marked by ^{b} in the 1400 MHz flux column. The 150 MHz flux is measured from the TGSS data (Intema et al. 2017).

Figure 3.9 depicts an example of four identified XRGs, whereas Figure 3.10 depicts an example of four identified ZRGs. The FIRST radio images are overlaid on the DSS2 red optical images. It should be noted that the DSS2 red images are only used for imaging purposes. The synthesized beams are indicated in the bottom-right corner of each image. However, all of the sources from Table 3.1 and Table 3.2 are presented in the Appendix section.

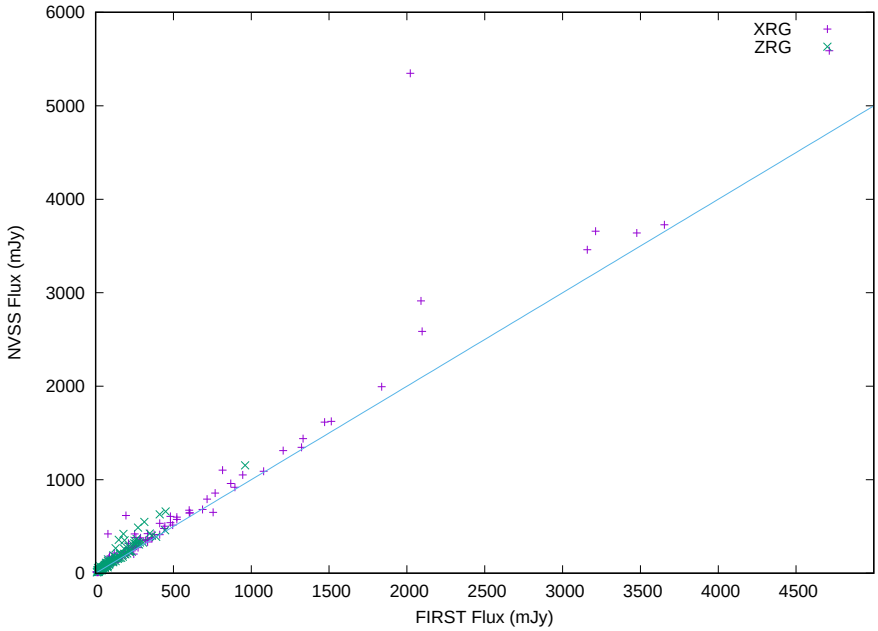

Figure 3.8: The plot incorporates the integrated flux values as measured from the FIRST and the NVSS data for all the identified XRGs and ZRGs.

For the entire calculation and throughout the work, we used the following cosmological parameters: $H_0 = 67.4$ km s^{-1} Mpc^{-1}, $\Omega_m = 0.315$ and $\Omega_{vac} = 0.685$ (Planck Collaboration et al. 2020). These cosmological constants are computed using final full-mission Planck observations of the cosmic microwave background (CMB) anisotropies, which combine data from the temperature and polarization maps, as well as the lensing reconstruction.

A short note on the calculated parameters like spectral index, radio luminosity, FR-dichotomy, etc. for the newly identified winged sources are discussed in the following subsections.

3.3.1 Spectral Index

Here, we use the definition of the spectral index (α) as $S_\nu \propto \nu^\alpha$, where S_ν is the radiative flux density at a given frequency ν. We calculate the two-point spectral index (α_{150}^{1400}) between 150 MHz and 1400 MHz. The spectral index is calculated for 186 winged sources. In particular, the spectral index is measured for 107 XRGs and 79 ZRGs. For the rest of the sources, the spectral index is unavailable. This is due to the greater rms in the TGSS images, which means those sources were not

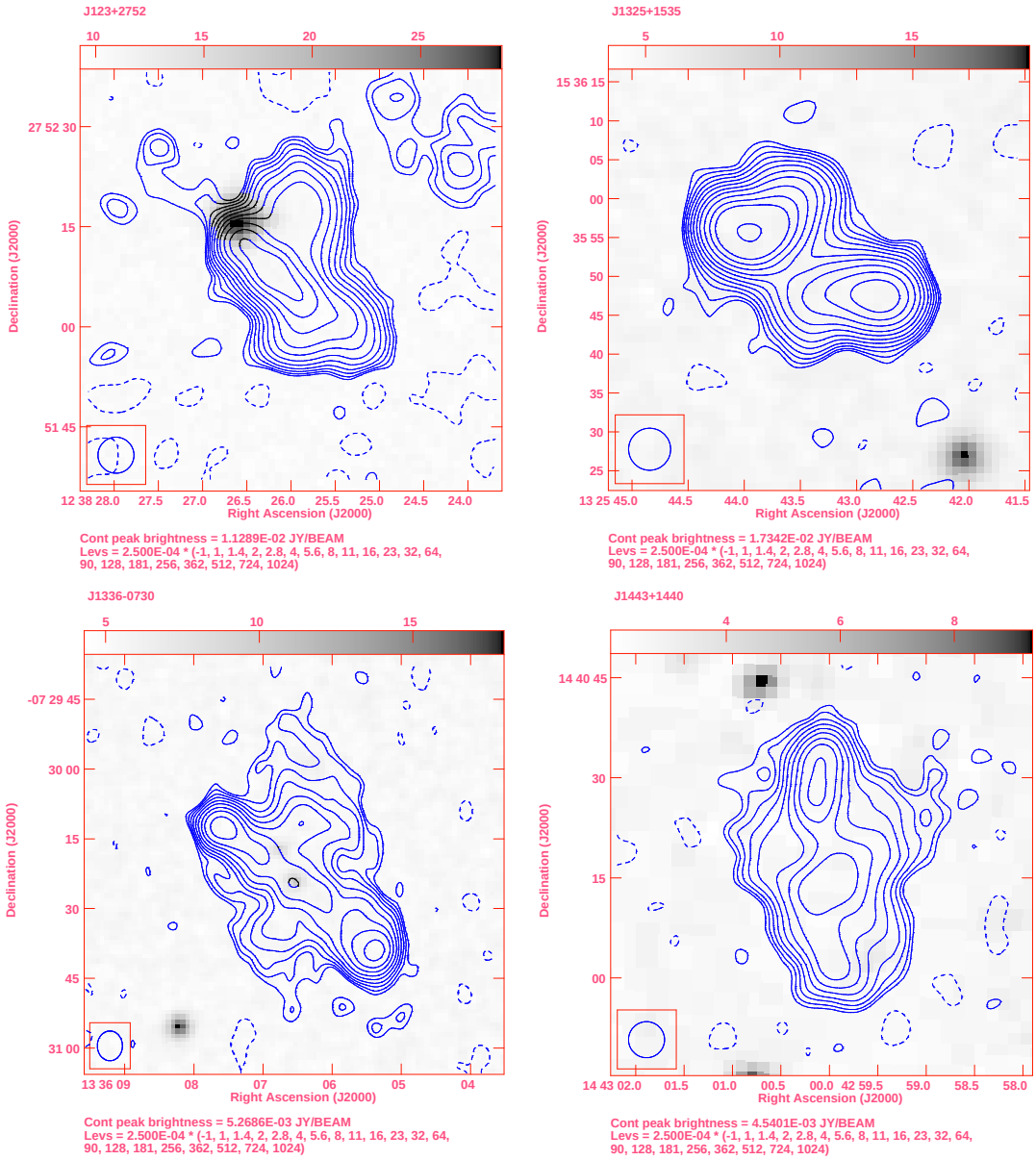

Figure 3.9: A sample of four FIRST images of X-shaped radio source (contours) overlaid on the DSS2 red image (gray-scale) is given. The relative radio contours are drawn with an increment of $\sqrt{2}$. Here, we use the $5''$ full-resolution FIRST radio images.

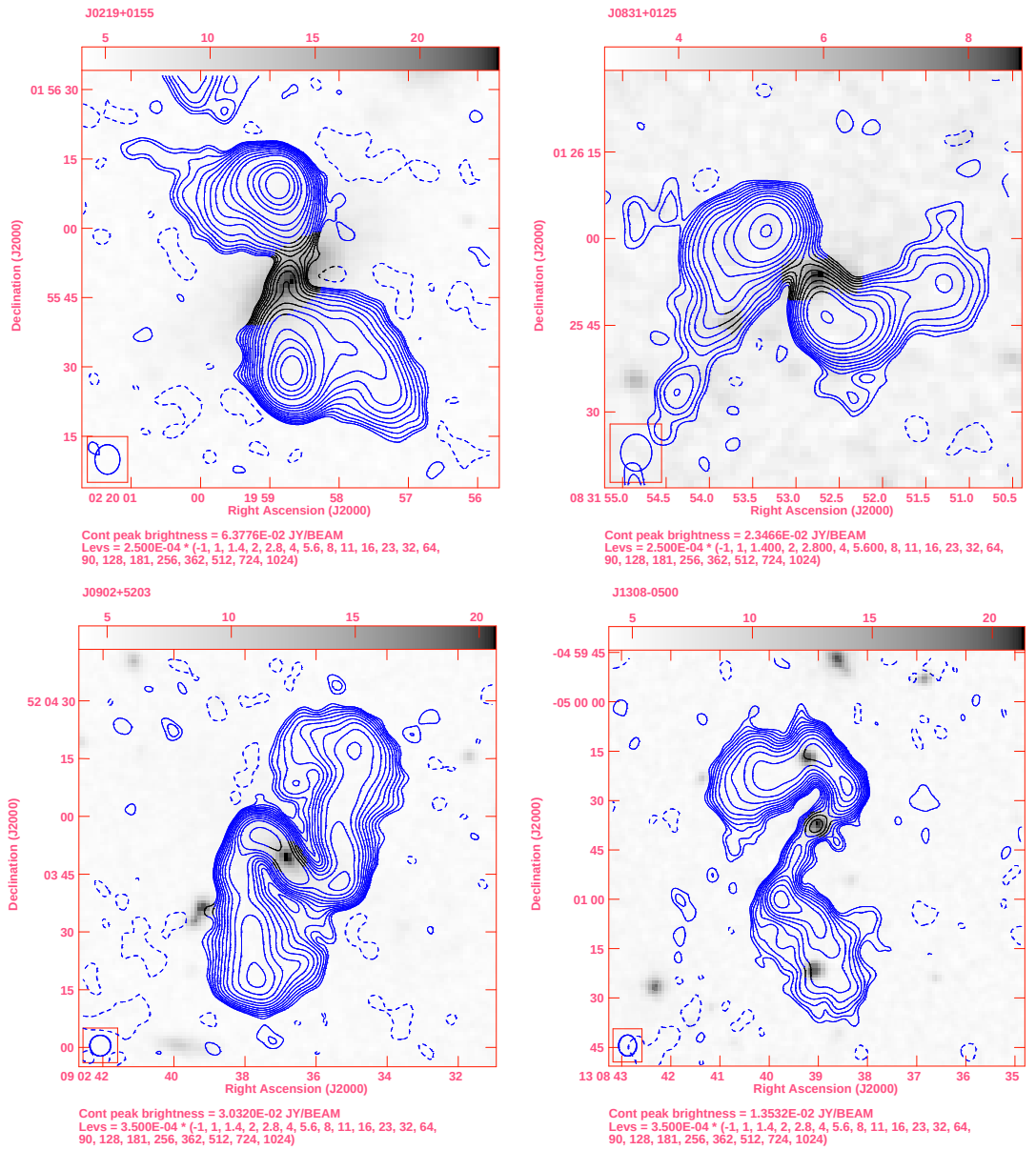

Figure 3.10: A sample of four FIRST images of Z-shaped radio source (contours) overlaid on the DSS2 red image (gray-scale) is presented. The relative radio contours are drawn with an increment of $\sqrt{2}$. Here, we use the 5″ full-resolution FIRST radio images.

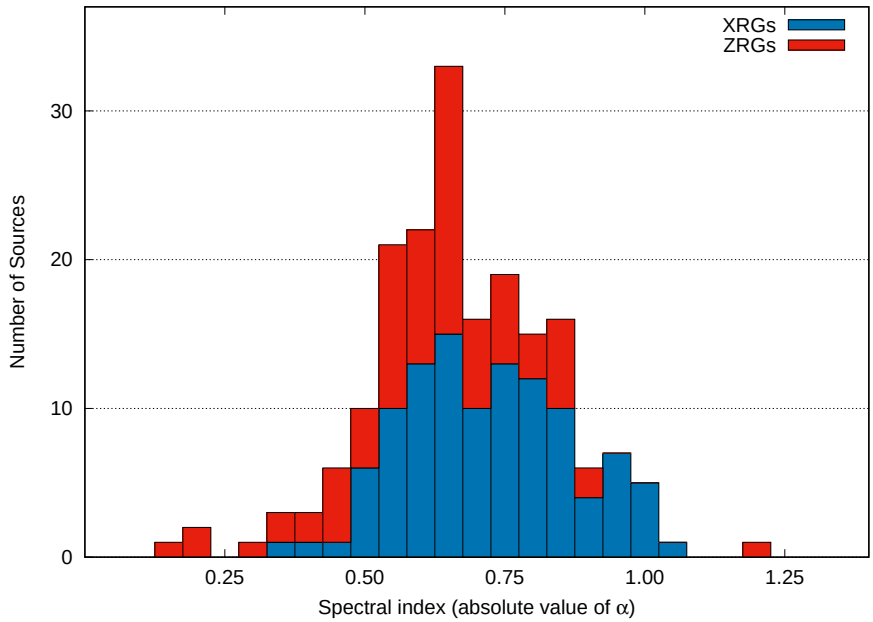

Figure 3.11: The histogram shows the spectral index ($|\alpha_{150}^{1400}|$) distribution of the winged radio galaxies (both XRGs and ZRGs), identified here.

detectable in the TGSS 150 MHz map.

A histogram representing the distribution of spectral index for all of these identified winged sources is presented in Figure 3.11. Histograms for only the XRGs and ZRGs are presented in Figure 3.12. Note that, in the histogram plots the absolute α value is taken. The spectral index value for all the winged sources has a range of – 0.14 to – 1.21. We see that most winged radio galaxies have a steep radio spectrum, i.e.; α_{150}^{1400} greater than 0.5, as predicted from a lobe-dominated radio source. The peaks in the histogram for XRGs and ZRGs are clearly different. The histogram for XRGs shows two peaks near 0.55 and 0.70, whereas the histogram for ZRGs shows a peak near 0.65. Individually, the α_{150}^{1400} range for XRGs is – 0.35 to – 1.05 and for ZRGs is – 0.14 to – 1.21. For the XRGs, J2249+020 has the most steep spectra with $|\alpha_{150}^{1400}| = 1.05$, while the XRG J0758+4406 most flat spectra with $|\alpha_{150}^{1400}| = 0.35$. The highest and lowest value of $|\alpha_{150}^{1400}|$ for the ZRGs are found for J1325+5736 (with – 1.21) and J1524+1627 (with – 0.14), respectively.

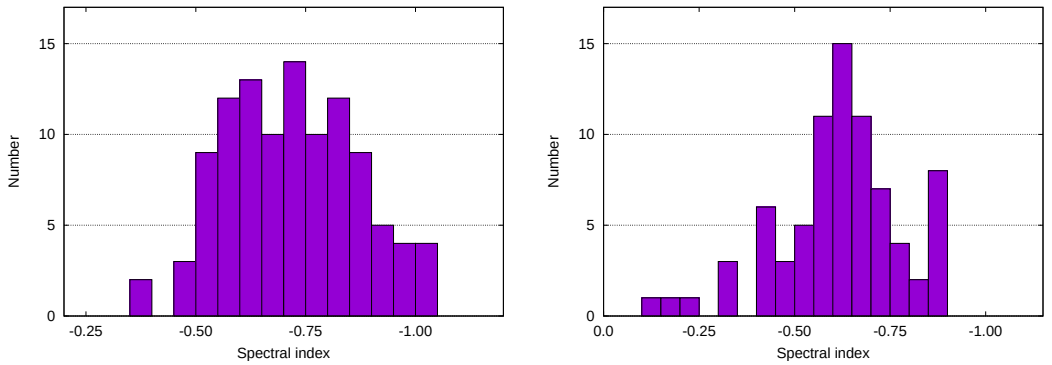

Figure 3.12: The plots represent the distribution of spectral index ($|\alpha_{150}^{1400}|$) for XRGS and ZRGs individually. The left panel shows the distribution for the X-shaped radio galaxies. The right panel presents the distribution for Z-shaped radio galaxies.

3.3.2 Radio Luminosity

The radio luminosity ($Lrad$) defines the overall strength of the source as well as the power of the jets. The radio luminosity is calculated using the formula –

$$L_{rad} = 1.2 \times 10^{27} D_{\rm Mpc}^2 S_0 \nu_0^{-\alpha} (1+z)^{-(1+\alpha)} \times (\nu_u^{(1+\alpha)} - \nu_l^{(1+\alpha)})(1+\alpha)^{-1} \text{erg s}^{-1} \quad (3\text{-}1)$$

where $D_{\rm Mpc}$ is the luminosity distance to the source in Mpc, S_0 is the flux density in Jy at a given frequency ν_0 (Hz), z is the redshift of the radio galaxy and α is the spectral index (from $S \propto \nu^{\alpha}$). Here, ν_u (Hz) and ν_l (Hz) are the upper and lower cut-off frequencies, respectively (O'Dea & Owen 1987). In our calculation, we assume the upper and lower cutoff frequencies as 100 GHz and 10 MHz, respectively. The luminosity distance ($D_{\rm Mpc}$) is measured from the available redshift (z) information using the Cosmological Calculator for the Flat Universe by Nick Gnedin[4]. Here, we measure the luminosity at 1.4 GHz and hence the L_{rad} is actually $L_{1.4GHz}$.

Radio luminosity is calculated for 101 sources (for 55 XRGs and 46 ZRGs). We found that out of the XRGs the most luminous XRG is J1124+4325 with $L_{1.4GHz} = 7.76 \times 10^{44} ergs^{-1}$, while the XRG J1354+5840 is the least luminous source with $L_{1.4GHz} = 3.19 \times 10^{38} ergs^{-1}$. Out of the ZRGs J1156+2138 and

[4]https://home.fnal.gov/ gnedin/cc/

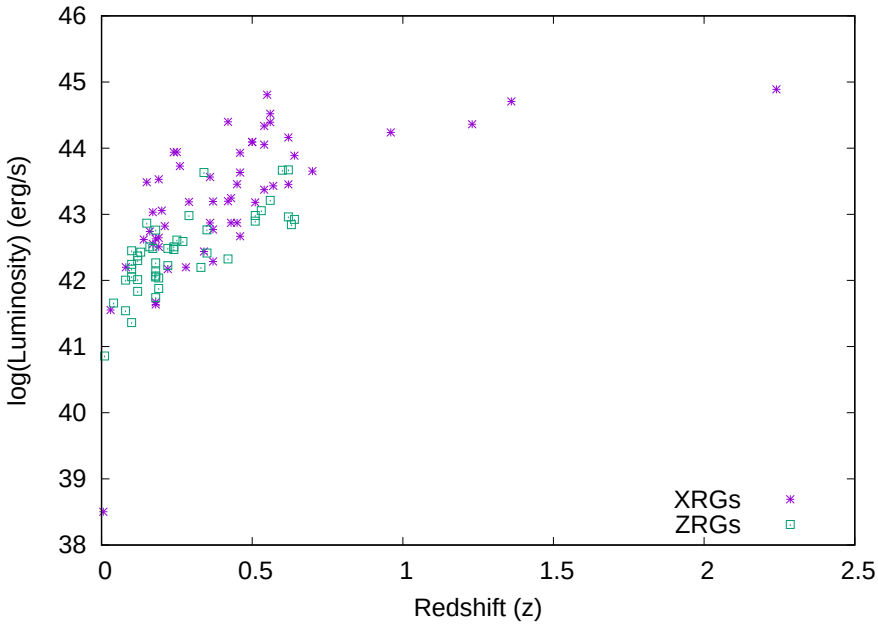

Figure 3.13: The plot represents the distribution of the radio luminosity ($L_{1.4GHz}$ in log scale) with the redshift (z) for the identified XRGs and ZRGs.

J1140+1743 are respectively the most and least luminous sources with luminosity $4.70 \times 10^{43} ergs^{-1}$ and $7.20 \times 10^{40} ergs^{-1}$. Figure 3.13 depicts the distribution of radio luminosities $log(L_{rad})$ of XRGs and ZRGs with known redshifts (z) from the current search.

3.3.3 Radio Power

Radio power (P_{rad}) at a preferred frequency ν is given by Donoso et al. (2009):

$$P_\nu = 4\pi D_L^2 S_\nu (1+z)^{(\alpha-1)} \tag{3-2}$$

where the parameters in the equation are D_L is the luminosity distance, S_ν is the radio flux at the reference frequency ν. The function $(1+z)^{(\alpha-1)}$ is standard k-correction, used in radio astronomy (Hogg et al. 2002). Here, spectral index (α) is assumed to be followed as $S_\nu \propto \nu^{-\alpha}$. From the available values, we have evaluated the radio power ($P_{1.4GHz}$).

The $P_{1.4GHz}$ is evaluated for 101 winged sources, out of which 55 are XRGs and rest 46 sre ZRG candidates. Among the XRGs the XRG J1124+4325 and XRG J1354+5840 are identified with the highest and lowest $P_{1.4GHz}$ with respective

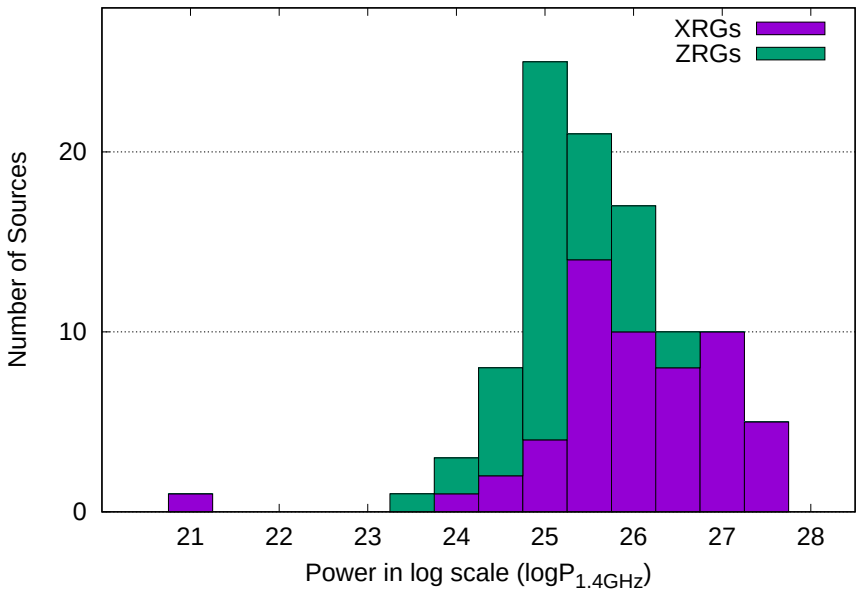

Figure 3.14: The histogram represents the $P_{1.4GHz}$ distribution in log scale for the winged sources.

values $4.40\times10^{27}WHz^{-1}$ and $8.89\times10^{20}WHz^{-1}$. Out of all the ZRGs, J1156+2138 has the maximum $P_{1.4GHz}$ value $3.03\times10^{26}WHz^{-1}$ and ZRG J1140+1743 has the minimum $P_{1.4GHz}$ value $2.76\times10^{23}WHz^{-1}$. In Figure 3.14, we present a histogram that depicts the $log(P_{1.4GHz})$ distribution among the number of sources for XRGs and ZRGs.

3.3.4 FR-dichotomy

The FR-dichotomy is a measure of the relative brightness of a radio source between the central core and the edges. To determine the FR type, we analyze the comparative brightness of the edges and the core region through visual inspection. The inspection was made for both the greyscale and contour images. For grayscale, the colour scale represents the relative brightness for distinct portions of a source, whereas the contour gradient represents the relative brightness in a contour image. As discussed earlier, for uniform source characterization we used radio maps starting at 0.25 mJy contour. We categorized a source as FR-I or FR-II on the basis of the position of the peak flux in the major axis lobes.

We found that a total of 149 sources show FR-II class while 93 sources show FR-

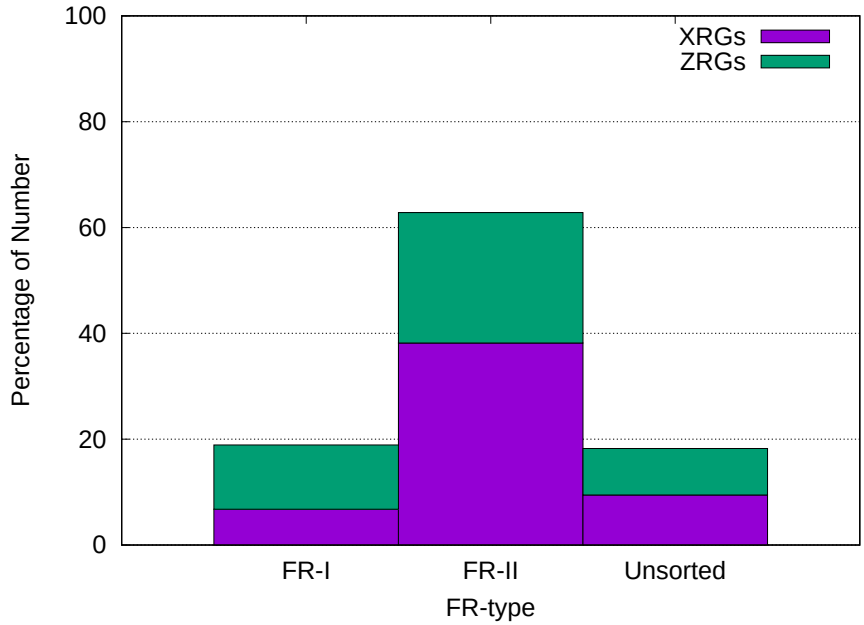

Figure 3.15: The plot shows the number of FR-I and FR-II radio sources from XRGs and ZRGs.

I. For its complicated morphology and brightness distribution, 54 sources are not classified as either FR-I or FR-II types. Particularly, out of the total 161 XRGs found 113 are classified as FR-II radio galaxies and 20 as FR-I radio galaxies. There are 28 XRGs, which are not classified. On the other hand, out of the 135 ZRGs, 36 are identified as FR-II type and 73 as FR-I type. For 26 ZRGs no FR classification is made. A histogram illustrating the number of FR-I and FR-II sources found among the reported XRGs and ZRGs is represented in Figure 3.15.

3.3.5 Some Characteristics of the XRGs

- *Major and Minor Axes*

The angular size of the major and minor axes are measured from their respective contour maps. A sample image for the measurement is given in Figure 3.16. The uniform contour maps give a relative measure for the major and minor axes' angular size estimation. A plot for the minor axis of XRGs with its major axis is given in Figure 3.17. There are 27 X-shaped sources where the secondary lobes are observed on one side of the primary lobes. These 27 one-sided XRGs are not

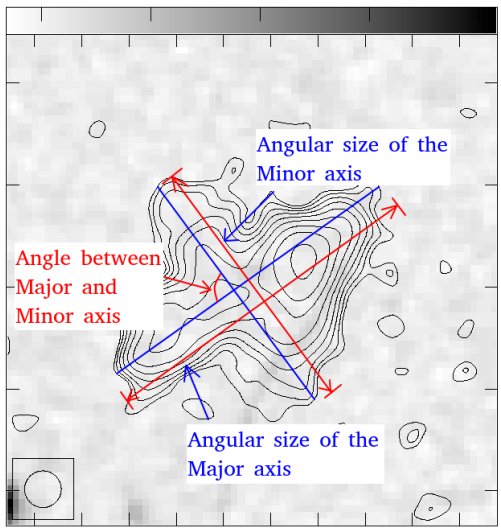

Figure 3.16: This is a sample image to show how the angular size of the major axis, minor axis, and their angle in between them is measured.

included in the plot.

We also plot a histogram, presented in Figure 3.18 to show the distribution of the ratio between the minor and major axes. We found that the angular size of the secondary jets or minor axis is in order of 50 to 75 percent the size of primary jets or the major axis for 47 sources. For 32 XRGs, the minor axis is found with 75 to 100 percent of the size of the major axis. Secondary jets are found larger than primary jets for seven XRGs. It is important to note that, the effect of projection may affect the size of the primary jets.

- *The angle between the Major and Minor Axes*

We consider two virtual lines with peak fluxes along the axes of the major and minor lobes. The acute angle produced by those two lines at their intersection point is defined as the angle of the X-shaped source (see Figure 3.16).

A histogram showing the angle distribution is given in Figure 3.20. Our study found that the majority of the sources (63 percent) have an angle between 70 and 90 degrees. The histogram reveals a 75-degree peak for the X-shaped radio galaxies. The histogram excludes the sources with one-sided wings. To eliminate angle measurement errors, sources with dispersed and nonlinear secondary lobes are also excluded from the study.

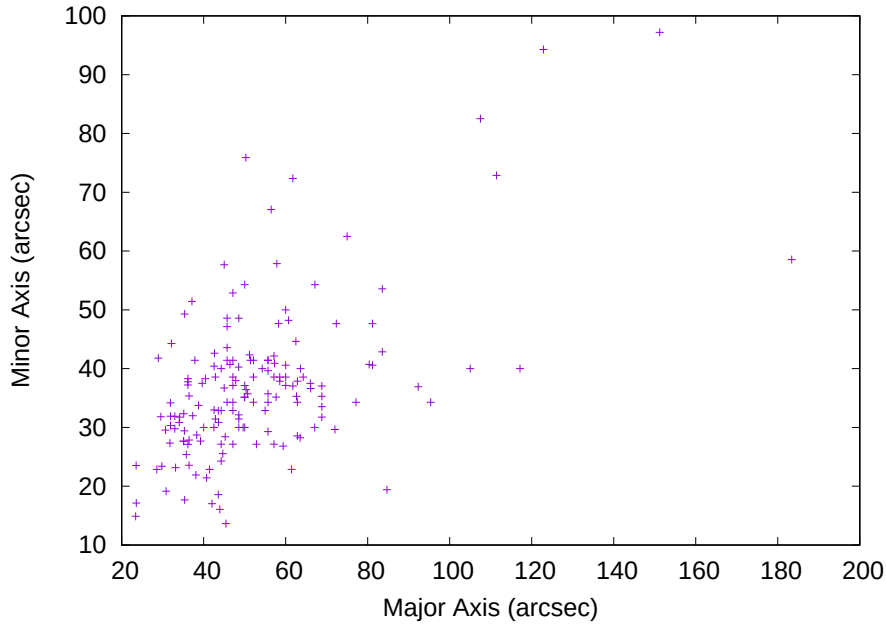

Figure 3.17: The figure represents the plot for the angular length of the major and the minor axis of the XRGs.

3.3.6 Some Characteristics of the ZRGs

- *Size of the Jet-length*

The size of the primary jet in between the two oppositely directed secondary lobes (wings) is defined as the size of the jet-length (see Figure 3.19). The jet-length may vary with the choice of the lowest contour level, a uniform choice of contour level will measure the size relatively accurately. We plot the histogram in Figure 3.21, prevailing the jet-length distribution for our identified ZRGs.

We saw that the angular size of the jet-length is less than 1 arc-minute for a majority of the sources. A sharp peak is found near $20''$. There are two sources namely, J1417+0812 and J1303+0339 have angular jet-length greater than $90''$. The angular jet-length size of $113''$ and $104''$ are measured for J1417+0812 and J1303+0339, respectively. The source J2137-0811 has the least angular jet-length with $9''$. With the available redshifts, we also estimate the equivalent linear jet-lengths. The highest and lowest linear jet-length sizes are found for J1319+0502 and J1140+1743 with respective lengths of 1.41 Mpc and 5.85 kpc. The source J0219+0155 has a jet-length 37.8 kpc. The sources J1303+0339 and J1536+2357

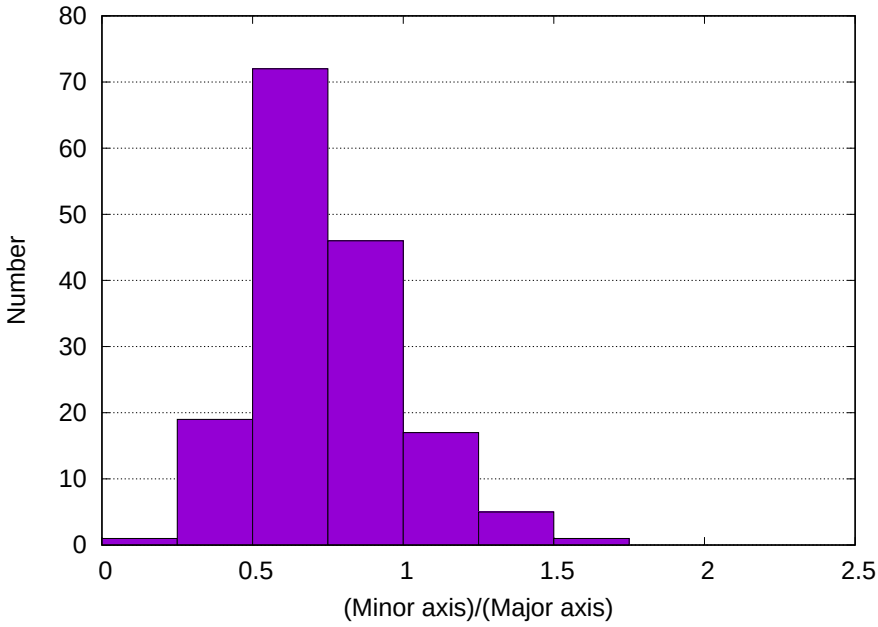

Figure 3.18: The histogram shows the ratio distribution of minor and major axes size ratio among the XRGs.

have linear jet-length values of 0.47 and 0.44 Mpc, respectively.

3.4 Analysis of the Results and Outcomes of the Study

In this work, we have done a rigorous search for the identification of winged sources in proper high-frequency data. Through a symmetric search of 95,243 selected sources, we identified a total of 296 new winged sources, out of which 161 sources are classified as X-shaped sources and the rest 135 as Z-shaped sources. This discovery contributes to a significant rise in the number of such sources. We catalog the newly identified sources. The bigger XRG and ZRG samples allow us to explore various statistical features and physical parameters of these sources. Our search findings may be put as –

(**i**) Redshifts (z) are available for a total $\sim 46\%$ of sources. For the XRGs the redshift value lies in the range $0.0057 < z < 2.24$. We checked that 53 sources have a redshift value less than 0.5 and 19 sources have a redshift value greater than 0.5. The highest available redshift is found for J1124+4325, with a redshift value of 2.245 (Richards et al. 2009). It is found that J1124+4325 is spectroscopically

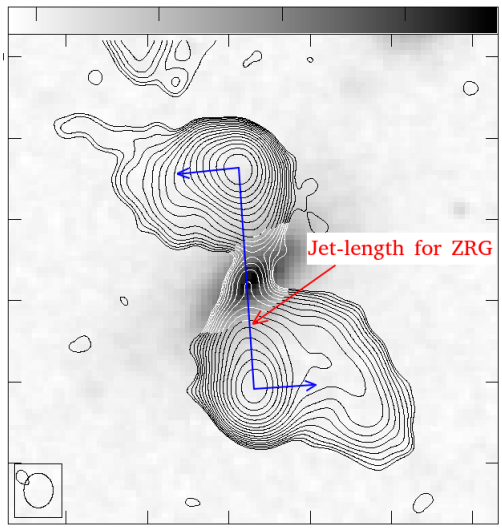

Figure 3.19: This is a sample image to show how the jet-lengths of the ZRGs are measured.

identified as a quasar (Xu & Han 2014). Among the other high redshift XRG sources, J1333+0219 and J0750+1144 have redshifts of 1.228 (Nilsson 1998) and 0.955 (Richards et al. 2009), respectively. For the ZRGs, the redshift span is $0.01 < z < 1.28$. The number of ZRGs with $z < 0.5$ are 53 while the number with $z > 0.5$ are 10. The ZRG with the highest redshift is J1319+0502 with redshift 1.285 (Richards et al. 2009). So, from our study, we found that the farthest known XRG and ZRG are J1124+4325 and J1319+0502. Before this, the farthest known X-shaped source was J0229+132, a large core dominant galaxy, with a redshift of 2.065 (Marecki et al. 2006). In the catalog of Cheung (2007) J1206+3812 with redshift 0.838, is the highest redshift source. According to the optical spectroscopy of X-shaped and Z-shaped sources previously described, a significant proportion of the sources are quasars (Cheung 2007). We expect a significant number of XRGs and ZRGs in these redshifts because the number density of quasars peaks at the redshift value $z \sim 1 - 2$ (Boyle et al. 2000). However, due to minor jets in faint sources (which are typically diffused) are not visible for many of the sources, and hence we are missing many of the XRGs and ZRGs with a redshift greater than 1.

(**ii**) Two supernovae are discovered inside the radio map for the XRG J0057-0123. SN 2010jo and SN 2007nq (Hakobyan et al. 2012) are located around 11.7″ and 21.6″ from the galaxy's center, respectively, on one of the galaxy's primary lobes.

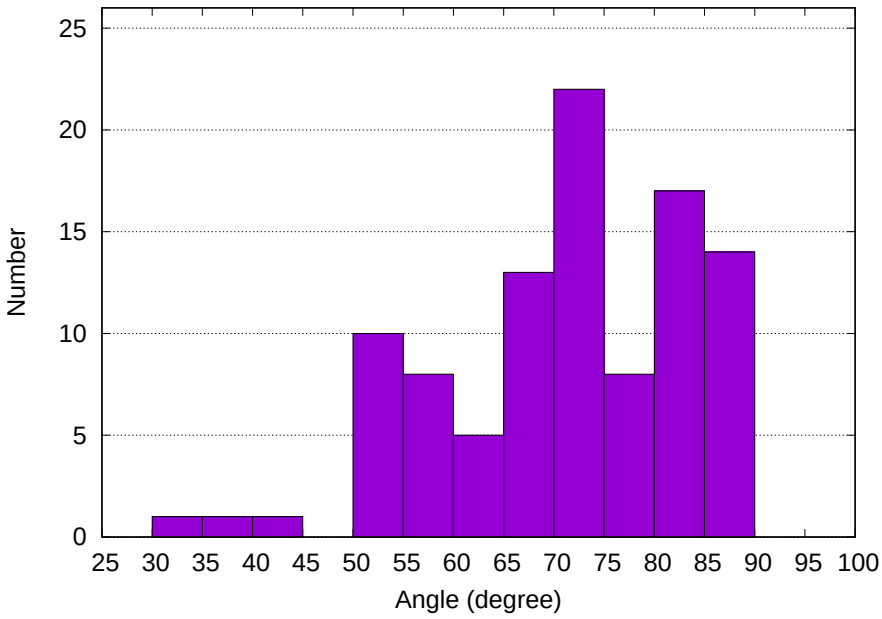

Figure 3.20: The histogram manifests the distribution of angle between the minor and major axes for the XRGs.

(**iii**) All of the XRGs with flux densities more than 2 Jy are found as FR II radio galaxies. J1001+2847 is the brightest radio galaxy among XRGs, with a flux density of F_{1400} = 5589 mJy. The XRG J1001+2847 is a Seyfert galaxy (Véron-Cetty & Véron 2006). The sources with flux (F_{1400}) more than 2 Jy are J0057–0123 (5384 mJy), J0655+5408 (3727 mJy), J1422+1935 (3659 mJy), J0950+1420 (3639 mJy), J1617+3222 (3222 mJy), and J1235+2120 (2013 mJy). There is no ZRG with flux greater than 2 Jy. The ZRG J1140+1743 has the highest flux of 1154 mJy.

(**iv**) Spectral index (α_{150}^{1400}) are estimated for 188 ($\sim$ 64%) sources. Individually, for XRGs the number is 109 ($\sim$ 68%) and for ZRGs the number is 79 ($\sim$ 58%). The mean and median for overall sources are – 0.67 and – 0.66, respectively. For XRGs, both the mean and median α_{150}^{1400} value is – 0.72. On the other hand for the ZRGs, those respective values are – 0.62 and – 0.63. For a large sample of radio sources, the spectral index ranges from – 0.75 to – 0.90 (Tiwari 2019). Radio sources with core-dominated AGNs give the average spectral index greater than – 0.7 (Randall et al. 2012). So, the winged sources have an average spectral index that lies in the range of previously measured values. We also found that most XRGs and ZRGs have a steep spectral index between 150 and 1400 MHz, and it

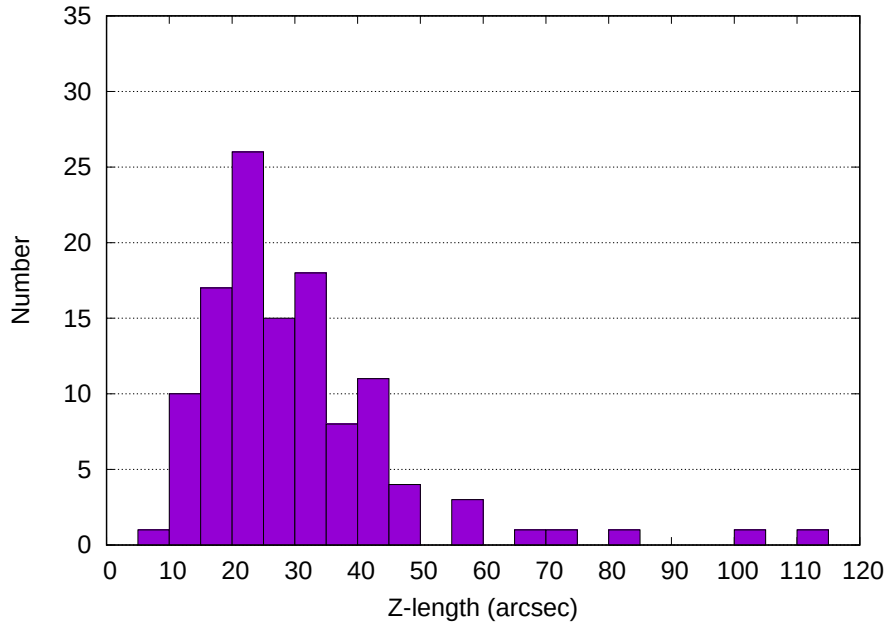

Figure 3.21: The histogram depicts the distribution of jet-length among the ZRGs.

is quite expected from lobe-dominated radio sources.

(**v**) At 1.4 GHz, the radio luminosity ($L_{1.4GHz}$) of the sources is in the order of $10^{43} ergs^{-1}$, which is somewhat less than that of a typical radio galaxy. Examining a collection of 540 double radio sources, Nilsson et al. (1993) found the average luminosity ($logL$) as 44.07 $ergs^{-1}$. The average value of $log(L_{1.4GHz})$ in $ergs^{-1}$ for XRGs is 43.24 and for ZRGs is 42.42. Hence, the average luminosity value for XRGs is found to be greater than that of ZRGs. The corresponding median values for the XRGs and ZRGs are 43.31 (with 1σ standard deviation of 1.05) and 42.42 (with 1σ standard deviation of 0.58), respectively. The Kolmogorov-Smirnov test (Peacock 1983; Smirnov 1948) to compare the distributions of XRGs and ZRGs is used and we discovered that they are consistent with each other, with $D = 0.52$ and $p-$value $= 7$.

(**vi**) For most ($\sim 64\%$) of the total sources the P_{rad} value lies in the order of $10^{25} to 10^{26} WHz^{-1}$. These are quite similar to a typical radio galaxy power. The mean and median values of $logP$ are found as 25.61 and 25.59 WHz^{-1}. Considering only the XRGs the respective mean and median values are found as 26.01 and 26.05 WHz^{-1}. X-shaped sources considered the transitional cases of FR classes with emission-line strength (L_{NLR}) $\sim 10^{35} W$ (Landt et al. 2010). Hence, we saw that our average P in the unit of W as $\sim 10^{26.01} \times frequency$ (when the frequency

is $1.4GHz = 1.4 \times 10^9 Hz$) supports the emission-line strength given by Landt et al. (2010). The ZRGs have the mean and median of 25.13 and 25.08 WHz^{-1}, respectively. So, we see that the average power of XRGs is more than that of the ZRGs.

(**vii**) Among the sources classified in FR-dichotomy, $\sim 62\%$ sources are FR-II sources. For XRGs, most of them ($\sim 76\%$) are identified as FR-II sources (Leahy & Parma 1992; Cheung 2007; Yang et al. 2019). Thus, our result supports the previous trend. Note that, none of the XRGs in this current sample contain FR-II secondary lobes. However, in contradiction, the FR-I and FR-II percentage for the ZRG sources is 78% and 22%, respectively. Saripalli & Roberts (2018) said that their sample contains only one FR I source (2.7%) out of 37 XRGs. Now in this search, we found more FR-I sources than Saripalli & Roberts (2018) because FR-I sources are statistically fainter than FR-II sources, and the present work did not impose any constraints on the dynamic range filtering out comparably fainter events. Despite the fact that the majority of XRGs in the current sample are still FR-II (70 percent), FR-I XRG sources are not negligible (13 percent), contrary to the findings of Saripalli & Roberts (2018).

(**viii**) We discovered 161 XRGs and 135 ZRGs, resulting in an XRG/ZRG ratio of 1.2. Previously, Saripalli & Roberts (2018) demonstrated using a Cheung (2007) sample that the ratio of XRG to ZRG in their sample is ~ 2. Because ZRGs are statistically fainter than XRGs, the current paper found more ZRGs than Cheung (2007), and Cheung (2007) missed many ZRGs due to its dynamic range-specific selection criterion.

(**ix**) Due to projection effects, the wings of XRGs and ZRGs may be greatly shortened. The flux-density imbalance detected in some XRGs may imply that the wings are close to our line of sight, and the flux-density asymmetry is caused by Doppler boosting. A few of the 26 sources with a one-sided wing could be extreme cases of Doppler boosting.

(**x**) In our sample, 127 sources are inversion symmetric, accounting for 43 percent of the total. 58 XRGs and 69 ZRGs are symmetric among the 127 sources. The inversion symmetric structure suggests a host-related cause for wing creation.

One commonly recognized explanation for explaining the nature of XRGs is the backflow of plasma. Because buoyancy-driven backflow cannot propagate faster than the external sound speed (Leahy & Parma 1992), the buoyancy-forced wings are not predicted to be longer than the primary radio lobes, which are known to progress supersonically. We discovered seven instances when the wings are

longer than the fundamental axes. Within their sample of 87 sources, Saripalli & Roberts (2018) discovered two such sources. Backflow may still occur in certain XRGs, although it is not the main explanation for all XRGs (especially for sources with longer wings). However, the alignment effect may still have a role in the primary jets, which appear shorter than the secondary jets.

To validate the nature of these sources, multifrequency high-resolution investigation is encouraged. The discovery of a large number of XRGs and ZRGs demonstrates that these types of sources are not uncommon, and we hope to find more such objects in a future deeper high-resolution search. However, this paper, along with Cheung (2007) and Yang (2019), assemble the discovery of a large number of XRGs and ZRGs from the FIRST survey (in high frequency), it should be noted that due to the high resolution in the FIRST image and the lack of antennas with shorter baseline, a large number of XRGs and ZRGs with larger sizes and diffused emission may be missed.

Table 3.1: **New candidate X-Shaped Radio Sources identified from VLA FIRST Survey**

Catalog Number	Host Name	R.A. (J2000.0) hh mm ss.ss	Decl. (J2000.0) dd mm ss.s	Ref.	Redshift (z)	F_{1400} (mJy)	F_{150} (mJy)	α_{150}^{1400}	Linear Size (kpc)	$L_{1.4GHz}$ (erg/s) ($\times 10^{42}$)	Other Catalogs
(1)	(2)	(3)	(4)	(5)	(6)	(7)	(8)	(9)	(10)	(11)	(12)
1	J0017–0149	00 17 32.20	–01 49 25.9	GALEXMSC	—	91	—	—	—	—	1, 2, 8
2	J0022–0807	00 22 55.64	–08 07 52.4	SDSS	0.44	98	—	—	796	—	1
3	J0023–0915	00 23 25.26	–09 15 38.2	SDSS	—	117	—	—	—	—	1
4	J0057–0123	00 57 34.92	–01 23 27.9	SDSS	0.04	5348	—	—	137	—	2, 3, 8, 9, 10, 11, 14, 24, 29
5	J0110–0924	01 10 34.36	–09 24 45.2	EE	—	135	—	—	—	—	1, 2, 8, 10
6	J0112–0804	01 12 42.41	–08 04 02.4	EE	—	365	—	—	—	—	1, 2, 8, 10
7	J0139+0131	01 39 57.25	+01 31 46.2	GALEXASC	0.26[30]	1312	4750	–0.58	415	53.65	1, 2, 4, 8, 9, 10, 11, 12
8	J0144+1212	01 44 36.38	+12 12 54.8	EE	—	11	38	–0.56	—	—	1
9	J0145–0941	01 45 03.87	–09 41 16.6	SSTSL2	—	90	—	—	—	—	—
10	J0152–0759	01 52 39.32	–07 59 13.8	SDSS	0.41	79	—	—	772	—	—
11[a]	J0212–0450	02 12 16.55	–04 50 38.8	EE	—	157	—	—	—	—	8
12	J0335–0719	03 35 48.23	–07 19 12.5	EE	—	86	—	—	—	—	1, 2
13	J0354–0522	03 54 04.69	–05 22 08.9	EE	—	608	—	—	—	—	1, 2, 4, 8, 9, 10
14	J0355–0553	03 55 24.70	–05 53 19.8	EE	—	80	—	—	—	—	1
15	J0654+5814	06 54 22.91	+58 14 26.0	EE	—	95	621	–0.84	—	—	—
16	J0655+5408	06 55 14.73	+54 08 57.2	GALEXASC	0.24[31]	3727	31666	–0.96	320	86.98	1, 2, 3, 10, 12
17	J0703+6014	07 03 11.18	+60 14 23.1	2MASX	—	55	154	–0.46	—	—	1
18	J0709+5716	07 09 58.26	+57 16 51.6	EE	—	271	1660	–0.81	—	—	1, 2, 6, 10, 12
19	J0712+5430	07 12 45.08	+54 30 10.8	EE	—	381	2406	–0.82	—	—	1, 2, 6, 10, 12
20	J0719+5519	07 19 36.64	+55 19 42.8	EE	—	61	424	–0.87	—	—	1
21	J0721+3551	07 21 29.03	+35 51 38.2	SDSS	—	503	4799	–1.01	—	—	—
22	J0723+3323	07 23 59.55	+33 23 20.2	EE	—	148	525	–0.57	—	—	1, 2, 6, 12, 20
23[a]	J0742+3339	07 42 59.47	+33 39 52.7	SDSS	0.64	334*	2729	–0.94	1214	77.05	—
24	J0743+1733	07 43 24.28	+17 33 41.3	EE	—	423	2494	–0.79	—	—	1, 2, 10, 12
25	J0747+2202	07 47 36.74	+22 02 15.9	SDSS	0.46	44	301	–0.86	606	4.65	1
26	J0748+2324	07 48 45.10	+23 24 45.8	SDSS	0.19	515	3238	–0.82	260	33.87	—
27	J0749+2007	07 49 19.08	+20 07 53.7	SDSS	0.37	139	960	–0.86	518	1.94	1, 2, 10, 12
28	J0750+1144	07 50 25.95	+11 44 52.0	SDSS	0.96	289	1846	–0.83	1512	172.51	15
29	J0758+4406	07 58 08.43	+44 06 17.0	EE	—	31	68	–0.35	—	—	1
30	J0758+1946	07 58 19.52	+19 46 56.5	SDSS	—	51	421	–0.94	—	—	1
31	J0758+1020	07 58 26.24	+10 20 18.6	SDSS	0.37	213	977	–0.68	447	15.63	1, 2, 12
32	J0802+6353	08 02 02.34	+63 53 03.3	LQAC	0.47	1052	—	—	1386	—	2, 6, 10, 12
33[a]	J0804+4659	08 04 53.99	+46 59 57.0	EE	—	52	—	—	—	—	1
34	J0811+2954	08 11 11.85	+29 54 53.6	EE	—	162	1550	–1.01	—	—	1, 2, 12, 20
35	J0817+2951	08 17 03.62	+29 51 47.1	TONS08w	0.37[32]	93	686	–0.89	316	5.88	1, 10
36	J0823+0335	08 23 16.90	+03 35 36.5	EE	—	90	214	–0.39	—	—	1
37	J0825+4623	08 25 24.05	+46 23 33.8	EE	—	38	148	–0.61	—	—	—
38	J0827+3748	08 27 05.80	+37 48 42.2	EE	0.21	379	3644	–1.01	446	6.65	1, 2, 4, 10, 12, 20
39	J0828+3057	08 28 03.00	+30 57 42.8	SDSS	0.36	102	460	–0.67	440	7.39	1, 2, 12, 20
40[a]	J0830+3510	08 30 36.26	+35 10 59.2	SDSS	—	76	—	—	—	—	1, 2
41	J0840+6413	08 40 25.47	+64 13 17.7	EE	—	30	213	–0.88	—	—	1

Table 3.1: **New candidate X-Shaped Radio Sources identified from VLA FIRST Survey**

Catalog Number	Host Name	R.A. (J2000.0) hh mm ss.ss	Decl. (J2000.0) dd mm ss.s	Ref.	Redshift (z)	F_{1400} (mJy)	F_{150} (mJy)	α_{150}^{1400}	Linear Size (kpc)	$L_{1.4GHz}$ (erg/s) ($\times 10^{42}$)	Other Catalogs
(1)	(2)	(3)	(4)	(5)	(6)	(7)	(8)	(9)	(10)	(11)	(12)
42	J0849+0949	08 49 40.02	+09 49 21.2	SDSS	0.36	575	3532	–0.81	816	36.52	2, 4, 8, 9, 10, 11, 15
43[a]	J0857–0339	08 57 11.73	–03 39 41.0	EE	0.17	1103	—	—	405	—	1, 2, 4, 8, 9, 10, 11, 15
44	J0858+5740	08 58 03.85	+57 40 13.8	SDSS	0.45	61	253	–0.64	427	7.45	1, 6, 12
45	J0906+1646	09 06 32.53	+16 46 05.6	SDSS	0.41	1616	—	—	818	—	3
46	J0914+6121	09 14 00.60	+61 21 11.6	EE	—	22	110	–0.72	—	—	—
47	J0917+4259	09 17 35.04	+42 59 07.6	SDSS	—	81	346	–0.65	—	—	1
48	J0931–0540	09 31 41.67	–05 40 48.0	EE	—	10	—	—	—	—	1
49	J0932+1610	09 32 43.96	+16 10 53.1	EE	—	273*	—	—	—	—	1, 2
50	J0933–0507	09 33 37.48	–05 07 18.8	EE	—	90	—	—	—	—	—
51	J0938+4520	09 38 34.68	+45 20 23.7	SDSS	0.45	258	1286	–0.72	906	28.51	1, 2, 6, 10, 12, 21
52	J0941+3853	09 41 04.00	+38 53 50.9	SDSS	0.62	682	4176	–0.81	1325	144.90	1, 2, 4, 10, 20
53	J0950+1420	09 50 10.79	+14 20 00.6	SDSS	0.55	3639	18298	–0.72	984	640.99	1, 2, 3, 11, 15
54[a]	J1001+2847	10 01 49.52	+28 47 08.9	SDSS	0.18	5589	—	—	561	—	2, 4, 10, 11, 20
55	J1021+4425	10 21 16.98	+44 25 39.8	EE	—	94	—	—	—	—	—
56	J1022+5213	10 22 12.66	+52 13 42.4	EE	—	151	1385	–0.99	—	—	1, 2, 7, 10, 12
57	J1023+4334	10 23 05.05	+43 34 33.2	EE	—	145	816	–0.77	—	—	—
58	J1031+5225	10 31 43.51	+52 25 35.1	SDSS	0.17	920	4846	–0.74	275	10.77	1, 2, 4, 10
59[a]	J1032+2730	10 32 57.60	+27 30 15.1	SDSS	—	72	262	–0.58	—	—	1, 16
60	J1049+5711	10 49 06.22	+57 11 53.0	EE	—	16	54	–0.54	—	—	1, 7
61	J1050+3240	10 50 11.17	+32 40 24.8	SDSS	—	33	119	–0.56	—	—	1, 7
62	J1107+5716	11 07 38.59	+57 16 00.4	EE	—	13	—	—	—	—	1
63	J1115+4314	11 15 21.25	+43 14 37.8	SDSS	0.46	350	1611	–0.68	540	42.78	6
64	J1122+0046	11 22 00.98	+00 46 31.5	EE	—	293	910	–0.51	—	—	1, 8, 10
65	J1124+4325	11 24 12.23	+43 25 50.0	SDSS	2.24	168	698	–0.64	3347	775.75	1, 2, 6, 10, 15
66	J1124+1717	11 24 57.40	+17 17 44.7	SDSS	0.14	12	—	—	113	—	1
67	J1130+3434	11 30 05.74	+34 34 28.8	EE	—	205	1315	–0.83	—	—	1, 7, 20
68	J1134+3835	11 34 03.87	+38 35 52.4	SDSS	0.50	324	—	—	852	—	1, 2, 12, 20
69	J1136–0329	11 36 01.40	–03 29 09.5	EE	—	292	—	—	—	—	1, 2, 10
70	J1138+1845	11 38 52.17	+18 45 33.2	SDSS	0.18	22	74	–0.54	172	0.43	1
71	J1141–0723	11 41 47.83	–07 23 24.7	APMUKS	—	114	—	—	—	—	1
72	J1142+5832	11 42 23.84	+58 32 01.5	EE	—	160	—	—	—	—	—
73	J1144+1031	11 44 20.33	+10 31 35.3	SDSS	0.28	38	160	–0.64	274	1.58	1
74	J1149+2554	11 49 08.01	+25 54 38.7	EE	—	62	410	–0.84	—	—	—
75	J1149+4618	11 49 50.67	+46 18 50.6	SDSS	0.62	129	776	–0.80	1025	28.40	1, 2, 6, 12, 21
76	J1150+3622	11 50 50.16	+36 22 03.7	SDSS	0.14	540	3435	–0.83	209	4.16	1, 2, 4, 10, 12, 20
77	J1155–0646	11 55 52.78	–06 46 37.9	EE	—	36	—	—	—	—	1
78	J1157+0845	11 57 54.33	+08 45 01.4	SDSS	0.43	176	873	–0.72	754	17.58	1, 2, 10
79	J1201+2520	12 01 24.72	+25 20 23.7	SDSS	0.50	857	4160	–0.71	977	123.97	1, 2, 4, 20
80	J1210+3157	12 10 37.57	+31 57 06.0	SDSS	0.39	274	—	—	1019	—	2, 7
81	J1211+5717	12 11 22.96	+57 17 51.7	SDSS	—	220	1999	–0.99	—	—	1, 2, 6
82	J1213+1343	12 13 06.68	+13 43 17.8	SDSS	0.17	225	884	–0.61	229	3.56	13, 16
83	J1220+6053	12 20 04.90	+60 53 16.5	SDSS	0.34	32	100	–0.51	383	2.74	1
84	J1222–0638	12 22 48.91	–06 38 01.7	EE	—	95	—	—	—	—	1, 2
85	J1235+2120	12 35 26.66	+21 20 34.7	SDSS	0.42	2913	21017	–0.88	2117	249.94	2, 3, 9, 10, 11

Table 3.1: **New candidate X-Shaped Radio Sources identified from VLA FIRST Survey**

Catalog Number	Host Name	R.A. (J2000.0) hh mm ss.ss	Decl. (J2000.0) dd mm ss.s	Ref.	Redshift (z)	F_{1400} (mJy)	F_{150} (mJy)	α_{150}^{1400}	Linear Size (kpc)	$L_{1.4GHz}$ (erg/s) ($\times 10^{42}$)	Other Catalogs
(1)	(2)	(3)	(4)	(5)	(6)	(7)	(8)	(9)	(10)	(11)	(12)
86	J1238+2752	12 38 26.08	+27 52 06.5	EE	—	72	268	–0.59	—	—	—
87	J1239+1706	12 39 04.34	+17 06 26.2	SDSS	—	44	272	–0.82	—	—	—
88	J1242+4244	12 42 37.96	+42 44 03.1	SDSS	—	277	1216	–0.66	—	—	4, 1
89	J1247+0807	12 47 55.91	+08 07 33.9	SDSS	0.43	68	288	–0.65	527	7.44	1
90	J1252–0120	12 52 30.70	–01 20 17.3	SDSS	0.36	269	—	—	612	—	1, 2, 8, 10
91[a]	J1258+4435	12 58 00.87	+44 35 28.7	SDSS	—	960	—	—	—	—	15
92	J1300+2215	13 00 49.09	+22 15 47.4	SDSS	0.22	47	154	–0.53	298	1.48	1, 13
93	J1311–0234	13 11 34.09	–02 34 08.0	EE	—	381	—	—	—	—	—
94	J1311+4101	13 11 44.32	+41 01 58.3	EE	—	420	—	—	—	—	—
95	J1325+1535	13 25 43.66	+15 35 52.1	SDSS	—	69	512	–0.90	—	—	—
96	J1333+0219	13 33 45.13	+02 19 12.0	SDSS	1.23	200	930	–0.69	2249	230.13	1, 2, 9
97[a]	J1336–0730	13 36 06.55	–07 30 25.5	APMUKS	—	70	—	—	—	—	1
98	J1336+3626	13 36 27.73	+36 26 27.3	EE	—	102	526	–0.73	—	—	1
99	J1338+3851	13 38 49.80	+38 51 11.7	EE	0.25	3461	23868	–0.86	363	87.07	1, 2, 3, 10, 12, 20
100	J1349+1858	13 49 06.04	+18 58 28.0	SDSS	0.19	189	839	–0.67	279	3.22	1, 2, 10, 12
101	J1354+5840	13 54 45.99	+58 40 00.7	SDSS	5.7E–3	15	44	–0.48	3	3.19E–4	1, 14, 15, 19
102[a]	J1358+1203	13 58 59.01	+12 03 58.7	EE	—	43	184	–0.65	—	—	1
103	J1400+2719	14 00 08.00	+27 19 14.1	EE	0.16	534	2738	–0.73	320	5.51	1, 2, 4, 20
104[a]	J1403+3827	14 03 11.75	+38 27 59.4	SDSS	0.54	674	3419	–0.73	1437	112.94	4
105	J1407+5131	14 07 24.20	+51 31 24.4	EE	—	420	—	—	—	—	—
106	J1412+1739	14 12 17.00	+17 39 48.0	EE	—	23	—	—	—	—	1
107	J1412+5839	14 12 47.81	+58 39 34.7	EE	—	40	235	–0.79	—	—	1
108	J1417+4051	14 17 58.37	+40 51 53.3	SDSS	—	252	1487	–0.79	—	—	—
109	J1418+2323	14 18 32.78	+23 23 34.7	EE	—	22	110	–0.72	—	—	—
110	J1419+2303	14 19 42.59	+23 03 27.6	EE	—	24	208	–0.97	—	—	—
111	J1420+5122	14 20 29.66	+51 22 33.9	SDSS	0.70	148	773	–0.74	771	44.98	16
112	J1422+5022	14 22 25.25	+50 22 13.3	SDSS	0.18	22	69	–0.51	131	0.47	1, 14
113	J1422+1935	14 22 58.76	+19 35 45.8	EE	—	3659	—	—	—	—	—
114[a]	J1424+0025	14 24 19.98	+00 25 36.5	SDSS	—	159	714	–0.67	—	—	1, 2, 8, 10
115[a]	J1440+6035	14 40 48.22	+60 35 46.0	SDSS	—	166	849	–0.73	—	—	1, 6
116	J1443+1440	14 43 00.08	+14 40 17.0	EE	—	66	276	–0.64	—	—	12
117[a]	J1454+0959	14 54 05.82	+09 59 52.6	SDSS	—	100	329	–0.53	—	—	12
118[a]	J1504+5749	15 04 08.06	+57 49 22.6	SDSS	—	94	—	—	—	—	1
119[a]	J1506+2027	15 06 19.14	+20 27 40.8	SDSS	—	293	2353	–0.93	—	—	12
120	J1516+3205	15 16 47.11	+32 05 14.7	SDSS	0.54	112	389	–0.56	480	23.56	1, 2, 6, 12
121	J1519+5342	15 19 36.72	+53 42 55.4	SDSS	0.48	479	—	—	772	—	15
122	J1519–0408	15 19 49.79	–04 08 42.9	EE	—	231	—	—	—	—	2, 8, 10
123	J1523+1130	15 23 27.56	+11 30 23.9	SDSS	0.20	413	1258	–0.50	247	11.37	1, 2, 12, 15
124[a]	J1523+2116	15 23 31.75	+21 16 56.8	SDSS	—	60	223	–0.59	—	—	1
125	J1537+3902	15 37 49.51	+39 02 37.6	SDSS	—	94	492	–0.74	—	—	21
126	J1539+5030	15 39 56.56	+50 30 08.7	EE	—	85	279	–0.53	—	—	1
127	J1553+2811	15 53 07.01	+28 11 24.7	EE	—	54	226	–0.64	—	—	1
128	J1553+2348	15 53 43.59	+23 48 25.4	SDSS	0.12	618	—	—	424	—	2, 4, 11, 12, 14, 15
129	J1558+3404	15 58 31.84	+34 04 44.0	SDSS	0.51	87	329	–0.60	556	15.17	1
130	J1605+1743	16 05 08.98	+17 43 47.6	SDSS	0.03	793	3092	–0.61	40	0.36	1, 2, 4, 11, 14, 19
131	J1607+1551	16 07 06.99	+15 51 33.9	SDSS	0.50	651	2044	–0.51	669	123.79	—
132	J1617+3222	16 17 42.53	+32 22 34.3	SDSS	0.15	2587	10002	–0.60	386	30.54	2, 3, 10, 11, 20
133	J1620+1736	16 20 21.82	+17 36 24.0	SDSS	0.56	1995	16503	–0.94	1148	330.25	2, 4, 11, 12, 15

Table 3.1: **New candidate X-Shaped Radio Sources identified from VLA FIRST Survey**

Catalog Number	Host Name	R.A. (J2000.0) hh mm ss.ss	Decl. (J2000.0) dd mm ss.s	Ref.	Redshift (z)	F_{1400} (mJy)	F_{150} (mJy)	α_{150}^{1400}	Linear Size (kpc)	$L_{1.4GHz}$ (erg/s) ($\times 10^{42}$)	Other Catalogs
(1)	(2)	(3)	(4)	(5)	(6)	(7)	(8)	(9)	(10)	(11)	(12)
134	J1626+4827	16 26 54.30	+48 27 39.1	SDSS	—	37	167	–0.67	—	—	1
135	J1628+1658	16 28 31.47	+16 58 33.3	SDSS	—	38	160	–0.64	—	—	1
136	J1633+3025	16 33 23.72	+30 25 00.4	SDSS	0.57	124	482	–0.61	565	26.93	20
137[a]	J1635+3722	16 35 02.53	+37 22 14.7	SDSS	0.46	645	2630	–0.63	862	84.95	4
138	J1643+3729	16 43 06.16	+37 29 30.3	SDSS	0.56	1440	8535	–0.80	906	246.99	—
139	J1650+3455	16 50 26.81	+34 55 36.0	SDSS	0.19	216	788	–0.58	255	4.42	20
140	J1708+2435	17 08 46.13	+24 35 28.8	SDSS	1.36	369	2176	–0.79	2890	508.52	—
141	J1709+3425	17 09 39.15	+34 25 50.8	SDSS	0.08	646	3534	–0.76	113	1.58	4, 10, 11, 12
142	J1712+3857	17 12 11.13	+38 57 06.8	SDSS	—	192	724	–0.59	—	—	1
143[a]	J1715+5420	17 15 39.44	+54 20 59.6	SDSS	0.18	320	2642	–0.94	229	4.24	1, 2, 4, 10, 12
144	J1719+6155	17 19 25.16	+61 55 33.9	EE	—	360	1989	–0.76	—	—	—
145	J1742+5917	17 42 43.67	+59 17 07.3	SDSS	—	1090	6030	–0.76	—	—	—
146	J1742+6145	17 42 51.59	+61 45 54.6	SDSS	0.54	1347	7048	–0.74	897	216.66	6
147	J2122+0001	21 22 17.10	+00 01 15.5	SDSS	0.42	157	722	–0.68	491	15.73	1, 12
148	J2123+1033	21 23 19.52	+10 33 26.0	SDSS	—	154	576	–0.59	—	—	1
149	J2153+0025	21 53 24.83	+00 25 25.7	EE	—	38	128	–0.54	—	—	1
150[a]	J2213–0854	22 13 12.57	–08 54 34.1	EE	—	600	—	—	—	—	—
151	J2213–0544	22 13 35.87	–05 44 22.7	EE	—	32	—	—	—	—	1
152	J2215–0525	22 15 01.79	–05 25 17.5	2MASX	0.09[33]	216	—	—	161	—	—
153	J2218+0012	22 18 30.16	+00 12 21.2	SDSS	0.29	412*	2763	–0.85	627	15.44	—
154	J2221–0326	22 21 29.54	–03 26 16.8	EE	0.36	83	—	—	475	—	1
155[a]	J2243–0954	22 43 49.64	–09 54 07.7	SDSS	—	87	—	—	—	—	—
156	J2248–0449	22 48 30.44	–04 49 45.2	EE	—	43	—	—	—	—	1
157	J2249+0209	22 49 40.32	+02 09 28.4	EE	—	182	1894	–1.05	—	—	1, 2, 12
158	J2257–0603	22 57 50.82	–06 03 42.5	EE	—	46	—	—	—	—	1
159	J2301+1136	23 01 57.79	+11 36 46.2	EE	—	161	860	–0.75	—	—	1, 2, 10, 12
160	J2324+1438	23 24 32.09	+14 38 21.9	SDSS	0.04	116*	—	—	46	—	1, 2, 11, 29
161	J2351–0109	23 51 56.12	–01 09 13.4	SDSS	0.17	1624	—	—	223	—	1, 2, 4, 8, 9, 10, 11, 14

Notes

[a] The soucre is present in Proctor (2011).

* The FIRST flux (at 1400 MHz) is used instead of NVSS flux (at 1400 MHz).

References

1: NVSS (Condon et al. 1998); 2: VLA Low-Frequency Sky Survey (VLSS; Cohen et al. 2007); 3: 3C (Bennett 1962; Edge et al. 1959); 4: 4C (Pilkington & Scott 1965; Gower et al. 1967; Caswell & Crowther 1969); 5: 5C (Kenderdine et al. 1966; Pooley & Kenderdine 1968; Pooley 1969; Willson 1970; Pearson 1975; Waggett 1977; Pearson & Kus 1978; Schuch 1981; Benn et al. 1982, 1988); 6: 6C (Baldwin et al. 1985; Hales et al. 1988, 1990, 1991, 1993a, 1993b); 7: 7C (McGilchrist et al. 1990; Kollgaard et al. 1994; Waldram et al. 1996; Vessey & Green 1998); 8: Parkes–MIT–NRAO (PMN; Griffith et al. 1994); 9: The Parkes Catalogue of Radio Ssources (PKS; Bolton et al. 1964); 10: Texas Survey of Radio Sources (TXS; Douglas et al. 1996); 11: Cul (Slee 1995); 12: 87 GB (Gregory & Condon 1991); 13: Automatic Spectroscopic K-means-based Classification (ASK; Sánchez et al. 2011); 14: Two Micron All Sky Survey Extended Objects–Final Release (2MASX; Skrutskie et al. 2006); 15: Galaxy Evolution Explorer All-sky Catalog (GALEXASC; Agüeros et al. 2005); 16: Galaxy Evolution Explorer Medium-deep Sky Catalog (GALEXMSC; Agüeros et al. 2005); 17: Gaussian Mixture Brightest Cluster Galaxy (GMBCG; Hao et al. 2010); 18: Maximum likelihood redshift Brightest Cluster Galaxy (MaxBCG; Koester et al. 2007); 19: New General Catalogue (NGC; Dreyer 1888); 20: B2 (Colla et al. 1970, 1972, 1973; Fanti et al. 1974); 21: B3 (Ficarra et al. 1985); 22: RC (Goss et al. 1992); 23: WHL (Wen et al. 2010); 24: MGC (Vorontsov-VelÝaminov & Arkhipova 1962); 25: Abell Clusters of Galaxies (ABELL; Abell 1958; Abell et al. 1989); 26: Wide-field Infrared Survey Explorer (WISE; Chung et al. 2011; Rebull et al. 2011); 27: WISE Blazar-like Radio-loud Sources (WB; White & Becker 1992); 28: Automated Plate Measurement United Kingdom Schmidt (APMUKS; Maddox et al. 1990); 29: Galaxy Identification Number (GIN; Wegner et al. 1996); 30: Ho & Kim (2009); 31: Hewitt & Burbidge (1991); 32: Brand et al. (2005); 33: Jones (2009)

Spitzer Space Telescope Source List version 4.2 (SSTSL2; Capak et al. 2013); Las Campanas Redshift Survey (LCRS; Shectman et al. 1996); Texas–Oxford NVSS Structure 08 h region (TONS08; Brand et al. 2003); TONS08 wider survey (TONS08w; Brand et al. 2005)

Table 3.2: **New candidate Z/S-Shaped Radio Sources identified from VLA FIRST Survey**

Catalog Number	Host Name	R.A. (J2000.0) hh mm ss.ss	Decl. (J2000.0) dd mm ss.s	Ref.	Redshift (z)	F_{1400} (mJy)	F_{150} (mJy)	α_{150}^{1400}	Linear Size (kpc)	$L_{1.4GHz}$ (erg/s) ($\times 10^{42}$)	Other Catalogs
(1)	(2)	(3)	(4)	(5)	(6)	(7)	(8)	(9)	(10)	(11)	(12)
1	J0002–0411	00 02 41.20	–04 11 55.2	GALEXASC	—	216	—	—	—	—	1, 2, 8, 10
2	J0047+1221	00 47 11.67	+12 21 24.9	EE	—	34	140	–0.63	—	—	—
3	J0126–0118	01 26 04.13	–01 18 22.2	EE	—	389*	—	—	—	—	—
4	J0133+0957	01 33 16.94	+09 57 30.8	SDSS	0.19	27	72	–0.44	192	0.76	1, 14
5	J0141+1213	01 41 09.94	+12 13 52.0	2MASX	—	348	—	—	—	—	—
6	J0145–0820	01 45 56.65	–08 20 26.3	SDSS	0.19	42	—	—	254	—	1
7	J0204–0915	02 04 06.30	–09 15 59.8	EE	—	207	—	—	—	—	1, 2, 8, 10
8	J0204–0716	02 04 54.96	–07 16 03.3	EE	—	263	—	—	—	—	1, 2, 8, 10
9[a]	J0206–0215	02 06 13.50	–02 15 04.1	EE	—	24	—	—	—	—	1
10	J0210–0310	02 10 30.61	–03 10 47.0	SDSS	0.24	25	—	—	240	—	1
11[b]	J0219+0155	02 19 58.72	+01 55 48.9	2MASS	0.04[30]	548	2063	–0.59	79	0.45	1, 2, 8, 9, 10
12	J0252–0756	02 52 27.53	–07 56 05.4	SDSS	0.08	112	—	—	91	—	1, 2, 13, 14
13	J0256+0016	02 56 40.12	+00 16 33.5	SDSS	—	20	92	–0.68	—	—	1
14	J0313–0631	03 13 29.05	–06 31 19.5	EE	—	80	—	—	—	—	1
15	J0325–0743	03 25 23.18	–07 43 48.5	SDSS	—	14	—	—	—	—	1
16[b]	J0710+3546	07 10 31.01	+35 46 50.5	EE	—	76	—	—	—	—	1, 6, 12
17	J0727+4228	07 27 28.88	+42 28 00.6	SDSS	—	54	175	–0.53	—	—	1, 16
18[a]	J0728+4935	07 28 01.48	+49 35 13.2	2MASX	0.08[31]	357	1531	–0.65	264	1.01	2, 10, 12
19	J0729+4142	07 29 55.79	+41 42 20.0	EE	—	117	488	–0.64	—	—	1, 2, 12, 21
20[a]	J0738+4820	07 38 37.70	+48 20 47.9	SDSS	—	26	102	–0.61	—	—	1, 14
21	J0738+3846	07 38 54.81	+38 46 27.8	SDSS	0.32	127	—	—	776	—	2, 20
22[b]	J0741+4618	07 41 01.91	+46 18 41.6	EE	—	230	1228	–0.75	—	—	1, 2, 10, 12, 21
23	J0746+4217	07 46 40.44	+42 17 09.2	SDSS	0.43	14	—	—	491	—	1
24	J0814+5059	08 14 31.27	+50 59 23.1	EE	—	60	329	–0.76	—	—	1, 6
25	J0816+0458	08 16 27.35	+04 58 47.6	2MASX	—	61	92	–0.18	—	—	8, 12, 22
26[a]	J0818+2247	08 18 54.09	+22 47 44.9	SDSS	0.10	308	1113	–0.58	146	1.48	1, 2, 10, 12
27[a]	J0831+0125	08 31 52.79	+01 25 53.3	SDSS	0.27	125	844	–0.86	468	3.88	—
28	J0832+4559	08 32 58.03	+45 59 28.2	SDSS	0.64	37	266	–0.88	710	8.38	1
29	J0839–0141	08 39 17.84	–01 41 58.1	MaxBCG	0.28	99	—	—	432	—	1
30	J0847+4934	08 47 51.14	+49 34 14.1	EE	—	234	1712	–0.89	—	—	1, 2, 10, 12
31	J0847+3147	08 47 58.65	+31 47 50.2	EE	—	164*	—	—	—	—	—
32	J0850+0153	08 50 51.71	+01 53 09.8	EE	—	50	192	–0.60	—	—	—
33	J0850+4753	08 50 53.41	+47 53 51.6	SDSS	0.18	67	273	–0.63	219	1.17	1, 2, 14
34	J0856+4951	08 56 18.72	+49 51 06.4	SDSS	0.62	37	167	–0.67	740	9.15	1
35[b]	J0859–0252	08 59 54.15	–02 52 41.8	EE	—	402	—	—	—	—	1, 2, 4, 8, 9, 10
36[a]	J0902+5203	09 02 36.84	+52 03 48.7	SDSS	0.10	425	2060	–0.71	229	1.75	1, 2, 6, 10, 12, 14
37	J0906+4752	09 06 20.55	+47 52 08.1	SDSS	0.24	154	—	—	446	—	14
38[a]	J0918–0650	09 18 13.05	–06 50 59.1	EE	—	58	—	—	—	—	1
39[a,b]	J0924+4034	09 24 01.17	+40 34 57.1	SDSS	0.16	320	2022	–0.82	313	3.21	1, 2, 10, 12, 14, 15, 21
40	J0926+2921	09 26 38.99	+29 21 22.6	SDSS	—	126	—	—	—	—	—

Table 3.2: **New candidate Z/S-Shaped Radio Sources identified from VLA FIRST Survey**

Catalog Number	Host Name	R.A. (J2000.0) hh mm ss.ss	Decl. (J2000.0) dd mm ss.s	Ref.	Redshift (z)	F_{1400} (mJy)	F_{150} (mJy)	α_{150}^{1400}	Linear Size (kpc)	$L_{1.4GHz}$ (erg/s) ($\times 10^{42}$)	Other Catalogs
(1)	(2)	(3)	(4)	(5)	(6)	(7)	(8)	(9)	(10)	(11)	(12)
41[a]	J0933–0310	09 33 10.69	–03 10 40.1	EE	—	75	—	—	—	—	1
42	J0940+1510	09 40 13.55	+15 10 53.2	SDSS	0.63	26	104	–0.62	685	6.98	1
43	J0941+0814	09 41 42.11	+08 14 0.5	EE	—	38	150	–0.61	—	—	—
44	J1004–0337	10 04 23.49	–03 37 26.8	EE	—	57	—	—	—	—	1
45	J1006–0621	10 06 48.08	–06 21 56.9	EE	—	267	—	—	—	—	1, 2, 8, 10
46[a,b]	J1011–0607	10 11 34.79	–06 07 53.0	EE	—	36	—	—	—	—	1
47	J1011+4353	10 11 49.38	+43 53 19.1	SDSS	—	329	1611	–0.71	—	—	1, 2, 6, 10, 12, 21
48[a]	J1014+3507	10 14 18.28	+35 07 29.1	SDSS	—	157	937	–0.80	—	—	1, 2, 7, 10, 12, 20
49[b]	J1018+1058	10 18 04.89	+10 58 41.7	EE	—	44	186	–0.64	—	—	1
50	J1028+0345	10 28 23.47	+03 45 31.4	SDSS	0.10	287	1477	–0.73	279	1.14	1, 2, 8, 10, 12, 14
51[a]	J1028+1943	10 28 56.38	+19 43 41.0	SDSS	0.60	231	1584	–0.86	944	46.33	15
52[a]	J1056+1128	10 56 14.77	+11 28 42.7	SDSS	0.42	21	92	–0.66	640	2.11	1
53	J1057+3012	10 57 20.44	+30 12 30.4	SDSS	0.24	79	272	–0.55	396	2.94	23
54[a]	J1122+2125	11 22 29.39	+21 25 02.4	EE	—	630	—	—	—	—	1, 2, 7, 9, 10, 11
55	J1127+1909	11 27 58.48	+19 09 27.3	EE	—	206	—	—	—	—	—
56[a]	J1138+2039	11 38 50.24	+20 39 18.3	SDSS	0.18	74*	267	–0.58	225	1.35	1, 13, 14
57	J1140+1743	11 40 16.98	+17 43 40.3	SDSS	0.01	1154	3884	–0.54	12	0.07	1, 2, 4, 10, 11, 14, 15, 19
58	J1145–0227	11 45 30.97	–02 27 11.2	SDSS	0.13	148	—	—	362	—	8
59	J1149+3802	11 49 50.18	+38 02 37.0	SDSS	0.53	62	250	–0.62	533	11.35	1
60[a,b]	J1156+2138	11 56 45.30	+21 38 09.1	SDSS	0.62	202	1004	–0.72	819	47.04	1, 2, 7, 12
61	J1157+3012	11 57 08.30	+30 12 17.1	EE	—	34	231	–0.86	—	—	1
62[b]	J1201+3257	12 01 51.87	+32 57 01.3	EE	—	158	—	—	—	—	6
63[a]	J1204+5531	12 04 06.72	+55 31 14.6	SDSS	—	459	—	—	—	—	15
64[a]	J1204+0345	12 04 25.76	+03 45 05.4	EE	—	62	220	–0.57	—	—	1
65	J1206–0621	12 06 26.31	–06 21 43.4	LCRS	—	130	—	—	—	—	1
66	J1208+2513	12 08 09.07	+25 13 57.0	EE	—	129*	257	–0.30	—	—	1
67	J1215+1709	12 15 43.82	+17 09 17.6	SDSS	0.10	488	1462	–0.49	233	2.81	1, 2, 10, 15
68	J1218+3548	12 18 19.04	+35 48 17.2	SDSS	0.25	129	576	–0.67	592	4.08	7, 10, 12, 14, 17, 20
69[a]	J1222+3758	12 22 09.68	+37 58 55.7	EE	—	170	—	—	—	—	—
70	J1223+2542	12 23 00.24	+25 42 02.9	SDSS	0.33	23	80	–0.56	493	1.58	1, 14
71	J1232+3130	12 32 11.44	+31 30 58.1	SDSS	0.35	80	320	–0.62	533	5.82	1
72	J1234–0804	12 34 37.40	–08 04 14.0	EE	—	88	—	—	—	—	1
73[a]	J1243–0613	12 43 34.68	–06 13 22.2	2MASX	0.14[32]	367	—	—	357	—	1, 2, 4, 8, 9, 10, 14, 15
74[a]	J1255+4405	12 55 54.60	+44 05 21.8	SDSS	—	51	156	–0.50	—	—	—
75	J1300–0337	13 00 31.44	–03 37 46.2	SDSS	—	170	—	—	—	—	—
76[a]	J1303+0339	13 03 59.47	+03 39 32.3	SDSS	0.18	420	2530	–0.49	657	5.77	2, 4, 9, 10
77[a]	J1304+2015	13 04 22.28	+20 15 56.3	SDSS	0.19	66	331	–0.72	225	1.09	1, 13, 14, 18, 23
78	J1305+3622	13 05 51.80	+36 22 53.0	MaxBCG	0.31	211	910	–0.65	417	9.85	20
79[a]	J1307+1218	13 07 55.53	+12 18 48.3	SDSS	0.18	60	199	–0.54	275	1.13	1, 15
80[a]	J1308–0500	13 08 39.03	–05 00 37.5	2MASX	—	272	—	—	—	—	28

Table 3.2: **New candidate Z/S-Shaped Radio Sources identified from VLA FIRST Survey**

Catalog Number	Host Name	R.A. (J2000.0) hh mm ss.ss	Decl. (J2000.0) dd mm ss.s	Ref.	Redshift (z)	F_{1400} (mJy)	F_{150} (mJy)	α_{150}^{1400}	Linear Size (kpc)	$L_{1.4GHz}$ (erg/s) ($\times 10^{42}$)	Other Catalogs
(1)	(2)	(3)	(4)	(5)	(6)	(7)	(8)	(9)	(10)	(11)	(12)
81	J1310+2600	13 10 46.12	+26 00 58.5	SDSS	—	100	348	–0.56	—	—	—
82[a]	J1319+0502	13 19 43.59	+05 02 43.0	SDSS	1.28	27	—	—	2457	—	1
83[a]	J1320+2532	13 20 00.19	+25 32 43.8	SDSS	0.13	316	1380	–0.66	207	2.68	1, 2, 7, 14, 20
84[a]	J1325+5736	13 25 11.19	+57 36 01.2	SDSS	0.12	110	1643	–1.21	297	0.68	14, 24, 25
85[a]	J1327+0007	13 27 57.49	+00 07 51.3	SDSS	0.51	62	275	–0.67	949	9.61	1
86	J1328+0150	13 28 42.37	+01 50 59.5	SDSS	—	10	43	–0.65	—	—	1
87	J1337+5348	13 37 57.66	+53 48 25.2	SDSS	0.10	29	72	–0.41	121	0.23	1
88[a]	J1339+1024	13 39 13.64	+10 24 47.9	SDSS	—	116	782	–0.85	—	—	1
89	J1345+3124	13 45 41.65	+31 24 06.4	SDSS	0.22	80	214	–0.44	258	3.05	1, 14
90[a]	J1346+6220	13 46 17.54	+62 20 45.4	SDSS	0.12	160	673	–0.64	173	1.03	1, 2, 6, 10, 12, 15, 26, 27
91[a]	J1349+4306	13 49 29.86	+43 06 10.2	EE	—	163	1129	–0.87	—	—	21
92	J1356+4555	13 56 59.94	+45 55 04.6	2MASX	0.24	95	355	–0.59	289	3.22	1, 21
93[a]	J1359+6119	13 59 54.22	+61 19 45.2	SDSS	0.18	30	104	–0.56	210	0.55	1
94	J1402+4612	14 02 32.38	+46 12 33.7	SDSS	0.56	93	500	–0.75	883	16.25	1, 2, 12, 15, 21
95	J1404+3701	14 04 11.63	+37 01 26.6	EE	—	26	142	–0.76	—	—	1
96[a]	J1410+3014	14 10 50.88	+30 14 09.6	2MASX	0.18[33]	84	235	–0.46	338	1.84	1, 18
97	J1411+4535	14 11 10.93	+45 35 18.1	EE	—	35	86	–0.40	—	—	1
98	J1417+0812	14 17 31.27	+08 12 30.1	SDSS	0.06	352	—	—	208	—	2, 14, 15, 19
99[a]	J1418+0952	14 18 13.47	+09 52 38.5	SDSS	0.34	333	692	–0.33	622	42.84	1, 2, 16
100[a]	J1418+3530	14 18 40.50	+35 30 01.6	2MASX	—	90	194	–0.34	—	—	1
101[a]	J1426+2158	14 26 23.01	+21 58 39.5	SDSS	0.20	81	—	—	359	—	1
102	J1426+3411	14 26 59.61	+34 11 59.6	SDSS	0.13	304	—	—	326	—	15
103	J1437+1616	14 37 16.71	+16 16 04.1	SDSS	0.27	38	—	—	493	—	1
104	J1439+1106	14 39 28.37	+11 06 02.7	EE	—	43	115	–0.44	—	—	1
105	J1442+5043	14 42 19.18	+50 43 57.9	SDSS	0.17	205	878	–0.65	326	3.04	1, 17
106	J1524+1627	15 24 19.50	+16 27 12.4	SDSS	0.15	191	262	–0.14	247	7.35	14
107	J1526+0053	15 26 42.05	+00 53 28.8	SDSS	0.12	236	612	–0.43	165	2.35	1, 2, 8, 12
108	J1529–0629	15 29 19.98	–06 29 21.5	EE	—	109	—	—	—	—	1
109	J1530+3301	15 30 22.23	+33 01 19.5	EE	—	12	41	–0.55	—	—	1
110	J1530–0703	15 30 58.88	–07 03 32.4	2MASS	—	147	—	—	—	—	—
111	J1536+2357	15 36 38.05	+23 57 06.1	SDSS	0.51	59	410	–0.87	767	7.89	1
112	J1536–0453	15 36 55.69	–04 53 50.0	EE	—	25	—	—	—	—	1
113[a]	J1540+1110	15 40 13.80	+11 10 08.6	EE	—	27	118	–0.66	—	—	1
114[a]	J1553–0323	15 53 06.36	–03 23 18.5	EE	—	134	—	—	—	—	—
115	J1604+2355	16 04 56.66	+23 55 57.6	SDSS	0.03	661	—	—	122	—	1, 2, 4, 14, 15, 19
116[a]	J1608+4309	16 08 04.52	+43 09 48.5	SDSS	0.08	76	224	–0.48	96	0.35	1, 13, 14
117	J1608+3505	16 08 29.68	+35 05 53.8	SDSS	0.35	37	153	–0.64	506	2.60	1
118	J1613+1921	16 13 35.02	+19 21 05.8	SDSS	—	195	803	–0.63	—	—	—
119	J1617+1420	16 17 52.73	+14 20 17.2	SDSS	—	37	156	–0.64	—	—	1
120	J1633+4220	16 33 13.40	+42 20 31.3	SDSS	0.12	110	179	–0.22	197	2.00	1, 12, 14, 21

Table 3.2: **New candidate Z/S-Shaped Radio Sources identified from VLA FIRST Survey**

Catalog Number	Host Name	R.A. (J2000.0) hh mm ss.ss	Decl. (J2000.0) dd mm ss.s	Ref.	Redshift (z)	F_{1400} (mJy)	F_{150} (mJy)	α_{150}^{1400}	Linear Size (kpc)	$L_{1.4GHz}$ (erg/s) ($\times 10^{42}$)	Other Catalogs
(1)	(2)	(3)	(4)	(5)	(6)	(7)	(8)	(9)	(10)	(11)	(12)
121[a]	J1643+2642	16 43 18.86	+26 42 35.3	EE	—	68	330	–0.71	—	—	1
122	J1649+5358	16 49 34.80	+53 58 16.0	2MASX	—	176	542	–0.50	—	—	—
123[a]	J1728+4200	17 28 43.50	+42 00 06.5	EE	—	31	—	—	—	—	—
124	J2107–0203	21 07 44.25	–02 03 40.4	EE	—	48	—	—	—	—	1
125	J2129–0549	21 29 00.88	–05 49 52.9	EE	—	33	—	—	—	—	1
126	J2137–0811	21 37 25.01	–08 11 05.6	SDSS	—	57	—	—	—	—	1
127	J2159–0211	21 59 15.62	–02 11 25.3	SDSS	0.30	58	—	—	332	—	1
128	J2210+1050	22 10 21.47	+10 50 55.4	EE	—	63	265	–0.64	—	—	1, 2
129	J2250–0439	22 50 56.53	–04 39 41.1	EE	—	30	—	—	—	—	1
130	J2306–0341	23 06 27.76	–03 41 23.3	EE	—	51	—	—	—	—	1
131	J2307+1253	23 07 16.28	+12 53 31.3	SDSS	0.22	57	206	–0.57	234	1.67	1, 12
132	J2321–0912	23 21 21.90	–09 12 42.8	SDSS	—	46	—	—	—	—	1
133[a]	J2322–0941	23 22 08.20	–09 41 53.1	EE	—	125	—	—	—	—	1
134	J2331–0129	23 31 13.39	–01 29 13.2	EE	—	328	—	—	—	—	16
135[a]	J2339+0042	23 39 00.34	+00 42 57.8	SDSS	0.18	29	—	—	260	—	1, 13, 14, 16

Notes

[a] The source is present in Proctor (2011).

[b] The soucre is cataloged as an XRG by Yang et al. (2019).

* The FIRST flux (at 1400 MHz) is used instead of the NVSS flux (at 1400 MHz).

References

1: NVSS (Condon et al. 1998); 2: VLSS (Cohen et al. 2007); 3: 3C (Bennett 1962; Edge et al. 1959); 4: 4C (Pilkington & Scott 1965; Gower et al. 1967; Caswell & Crowther 1969); 5: 5C (Kenderdine et al. 1966; Pooley & Kenderdine 1968; Pooley 1969; Willson 1970; Pearson 1975; Waggett 1977; Pearson & Kus 1978; Schuch 1981; Benn et al. 1982, 1988); 6: 6C (Baldwin et al. 1985; Hales et al. 1988, 1990, 1991, 1993a, 1993b); 7: 7C (McGilchrist et al. 1990; Kollgaard et al. 1994; Waldram et al. 1996; Vessey & Green 1998); 8: PMN (Griffith et al. 1994); 9: PKS (Bolton et al. 1964); 10: TXS (Douglas et al. 1996); 11: Cul (Slee 1995); 12: 87 GB (Gregory & Condon 1991); 13: ASK (Sánchez et al. 2011); 14: 2MASX (Skrutskie et al. 2006); 15: GALEXASC (Agüeros et al. 2005); 16: GALEXMSC (Agüeros et al. 2005); 17: GMBCG (Hao et al. 2010); 18: MaxBCG (Koester et al. 2007); 19: NGC (Dreyer 1888); 20: B2 (Colla et al. 1970, 1972, 1973; Fanti et al. 1974); 21: B3 (Ficarra et al. 1985); 22: RC (Goss et al. 1992); 23: WHL (Wen et al. 2010); 24: MGC (Vorontsov-VelẎaminov & Arkhipova 1962);25: ABELL (Abell 1958; Abell et al. 1989); 26: WISE (Chung et al. 2011; Rebull et al. 2011); 27: WB (White & Becker 1992); 28: APMUKS (Maddox et al. 1990); 29: GIN (Wegner et al. 1996); 30: Falco et al. (1999); 31: Machalski (1998); 32: Jones (2009); 33: Rykoff et al. (2012)

SSTSL2 (Capak et al. 2013); LCRS (Shectman et al. 1996); TONS08 (Brand et al. 2003); TONS08w (Brand et al. 2005)

References

Abell, G. O. 1958, ApJS, 3, 211
Abell, G. O., Corwin H. G. Jr., & Olowin, R. P. 1989, ApJS, 70, 1
Agüeros, M. A., Ivezić, Ž., Covey, K. R., et al. 2005, The Astronomical Journal, 130, 1022
Baldwin, J. E., Boysen, R. C., Hales, S. E. G., et. al 1985, MNRAS, 217, 717
Becker, R. H., White, R. L., & Helfand, D. J. 1994, ASP Conference Series, 61, 165
Becker, R. H., White, R. L., & Helfand, D. J. 1995, ApJ, 450, 559
Benn, C. R., Gruff, G., Vigotti, M., & Wall, J. V. 1982, MNRAS, 200, 747
Benn, C. R., Grueff, G., Vigotti, M., & Wall, J. V. 1988, MNRAS, 230, 1
Bennett, A. S. 1962, MmRAS., 68, 163
Bolton, J., Gardner, F., & Mackey, M. 1964, Australian J. Phys., 17, 340
Boyle, B. J., Shanks, T., Croom, S. M., et al. 2000, MNRAS, 317, 1014
Brand, K., Rawlings, S., Hill, G. J., Lacy, M., Mitchell, E., & Tufts, J. 2003, MNRAS, 344, 283
Brand, K., Rawlings, S., Hill, G. J., & Tufts, J. R. 2005, MNRAS, 357, 1231
Capak, P. L., Teplitz, H. I., Brooke, T. Y., Laher, R., Science Center, Spitzer 2013, AAS Meeting, 221, id.340.06
Caswell, J. L., & Crowther, J. H. 1969, MmRAS, 145, 181
Cheung, C. C. 2007, AJ, 133, 2097
Chung, S. M., Eisenhardt, P. R., Gonzalez, A. H., et al. 2011, ApJ, 743, 10
Cohen, A. S., Lane, W. M., Cotton, W. D., et al. 2007, AJ, 134, 1245
Colla, G., Fanti, C., Ficarra, A., et al. 1970, A&AS, 1, 281
Colla, G., Fanti, C., Fanti, R., et al. 1972, A&AS, 7, 1
Colla, G., Fanti, C., Fanti, R., et al. 1973, A&AS, 11, 291
Condon, J. J., Cotton, W. D., Greisen, E. W., et al. 1998, AJ, 115, 1693
Douglas, J. N., Bash, F. N., Bozyan, F. A., Torrence G. W., & Wolfe, C. 1996, AJ, 111, 1945
Dreyer, J. L. E. 1888, MmRAS, 49, 1
Edge, D. O., Shakeshaft, J. R., McAdam, W. B., Baldwin, J. E., & Archer, S. 1959, MmRAS, 68, 37
Falco, E. E., Kurtz, M. J., Geller, M. J., et al. 1999, PASP, 111, 438
Fanti, C., Fanti, R., Ficarra, A., & Padrielli, L. 1974, A&AS, 18, 147
Ficarra, A., Grueff, G., & Tomassetti, G. 1985, A&A, 59, 255
Goss, W. M., Pariiskii, Y. N., Soboleva, N. S., et al. 1992, Soviet Astronomy, 36,

343
Gower, J. F. R., Scott, P. F., & Wills, D. 1967, MmRAS, 71, 49
Gregory, P. C., & Condon, J. J. 1991, ApJS, 75, 1011
Griffith, M. R., Wright, A. E., Burke, B. F., & Ekers, R. D. 1994, ApJS, 90, 179
Gunn, J. E., Walter, A. S., Edward, J. M., et al. 2006, AJ, 131, 2332
Hakobyan, A. A., Adibekyan, V. Z., Aramyan, L. S., et al. 2012, A&A, 544, 81
Hales, S. E. G., Baldwin, J. E., & Warner, P. J. 1988, MNRAS, 234, 919
Hales, S. E. G., Masson, C. R., Warner, P. J., & Baldwin, J. E. 1990, MNRAS, 246, 256
Hales, S. E. G., Baldwin, J. E., & Warner, P. J. 1993a, MNRAS, 263, 25
Hales, S. E. G., Masson, C. R., Warner, P. J., Baldwin, J. E., & Green, D. A. 1993b, MNRAS, 262, 1057
Hales, S. E. G., Mayer, C. J., Warner, P. J., & Baldwin, J. E. 1991, MNRAS, 251, 46
Hao, J., McKay, T. A., Koester, B. P et al. 2010, ApJS, 191, 254
Hewitt, A., Burbidge, G. 1991, ApJS, 75, 297
Ho, L. C., & Kim, M. 2009, ApJS, 184, 398
Intema, H. T., Jagannathan, P., Mooley, K. P., & Frail, D. A. 2017, A&A, 598, A78
Jones, D. H., Read, M. A., Saunders, W., et al 2009, MNRAS, 399, 683
Kenderdine, S., Ryle, M. S., & Pooley, G. G. 1966, MNRAS, 134, 189
Koester, B. P, McKay, T. A., Annis, J., et al. 2007, ApJ, 660, 239
Kollgaard, R. I., Brinkmann, W., Chester, M. M., et al. 1994, ApJS, 93, 145
Lasker, B. 1994, STScI Newsletter 11, 2, 39
Leahy, J. P., & Parma, P. 1992, in Proc. IAP Meeting 7, Extragalactic Radio Sources. From Beams to Jets, ed. J. Roland et al. (Cambridge: Cambridge Univ. Press), 307
Machalski, J. 1998, A&AS, 128, 153
Maddox, S. J., Efstathiou, G., Sutherland, W. J., & Loveday, J. 1990, MNRAS, 243, 692
McGilchrist, M. M., Baldwin, J. E., Riley, J. M., et al. 1990, MNRAS, 246, 110
Nilsson, K. 1998, A&AS, 132, 31
Nilsson, K., Valtonen, M. J., Kotilainen, J., & Jaakkola, T. 1993, ApJ, 413, 453
O'Dea, C. P., & Owen, F. N. 1987, ApJ, 316, 95
Peacock, J. A. 1983, MNRAS, 202, 615
Pearson, T. 1975, MNRAS, 171, 475
Pearson, T., & Kus, A. J. 1978, MNRAS, 182, 273

Pilkington, J. D. H., & Scott, J. F. 1965, MmRAS, 69, 183
Planck Collaboration, Aghanim, N., Akrami, Y., et al. 2020, A&A, 641, A6
Pooley, G. G. 1969, MNRAS, 144, 101
Pooley, G. G., & Kenderdine, S. 1968, MNRAS, 139, 529
Proctor, D. D. 2011, ApJS, 194, 31
Randall, K. E., Hopkins, A. M., Norris, R. P., et al. 2012, MNRAS, 421, 1644
Rebull, L. M., Koenig, X. P., Padgett, D. L., et al. 2011, ApJS, 196, 19
Richards, G. T., Myers, A. D., Gray, A. G., et al. 2009, ApJS, 180, 67
Rykoff, E. S., Koester, B. P., Rozo, E, et al., 2012, ApJ, 746, 178
Sánchez, A. J., Aguerri, J. A. L., Muñoz-Tuñón, C., & Huertas-Company, M. 2011, ApJ, 735, 15
Saripalli, L., & Roberts, D. H. 2018, ApJ, 852, 48
Schuch, N. 1981, MNRAS, 196, 695
Shectman, S. A., Landy, S. D., Oemler, A., Tucker, D. L., Lin H., Kirshner, P., & Schechter, P. L. 1996, ApJ, 470, 172
Skrutskie, M. F., Cutri, R. M., Stiening, R., et al. 2006, AJ, 131, 1163
Slee, O. 1995, Australian J. Phys., 48, 143
Smirnov, N. 1948, Ann. Math. Stat., 19, 279
Spinrad, H., Djorgovski, S., Marr, J., & Aguilar, L. 1985, Publ. Astron. Soc. Pacific, 97, 932
Tiwari, P. 2019, RAA, 19, 096
Véron-Cetty, M. P., & Véron, P. 2006, A&A, 455, 773
Vessey, S. J., & Green, D. A. 1998, MNRAS, 294, 607
Vorontsov-Vel'Yaminov, B. A., & Arkhipova, V. P. 1962, Morpholoqical Trudy Gos. Astron. Inst. Shternberga, 1
Waggett, P. 1977, MNRAS, 181, 547
Waldram, E. M., Yates, J. A., Riley, J. M., & Warner, P. J. 1996, MNRAS, 282, 779
Wegner, G., Colless, M., Baggley, G., et al. 1996, ApJS, 106, 1
Wen, Z. L., Han, J. L., & Liu, F. S. 2010, ApJS, 187, 272
White, R. L., & Becker, R. H. 1992, ApJS, 79, 331
White, R. L., Becker, R. H., Helfand, D. J., & Gregg, M. D. 1996, ApJ, 475, 479
Willson, M. 1970, MNRAS, 151, 1
Xu, J., & Han, J. L. 2014, MNRAS, 442, 3329
Yang, X., Joshi, R., Gopal-Krishna, et al. 2019, ApJS, 245, 1

Chapter 4

'Winged' Radio Sources from LoTSS DR1

The stars don't look bigger.
But they do look brighter.

—Sally Ride

After the systematic search for winged radio sources in the high-frequency data, the FIRST survey data at 1400 MHz, we will now continue our search for the sources in the low-frequency range. In this Chapter, we will search for winged sources from the LoTSS DR1 at 144 MHz. The LoTSS DR1 is the first data released by the LOFAR telescopic systems. Due to its better resolution and sensitivity than other existing data surveys, LoTSS DR1 is an appropriate choice for our findings. There are numerous studies, already done from the LOFAR (as well as LoTSS DR1). The science goal of this survey includes the study of the following fields: compact objects, active galactic nuclei, galaxy formation, and its evolution, cosmology, large-scale structure and lensing, and exoplanets. The details of the LOFAR survey and its superiority are given in the first sections. In the next section we describe our methodology for the search. In the last two sections we present the results and the analysis of our study.

4.1 LOFAR

The LOw-Frequency Array (LOFAR) is a massive radio telescope with a network of antennas primarily in the Netherlands (van Haarlem et al. 2013). As of now,

LOFAR is currently the largest ground-based radio telescope operating at the lowest frequency ranges[1]. As of 2019, it had spread to seven more European nations. The Netherlands Institute for Radio Astronomy, known as ASTRON, initially developed and set up the instrument. The facility opened in 2010 and since then it has been maintained by ASTRON on behalf of the International LOFAR Telescope (ILT) collaboration. The LOFAR is made up of a massive array of omnidirectional radio antennas that use a new idea in which the signals from the individual antennas are not directly electrically coupled to serve as a single giant antenna, as they are in traditional array antennas, rather, LOFAR dipole antennas (of two kinds) are dispersed in stations, where the antenna signals can be partially merged in analog electronics, then digitized, and finally combined over the entire station. This step-by-step technique allows significant flexibility in configuring and swiftly adjusting an antenna. This gives the station's directional sensitivity to the sky. Hence, the LOFAR (since 2019) has been an interferometric array, employs around 20,000 tiny antennas, and is focused on 52 stations. Thus, the architecture of LOFAR makes it a particularly effective survey device. Individual dipoles are sensitive to most of the visible sky, whereas dipole arrays have hundreds of square degrees of field of view at the lowest frequencies accessible to LOFAR. The LOFAR incorporates elements of previous telescopes. It employs omnidirectional dipole antennas as phased array elements at separate stations and then merges those phased arrays using the aperture synthesis technique. The LOFAR observes in the frequency range of 10 MHz to 240 MHz. There are two types of antennas: Low Band Antenna (LBA) and High Band Antenna (HBA), which are designed for 10-80 MHz and 120-240 MHz frequency ranges, respectively. The LOFAR system is sometimes termed a Software Telescope because the electric signals from the LOFAR stations are digitized, sent to a central digital processor, and merged into software to map the sky. An upgraded version known as LOFAR2.0 is also planned. Some sample images of the LOFAR are presented in 4.1.

Performing high sensitive surveys is always a key astronomical endeavor. When compared to existing radio telescopes, the LOFAR telescope provides a transformative boost in radio survey speed. It also provides access to a previously unexplored low-frequency portion of the electromagnetic spectrum. Conducting a large and thorough survey is the major aim that has motivated the development of LOFAR from its start. Because of the large number of array elements, LOFAR will have enough fidelity and sensitivity to observe weak structures between these brilliant

[1]https://www.astron.nl/telescopes/lofar

Figure 4.1: These are some LOFAR images: the left panel is the LOFAR core near Exloo, Netherlands. The middle one is a station (150m). The right panel is a sample image of LOFAR low band antennas. (Courtesy: ASTRON).

sources (Shimwell et al. 2017). The LOFAR was envisioned as a novel endeavor to enforce a breakthrough in sensitivity for astronomical investigations at radio frequencies lower than 250 MHz. Note that, until the Square Kilometre Array (SKA) becomes operational in the late 2020s, LOFAR will be the most sensitive radio observatory so far at its low observation frequency. Even then, the angular resolution of LOFAR will continue to be significantly greater with respect to the SKA, as the SKA will observe at frequencies above 50 MHz.

The LOFAR is destined to conduct the following sky surveys:

• **MSSS:** The LOFAR Multifrequency Snapshot Sky Survey (MSSS) is known as MSSS. This was the first LOFAR-based wide-area northern-sky survey. The first data release is explained by Heald et al. (2015). It covers the whole northern sky with a resolution of 2 arcmins and a depth of $\sim$ 10 mJy beam^{-1}.

• **LoTSS wide area:** The current LOFAR Two-metre Sky Survey (LoTSS) is an HBA 120-168MHz wide-area survey (Shimwell et al. 2017). A detailed discussion on the LoTSS wide area is given in the next section.

• **LoTSS deep fields:** LoTSS Depp fields observation is done through the repeated observations of northern hemisphere fields using the highest-quality multi-wavelength data at several-degree scales. These observations, made with the same frequency coverage as the all-sky survey, will have far higher sensitivity. The first three fields being investigated are Boötes (Tasse et al. 2021), Elais-N1 (Sabater et al. 2021), and Lockman Hole (Tasse et al. 2021). All of these three fields are observed in at least 100 hours of HBA data. Further studies like multi-wavelength observations, source association, and cross-matching are also done (Kondapally et al. 2021), with respective photometric redshifts (Duncan et al. 2021). The final goal of this survey is to study the complete range of cosmic environments at high redshift at depths reaching 10 μJy beam^{-1} (nearly five times deeper than

the finest all-sky LoTSS pointings) over combined sky areas in the order of many tens of square degrees. This will allow investigating the star formation and AGN activity throughout cosmic time by combining with high-quality auxiliary data. Now, the new LBA observations will supplement the HBA deep surveys. The first release of a deep LBA observation of the Boötes field was done by Williams et al (2021). The final 15 arcsec resolution image, made from 56 hrs of observations, achieves an rms of 0.65 mJy/beam in the central region, and < 1.2 mJy beam^{-1} over 50% of the map. The source catalog contains 1,948 sources detected over an area of 23.6 square degrees. The 829 sources within the deep optical coverage area are matched to the HBA catalog at 144 MHz.

• **LoLSS wide-area:** LOFAR LBA Sky Survey (LoLSS) is a planned survey that is supposed to cover the entire northern sky with a frequency range of $42-66$ MHz. This survey will have a resolution of 15 arcsec with an average rms noise of 1 mJy beam^{-1}. The LoLSS will be a game-changer in the search for new ultra-steep spectrum sources, such as high redshift radio galaxies, dying radio-emitting plasma, and radio-emitting exoplanets. The LOFAR LBA Sky Survey for the HETDEX (Hobby-Eberly Telescope Dark Energy Experiment) spring field region is released. The area covers about 700 square degrees and is centered in the RA range of 10h45m00s to 15h30m00s and the DEC range of 45d00m00s to 57d00m00s. This preliminary version features a 47″ resolution and a 4 mJy beam^{-1} median rms noise level (de Gasperin et al. 2021).

• **WEAVE-LOFAR:** WEAVE-LOFAR[2] is a spectroscopic study of the LOTSS sky using the William Herschel Telescope's WEAVE fiber spectrograph. It will give redshifts for the LOTSS broad and deep tiers. This project is led by Dan Smith.

4.2 LoTSS wide area

The LOFAR Surveys Key Science Project is carrying out a survey with three levels of observation. The Principal Investigator of the project is Prof. Dr. H. J. A. Röttgering of Leiden University. The three levels of observations are Tier 1, Tier 2, and Tier 3. Tier 1 is the widest tier. It includes a low-band antenna (LBA) and high-band antenna (HBA) observations throughout the entire 2 steradians of the northern sky. The Tier 2 and Tier 3 observations are relatively deeper and these two observations concentrate on smaller areas with high-quality multi-wavelength datasets. The LOFAR Two-metre Sky Survey or LoTSS is the LOFAR HBA 120–

[2]https://ingconfluence.ing.iac.es:8444/confluence//display/WEAV/WEAVE-LOFAR

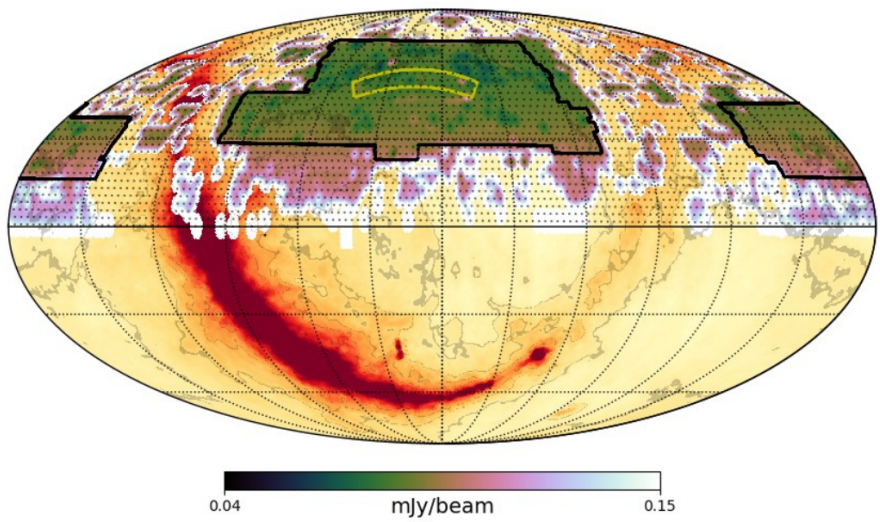

Figure 4.2: The image shows the sky coverage area of LoTSS survey. The region outlined by the yellow line is the LoTSS DR1 coverage area and the region inside the black line is the LoTSS DR2 coverage area (Courtesy: ASTRON).

168 MHz Tier 1 survey. This LoTSS survey is the second survey in the northern hemisphere to be carried out with the LOFAR HBA, after MSSS (Heald et al. 2015). This also done more deeper survey than the MSSS. The LoTSS survey is a long-term undertaking project. It has already covered over 2000 square degrees of the northern sky. It is continuously observing and collecting data and will eventually cover the entire northern sky (Shimwell et al. 2017). In the frequency range 120–168 MHz, 20% of the northern sky has already been observed.

The first full-quality public data release of the LoTSS survey is known as LoTSS DR1 (Shimwell et al. 2019; Williams 2019). The LoTSS DR1 covers the skies over the HETDEX field area in the span of right ascension (R.A.) from 10 h 45 m 00 s to 15 h 30 m 00 s and declination (Decl.) from 45°00′00″ to 57°00′00″. The total coverage area is 424 square degrees, which is actually equal to 2% of the ultimate coverage. The sky coverage of LoTSS DR1 is presented in Figure 4.2. The median sensitivity (S_{144MHz}) is 71 μJy beam^{-1}. At an integrated flux density of 0.45 mJy, the point-source completeness is 90%. The LoTSS DR1 has a resolution of 6″ and it has a positional accuracy within 0.2″ (Shimwell et al. 2019). The next data release, LoTSS-DR2 covers 26% of the Northern sky (4.2).

Table 4.1: **Comparison of LoTSS DR1 properties with other surveys**

Survey properties	NVSS	TGSS ADR1	VLA FIRST	LoTSS DR1
Frequency	1.4 GHz	147.5 MHz	1.4 GHz	120-168 MHz
Sky coverage	north of J2000.0 $\delta = -40°$	36,900 square degrees	10,575 square degrees	424 square degrees
RMS noise (median)	0.45 mJy beam^{-1}	3.5 mJy beam^{-1}	0.15 mJy beam^{-1}	71 μJy beam^{-1}
Resolution	$45''$	$25''$	$5''$	$6''$
Number of sources	> 1.8 million ($\sim 2{\times}10^6$)	623,604	946,432	325,694
Sources per square degree	~ 50	~ 20	~ 90	~ 750

4.2.1 Why LoTSS is important?

In the previous chapter (Chapter 3), we have identified winged radio sources from high-frequency data, VLA FIRST data (Becker et al. 1995). The VLA FIRST has a better resolution compared to the other high-frequency survey data. Now, we would like to continue our search method in the low-frequency range. In the low-frequency range, apart from LoTSS, the available radio surveys are TIFR GMRT Sky Survey alternative data release (TGSS ADR; Intema et al. 2017), LOFAR Multifrequency Snapshot Sky Survey (MSSS; Heald et al. 2015), Galactic and Extragalactic All-sky MWA (GLEAM; Wayth et al. 2015), and the Very Large Array Low-frequency Sky Survey Redux (VLSSr; Lane et al. 2014). In comparison to these low-frequency surveys, the LoTSS is 50 to 1000 times better in sensitivity and 5 to 30 times better in resolution (Shimwell et al. 2017). The LOFAR has advantages not only in the low-frequency range, but it also has edges over any other available high-frequency full-sky surveys like VLA FIRST and NVSS (Condon et al. 1998), in most aspects. In Table 4.1 we show some aspects of the data survey such as sky coverage, rms noise (median), resolution, number of detected sources, and number of sources per square degree for NVSS, TGSS ADR1, VLA FIRST, and LoTSS DR1. A comparative plot for image rms, frequency, and resolution is given in Figure 4.3. Because of its unrivaled capabilities at low frequency, LoTSS (LOFAR) is already playing a pivotal role in this field of study (Brienza et al. 2016).

The LoTSS DR1 is a wonderful resource for wide-area low-frequency selection of extended extragalactic sources. The LoTSS DR1 is approximately 10 times deeper than the FIRST but has a comparable resolution. The most important feature is that it has the short baselines required to image all but the largest-scale features in the radio sky. The emission from extragalactic sources, such as winged radio emitters, is dominated at low frequencies by the far more isotropic large-scale lobes. As a result, LoTSS DR1 is a potential database for detecting new

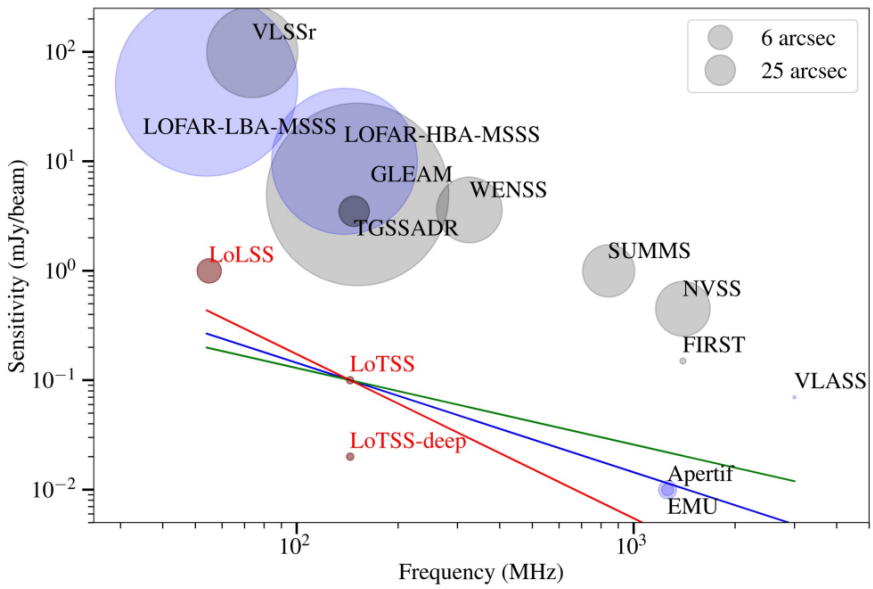

Figure 4.3: A plot of the LoTSS-DR1 image properties with other surveys. Here, we present the rms, frequency, and angular resolution (linearly proportional to marker radius) in comparison to a selection of existing wide-area completed radio surveys (in grey) or in planning for the near future (in blue). For surveys with large fractional bandwidths, the horizontal lines show the frequency coverage. The green, blue and red lines represent the corresponding LoTSS sensitivity for small radio-emitters with spectral indices of – 0.7, – 1.0, and – 1.5, respectively (Courtesy: Shimwell et al. (2017); Shimwell et al. (2019)).

winged radio sources. In Figure 4.4 we present a radio contour map of an XRG J1243+5212, drawn from NVSS, TGSS ADR1, VLA FIRST, and LoTSS DR1. We can clearly see that, there is no proper morphological wing structure is found except in the LoTSS DR1 image.

4.3 Methodology

4.3.1 Sample Data Selection

The LoTSS DR1 catalog contains a total of 325 694 sources. The sources are detected with a signal of at least five times the noise level (Shimwell et al. 2019). For the first step, we ran a filtering procedure in which we filtered radio sources

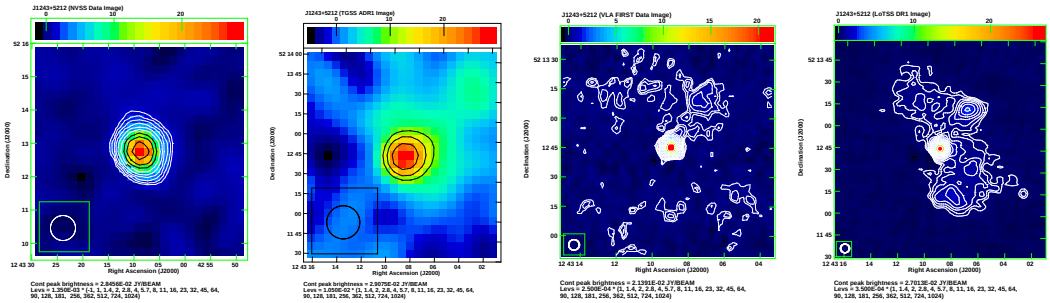

Figure 4.4: In this Figure, we present a comparative radio image of an XRG J1243+5212 (identified from LoTSS DR1) in NVSS, TGSS, VLA FIRST and LoTSS DR1. From the left, the first two images (from NVSS and TGSS ADR1 data, respectively) show unresolved structures. This is due to the poor resolution of NVSS and TGSS. The next (third) image is from VLA FIRST data. This image exhibits an extension of the primary lobe in the northwest direction; however, no other extended emissions have been found. The last one (the fourth one), on the right side of the panel, is the LoTSS DR1 image. A clear X-shape is depicted by the LOFAR image.

having an angular size more than or equal to 12″; that is, at least twice the size of the convolution beam. To acquire decently extended bright sources, we set the selection condition to 12″. We used the fitted Gaussian primary axis to calculate the size of the source. Here, we employed the search algorithm done by Bera et al. (2020), as in the previous chapter where winged sources are identified from the VLA FIRST survey. The previous searches (e.g.; Cheung (2007), Yang et al. (2019)) had some selection cuts in place to reduce false positives, particularly those based on visual examination. Cheung (2007), for example, did the search using sources in high dynamic ranges with the primary axis of the sample more than 15″. Yang et al. (2019) applied a similar selection strategy, with a cutoff of 10″ for the major axis (see Subsection 3.2.1).

The filtering method yields a total of 18,500 sources. Then we went through each field, looking for probable winged radio sources. The images for each source are obtained from the LoTSS DR1 Image Cutout Service[3], which is managed by ASTRON[4]. To see a better-resolved structure, we used LOFAR 6″ full-resolution photos instead of 20″ low-resolution images. The LOFAR survey website also provides a simplified and direct online representation of the whole LoTSS DR1

[3]https://vo.astron.nl/hetdex/lotss-dr1-img/cutout/form
[4]https://www.astron.nl/

data field[5,6].

4.3.2 Identification and Classification of Winged Sources

The wings or secondary lobes appear to be expelled from the primary lobes, albeit the point of ejection varies across individual cases. Based on their ejection point, we divide winged radio sources into two classes: XRGs and ZRGs. Secondary lobes that appear to emerge from the central core or around the central area are classified as "X"-shaped sources. Whereas the wings appear near the borders of the major lobes, the sources are categorized as "Z" shaped. The area covered by 25% of the primary jet length from the center site is described as the near central region (Bera et al. 2020). The XRGs with wings equivalent to active jets and at angles of $\sim 90^{\circ}$, known as bonafide, are also examined.

4.3.3 Optical Counterpart Identification

Most radio galaxies have an optical galaxy in their core area. The optical galaxy is often referred to as the optical host galaxy. The optical host galaxy is viewed as the radio source's optical counterpart. The identification of optical counterparts for diffused radio sources is quite important (see Subsection 3.2.3). We used the Sloan Digital Sky Survey (SDSS) data catalog (Gunn et al. 2006) and the NASA/IPAC Extragalactic Database (NED)[7] to look for the equivalent optical counterpart for each of the winged radio sources. The SDSS data release 12 (DR12) (Alam et al. 2015) is used in our work. We look for an optical galaxy around the central area of the winged radio sources. By visual estimation, the optical galaxy is selected as the optical counterpart based on its position in the overlaid radio map, where the radio image (LoTSS DR1) was overlaid on the optical image (SDSS). However, the radio contours were created by overlaying LoTSS DR1 radio images on the Digitized Sky Survey 2 (DSS2) (Lasker 1994) images. The DSS2 pictures are solely utilized for imaging.

[5]https://www.lofar-surveys.org/lotss-tier1.html
[6]https://lofar-surveys.org/public/HIPS/high_hips_new/
[7]https://ned.ipac.caltech.edu/classic/

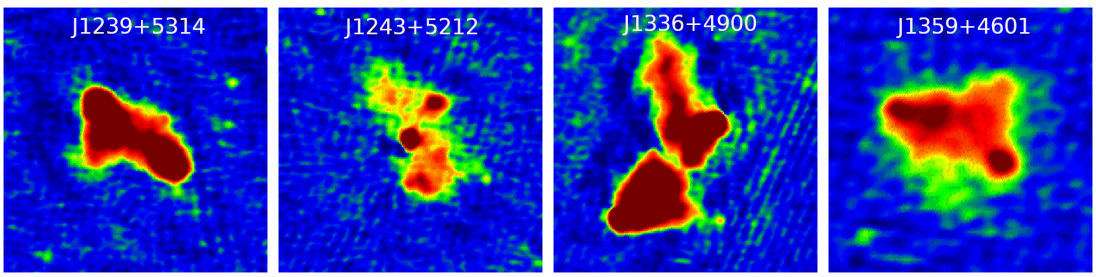

Figure 4.5: The radio colour stamp images of four sample newly identified XRGs is presented.

4.4 Results

We exhaustively scanned the LoTSS DR1 for winged radio sources and found a total of 40 such sources. 14 of these 40 sources were previously classified as winged radio sources. In particular, six of these 14 sources were found each in the Cheung (2007) and Yang et al. (2019) catalogs, while two more are located in the Bera et al. (2020) collection (given in the previous chapter). We did not include previously discovered sources in this list, the rest 26 newly identified winged sources are only cataloged. However, we did not exclude the sources present in Proctor (2011) as the sources in Proctor (2011) list are not verified as winged sources. There are one XRG and two ZRGs in our list, which are common with Proctor (2011) list. A total of 14 of these 26 newly identified sources are classified as XRGs and the rest 12 as ZRGs. In Figure 4.5 and Figure 4.6, colour stamp radio images of four sample X-shaped sources and Z-shaped sources are presented, respectively.

The newly identified XRG and ZRG sources are presented in Table 4.2 and Table 4.3, in the ascending order of right ascension (R.A.), respectively. The basic parameters and properties of these newly discovered XRGs and ZRGs are also listed in these two tables. The following columns are listed for both the tables: column (1)– Catalog Number (the sources present in Proctor (2011) are marked by †), column (2)– Host Name of the identified XRG or ZRG, column (3)– R.A. in J2000 (in hh mm ss.ss format), column (4)– Declination (Decl.) in J2000 (in ±dd mm ss.s format), column (5)– Position references, column (6)– Corresponding redshift (z) values (For the Tables, the redshift values are approximated up to three decimal figures. However, in the computation, we utilize the real redshift values rather than the approximated values.), column (7)– Integrated flux of the source at 144 MHz (F_{144}), column (8)– Integrated flux of the source at 1400 MHz (F_{1400}), column (9)– Two point spectral index in between 1400 MHz and 144 MHz

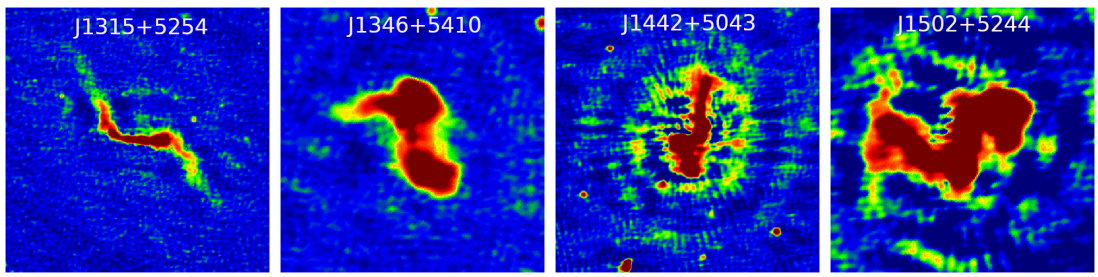

Figure 4.6: The radio colour stamp images of four sample newly identified ZRGs is shown.

(α_{1400}^{144}) (For the Tables, the spectral index values are approximated to two decimal places, while the real estimated values are utilized for computation.), column (10)– Radio luminosity at 144 MHz (L_{144MHz}) (The luminosity values are given in the order of 10^{42} in the unit erg s^{-1}. The values in the tables are estimated to two decimal figures). column (11)– Radio power at 144 MHz (P_{144MHz}) (The radio powers are given in the order of 10^{25} in the unit W Hz^{-1}. The values in the tables are estimated up to two decimal numbers.), column (12)– FR-classification of the sources, column (13)– Name of other catalogs where the source also identified.

The location co-ordinate of a certain radio source is identified as the position parameter of its optical counterpart. The optical counterparts are found in the SDSS catalog. All of the winged sources have SDSS optical counterparts. The redshift is estimated from the 12th data release of the SDSS catalog (DR12) (Alam et al. 2015). Redshifts are found for all XRGs. For ZRGs except one, redshifts are available for all sources. The spectroscopic redshifts are presented here. The photometric redshifts are used when the spectroscopic values are unavailable. The photometric redshifts are marked with the * sign in column 6 for both the tables. For three XRGs and ZRGs, no spectroscopic z is available, photometric z values are used for these six cases. The integrated flux in 144 MHz is measured from the LoTSS DR1 data image. The flux in 1400 MHz is measured from NVSS (Condon et al. 1998). We use the NVSS image as the NVSS employed the lower-resolution VLA configuration D, meaning that the NVSS is best adapted to recognize the most extensive radio structure.

Table 4.2: **New candidates of Winged Radio Sources with X-shape from LoTSS DR1**

Cat No.	Host Name	R.A. (J2000.0)	Decl. (J2000.0)	Ref.	Redshift (z)	F_{144} (mJy)	F_{1400} (mJy)	α_{144}^{1400}	L (erg/s) ($\times 10^{42}$)	P (W/Hz) ($\times 10^{25}$)	FR-type (I/II)	Oth Cat
1†	J1112+4755	11 12 17.58	+47 55 56.6	SDSS	0.459	2146	239	− 0.96	25.37	177.37	II	1, 2,4, 8, 9
2	J1115+5600	11 15 29.59	+56 00 39.6	SDSS	0.579	107	22	− 0.70	4.44	13.59	II	1
3	J1129+5407	11 29 19.35	+54 07 33.9	SDSS	0.069	378	22	− 1.25	0.05	0.48	—	1
4	J1132+5558	11 32 22.74	+55 58 18.5	SDSS	0.050	695	55	− 1.11	0.05	0.45	—	1, 2
5	J1154+4835	11 54 18.72	+48 35 21.1	SDSS	0.170*	665	104	− 0.82	1.19	5.56	II	1, 4, 9, 10
6	J1216+5243	12 16 23.68	+52 43 59.9	SDSS	0.121	210	62	− 0.54	0.53	0.83	II	1, 12
7	J1239+5314	12 39 15.39	+53 14 14.6	SDSS	0.202	264	54	− 0.70	1.02	3.15	II	9
8	J1243+5212	12 43 08.97	+52 12 45.0	SDSS	0.200	112	41	− 0.44	1.25	1.26	II	1, 10
9	J1302+5120	13 02 59.64	+51 20 01.7	SDSS	0.376*	1380	282	− 0.70	21.30	65.82	—	1, 2, 4
10	J1324+5041	13 24 35.20	+50 41 02.3	SDSS	0.287	618	40	− 1.20	1.89	18.28	II	2, 4
11	J1336+4900	13 36 14.99	+49 00 04.8	SDSS	0.233*	596	112	− 0.74	2.71	9.80	II	1, 9
12	J1345+5403	13 45 57.55	+54 03 16.6	SDSS	0.162	3139	340	− 0.98	3.42	24.52	II	6, 9
13	J1359+4601	13 59 08.72	+46 01 13.7	SDSS	0.056	47	8	–0.78	0.03	0.14	II	—
14	J1416+5425	14 16 29.03	+54 25 32.1	SDSS	0.314	983	52	− 1.29	3.67	36.51	II	4

Notes

† The source is present in Proctor (2011).

* These redshifts are photometric redshift, when the unmarked z are spectroscopic.

References

SDSS: (Fan et al. 1999; Tumlinson et al. 2013); 1: NVSS (Condon et al. 1998); 2: VLSS (Cohen et al. 2007; Helmboldt et al. 2008); 3: B3 (Ficarra et al. 1985); 4: 6C (Baldwin et al. 1985; Hales et al. 1988, 1990, 1991, 1993a, 1993b); 5: 7C (McGilchrist et al. 1990; Kollgaard et al. 1994; Waldram et al. 1996; Vessey & Green 1998); 6: 8C (Hales et al. 1995); 7: 9C (Waldram et al. 2003, 2010); 8: TXS (Douglas et al. 1996); 9: 87 GB (Gregory & Condon 1991); 10: GB6 (Gregory et al. 1996); 11: ATATS (Croft et al. 2010), 12: VSA (Taylor et al. 2003; Cleary et al. 2008)

Table 4.3: **New candidates of Winged Radio Sources with Z/S-shape from LoTSS DR1**

Cat No.	Host Name	R.A. (J2000.0)	Decl. (J2000.0)	Ref.	Redshift (z)	F_{144} (mJy)	F_{1400} (mJy)	α_{144}^{1400}	L (erg/s) ($\times 10^{42}$)	P (W/Hz) ($\times 10^{25}$)	FR-type (I/II)	Oth Cat
1	J1056+5112	10 56 44.29	+51 12 14.2	SDSS	0.372*	94	19	− 0.70	1.40	4.35	—	1
2	J1121+5344	11 21 26.44	+53 44 56.7	SDSS	0.104	697	95	− 0.88	0.36	2.04	II	4
3†	J1224+5623	12 24 37.88	+56 23 40.0	SDSS	0.205	375	106	− 0.56	2.65	4.53	—	1, 4, 10
4	J1314+5439	13 14 04.60	+54 39 37.9	SDSS	0.346	394	65	− 0.79	3.67	15.92	II	1, 9
5	J1315+5254	13 15 31.08	+52 54 37.6	SDSS	0.121	203	41	− 0.70	0.26	0.80	II	1, 9, 11
6	J1346+5410	13 46 32.69	+54 10 31.6	SDSS	0.273*	265	43	− 0.80	1.42	6.32	II	1, 11
7	J1442+5043	14 42 19.18	+50 43 57.9	SDSS	0.174	1140	204	− 0.76	2.61	10.01	—	1, 4, 9
8	J1446+4831	14 46 29.46	+48 31 54.1	SDSS	0.362	177	31	− 0.76	2.02	7.85	I	11
9	J1453+5317	14 53 21.20	+53 17 52.3	SDSS	—	676	121	− 0.76	—	—	—	2, 4, 8, 9
10	J1502+5304	15 02 09.53	+53 04 19.9	SDSS	0.287	147	31	− 0.68	1.30	3.81	I	1, 11
11†	J1502+5244	15 02 29.04	+52 44 02.1	SDSS	0.133	820	205	− 0.61	1.83	3.94	—	1, 2, 9, 11
12	J1519+5007	15 19 33.73	+50 07 25.0	SDSS	0.358*	310	38	− 0.92	2.24	14.07	—	1

Notes

† The source is present in Proctor (2011).

* These redshifts are photometric redshift, when the unmarked z are spectroscopic.

References

SDSS: Fan et al. (1999), Tumlinson et al. (2013); 1: NVSS (Condon et al. 1998); 2: VLSS (Cohen et al. 2007; Helmboldt et al. 2008); 3: B3 (Ficarra et al. 1985); 4: 6C (Baldwin et al. 1985; Hales et al. 1988, 1990, 1991, 1993a, 1993b); 5: 7C (McGilchrist et al. 1990; Kollgaard et al. 1994; Waldram et al. 1996; Vessey & Green 1998); 6: 8C (Hales et al. 1995); 7: 9C (Waldram et al. 2003, 2010); 8: TXS (Douglas et al. 1996); 9: 87 GB (Gregory & Condon 1991); 10: GB6 (Gregory et al. 1996); 11: ATATS (Croft et al. 2010), 12: VSA (Taylor et al. 2003; Cleary et al. 2008)

We present four sample contour radio images of newly identified X-shaped and Z-shaped radio sources in Figure 4.7 and Figure 4.8, respectively. In the Appendix section, all of the identified XRGs and ZRGs are given. The sources that are also identified from VLA FIRST (i.e., the common 14 sources) are also presented in the Appendix section with respective LoTSS DR1 maps. The contour LOFAR plots are overlaid on the red DSS2 image (in greyscale). The DSS pictures are only used for imaging, to display the optical host position. The contour levels are drawn from the flux value of 0.25 mJy (at least). To ensure a valid radio structure for morphology classification, we set the lower contour level limit at more than three times the sensitivity of LoTSS DR1 (71μJy). We have increased the consecutive higher contour levels by $\sqrt{2}$. For each image at the bottom-right corner, the synthesized beams are indicated.

The following cosmology parameters: $H_0 = 67.4$ km s^{-1} Mpc^{-1}, $\Omega_m = 0.315$ and $\Omega_{vac} = 0.685$ (Planck Collaboration et al. 2020), are used in our work and calculations. These cosmological constants are derived from the final full-mission Planck measurements of cosmic microwave background (CMB) anisotropies, which integrate data from temperature and polarisation maps, as well as the lensing reconstruction. All of the imaging, maps, and different measurements (like integrated flux, peak flux, angular size, etc.) are done through their respective tasks in Astronomical Image Processing System (AIPS)[8] (see Section 3.2.4). In the next sections, we provide a brief overview of the derived parameters (such as spectral index, radio luminosity, radio power, and FR-dichotomy) for the newly detected winged sources.

4.4.1 Spectral Index

The spectral index is calculated as $S_\nu \propto \nu^\alpha$, where S_ν is the flux at a particular frequency ν. We calculate the spectral index, α_{144}^{1400} in between 144 MHz and 1400 MHz. The integrated fluxes at 144 MHz (F_{144}) and at 1400 MHz (F_{1400}) are evaluated from the LoTSS and NVSS data, respectively. For the NVSS flux, the corresponding NVSS image is downloaded from the NVSS postage stamp server[9]. The spectral indices are found for all 26 sources.

The value ($|\alpha_{144}^{1400}|$) ranges from 0.44 to 1.29 for all of our winged sources. The radio source J1416+5425, which is an XRG has the highest spectral index value

[8]https://www.aips.nrao.edu/

[9]https://www.cv.nrao.edu/nvss/postage.shtml

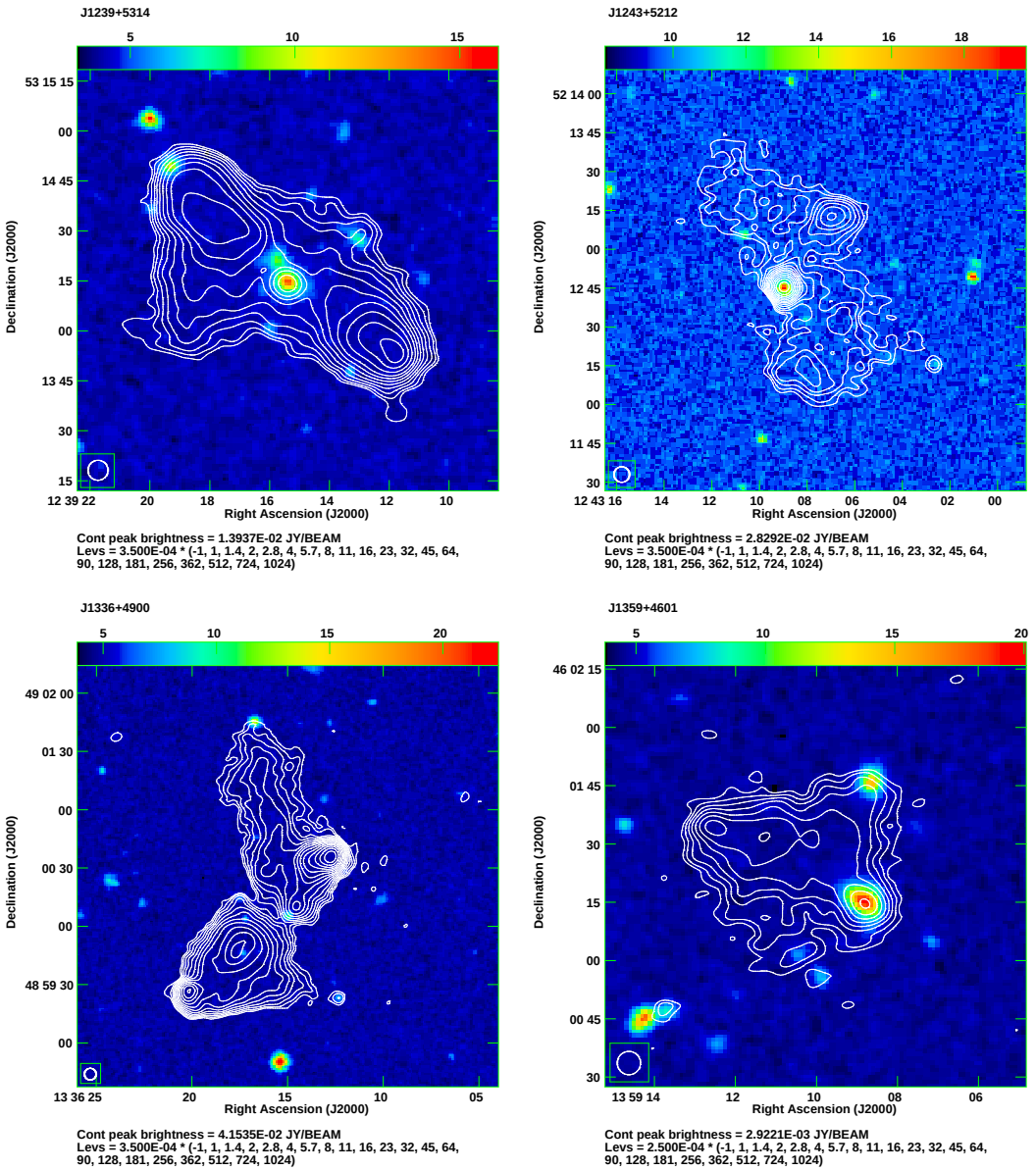

Figure 4.7: Here, we present the radio contour image for four newly identified XRGs from the LOFAR data. The LOFAR radio images are presented in contours, overlaid on the optical DSS2 red images in gray-scale. The radio contours are started from at least 3 times to the surrounding noise and the subsequent levels are drawn with an increment of $\sqrt{2}$. The LOFAR 6″ full-resolution radio images are used for better-resolved structure.

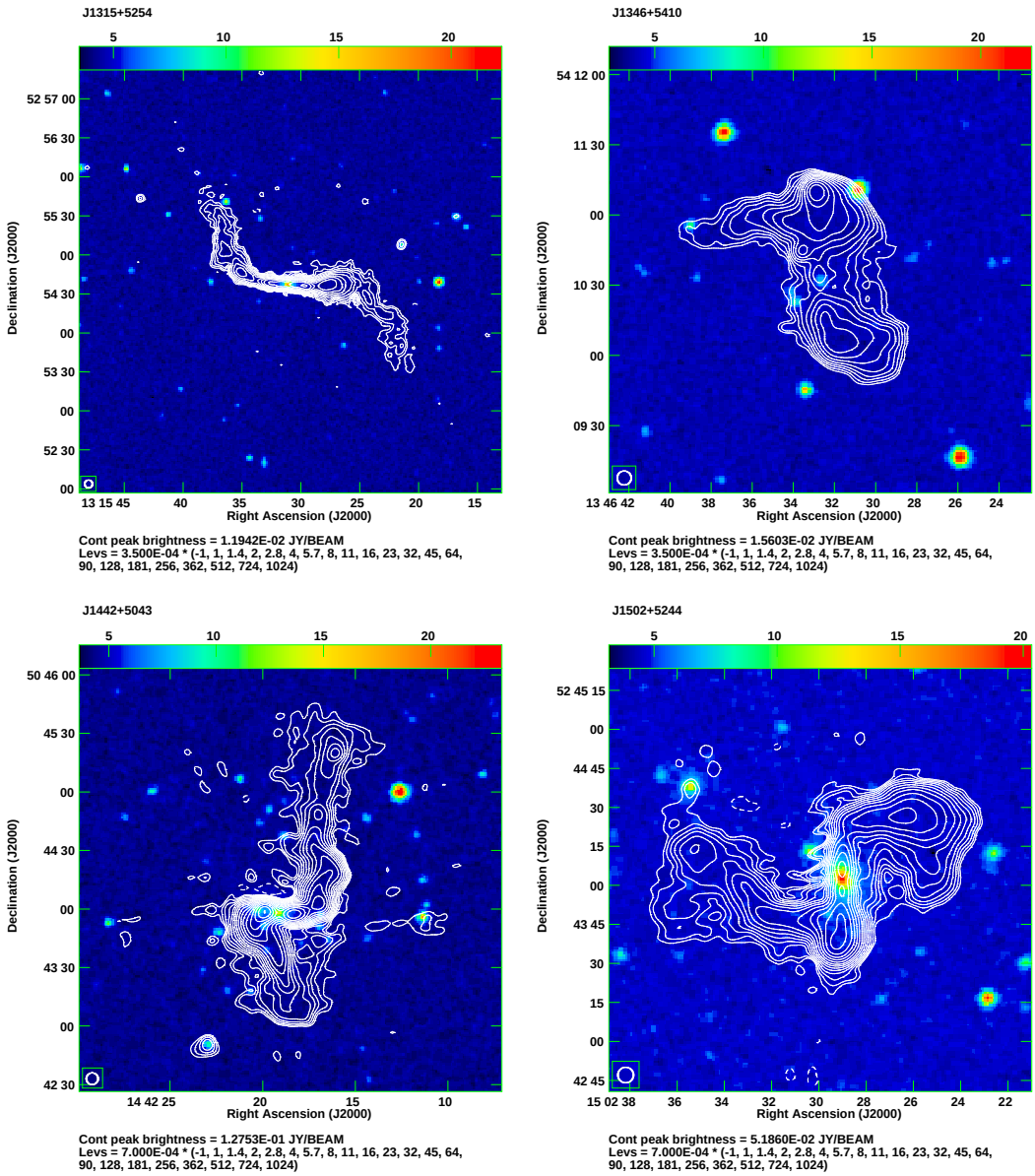

Figure 4.8: Here, we present the radio contour image for four newly identified XRGs from the LOFAR data. The LOFAR radio images are presented in contours, overlaid on the optical DSS2 red images in gray-scale. The radio contours are started from at least 3 times to the surrounding noise and the subsequent levels are drawn with an increment of $\sqrt{2}$. The LOFAR 6″ full-resolution radio images are used for better-resolved structure.

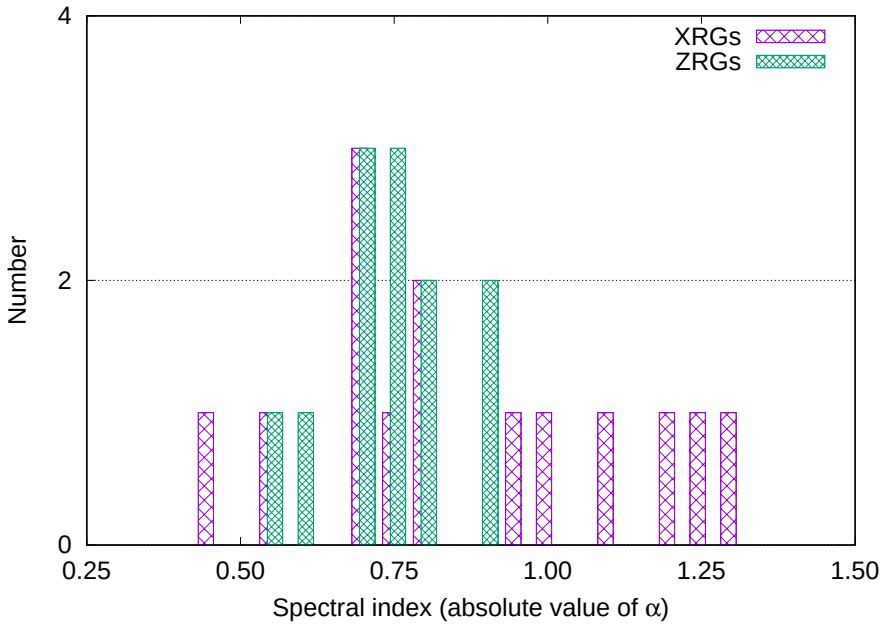

Figure 4.9: The histogram depicts the distribution of spectral index ($|\alpha_{1400}^{144}|$) for the newly identified XRGs and ZRGs.

–1.29. The XRG J1243+5212 has the lowest spectral index value –0.44. The spectral index range for ZRGs is –0.56 to –0.92. The highest and lowest spectral index is found for J1519+5007 (–0.92) and J1224+5623 (–0.56), respectively. A histogram for the spectral index distribution (in absolute value) is presented in Figure 4.9. The plot shows that most of the sources lie in the range of –0.70 to –0.80 range. The histogram also indicates a Gaussian distribution, however, the low number of sources restricts us to fit the Gaussian properly.

4.4.2 Radio Luminosity

The radio luminosity (L_{rad}) is evaluated from the calculated using the formula as given by (O'Dea & Owen 1987) (see 3-1).

$$L_{rad} = 1.2 \times 10^{27} D_{\rm Mpc}^2 S_0 \nu_0^{-\alpha} (1+z)^{-(1+\alpha)} \times (\nu_u^{(1+\alpha)} - \nu_l^{(1+\alpha)})(1+\alpha)^{-1} \text{erg s}^{-1} \quad (4\text{-}1)$$

In the above equation, the $D_{\rm Mpc}$ is the calculated luminosity distance to the source in Mpc, which is estimated from the available redshift (z) information. Here, we

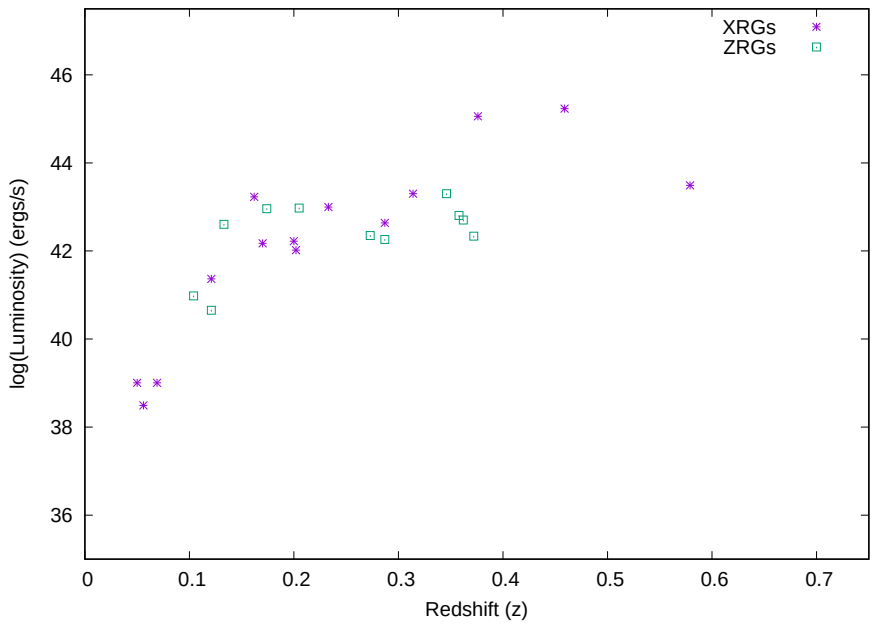

Figure 4.10: The plot shows the distribution of calculated radio luminosity ($log(L_{144MHz})$) of the XRGs and ZRGs with redshift (z) values.

use the Cosmological Calculator for the Flat Universe by Nick Gnedin[10]. The S_0 is the flux density in Jy for a certain frequency ν_0 (Hz). The α is the spectral index (as calculated from $S \propto \nu^{\alpha}$). The ν_u (Hz) and ν_l (Hz) are the upper and lower cut-off frequencies, respectively. In this luminosity calculation, we assume the ν_u and ν_l as 100 GHz and 10 MHz, respectively. We compute radio luminosity with the reference frequency 144 MHz and hence L_{rad} is L_{144MHz}.

The radio luminosity (L_{144MHz}) is evaluated for all winged sources, except the ZRG J1453+5317, as there is no redshift information available for this ZRG. The XRG J1112+4755 has the highest luminosity $25.37 \times 10^{42} ergs^{-1}$. There is another XRG J1302+5120, that has luminosity in the order of $10^{43} ergs^{-1}$. The minimum L_{144MHz} is found for XRG J1359+4601, with luminosity $0.03 \times 10^{42} ergs^{-1}$. There are two more XRG sources (J1129+5407 and J1132+5558) that have luminosity $\sim 10^{40} ergs^{-1}$. Among the ZRGs, the highest and lowest luminosity are found for J1314+5439 and J1315+5254 with L_{144MHz} values $3.67 \times 10^{42} ergs^{-1}$ and $0.26 \times 10^{42} ergs^{-1}$, respectively. All the ZRGs have luminosity in the order of $10^{42} ergs^{-1}$, except two sources where luminosity is found in the order of $10^{41} ergs^{-1}$. The

[10]https://home.fnal.gov/ gnedin/cc/

radio luminosity (L_{144MHz}) distribution in log scale for the winged sources with respective is presented in Figure 4.10.

4.4.3 Radio Power

The radio power (P) for a reference frequency ν is given by Donoso et al. (2009) as–

$$P_\nu = 4\pi D_L^2 S_\nu (1+z)^{(\alpha-1)} \tag{4-2}$$

In this equation, D_L– the luminosity distance, S_ν– the radio flux at the reference frequency ν. The term $(1+z)^{(\alpha-1)}$ is the standard k-correction, used in radio astronomy (Hogg et al. 2002). Here, the spectral index (α) is supposed to be defined as $S_\nu \propto \nu^{-\alpha}$. With the available values, we have calculated the radio power (P_{144MHz}).

The $log(P_{144MHz})$ has a range between $177.37 \times 10^{25} - -0.14 \times 10^{25}$ in WHz^{-1}. Among the XRGs, XRG J1112+4755 and XRG J1359+4601 have the highest and lowest radio power with values of $177.37 \times 10^{25} WHz^{-1}$ and $0.14 \times 10^{25} WHz^{-1}$, respectively. For the ZRGs, the highest and lowest radio power are $15.92 \times 10^{25} WHz^{-1}$ and $0.80 \times 10^{25} WHz^{-1}$ for ZRG J1314+5439 and ZRG J1315+5254, respectively.

4.4.4 FR-dichotomy

We analyze the relative brightness of each candidate's edges and core area, to find if the radio source is an edge-darken (FR-I type) or edge-brightened (FR-II type) source (Fanaroff & Riley 1974). We visually examine the relative brightness. Both the greyscale and contour pictures show relative brightness. The colour scale represents the relative brightness for distinct regions of a source in a grayscale image, whereas the contour gradient concentration represents the relative brightness in a contour image.

We discovered that all of the XRGs are FR-II types, albeit no conclusions can be taken for three sources as they show some complex brightness distribution. For the case of ZRGs, we found four sources as FR-II type, two sources as FR-I type, and no conclusion for six sources due to their complex luminosity distribution nature. A histogram to show the distribution of FR-types among the XRGs and ZRGs is presented in 4.11.

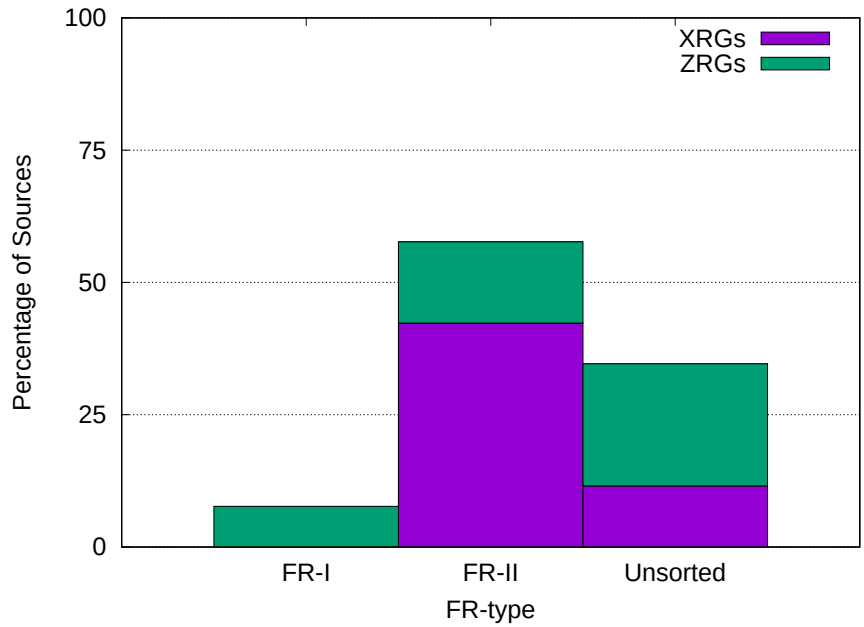

Figure 4.11: Histogram to show the distribution of FR-dichotomy for the newly identified XRGS and ZRGs.

Here, we draw the radio contours starting from a certain value; at least greater than three-time to the local noise. This implies that the contour levels are not uniform for all the sources. Due to this fact, some studies of XRGs such as the angular size of the major and minor axis, their ratio, and the angle between them are not possible accurately. The measurement for 'jet-length' for the ZRGs is also not possible, precisely.

4.5 Analysis of the Results and Outcomes of the Study

A visual search for winged radio sources from LoTSS DR1 is presented in this chapter. The contour maps are drawn to identify the wings. The contour level is determined by the local noise of the source field. A comprehensive visual examination of 18,500 sources yields 40 winged sources among which 26 sources are newly identified. To avoid misidentification, we use the following two-step precautions. First, the selection criteria: a $12''$ selection cut (twice the convolution beam size) is employed here. The minimum angular size of our identified winged sources is $41''$. Because there is no population of winged sources between the $12''$ to $41''$ range, the selection criterion $12''$ is a significant choice and comprehensive in our

case. Second, the visual inspection: as the sources are validated by the contour map, there is only a minor probability of misidentification. Furthermore, because the winged sources are chosen visually, the probability of missing a source is lower than in automated systems. We got the following outcomes through our search–

(**i**) The redshift values for the newly identified winged sources have a range from 0.050 to 0.579. The redshifts of the XRGs range from 0.050 to 0.579, whereas the redshifts of the ZRGs range from 0.104 to 0.372. Except for one ZRG (J1453+5317), all sources have redshifts. A total of 19, or 76% of the sources, have spectroscopic redshift (11 XRGs and 8 ZRGs), whereas six (3 XRGs and 3 ZRGs) have photometric redshift. The XRG with the highest redshift is J1115+5600 ($z = 0.579$) and the farthest ZRG is J1056+5112 ($z = 0.372$).

(**ii**) The mean spectral index value calculated is – 0.81, while the median is – 0.76. The mean and median values for only XRGs are – 0.87 and – 0.80, respectively, while the values for the ZRGs are – 0.74 and – 0.76. Radio sources dominated by core-dominated AGNs flatten the average spectral index to greater than– 0.7 (Randall et al. 2012). For a large sample of radio sources, the prominent peak of the spectral index is found in the range of – 0.75 to – 0.90 (Tiwari 2019). It can also be observed that the spectral index has a peak with a value of – 0.763 $\pm$ 0.211 for reasonably big radio sources (Tiwari 2019). The spectral values for our winged sources lie in the typical radio source range. Except for XRG J1243+5212, which has a relatively flat spectrum ($\alpha = -0.44$), all of the winged sources have a steep radio spectrum of ($|\alpha| > 0.5$). This is supposed to be anticipated from lobe-dominated radio sources.

(**iii**) The calculated radio luminosities (L_{144MHz}) had mean and median values of 3.47×10^{42} erg s^{-1} and 1.83×10^{42} erg s^{-1}, respectively. The mean and median luminosity values for the XRGs are 4.78×10^{42} erg s^{-1} and 1.57×10^{42} erg s^{-1}, respectively. Considering only the ZRG sources, the respective values are 1.80×10^{42} erg s^{-1} and 1.83×10^{42} erg s^{-1}. Given that the median luminosity for both XRG and ZRG shows an opposite trend to mean luminosity, which tells that the average luminosity of XRGs and ZRGs are the same. So, we conclude that in this case, there is no major difference in brightness between the two subclasses. Our winged sources had an average $logL$ value of 42.11 erg s^{-1}. Through the magneto-hydro-dynamic (MHD) simulation, it has been discovered that an X-shaped morphology may be caused by a jet with a radio power of less than 10^{44} erg s^{-1} (Rossi et al. 2017). Hence, our measured average luminosity agrees with predictions of XRG creation by Rossi et al. (2017).

(**iv**) We noticed that $log(P_{144MHz})$ for all winged candidates lies between 24.15 and 27.25 W Hz^{-1}. The mean and median of $log(P_{144MHz})$ are 25.72 and 25.74 W Hz^{-1}, respectively. The mean and median of $log(P_{144MHz})$ for XRGs only are 25.72 and 25.87 W Hz^{-1}, respectively, while for ZRGs solely are 25.70 and 25.66 W Hz^{-1}. The X-shaped radio galaxies reflect a transition population of FR-dichotomy in terms of radio power and emission-line strength (L_{NLR}) (Landt et al. 2010). Landt et al. (2010) depicted the transition and demonstrated that the transition point between the two FR classes can be determined at $L_{NLR} \sim 10^{35}W$ and radio power $\sim 10^{25.6}WHz^{-1}$ values. Our average radio power might be a clue to the transitional morphology between the two FR classes.

(**v**) The FR classification is achieved for 17 sources, however, no classification is completed for the rest nine. It is found that 15 (i.e., 88%) of these 17 sources are FR-II type and two are FR-I type. It is seen that most of the XRGs show FR-II characteristics (Leahy & Parma 1992; Cheung 2007; Yang et al. 2019; Bera et al. 2020). In our search, we saw that all of the XRGs (except one) are FR-II type and thus our findings hold up to the previous results.

(**vi**) A total of 13 sources have been discovered as giant radio galaxies (GRGs), i.e., having a linear size of 0.7 Mpc (Dabhade et al. 2020). Seven of these 13 GRGs are from the XRG collection, while six are from the ZRG catalog. Seven of the 13 discovered GRGs (4 XRGs and 3 ZRGs) were previously reported by Dabhade et al. (2020). We also saw that our average $logP$ value is similar to the average power reported by Dabhade et al. (2020).

Here, twenty-six "winged" sources are cataloged, along with their physical features, which have already been studied. Based on our visual evaluation, the given winged radio sources are the best choice. Two sources (ZRG J1324 +5041 and ZRG J1416+5425) with marginal evidence of secondary lobes are found. Small lobes can be caused by projection effects, wing faintness, and other factors. However, we are unable to identify them in the visual selection. More detailed observations are necessary for confirmation, and we must use caution when relying on these sources. A total of nine sources are found as bonafide XRGs in our catalog. The origin and general properties of the wings are unknown and outside the scope of this chapter. More identification of such sources, as well as multiwavelength studies of such sources and their properties, may help us better understand this fascinating class of radio emitters. This kind of research aids in the analysis of the mechanism underlying such sources as well as the exploration of the properties of winged sources in general (see Chapter 5).

References

Alam, S., Albareti, F. D., Allende Prieto, C., et al. 2015, ApJS, 219, 12A
Baldwin, J. E., Boysen, R. C., Hales, S. E. G., et al. 1985, MNRAS, 217, 717
Becker, R. H., White, R. L., & Helfand, D. J. 1995, ApJ, 450, 559
Bera, S., Pal, S., Sasmal, T. K., & Mondal, S. 2020, ApJS, 251, 9
Brienza, M., Morganti, R., Shulevski, A., Godfrey, L., & Vilchez, N. 2016, AN, 337, 31
Cheung, C. C. 2007, AJ, 133, 2097
Cleary, K. A., Taylor, A. C., Waldram, E., et al. 2008, MNRAS, 386, 1759
Cohen, A. S., Lane, W. M., Cotton, W. D., et al. 2007, AJ, 134, 1245
Condon, J. J., Cotton, W. D., Greisen, E. W., et al. 1998, AJ, 115, 1693
Croft, S., Bower, G. C., Ackermann, R., et al. 2010, ApJ, 719, 45
Dabhade, P., Röttgering, H. J. A., Bagchi, J., et al. 2020, A&A, 635, A5
de Gasperin, F., Williams, W. L., Best, P., et al., 2021, A&A, 648, 104
Donoso, E., Best, P. N., & Kauffmann, G. 2009, MNRAS, 392, 617
Douglas, J. N., Bash, F. N., Bozyan, F. A., Torrence, G. W., & Wolfe, C. 1996, AJ, 111, 1945
Duncan, K. J., Kondapally, R., Brown, M. J. I., et al., 2021, A&A, 648, A4
Fan, X., Strauss, M. A., Schneider, D. P., et al. 1999, AJ, 118, 1
anaroff, B. L., & Riley, J. M. 1974, MNRAS, 167, 31P
Ficarra, A., Grueff, G., & Tomassetti, G. 1985, A&AS, 59, 255
Gregory, P. C., & Condon, J. J. 1991, ApJS, 75, 1011
Gregory, P. C., Scott, W. K., Douglas, K., & Condon, J. J. 1996, ApJS, 103, 427
Gunn, J. E., Walter, A. S., Edward, J., et al. 2006, AJ, 131, 2332
Hales, S. E. G., Baldwin, J. E., & Warner, P. J. 1988, MNRAS, 234, 919
Hales, S. E. G., Baldwin, J. E., & Warner, P. J. 1993a, MNRAS, 263, 25
Hales, S. E. G., Masson, C. R., Warner, P. J., & Baldwin, J. E. 1990, MNRAS, 246, 256
Hales, S. E. G., Masson, C. R., Warner, P. J., Baldwin, J. E., & Green, D. A. 1993b, MNRAS, 262, 1057
Hales, S. E. G., Mayer, C. J., Warner, P. J., & Baldwin, J. E. 1991, MNRAS, 251, 46
Hales, S. E. G., Waldram, E. M., Rees, N., & Warner, P. J. 1995, MNRAS, 274, 447
Heald, G. H., Pizzo, R. F., Orrú, E., et al. 2015, A&A, 582, A123
Helmboldt, J. F., Kassim, N. E., Cohen, A. S., Lane, W. M., & Lazio, T. J. 2008,

ApJS, 174, 313
Hogg, D. W., Baldry, I. K., Blanton, M. R., & Eisenstein, D. J. 2002, arXiv:astro-ph/0210394
Intema, H. T., Jagannathan, P., Mooley, K. P., & Frail, D. A. 2017, A&A, 598, A78
Kollgaard, R. I., Brinkmann, W., Chester, M. M., et al. 1994, ApJS, 93, 145
Kondapally, R., Best, P. N., Hardcastle, M. J. , et al. 2021, A&A, 648, 31
Landt, H., Cheung, C. C., & Healey, S. E. 2010, MNRAS, 408, 1103
Lane, W. M., Cotton, W. D., van Velzen, S., et al. 2014, MNRAS, 440, 327
Lasker B., 1994, STScI Newsletter 11, 2, 39
Leahy, J. P., & Parma, P. 1992, in Extragalactic Radio Sources: From Beams to Jets, ed. J. Roland, H. Sol, & G. Pelletier (Cambridge: Cambridge Univ. Press), 307
McGilchrist, M. M., Baldwin, J. E., Riley, J. M., et al. 1990, MNRAS, 246, 110
OĆea, C. P., & Owen, F. N. 1987, ApJ, 316, 95
Planck Collaboration, Aghanim, N., Akrami, Y., et al. 2020, A&A, 641, A6
Proctor, D. D. 2011, ApJS, 194, 31
Randall, K. E., Hopkins, A. M., Norris, R. P., et al. 2012, MNRAS, 421, 1644
Rossi, P., Bodo, G., Capetti, A., & Massaglia, S. 2017, A&A, 606, A57
Sabater, J., Best, P. N., Tasse, C., et al. 2021, A&A, 648, 20
Shimwell, T. W., Röttgering, H. J. A., Best, P. N., et al. 2017, A&A,598, A104
Shimwell, T. W., Tasse, C., Hardcastle, M. J., et al. 2019, A&A, 622, A1
Tasse, C., Shimwell, T., Hardcastle, M. J., et al. 2021, A&A, 648, 18
Taylor, A. C., Carreira, P., Cleary, K., et al. 2003, MNRAS, 341, 1066
Tiwari, P. 2019, RAA, 19, 096
Tumlinson, J., Thom, C., Werk, J. K., et al. 2013, ApJ, 777, 59
van Haarlem, M. P., Wise, M. W., Gunst, A. W., et al. 2013, A&A, 556, A2
Vessey, S. J., & Green, D. A. 1998, MNRAS, 294, 607
Waldram, E. M., Pooley, G. G., Davies, M. L., Grainge, K. J. B., & Scott, P. F. 2010, MNRAS, 404, 1005
Waldram, E. M., Pooley, G. G., Grainge, K. J. B., et al. 2003, MNRAS, 342, 915
Waldram, E. M., Yates, J. A., Riley, J. M., & Warner, P. J. 1996, MNRAS, 282, 779
Wayth, R. B., Lenc, E., Bell, M. E., et al. 2015, PASA, 32, e025
Williams, W. L., de Gasperin, F., Hardcastle, M. J. H., et al., 2021, A&A, 655, 40
Williams W. L., Hardcastle M. J., Best P. N., et al., 2019, A&A 622, A2
Yang, X., Joshi, R., Gopal-Krishna, et al. 2019, ApJS, 245, 17

Chapter 5

Discussion and Conclusion

In all chaos there is a cosmos,
in all disorder a secret order.

—Carl Gustav Jung

In the present work, we have done two pilot surveys. A systematic search for an exotic subclass of radio sources, namely the winged radio source is done. Among the two surveys, one is the best available high-frequency data survey, the VLA FIRST, and another one is the best available low-frequency data survey, the LoTSS DR1. From, the high-frequency search at 1.4 GHz, we present the largest catalog of winged sources (originally total of 458 winged sources are identified), reported till now. The better result of our study is mainly due to a systematic thorough visual search for all sources with a single selection cut (a simple and reliable selection cut on the source size) compared to the previous multiple selection criteria (described in Chapters 3 and 4). The catalog contains with both XRG and ZRG sources. We also define and present a ZRG catalog, for the first time in literature. The search for winged sources from a low-frequency survey; from LOFAR data at 144 MHz, is also done for the first time in the literature. A total of 40 winged sources are identified from this search. Individual catalogs for XRGs and ZRGs are also presented here. The outcomes of our search results are given in previous chapters; Chapter 3 and Chapter 4, respectively. The total number of sources detected in 144 MHz LoTSS DR1 seems to be low compared to the total sources from the high-frequency VLA FIRST data. Now, if you consider the three catalogs of winged sources from FIRST, i.e.; Cheung (2007), Yang et al. (2019), and Bera et al.

(2020), the total source count adds up to 686. When from the LoTSS DR1 a total of 40 sources are detected (Bera et al. 2022). Now, the FIRST has a sky coverage of 10,575 square degrees and hence the number of sources identified per square degree is 0.065. On the other hand, the LoTSS DR1 has a sky coverage of 424 square degrees. This yields the detection rate for winged sources in LoTSS DR1 is 0.094. This result indicates that LoTSS DR1 has a noticeably higher detection rate. It also ensures the superiority of LOFAR over other radio telescope systems and their respective data surveys.

However, after these catalogs, we also need to understand that there is also some scope of missing a few sources and also misidentification of some sources. The primary reason for the missing sources is the selection cut, that we imposed. However, more strict selection cuts are also done by the previous authors. In the two catalogs, we present the best candidate for winged sources, and this may lead to another reason for missing some sources. On the other hand, the misidentification of sources is primarily due to the projection effect, and relative position of the source with respect to our line of sight.

Through the two major searches, we were able to ensamble a sufficiently large number of winged sources. In the last section of Chapter 2 (Section 2.4), we see that a major issue to study the winged sources is the rarity of such sources in the literature. Now, we have overcome this by ensembling more than 700 such sources. By taking into account all of the identified winged sources both from our catalog and from the previous catalogs, we will understand the winged sources through their global properties as a population. We also try to underlook the origin of such sources, which is still elusive.

5.1 Inherent Properties

5.1.1 Sky distribution

First, let us try to see the sky distribution of the winged sources. This will give the answer if such sources are confined to a particular region of the sky or if they are systematically distributed or if they are distributed uniformly over the sky. Here, we present th sky distribution for sources presented in Cheung (2007) (in Figure 5.1), Yang et al. (2019) (in Figure 5.2), and Bera et al. (2020) (in Figure 5.3) catalog. Note that, here we did not include the winged sources identified from the LoTSS DR1 (from Bera et al. (2022)), as the LoTSS DR1 is not an all-sky data

survey. The identified sources are plotted on the basis of their position (R.A. and Decl. given in the catalog) in the sky. The source positions are marked by red squares in the sky image.

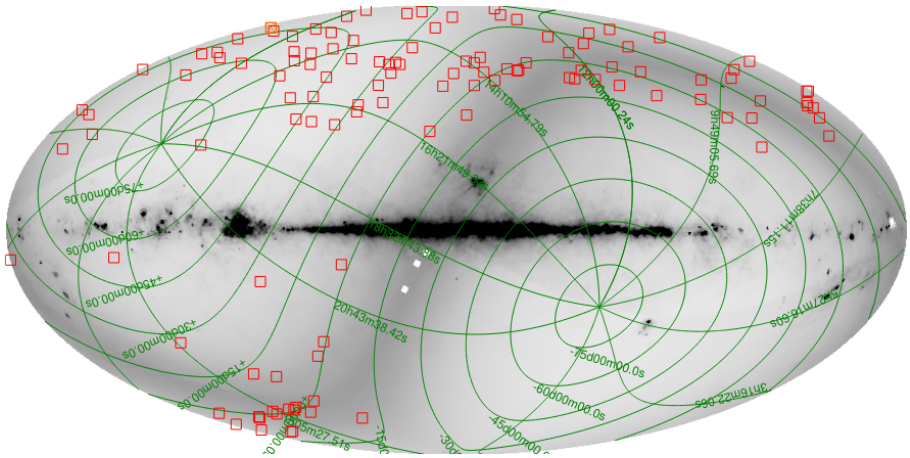

Figure 5.1: The plot shows the sky distribution of XRGs identified by Cheung (2007).

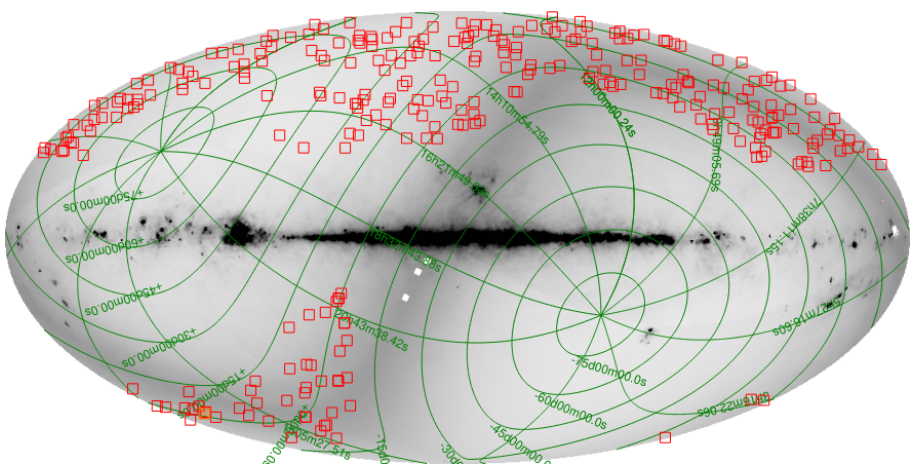

Figure 5.2: This is the sky distribution for the XRGs from Yang et al. (2019) catalog.

All of the sky distribution shows that there is no region-specific concentration or dilution for the sources. Considering the survey area of VLA FIRST, the sky distribution depicts that the sources are quite uniformly distributed over the sky. Note that here, the LoTSS DR1 survey result is not included as the LoTSS DR1 has a small coverage area to draw the sky distribution.

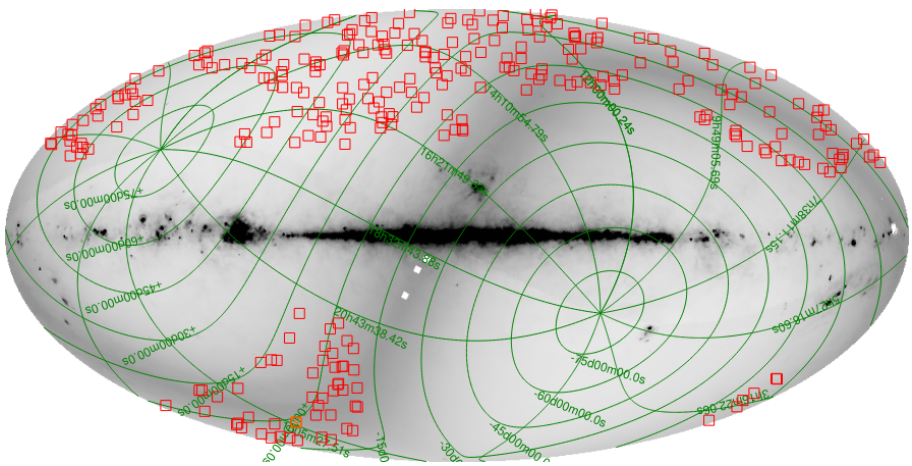

Figure 5.3: Here, we present the sky distribution for the XRGs and ZRGs, as identified in Bera et al. (2020).

5.1.2 Redshift Distribution

Now, we will try to see the redshift distribution of winged radio sources. We plot a histogram (presented in Figure 5.4) to see the redshift distribution of the identified winged sources. The available redshifts for XRGs from Cheung (2007), strong and possible XRGs from Yang et al. (2019), XRGs and ZRGs from Bera et al (2020), and Bera et al. (2022) are presented in respective colour schemes in the figure. To get an overall idea of redshift distribution, here we consider both the spectroscopic and photometric redshifts. All of the sources have redshift value below 1.0, except five sources that have a higher redshift values. The five sources include the stand-alone furthest XRG J1124+4325 (Bera et al. 2020) with a redshift value of 2.245 (Richards et al. 2009). There is a total of 413 redshifts are plotted. We check that most of the winged sources ($\sim 93\%$) have a redshift under 0.70. We also see that majority of the sources, $\sim 70\%$ have redshift in the range $0 < z < 0.5$, while the rest $\sim 30\%$ have $z > 0.5$.

5.2 Radio properties

In this section, we will understand the global properties of the winged sources as a population. Here we will do some statistical analysis of the physical parameters and characteristic morphological properties of these exotic sources. However, we do not discuss or try to understand the exact triggering mechanisms behind the

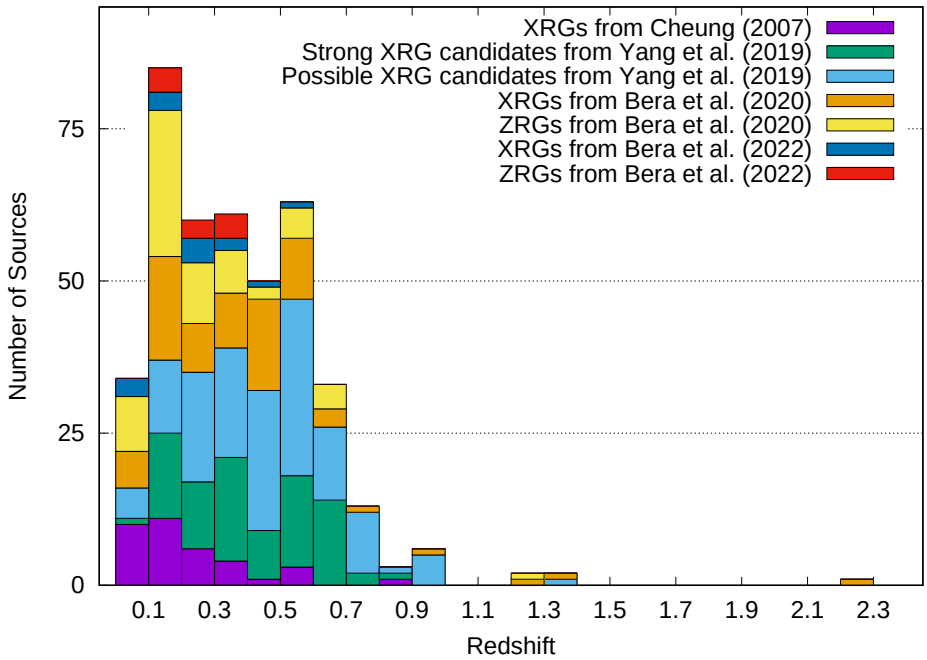

Figure 5.4: The histogram plot represents the redshift distributions of the winged sources.

peculiar morphological structure.

5.2.1 Global Spectral Index

To check the spectral index (α) property of winged radio sources as a population, we draw a global spectral plot for all the available cataloged winged sources. A histogram to show the spectral properties is presented in Figure 5.5. To ensure a complete distribution picture, we include the sources from Cheung (2007), and Yang et al. (2019) with our newly identified sources from Bera et al. (2020) (which are presented in Chapter 3) and Bera et al. (2022) (presented in Chapter 4), in the histogram plot. The histogram is plotted for the two-point spectral index α_{150}^{1400}, except for the sources from Bera et al. (2022). For Bera et al. (2022) sources, we considered the measured α_{144}^{1400} values. As the lower frequencies (144 MHz for Bera et al. (2022) and 150 MHz for others) flux does not give a major difference in the spectral index value, and both α_{144}^{1400} and α_{150}^{1400} depicts more or less the same spectral characteristic. The Cheung (2007) XRG source catalog does not have the 150 MHz flux and hence the spectral index. We measure the 150 MHz flux

from the TGSS catalog (Intema et al. 2017) and then calculate the respective α_{150}^{1400} values. For the Yang et al. (2020) catalog α_{150}^{1400} values are given for only the strong candidates' XRGs. We evaluated the spectral index for the possible candidates. However, in this case, the 150 MHz fluxes are presented in the catalog. For Bera et al. (2020), the spectral indices for XRGs and ZRGs are directly taken from their respective catalogs. So, in the histogram (5.5) we plot the XRGs from Cheung (2007), strong XRG candidates from Yang et al. (2019), possible XRG candidates from Yang et al. (2019), newly identified XRGs and ZRGs from Bera et al. (2020) and newly identified XRGs and ZRGs from Bera et al. (2022). The sources from different catalogs are plotted in different colour scales as mentioned in the figure. Note that, here we did not include the winged sources from Proctor (2011) as the sources are yet to be visually confirmed. However, a number of sources from the Proctor (2011) list are present in Yang et al. (2019), Bera et al. (2020), and Bera et al. (2022). So, basically, we also cover a quite few sources from Proctor (2011) catalog. Here, we plot the absolute values of the spectral indices to avoid the sign convention confusion of the spectral index.

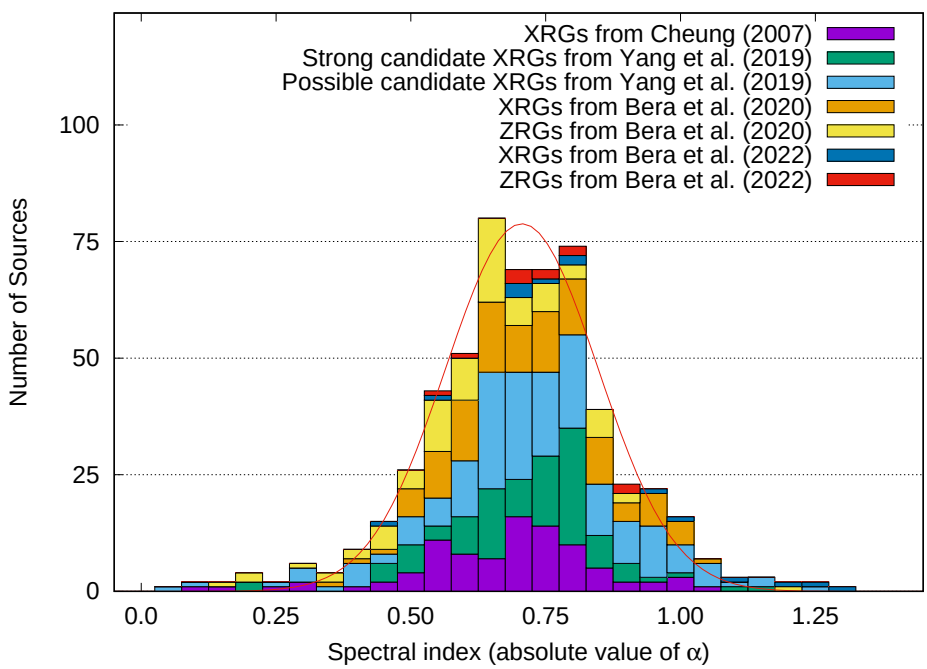

Figure 5.5: The global spectral index (in absolute value) is plotted for all the winged sources.

The mean and median of spectral index, α_{150}^{1400} for the XRGs from Cheung

(2007) is found as –0.68 and –0.70 with a standard deviation of 0.17. The strong and possible XRG candidates from Yang et al. (2019) have the mean, median of –0.70, –0.73 (standard deviation = 0.15), and –0.73 and –0.72 (standard deviation = 0.19), respectively. The mean and median for Bera et al. (2020) are –0.67 and –0.66 (see Chapter 3). So, we see that the mean spectral index for the sources is similar. However, the mean spectral index (α_{144}^{1400}) for winged sources identified from the low-frequency LoTSS DR1 is –0.81 (see Chapter 4). It shows a little higher than the sources identified in the high-frequency VLA FIRST data. Although, we see that all of the mean values fall in the spectral range, i.e.; $|\alpha| > 0.50$. To measure the global mean, we fit a Gaussian (see Figure 5.5) in the spectral index distribution. The global mean spectral index of winged sources as a class (or population) is found as -0.70 ± 0.01.

The majority of the sources ($\sim$ 60%) have a spectral index in the range –0.60 to –0.80. We also estimate that most of the winged sources ($\sim$ 91%) have relatively steep spectra. The general consequence of this steep spectrum result is that the sources are lobe-dominated radio sources, which is obvious for the XRGs. Now, the question is if the relative steep spectrum corresponds to the young radio emission or not. If this is so then winged sources are considered as the relatively young radio sources and they are at their initial stage of life-span. However, at this stage, we can not confirm this through the two-point spectral index calculated from the integrated fluxes, a spectral map for the sources are needed.

5.2.2 Global Luminosity

The radio luminosity (L_{rad}) is a measure of the strength of the overall source. Here, we primarily look at two aspects of radio luminosity for winged radio sources: (i) how the radio luminosity changes over redshift (z), and (ii) what is the mean luminosity value for a winged radio source in general. To estimate these two characteristics we first draw the distribution of luminosity with redshift, presented in Figure 5.6, and the source luminosity distribution through histogram, presented in Figure 5.7. The luminosity for all the identified winged sources is included. The luminosity is calculated using Equation 3-1 (or 4-1). However, here the luminosity is estimated in W Hz^{-1}. Here we use the cosmology parameters: $H_0 = 67.4$ km s^{-1} Mpc^{-1}, $\Omega_m = 0.315$ and $\Omega_{vac} = 0.685$ (Planck Collaboration et al. 2020). The luminosity distances are calculated from Cosmological Calculator for the Flat

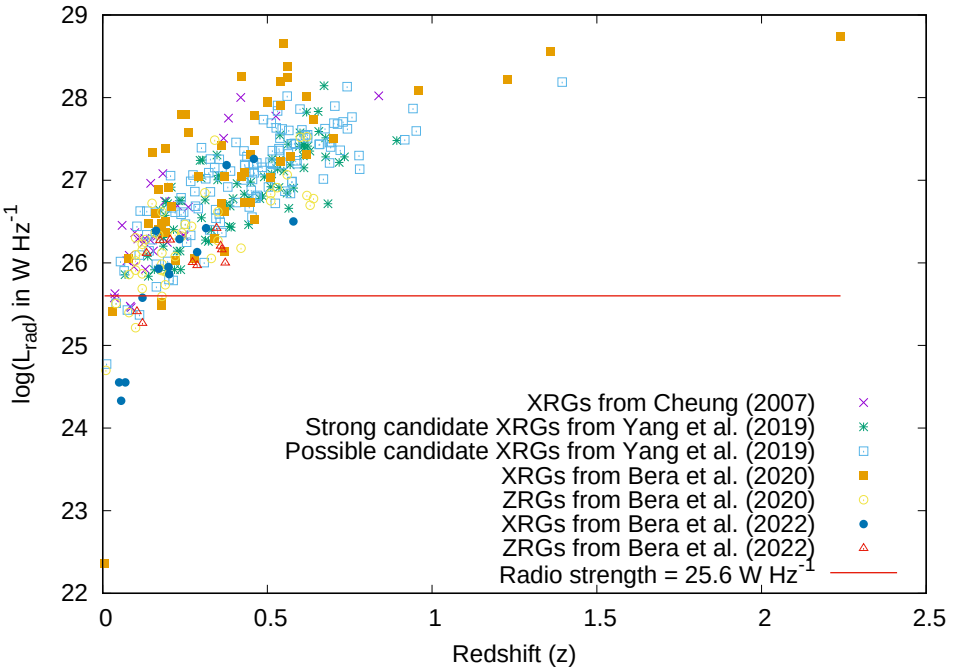

Figure 5.6: The plot depicts the distribution of radio luminosity (L_{rad}) for all winged radio sources with their respective redshift (z).

Universe by Nick Gnedin[1]. We calculate the luminosity for XRGs from Cheung (2007), strong XRG candidates from Yang et al. (2019), possible XRG candidates from Yang et al. (2019), newly identified XRGs and ZRGs from Bera et al. (2020), and Bera et al. (2022) and plot them separately on a log scale (see Figures 5.6 and 5.7). The sources from different catalogs and types are indicated by the respective colour, indicated in the plots. Here, a total of 359 data are plotted.

Landt et al. (2010) proposed that the X-shaped radio galaxies represent a transition population of FR-dichotomy with reference to the radio power and emission-line strength (L_{NLR}). They have shown the transition and asserted that the transition point between the two FR classes for $L_{NLR} \sim 10^{35}$ W and radio strength $\sim 10^{25.6} WHz^{-1}$ values. In the plot, the red line, parallel to the redshift axis is the line corresponding to the radio strength $25.6 WHz^{-1}$. We check that only $\sim 5\%$ of the total winged source lies below the radio strength level.

The histogram of global distribution for the luminosity of winged source shows that most of the sources ($\sim 80\%$) have luminosity in between the range 10^{26} –

[1]https://home.fnal.gov/ gnedin/cc/

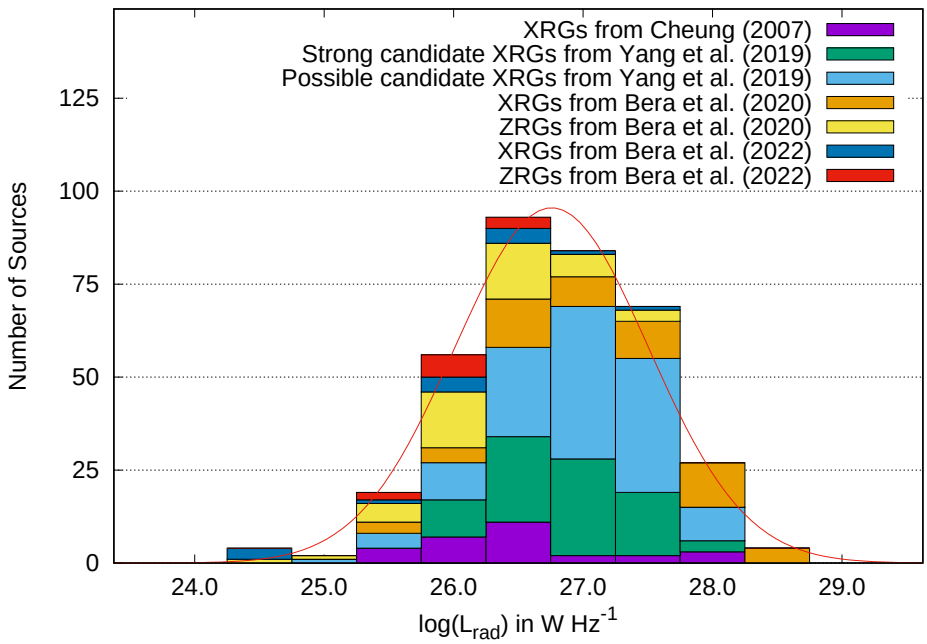

Figure 5.7: The histogram shows the global radio luminosity distribution for all winged radio sources.

$10^{28} WHz^{-1}$. Note that, in the histogram plot we exclude the XRG J1354+5840 (from Bera et al. (2020)) as the source has an extreme minimum luminosity and the presence of the sources is redundant in the Gaussian fit plot. We see a peak in the histogram at the luminosity value $10^{26.5} WHz^{-1}$. Considering the values in log-scale in the unit of WHz^{-1}, the mean luminosity for XRGs from Cheung (2007) is found as 26.50 with a median of 26.32 and a standard deviation of 0.72. For the strong XRGs from Yang et al. (2019) the mean and median values are 26.86 and 26.84 with a standard deviation of 0.52. The respective values for the possible XRGs from Yang et al. (2019) are 27.00, 27.10, and 0.62. The mean luminosity for winged sources from Bera et al. (2020) is found as 26.71 (median = 26.62 and standard deviation = 0.95). For Bera et al. (2022), the winged sources have a mean and median of 25.91 and 26.06 with 0.67. We also fit a Gaussian to measure the global mean of radio luminosity for winged radio sources and found the mean luminosity as $26.77 WHz^{-1}$.

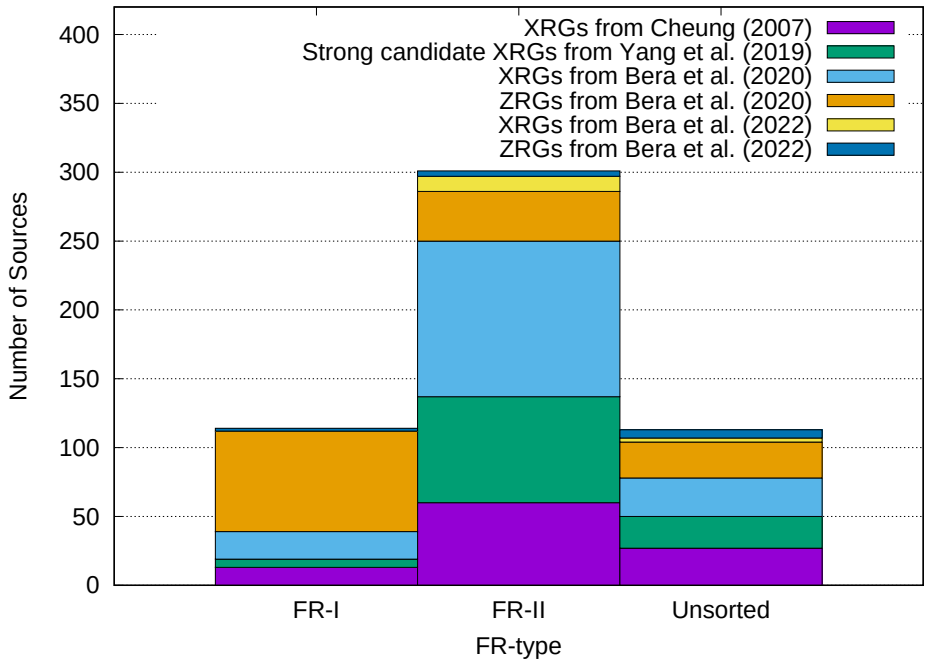

Figure 5.8: Histogram showing the global winged sources distribution among their respective FR-classification.

5.2.3 Global FR-dichotomy

The FR characterization is a major information for a radio source. The FR-dichotomy importantly gives a look at the evolutionary aspects of radio sources. Here, we present a global map to show the distribution of the identified winged sources. The FR-categorization was done by visual inspection of the relative brightness distribution along the edge to the core. Here, we plot a total of 528 sources. Out of these 528 sources for 113 sources, no classification was made as the sources show a complex brightness distribution. A total of 415 sources are classified as either FR-I or FR-II sources. We see that most of the sources $\sim 73\%$ (301) show FR-II characteristics while the rest $\sim 27\%$ show FR-I. Note that, there are no edge-brightened (FR-II) characteristics are found for the secondary lobes or wings. We see that the major contribution to the FR-I category comes from the ZRGs. This fact indicates the fact that when it comes to a winged source with the edge-darken property the radio source has a tendency to show a Z-shape, instead of an X-shape. The histogram plot for FR-type distribution is presented in Figure 5.8. We should keep this fact in mind that the 113 sources, which are

not categorized as either FR-I or FR-II, may be checked more deeply to identify as either of the FR-type. These sources may also be the candidates of FR0 class or the HyMORS candidate.

Moreover, it is said that the X-shaped sources are preferentially found in low-luminosity FR-II type of galaxies (Leahy & Parma 1992; Dennett-Thorpe et al. 2002). Hence, our result supports and confirms the statement.

5.3 Morphological properties

5.3.1 Global Angle

Now, we will check one of the morphological properties of the XRGs, the angle which is defined as the acute angle produced by the major and minor axes at the center of the source. The angle is measured as discussed given in Section 3.3.5. Here, we consider only high-frequency true XRG candidates. So, in this calculation, we did not include the possible XRGs from Yang et al. (2019) and low-frequency XRG candidates from Bera et al. (2022). The possible XRG candidates from Yang et al. (2019) are not included as the sources are yet to be confirmed morphologically. On the other hand, each XRG from the LOFAR (Bera et al. 2022) has a different contour level setting and hence the angle measurements may not give a uniform and accurate distribution value. We plot a histogram to see the angle distribution among the XRG sources. The histogram (given in Figure 5.9) shows the angle distribution among the XRG sources from Cheung (2007), Yang eat al. (2019), and Bera et al. (2020). In this calculation, we did not include the sources that have one-sided secondary lobes and the sources that have a complex morphology to draw an angle.

Here, we plot angles for a total of 245 sources. We see that histogram has an exponential nature with its peak at angle 90°. We check $\sim$ 96% (most) of the sources have an angle greater than 50°. This implies that the XRG with a lower angle is a much rare kind. We also check that a major number of sources, $\sim$ 61% have an angle greater than 70°. This information ensures that a certain good fraction of X-shaped sources may be the bonafide source. A bonafide XRG source is defined as a winged source that has a minor axis or secondary lobe length comparable to the major axis or primary lobe and has an angle in the order of $\sim$ 90° (Bera et al. 2022). However, to confirm exactly what proportion of the sources are bonafide we need the relative secondary lobe length value, which we

will discuss in the next section.

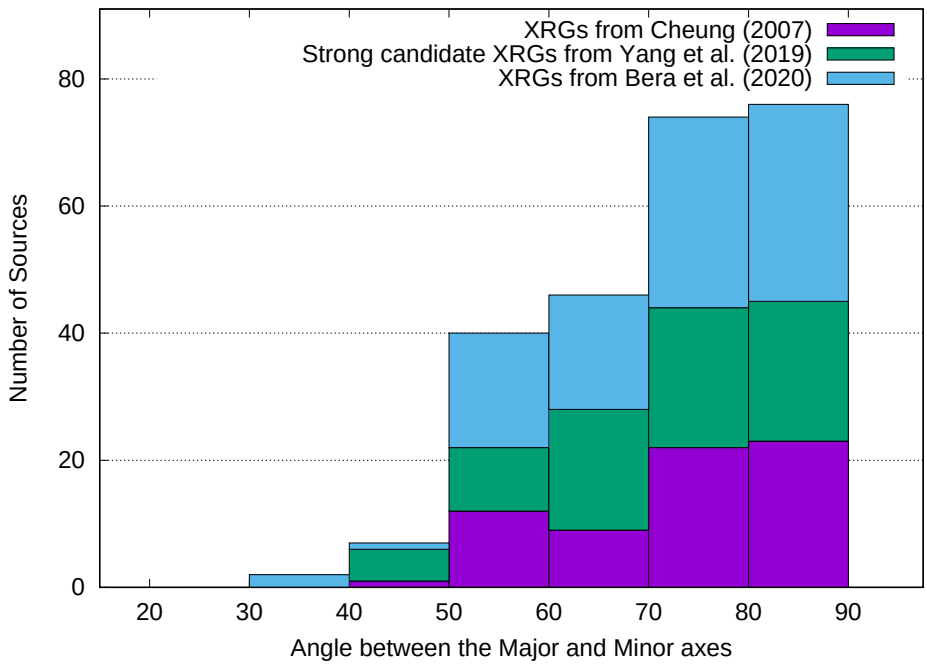

Figure 5.9: The histogram plot shows the angle distribution of all the discovered XRGs.

5.3.2 Global Jet-ratio

Let us look at another morphological aspect of XRG, the jet-ratio, i.e.; the ratio of minor axis or secondary lobe to major axis or primary lobe. The jet-ratio is measured as given in Section 3.3.5. In this analysis, we consider the XRGs from Cheung et al. (2007), strong XRG candidates from Yang et al. (2019), and XRGs from Bera et al. (2020). As for the case of angle calculation, here we also exclude the possible XRG sources from Yang et al. (2019) and XRGs from Bera et al. (2022). We plot a histogram to see the jet-ratio distribution among the sources. The histogram is presented in Figure 5.10. Here, we also keep out the sources that have a one-sided lobe or have a complex morphology to measure the relative lobe lengths.

A total of 246 data points are plotted. We see that most ($\sim$ 71%) of the total sources have jet-ratio in the range of 0.50 to 1.00. Approximately, 21%

of the sources have a larger secondary lobe compared to the primary lobe, i.e; the sources have jet-ratio greater than 1.00. We also fit a Gaussian to measure the global mean of jet-ratio and found the mean as 0.77. The jet ratio gives an important characteristic of an XRG as it defines the fundamental property of an XRG; the secondary lobes, and the wings.

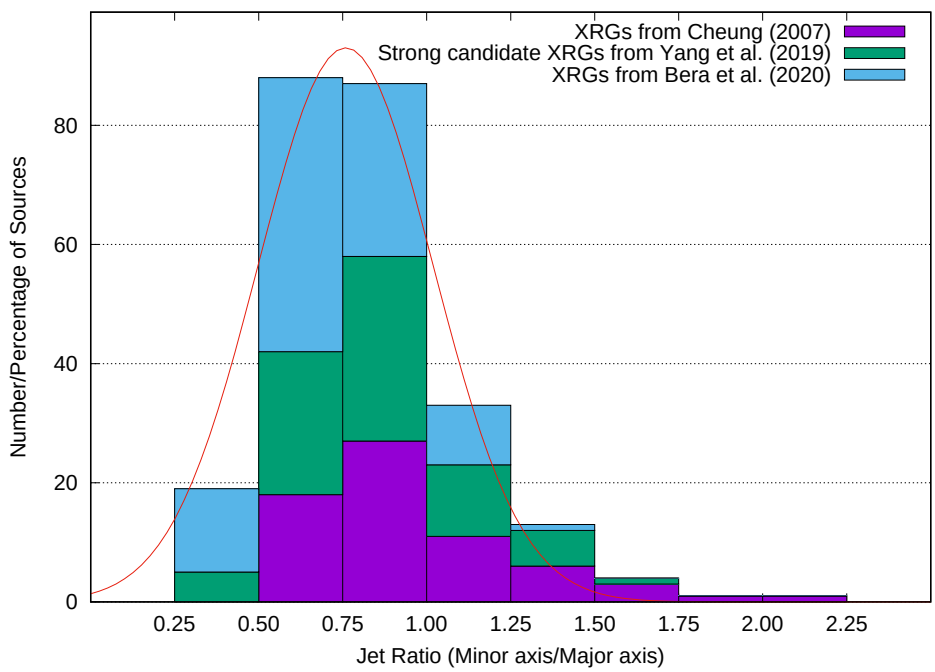

Figure 5.10: The histogram represents the jet-ratio histogram of XRGs that deals with the jet-ratio distribution among the sources.

Now to ensure the bonafide XRG candidates in the sample, we check the sources that have comparable secondary lobe length with the primary lobe. We see that $\sim$ 49% of the sources have a comparable secondary lobe. Note that, here we consider the sources that have secondary lobe lengths 75% to 125% to the primary lobe. Combining this result with the result of the global angle, we conclude that $\sim$ 50% of the identified sources are bonafide X-shaped sources.

5.4 On the Origin of the Wings

A satisfactory explanation for the formation of the winged radio galaxies' distinctive morphologies remains elusive. As we discussed before, this is mostly due to

the little number of detailed research, as well as the short overall number of known cases accessible for systematic analyses. Hence following our primary motivation we were focused on ensembling (identifying) a large number of sources sample. We also make statistical studies on these sources to conclude on different global parameters and properties of such exotic sources. However, the proper explanation for the origin is not available and is currently out of our work at present and in progress (see Future Plans in Chapter 6).

However, we may conclude the following conclusive aspects of winged sources–

(i) The backflow of plasma is one concept to explain the winged sources. As the buoyancy-driven backflow cannot propagate faster than the external sound speed (Leahy & Parma 1992), the buoyancy-driven wings are not predicted to be longer than the main radio lobes, which are known to progress supersonically. For 21% of the total winged sources have minor axis, longer than the major axes. Through observations of a sample of 87 sources, Saripalli & Roberts (2018) discovered two such sources. So, the backflow may be considered as a possible origin for the rest of the sources, however, this model can not explain the sources with longer wings. Regardless, it is still plausible that the alignment effect plays a role in the primary jets, which appear shorter than the secondary jets.

(ii) Considering the post-merger star-forming galaxy (Hota et al. 2012), the wings may have evolved as a result of pre-merger gravitational interaction between the two galaxies. This event may be the case of 'Z'-shaped sources.

(iii) Here, we make a catalog of ZRG sources, which are considered to be a part of winged sources as X-shaped sources. We see that a certain number of winged sources are contributed as ZRG. Merritt & Ekers (2002) proposed that if the active SMBH's spin reorients owing to an impulsive torque of external origin, the subsequent flip of its spin vector might result in an X-shaped radio morphology (Blandford & Icke 1978; Murgia et al. 2001). If the torque works on the SMBH only gradually, i.e., its duration is greater than the jet outflow time-frame, a 'Z'-shaped radio morphology would emerge (Yang et al. 2019). An impulsive torque is particularly probable in the case of the radio galaxy NGC 326 (Fanti et al. 1977) because its host is a dumbbell galaxy formed of two large ellipticals in gravitational contact (Battistini et al. 1980). If the outflow and spin reorientation periods are comparable, one can anticipate to discover sources with an intermediate morphology (between Z-shape and X-shaped).

(iv) The majority of the winged sources show relatively steep radio spectra between 150 MHz and 1.4 GHz, as predicted. The global mean of all the identified

winged sources also falls in the steep spectral region. Lal et al. (2019) recently demonstrated that, in terms of radio spectral index, active lobes do not appear to vary from (fainter) wings, which may support the twin AGN hypothesis, in which the spectra of the primary and secondary wings are predicted to be uncorrelated. A comparable approach for our genuine XRGs would be fascinating in order to impose stricter limitations on the models of X-shaped radio sources.

(v) There are fourteen sources that showed winged characteristics both in high frequency 1.4 GHz FIRST and low frequency 144 MHz LoTSS DR1 data (see Appendix). The radio map shows these sources have quite similar wing distribution and properties such as angle, lobe orientation, symmetry, etc.

The above facts yield that when certain sources can be explained by one mechanism, the other sources could not be described or are not valid for that mechanism. They must be referred to another hypothesis. Thus, for now, it may be concluded that one single mechanism is not responsible. In other words, we can not explain all the winged sources through one single mechanism, at least for this time being. Better comprehension is required, as well as further work is needed to establish the origin of winged sources.

References

Battistini, P., Bonoli, F., Silvestro, S., et al. 1980, A&A, 85, 101
Blandford, R. D., & Icke, V. 1978, MNRAS, 185, 527
Bera, S., Pal, S., Sasmal, T. K., & Mondal, S. 2020, ApJS, 251, 9
Bera, S., Sasmal, T. K., Patra, D., & Mondal, S. 2022, ApJS, 260, 7
Cheung, C. C. 2007, AJ, 133, 2097
Dennett-Thorpe, J., Scheuer, P. A. G., Laing, R. A., et al. 2002, MNRAS, 330, 609
Fanti, C., Fanti, R., Gioia, I. M., et al. 1977, A&AS, 29, 279
Hota, A., Rey, S.-C., Kang, Y., et al. 2012, MNRAS, 422, L38
Lal, D. V., Sebastian, B., Cheung, C. C., & Rao, A. P. 2019, AJ, 157, 195
Landt, H., Cheung, C. C., & Healey, S. E. 2010, MNRAS, 408, 1103
Leahy, J. P., & Parma, P. 1992, in Extragalactic Radio Sources: From Beams to Jets, ed. J. Roland, H. Sol, & G. Pelletier (Cambridge: Cambridge Univ. Press), 307
Merritt, D., & Ekers, R. D. 2002, Sci, 297, 1310
Murgia, M., Parma, P., de Ruiter, H. R., et al. 2001, A&A, 380, 102
Planck Collaboration, Aghanim, N., Akrami, Y., et al. 2020, A&A, 641, A6
Proctor, D. D. 2011, ApJS, 194, 31
Richards, G. T., Myers, A. D., Gray, A. G., et al. 2009, ApJS, 180, 67
Saripalli, L., & Roberts, D. H. 2018, ApJ, 852, 48
Yang, X., Joshi, R., Gopal-Krishna, et al. 2019, ApJS, 245, 17

Chapter 6

Future Plans

We are all stardust.

—Stefan Klein

Through this work, we have discussed the identification of a large sample of winged-shaped radio sources. The identification of some major aspects, properties, and parameters of this exciting source class were also evaluated. However, the origin is yet to be established. To find the origin, we need to do multi-frequency observation for these sources. We also need to analyze the results for different observations to ensure which mechanism is responsible for the creation of wings. Here, we may also fit data in the given proposed models and those may be helpful in this regard. We also need to study the significance of such peculiar sources.

6.1 Spectral Ageing Analysis

In the first step towards understanding this class, we wish to conduct multi-frequency observations. One of the major outcomes of the multi-frequency analysis is the spectral ageing analysis. The spectral ageing assessments of radio galaxies provide useful insight into the physical features and physical processes occurring within radio lobes. Large double-lobed FR-II radio galaxies are useful for examining spectral age features. Note that, we already saw that our winged radio sources are primarily FR-II type sources and hence this will be an effective analysis. Particles at hotspots in such FR-II radio sources are accelerated and spread

outwards to generate long radio emission lobes and bridges. Because of radiative losses, the spectra increase steeper as one moves away from the hotspots. Nonetheless, if there is significant re-acceleration of the particles throughout the lobes of these sources, the variation of the spectral index from the hotspot can be modified. If there is no significant re-acceleration, the steepening of the spectral index with distance from the hotspots can be used to calculate the spectral age of the radiating particles. The form of an electron population's energy spectrum can be determined, providing a detailed picture of the underlying physics of a radio source. The synchrotron radiation in an area with a fixed magnetic field loses energy in the form of $dE/dt \propto \nu^2$. As a result, the cooling of higher energy electrons leads to a steeper and curved spectrum in the plasma of the older region. As a result, spectral ageing has become a widely utilized tool for understanding the dynamics in galaxies. Several researchers have clearly defined the theory of spectral ageing analysis (Kardashev 1962; Pacholczyk 1970; Jaffe & Perola 1973; Tribble 1993). The physical reality of spectral ageing modes has previously been studied (Alexander & Leahy 1987; Machalski et al. 2009). The age of the powerful radio galaxy may be calculated using these models, and the dynamics of the galaxy can be examined. Constraints affecting the evolution of the local magnetic field in the lobes must be considered when doing spectral ageing (Wiita & Gopal-Krishna 1990; Rudnick et al. 1994; Kaiser et al. 2000). There are mostly two spectral ageing models; KP model proposed by Kardashev (1962) and Pacholczyk (1970) and JP model proposed by Jaffe & Perola (1973). Both of the models are based on a single electron injection energy distribution at radio galaxy hotspots. The pitch angle is assumed to be constant for each electron but varies for each electron in the KP model. The JP model assumes that the pitch angles will be distributed and isotropized over a considerably shorter time scale than the spectral age of the source.

6.2 Study of the Optical Properties with Large-scale Environment

In the next step, we wish to study the optical properties of the host galaxies of the winged radio sources. The study also accommodates the following properties: radio axes alignment, interstellar medium, black hole mass, and large-scale environment. This study will help to introspect the proposed models on the origin of winged sources. Note that, in this work we will mainly focus on the X-shaped sources.

The environment study of the X-shaped and 'Z'-shaped sources is also in our very next stage. The environment of X-shaped sources is done by Joshi et al. (2019), however, they used the 106 strong candidate X-shaped sources from Yang et al. (2019). With an enhanced sample size we will do a more depth study. Previously Liu et al. (2019) did an environment study of 'Z'-shaped sources from Proctor (2011) catalog. Now, morphologically the source samples of Proctor (2011) are not confirmed. But for now, we have a visually confirmed proper catalog of Z-shaped radio sources, that definitely will help to conclude a better result. We also wish to extend the work of Roberta et al. (2015a), Roberts et al.(2017), Saripalli & Roberts (2018). Using our ensembled large number of sources we may ensure more concrete results. So far the previous authors have already done with relatively small sample size. The study of the unified framework governed by Garofalo et al. (2020) is also on the to-do list. Our team also will do the magneto-hydro-dynamic (MHD) simulation to find the origin of 'X'-shaped sources, as previously done by Capetti et al. (2002), Rossi et al. (2017).

6.3 X-shaped Radio Sources and Low-frequency GWB

Now comes a very important aspect and application of the X-shaped radio source. The coalescence of supermassive black holes (SMBHs) in galaxy mergers may be the primary source of the low-frequency gravitational wave background (GWB). Previously we mentioned that Merritt & Ekers (2002) argued that X-shaped radio galaxies are signs of such coalescences and that their abundance might be utilized to forecast the magnitude of the GWB. The low-frequency GWB is supposed to be in the nano-hertz range. A primary study on this has been done by Roberts et al. (2015b) using the Cheung (2007) sample. Now, through our findings, we have a large sample of X-shaped sources. Hence, this large collection will be utilized to standardize detailed computations of the SMBH coalescence rate and GWB.

References

Alexander, P., & Leahy, J. P. 1987, MNRAS, 225, 1
Capetti, A., Zamfir, S., Rossi, P., et al. 2002, A&A, 394, 39
Cheung, C. C. 2007, AJ, 133, 2097
Garofalo, D., Joshi, R., Yang, X., et al. 2020, ApJ, 889, 91
Jaffe, W.J., & Perola, G.C. 1973, A&A, 26, 423
Joshi, R., Gopal, K., Yang, X., et al. 2019, ApJ, 887, 266
Kaiser, C.R., Schoenmakers, A. P., & Röettgering, H. J. A. 2000, MNRAS, 315, 381
Kardashev, N.A. 1962, SvA, 6, 317
Machalski, J., Jamrozy, M., & Saikia, D. J. 2009, MNRAS, 395, 812
Merritt, D., & Ekers, R. D. 2002, Sci, 297, 1310
Pacholczyk, A.G. 1970, Radio Astrophysics. Freeman & Co., San Francisco
Proctor, D. D. 2011, ApJS, 194, 31
Roberts, D.H., Cohen, J. P., Lu, J., Saripalli, L., & Subrahmanyan, R. 2015a, ApJS, 220, 32
Roberts, D. H., Saripalli, L., & Subrahmanyan, R. 2015b, ApJL, 810, L6
Roberts, D. H., Saripalli, L., Wang, K. X., et al. 2017, ApJ, 852, 47
Rossi, P., Bodo, G., Capetti, A., & Massaglia, S. 2017, A&A, 606, A57
Rudnick, L., Katz-Stone, D.M., & Anderson, M.C. 1994, ApJS, 90, 955
Saripalli, L., & Roberts, D. H. 2018, ApJ, 852, 48
Tribble, P. 1993, MNRAS, 261, 57
Wiita, P.J., & Gopal-Krishna 1990, ApJ, 353, 476
Yang, X., Joshi, R., Gopal-Krishna, et al. 2019, ApJS, 245, 17

Appendix

Here we present all of the newly identified winged radio sources from the VLA FIRST and LoTSS DR1. All the radio images are plotted in the contour scale overlaid on the optical gray images. The optical images are taken from DSS 2 red images. There are five sets of images; the first set of images (A) shows the total of 161 newly identified XRG sources as identified from VLA FIRST data, the second set of images (B) presents the 135 newly identified ZRG sources as identified from VLA FIRST data, the third set of images (C) gives the radio plot of 14 freshly identified XRG sources from LoTSS DR1 and the fourth set of images (D) depicts the 12 freshly identified ZRG sources from LoTSS DR1. In the fifth set of images (E), we represent a comparative radio map for the 14 common winged sources, which are identified both in VLA FIRST and LoTSS DR1.

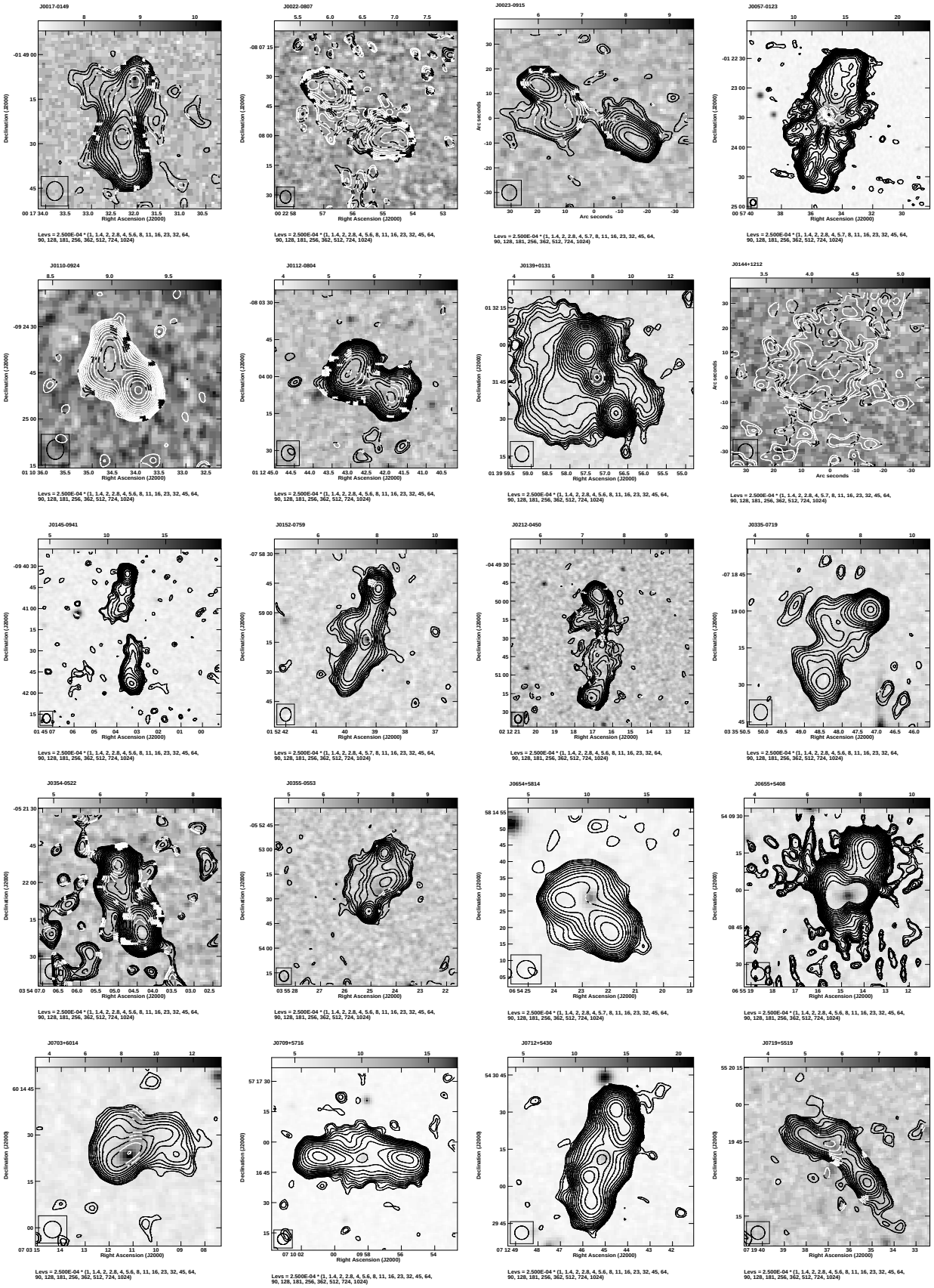

Figure 6: (A) The VLA FIRST image of the 161 newly identified X-shaped radio sources (in contours) overlaid on the DSS2 red image (in gray-scale). The contour levels are drawn from 0.25 mJy and increased in the order of $\sqrt{2}$.

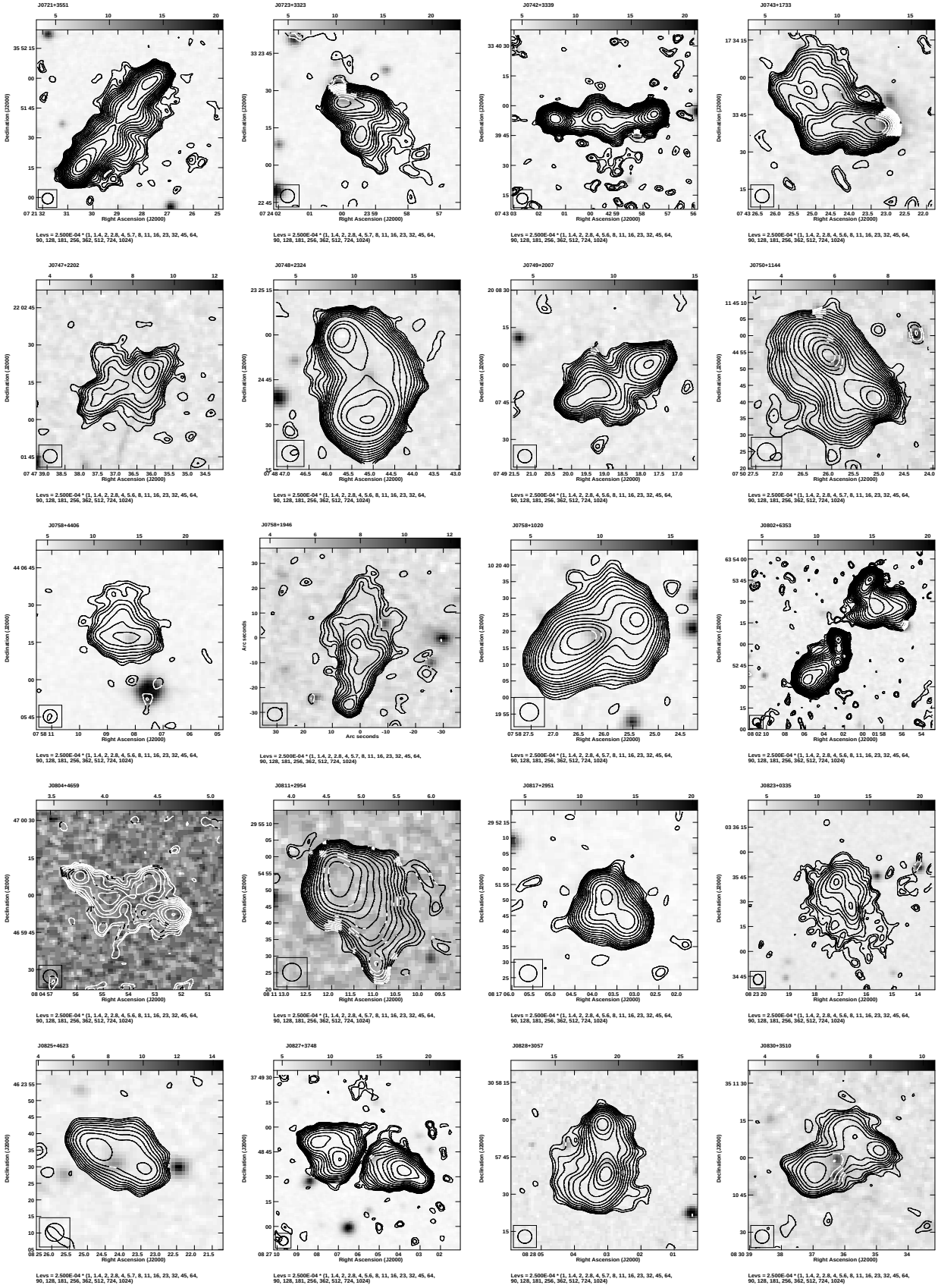

Figure 6: (A) *Continued*

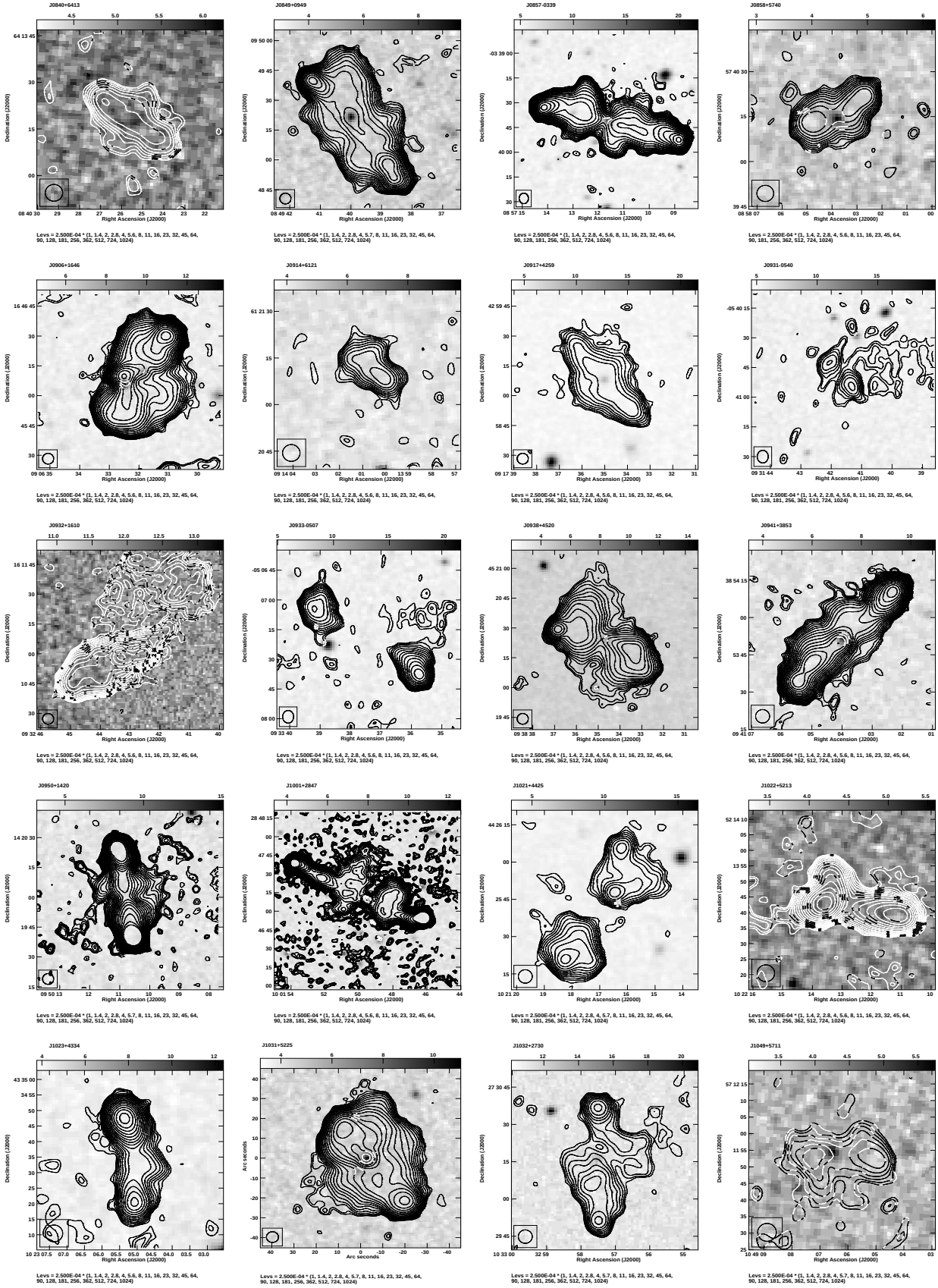

Figure 6: (A) *Continued*

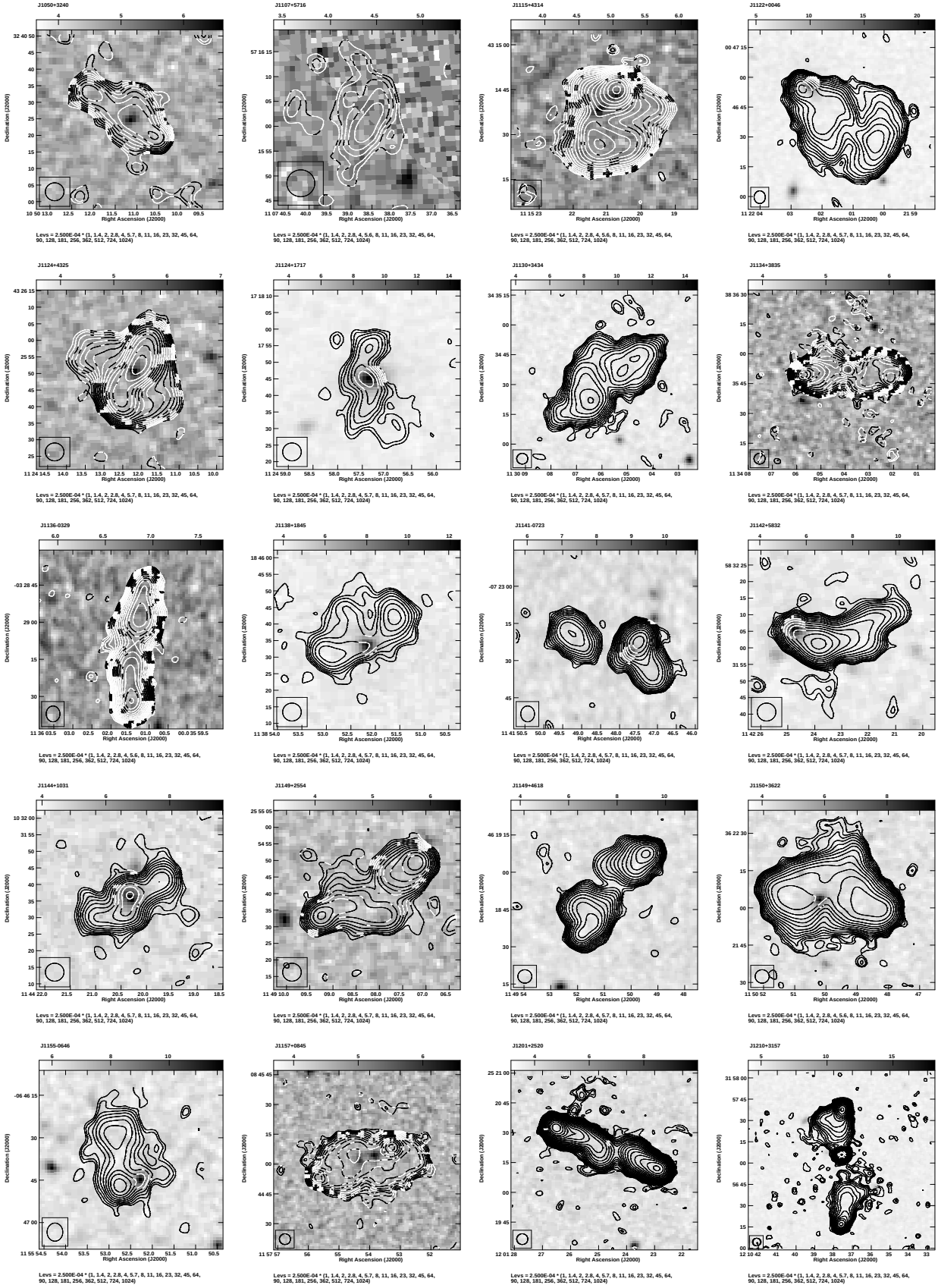

Figure 6: (A) *Continued*

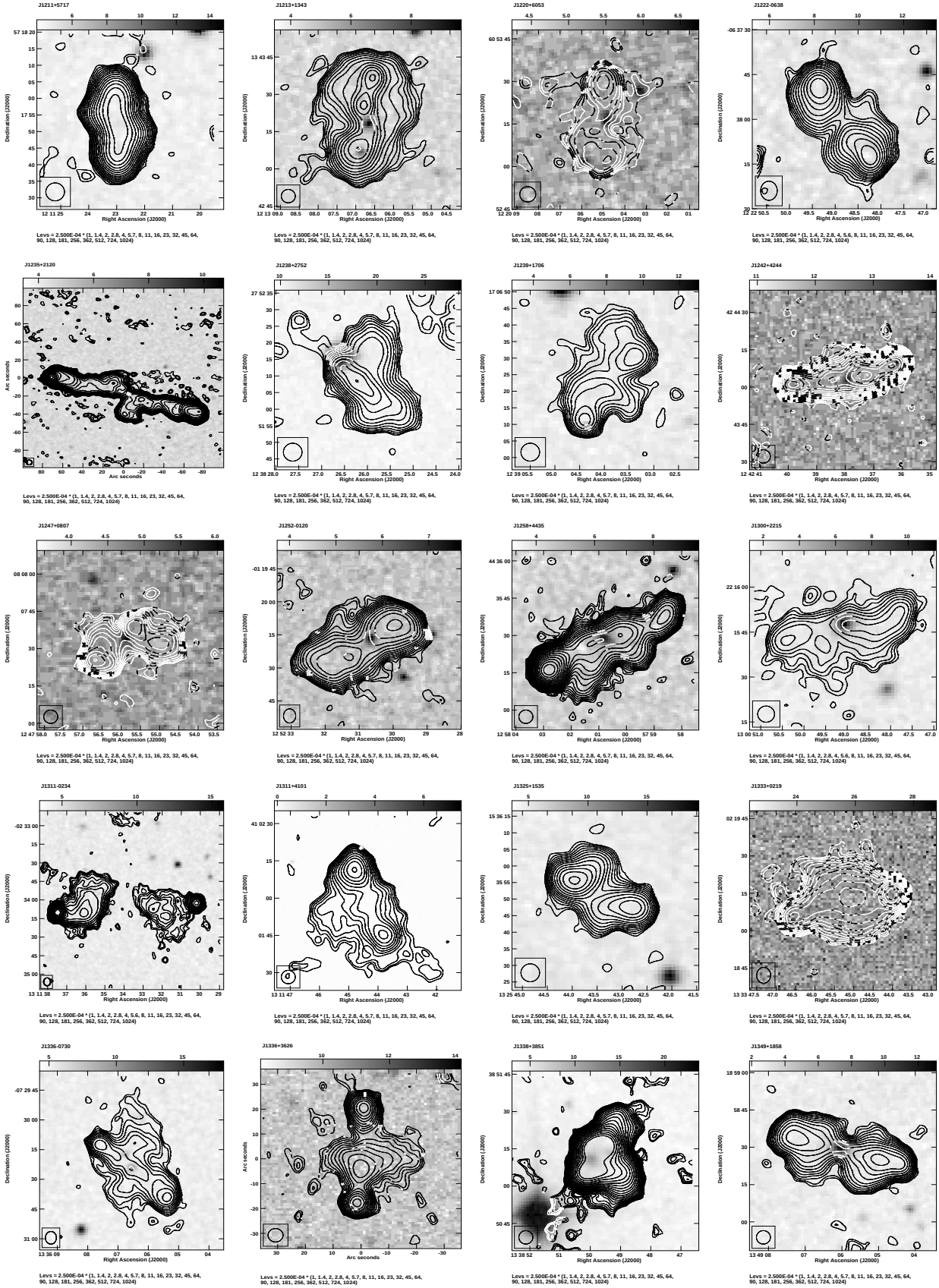

Figure 6: (A) *Continued*

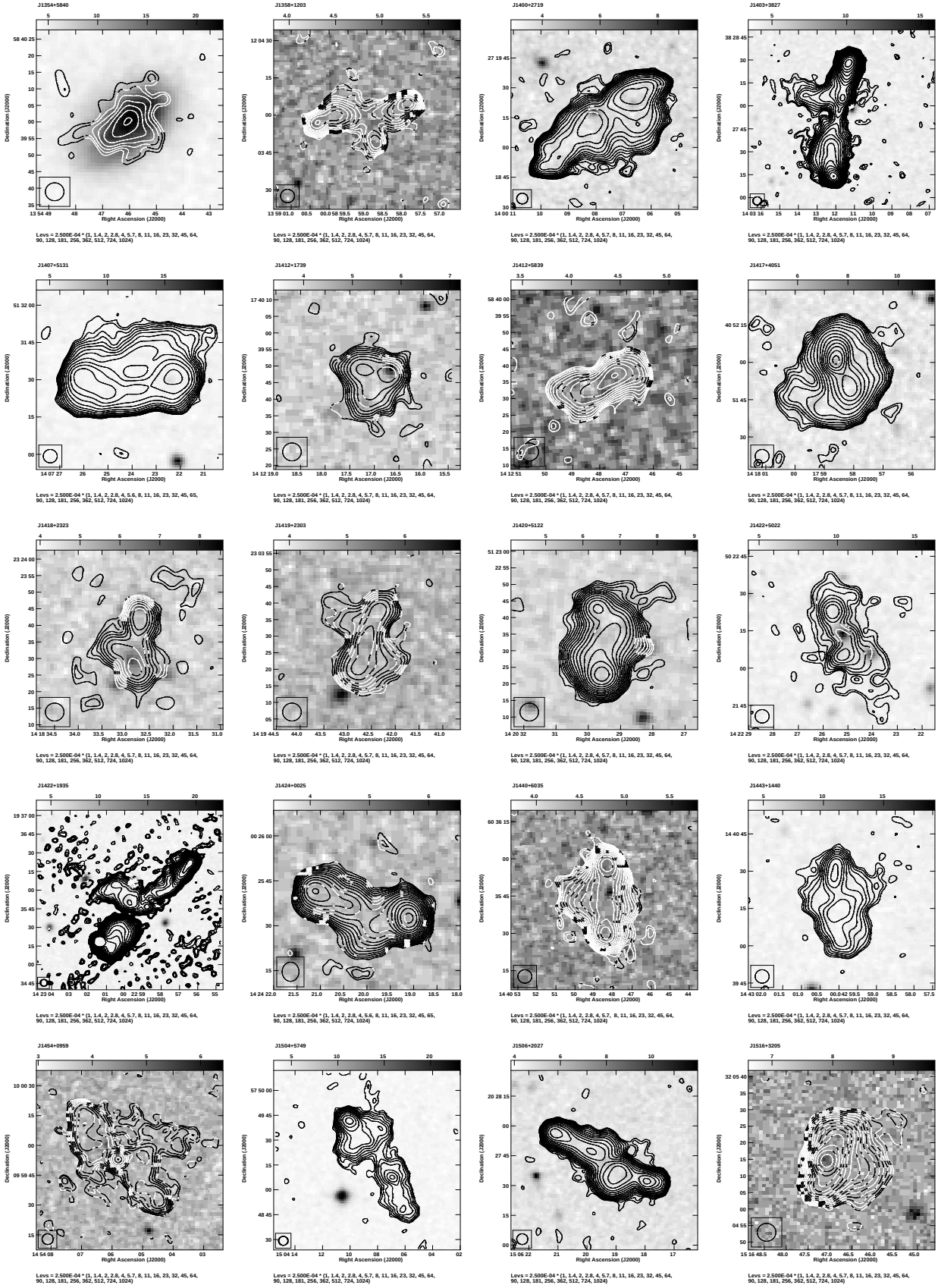

Figure 6: (A) *Continued*

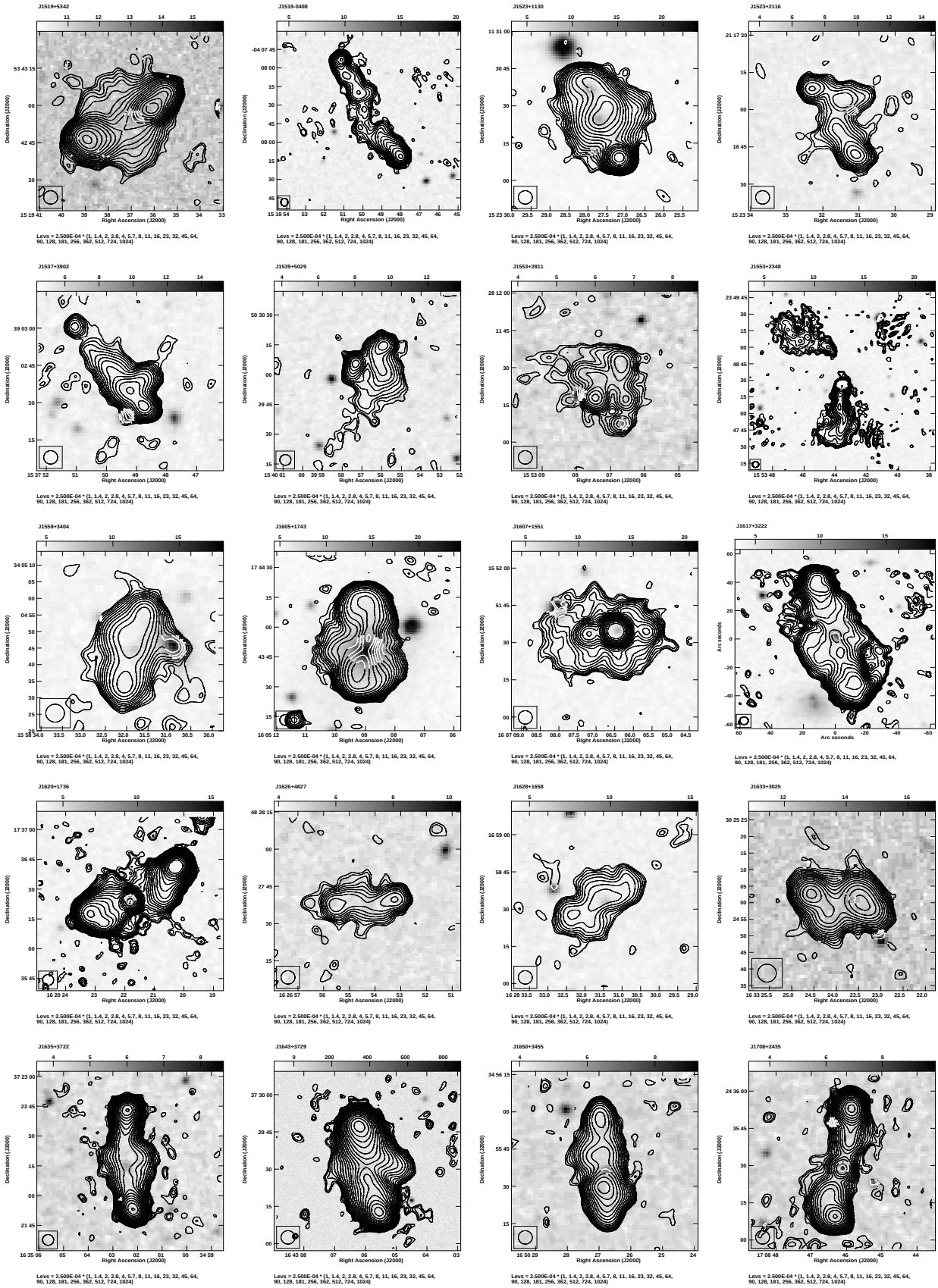

Figure 6: (A) *Continued*

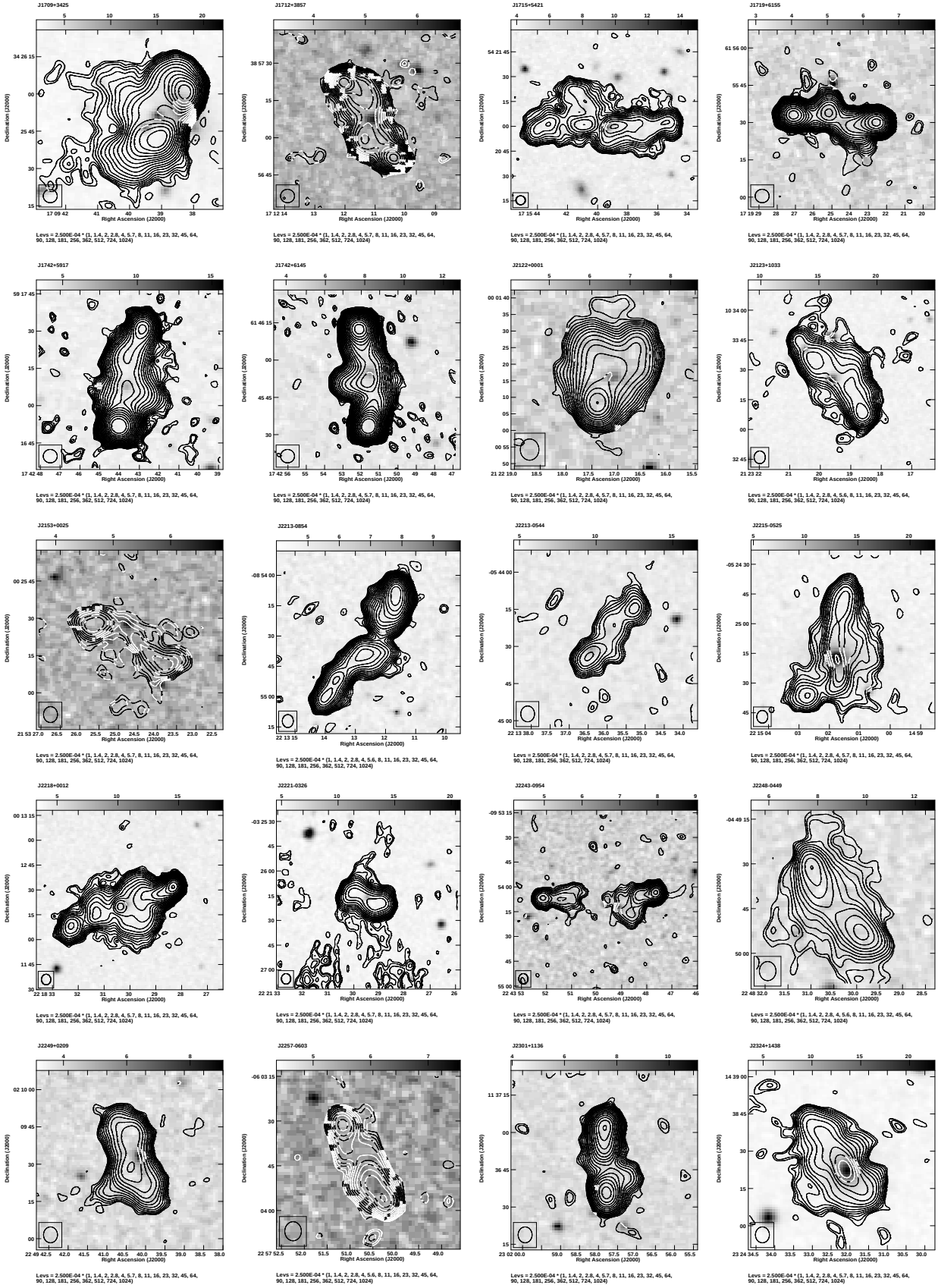

Figure 6: (A) *Continued*

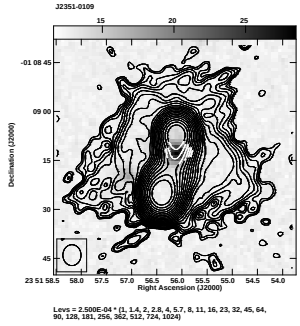

Figure 6: (A) *Continued*

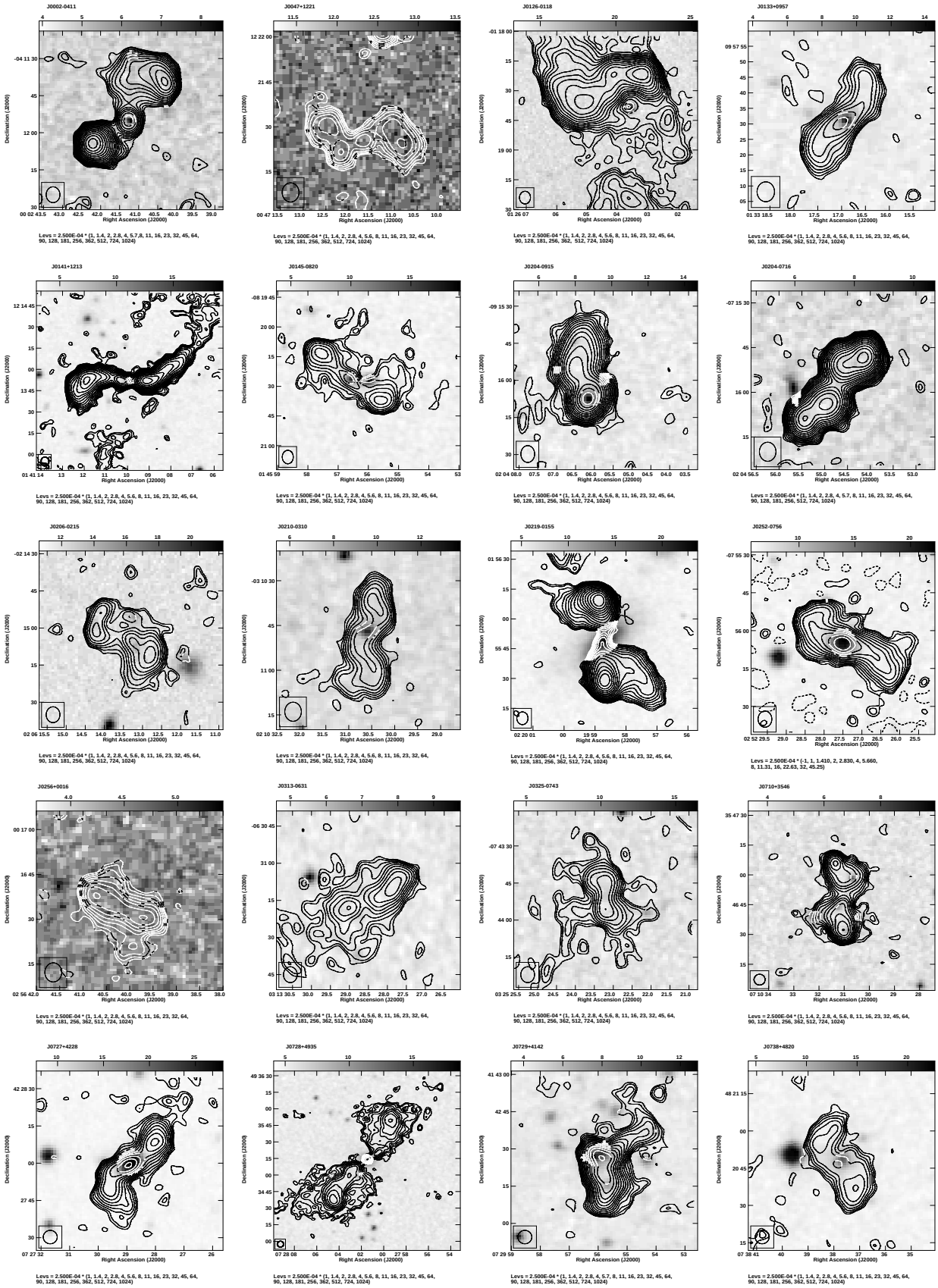

Figure 6: (B) The VLA FIRST image of the 135 newly identified Z-shaped radio sources (in contours) overlaid on the DSS2 red image (in gray-scale). The contour levels are drawn from 0.25 mJy and increased in the order of $\sqrt{2}$.

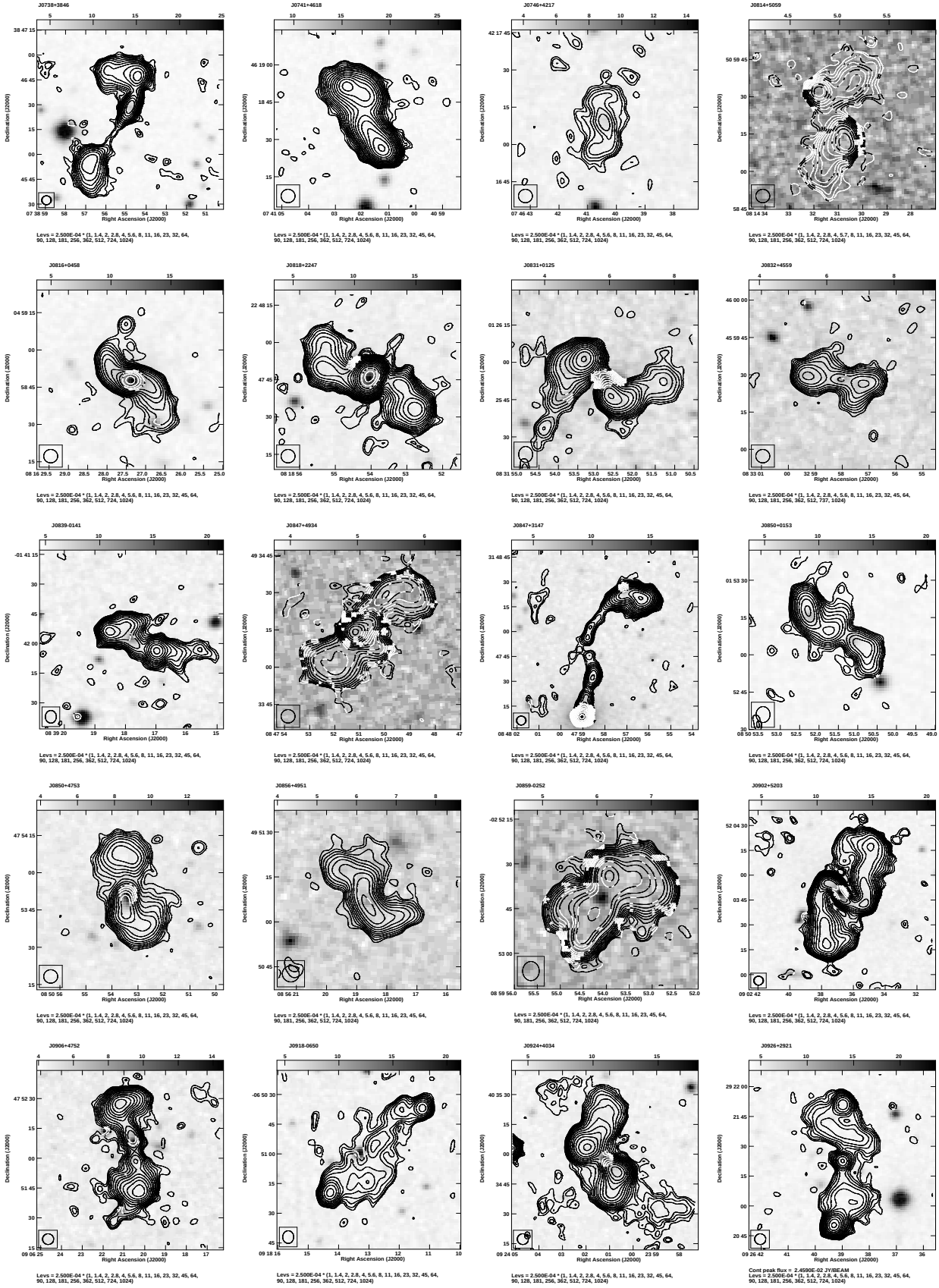

Figure 6: (B) *Continued*

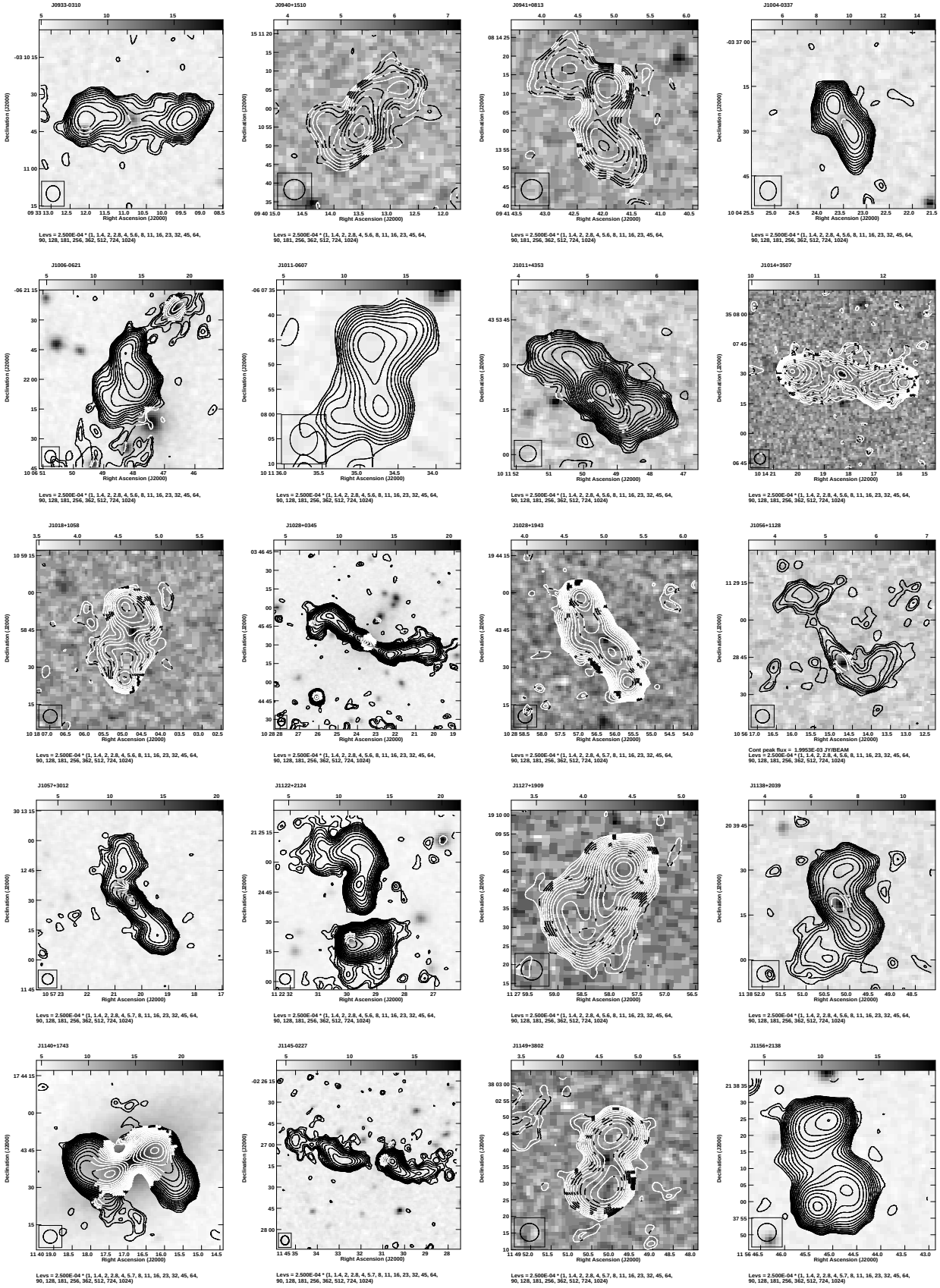

Figure 6: (B) *Continued*

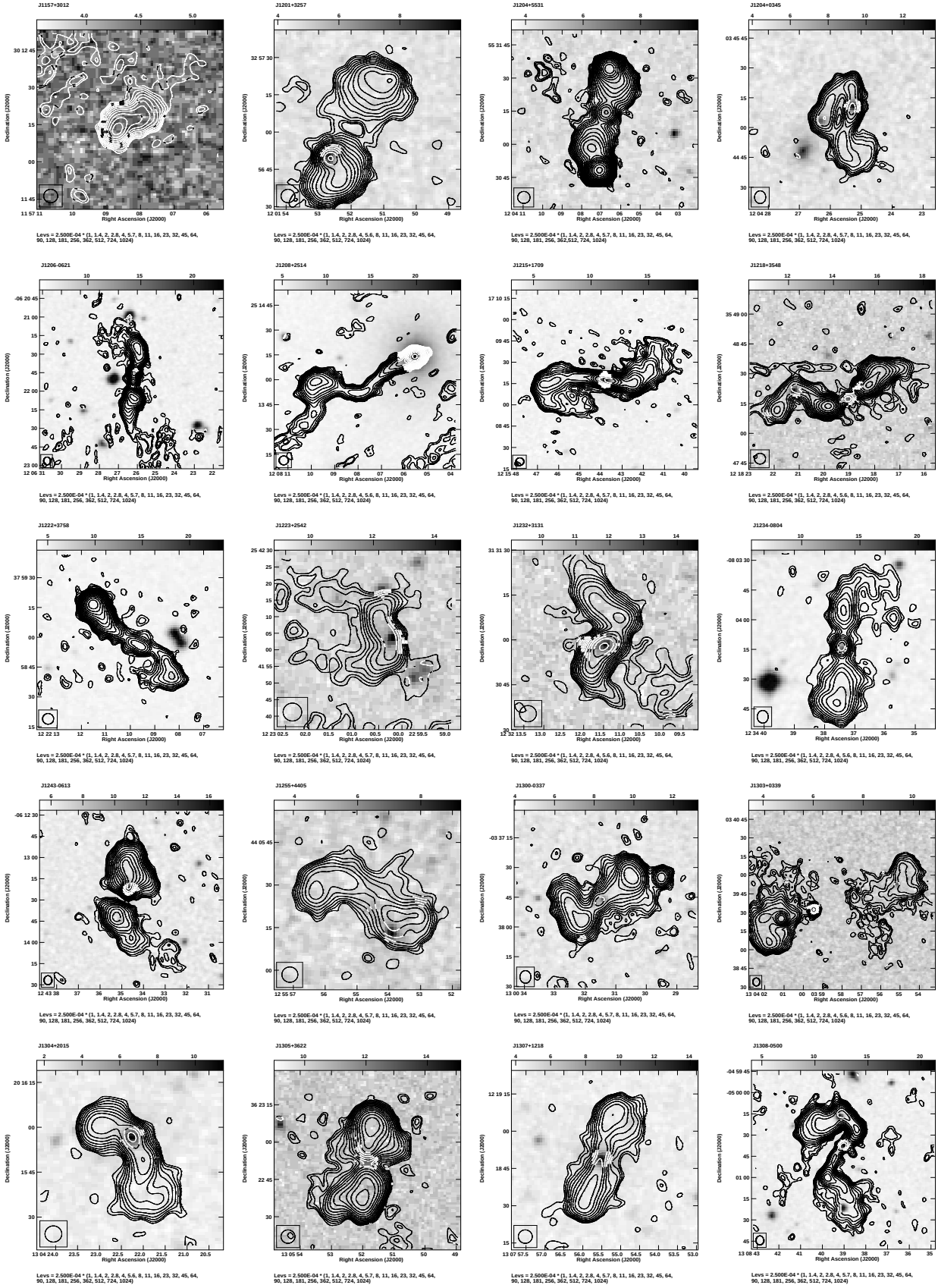

Figure 6: (B) *Continued*

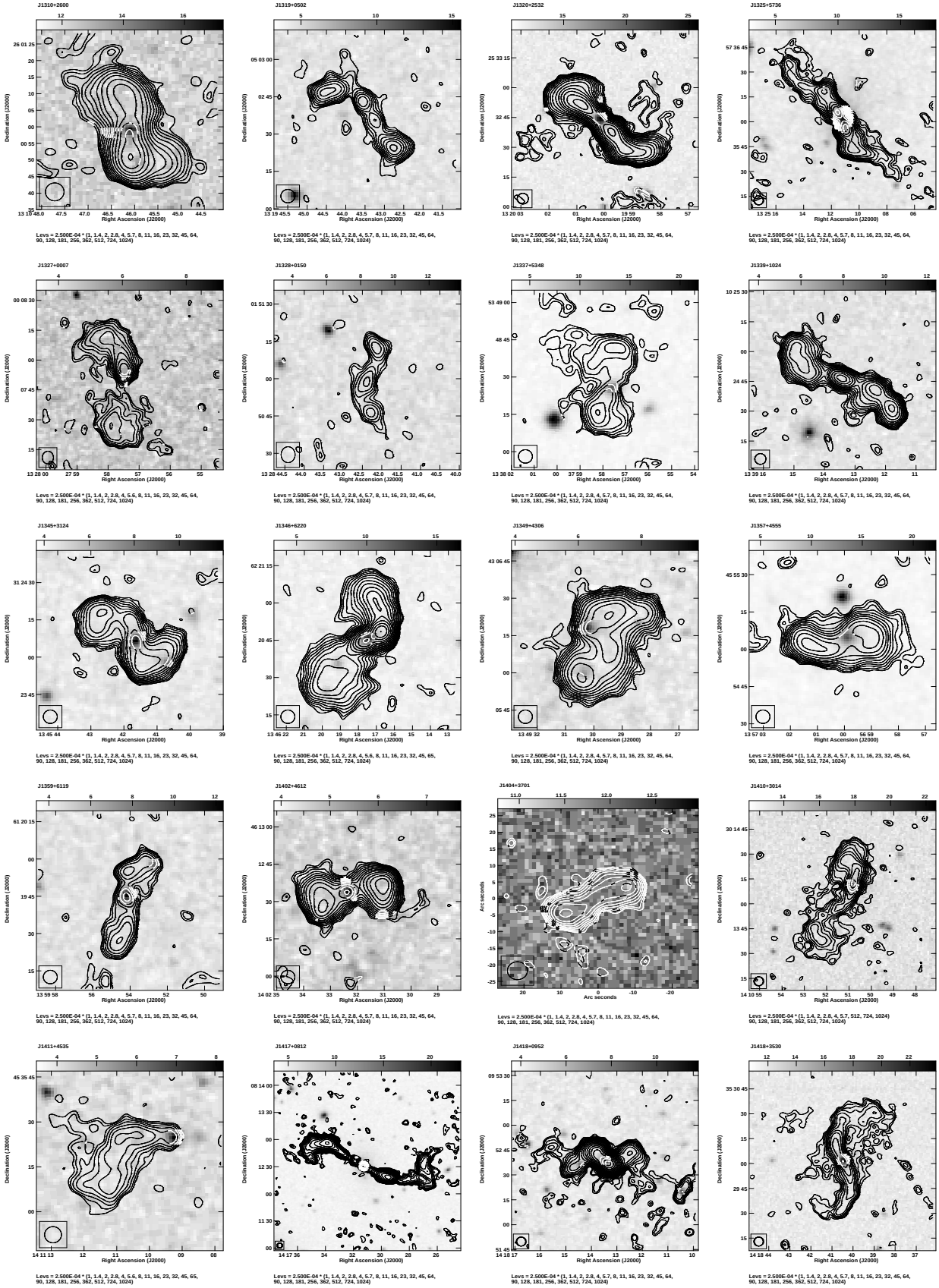

Figure 6: (B) *Continued*

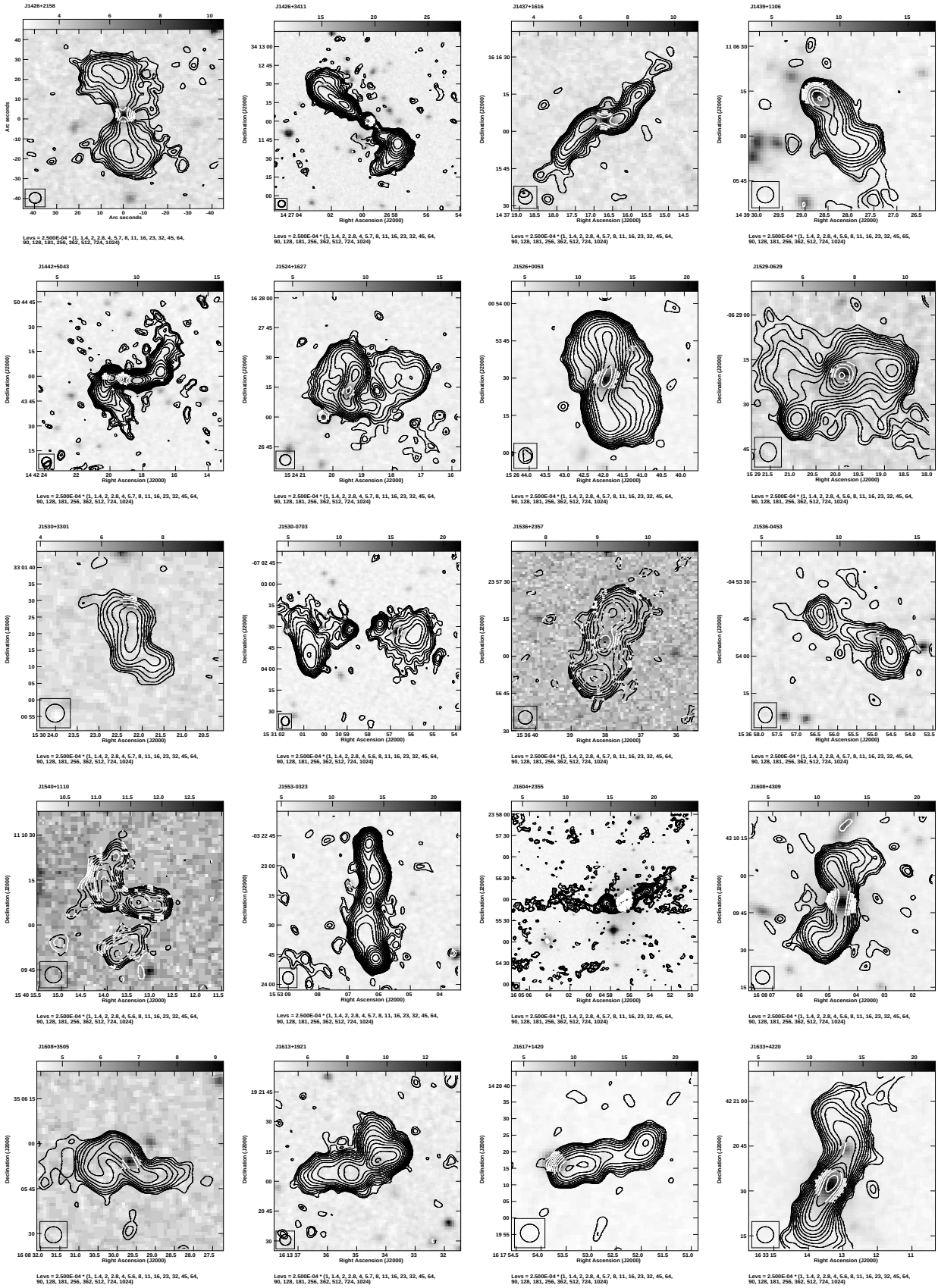

Figure 6: (B) *Continued*

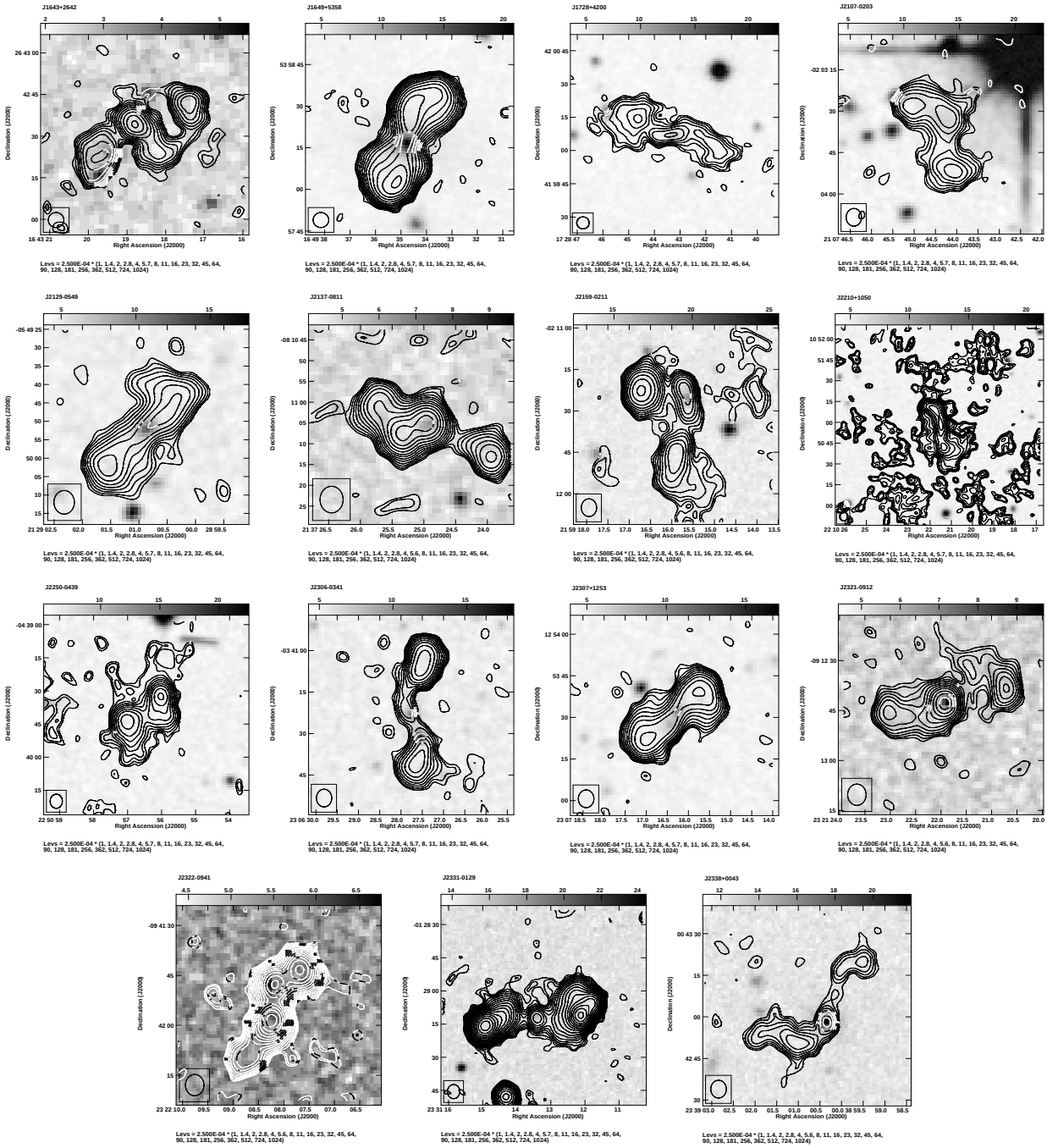

Figure 6: (B) *Continued*

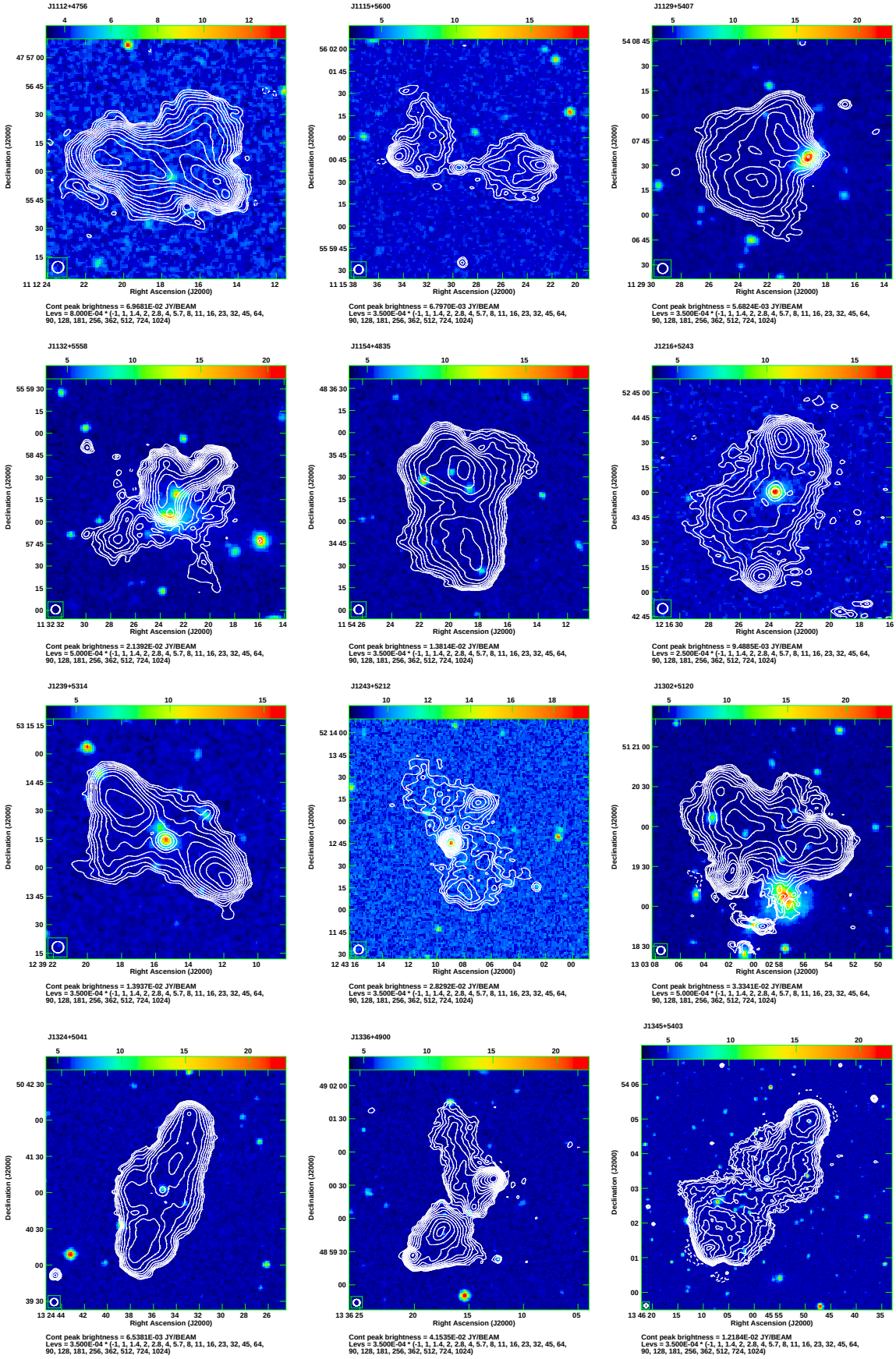

Figure 6: (C) LOFAR image of the X-shaped radio source (contours) overlaid on the DSS2 red image (gray scale). The relative radio contours are drawn from at least 3σ level with an increment of $\sqrt{2}$. Here, we use LOFAR $6''$ full resolution radio images for better-resolved structure.

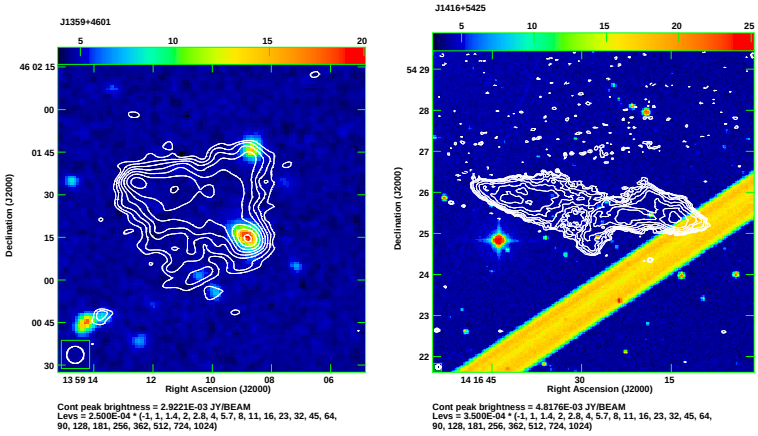

Figure 6: (C) *Continued*

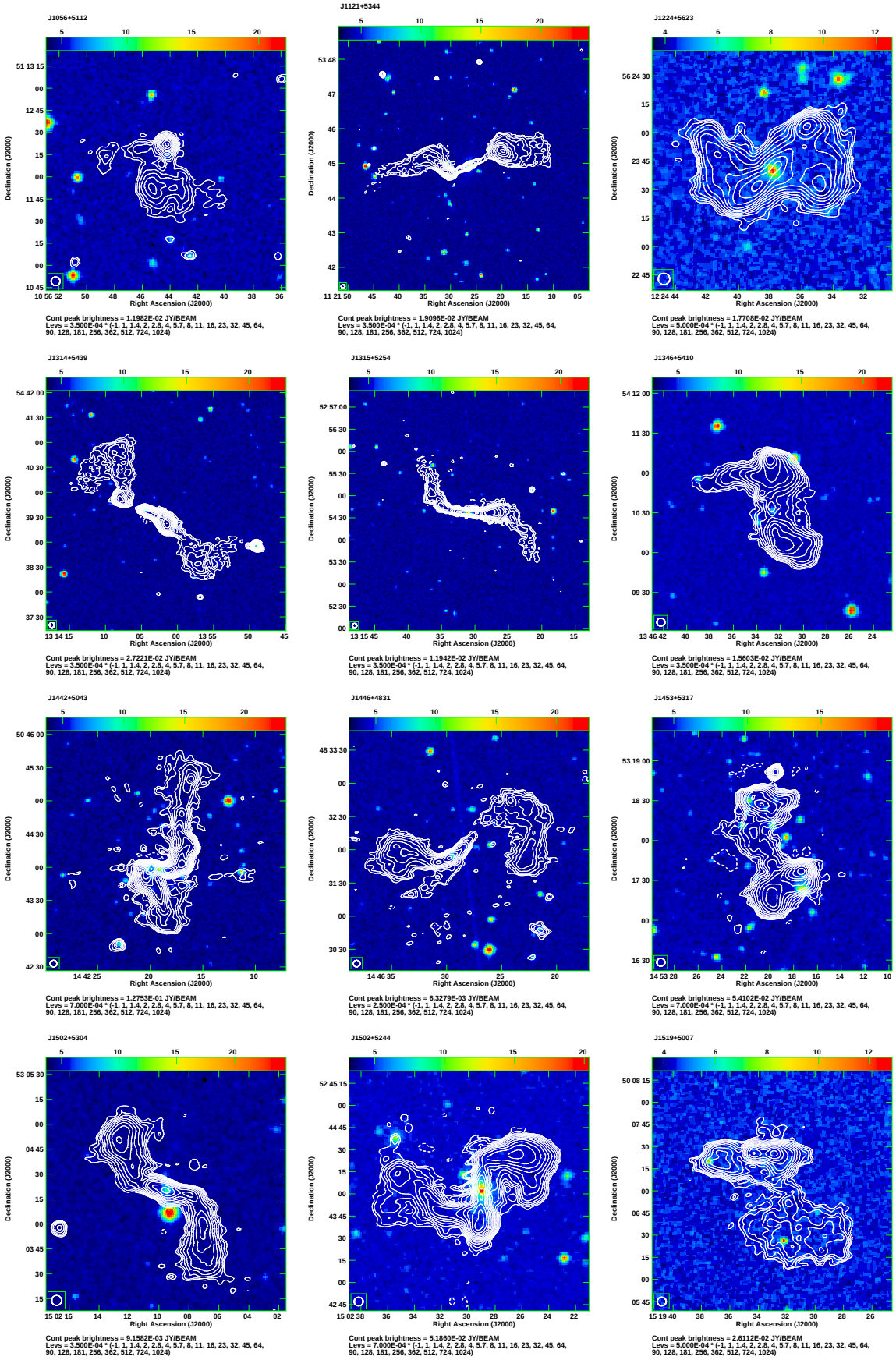

Figure 6: (D) LOFAR image of the Z-shaped radio source (contours) overlaid on the DSS2 red image (gray-scale). The relative radio contours are drawn from at least 3σ level with an increment of $\sqrt{2}$. Here, we use LOFAR $6''$ full resolution radio images for better-resolved structure.

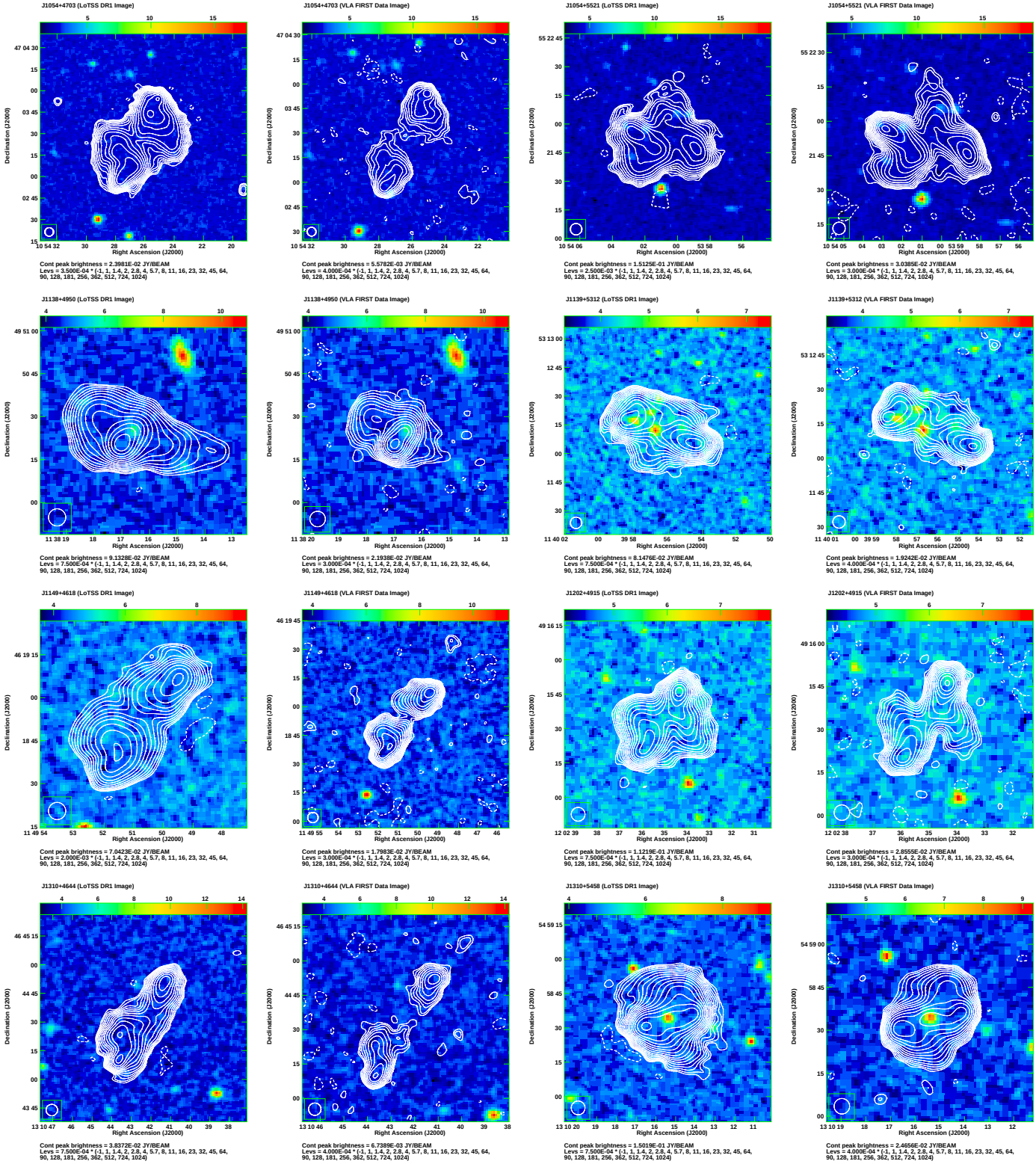

Figure 6: (E) A comparative presentation of the contour plots for the 14 sources, which are previously identified either in Cheung (2007) or Yang et al. (2019), or Bera et al. (2020) from VLA FIRST data. The LoTSS DR1 image and VLA FIRST image are presented side by side for each of the 14 sources. The radio contour images are overlaid on the respective optical DSS2 images.

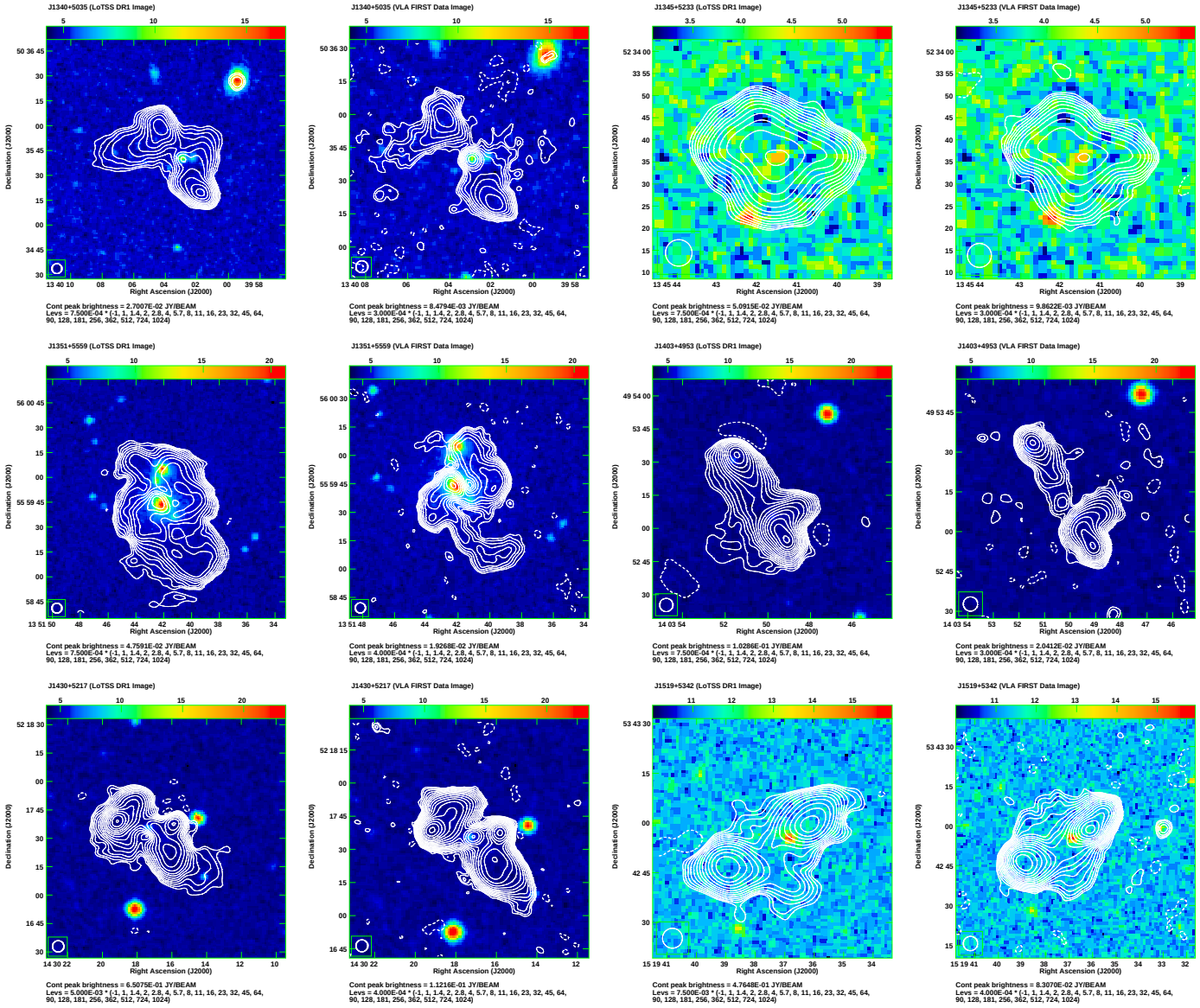

Figure 6: (E) *Continued*